Dissertation

SUBMITTED TO THE

Combined Faculties of the Natural Sciences and Mathematics
of the Ruperto-Carola-University of Heidelberg, Germany

FOR THE DEGREE OF

Doctor of Natural Sciences

Put forward by

Florian Lenz

born in: Nuremberg, Germany

Oral examination: December 9th, 2009

Classical and quantum dynamics of driven elliptical billiards

Referees:

Prof. Dr. Peter Schmelcher
Prof. Dr. Fotis K. Diakonos

Zusammenfassung

Klassische und quantenmechanische Dynamik von getriebenen elliptischen Billiards

Gegenstand dieser Arbeit ist die Untersuchung der klassichen Dynamik von getriebenen ellipitschen Billiards, sowie die Entwicklung einer numerischen Methode, welche die Propagation von beliebigen Anfangszuständen im entsprechenden quantenmechanischen System ermöglicht. Wir zeigen, dass im klassischen Billiard Fermi Beschleunigung existiert. Im Impulsraum zeigt der dazugehörige Transportprozess einen Übergang von sub- zu normaler Diffusion. Dieser Übergang wird nicht durch die Änderung eines externen Parameters hervorgerufen, sondern passiert dynamisch während der Zeitentwicklung eines Ensembles von Teilchen. Eine detaillierte Analyse des vierdimensionalen Phasenraums zeigt, dass dieser sich in verschiedenen Geschwindigkeitsbereichen unterschiedlich zusammensetzt. Eng verknüpft damit ist die sogenannte “stickiness”, welche letztentlich den Diffusionsprozess prägt. Da das Ensemble mit der Zeit beschleunigt wird, erkundet es nach und nach verschiedene Teile des Phasenraums mit dementsprechend unteschiedlichen “stickiness” Eigenschaften. Dies führt zu dem erwähnten Diffusionsübergang. Für das quantenmechanische Billiard wenden wir eine auf die Ellipse maßgeschneiderete Serie von Transformationen an. Dadurch umgehen wir die ansonsten schwierig zu behandelnden zeitabhängigen Randbedingungen. Mit Hilfe eines Entwicklungsansatzes erhalten wir so ein System von gekoppelten gewöhnlichen Differentialgleichungen, welche mit Standardverfahren gelöst werden können.

Abstract

Classical and quantum dynamics of driven elliptical billiards

Subject of this thesis is the investigation of the classical dynamics of the driven elliptical billiard and the development of a numerical method allowing the propagation of arbitrary initial states in the quantum version of the system. In the classical case, we demonstrate that there is Fermi acceleration in the driven billiard. The corresponding transport process in momentum space shows a surprising crossover from sub- to normal diffusion. This crossover is not parameter induced, but rather occurs dynamically in the evolution of the ensemble. The four-dimensional phase space is analyzed in depth, especially how its composition changes in different velocity regimes. We will show that the stickiness properties, which eventually determine the diffusion, are intimately connected with this change of the composition of the phase space with respect to velocity. In the course of the evolution, the accelerating ensemble thus explores regions of varying stickiness, leading to the mentioned crossover in the diffusion. In the quantum case, a series of transformations tailored to the elliptical billiard is applied to circumvent the time-dependent Dirichlet boundary conditions. By means of an expansion ansatz, this eventually yields a large system of coupled ordinary differential equations, which can be solved by standard techniques.

Contents

1 Introduction

Billiards are a widespread paradigm to study nonlinear dynamics in many areas of physics. Although being conceptually rather simple, they possess many classical and quantum mechanical properties of much more complex dynamical systems [1]. Billiard systems can be realized experimentally in different ways, such as using semi-conductor heterostructures [2], quantum dots [3], atom optical [4, 5] and (superconducting) microwave setups [6, 7]. Very recent applications of their dynamics are the investigation of directed emission from laser-microcavities [8–13] and the design of improved thermoelectric efficiency, where billiards are used to tailor the desired microscopic properties [14].

From a theoretical point of view, billiards have pioneered the fields of quantum chaos, modern semiclassics and transport at the mesoscopic scale (see [1] and Refs. therein). Furthermore, a justification of a probabilistic approach to statistical mechanics is based on billiards [15, 16]. Recently, it has been shown [17], that there is actually a connection between billiards and one of the major unsolved problems in mathematics, the Riemann hypothesis: the authors found an analytic expression for the escape rate of a circular billiard with two holes, involving a sum over the zeros of the Riemann zeta function.

A natural generalization of billiards with a static boundary is to apply a driving law to the billiard wall. For instance, 'Bohr's liquid drop model' from nuclear physics can be regarded as a time-dependent billiard [18]. The model assumes that the nucleus is populated by particles moving like billiard balls. Collisions among these particles are neglected, so energy exchange occurs only between the particles and the deforming nucleus. This simplistic looking model is still useful and many questions remain open [19]. Another example is plasma physics, where time-dependent billiards represent models for acceleration of particles in magnetic bottles. In particular, time-dependent billiards allow the investigation of non-equilibrium processes such as Fermi acceleration, which is the unbounded energy gain of an ensemble of particles exposed to driving forces [20].

1.1 Historical remarks and experimental realizations of billiards

The modern notion of a classical dynamical *billiard* goes back to Birkhoff in 1927 [21], who defined a billiard as the free motion of point-particles moving inside a bounded (two-dimensional) region, reflecting elastically upon collisions with the boundary of the billiard. The classical dynamics of such two-dimensional billiards can be either integrable, mixed, or fully chaotic [22]. In general, billiards possess mixed dynamics, i.e. regions of regular (integrable) and chaotic motion coexist in the corresponding phase space. Birkhoff conjectured that the only two-dimensional integrable billiards with smooth boundaries are the circle and the ellipse [21]. According to Bunimovich [23–27], the regular phase space of circular and elliptic billiards is due to focusing components of the boundary. On the other hand, billiards with strong chaotic properties usually have boundaries which are everywhere dispersing [28]. Yet, there are chaotic billiards with both focusing and dispersing components of the boundary, or even nowhere dispersing boundaries [23, 24]. Here, the mechanism causing chaos is not dispersion but defocusing [25, 26]. As already mentioned, most billiards have mixed dynamics. In phase space, the regions corresponding to integrable and chaotic motion are not separated, but interwoven in a complicated manner. This is actually not only true for billiards, but in general for most physical systems. In 2001, Bunimovich introduced a new class of billiards [29] with a mixed phase space, the so-called *mushroom* billiards [30–33], which have a remarkable property: The regular and chaotic parts in phase space are well separated from each other, i.e there is no hierarchical structure in phase space like it is typically the case.

In classical mechanics, *chaos* is defined by the great sensitivity of the motion to infinitely small changes of the initial conditions. Chaotic trajectories diverge exponentially in phase space from closely neighboring ones, whereas regular (integrable) trajectories diverge only linearly in time [34]. In quantum mechanics, this definition of chaos is not applicable [35], since it requires the simultaneous knowledge of the exact position and the exact momentum of a particle, which is of course due to the Heisenberg uncertainty principle not possible. A famous approach to chaos in quantum mechanical systems is the Bohigas-Giannoni-Schmit (BGS) conjecture [36], which states, among others, that the level spacing distribution of the energies of time-reversal-invariant quantum mechanical systems whose classical analogs are K systems[1] follow a Wigner distribution, predicted by random matrix theory for Gaussian orthogonal ensembles [1]. This is also called the *universality of the laws of level fluctuations* in quantal spectra.

Now, two-dimensional (2D) quantum mechanical billiards represent the ideal systems for the investigation of quantum chaos, for the following two reasons: Firstly, a reasonable classical analog (in the sense of the BGS conjecture) can be straightforwardly defined. Secondly, the Schrödinger equation for a 2D billiard is completely equivalent to the 2D Helmholtz equation [1] describing the propagation of classical waves in a 2D billiard, for example, the propagation of electric and magnetic fields [37]. This means, experimental studies of quantum chaos can be performed by investigating classical waves in 2D chaotic billiards, for example by studying irregularly shaped microwave cavities [6]. Stöckmann actually conjectures that *"Probably there is no essential aspect of quantum chaos which cannot be found in chaotic billiards"* [1].

The first experiment which can be regarded as the study of a billiard goes back to the end of the eighteenth century. Chladni randomly distributed dust over glass and metal plates and put these plates into vibrations by using a violin bow. He noticed that the dust forms certain patterns, the so-called *Chladni figures*. Even Napoleon showed interest in these experiments and announced a prize of 3000 francs for the correct mathematical explanation of the Chladni figures [38]. Not much experimental progress has been made concerning billiards until the end of the twentieth centuries. In 1990, the first microwave experiment has been performed [6], addressing issues of quantum chaos. Microwave billiards allow not only to study the spectrum, but also provide direct access to the wave function of a billiard. Since then, microwave billiards are one of the major experimental workhorses to study quantum chaos [1]. To obtain sharper resonances in the spectrum, superconducting microwave cavities have been employed [7, 39]. Beside chaotic billiards, systems with pseudointegrable or mixed dynamics [40–43] have been investigated. Other aspects addressed by microwave billiards include localization effects [44], systems with time-reversal broken

---

[1] K systems have positive Kolmogorov entropy, i.e. trajectories of a connected region in phase space possess a positive Lyapunov exponent [34], colloquially, these systems are called *chaotic*

symmetry [45] or even Floquet theory [46], to just mention a few.

Microwave billiards are macroscopic objects, with sizes ranging up to one meter. Whereas in these systems mainly properties concerning the energy spectrum have been addressed, mesoscopic structures are often used to study transport properties of 2D billiards [47]. Possible experimental realizations range from antidot lattices [48], over quantum dots [3] to quantum corrals [49, 50].

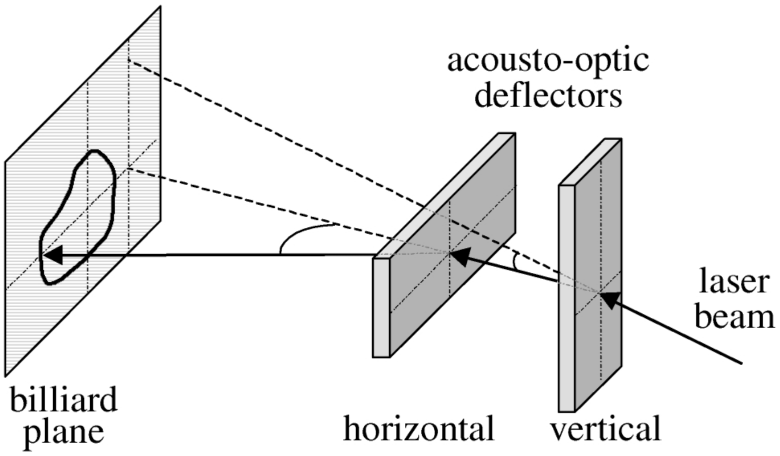

Figure 1.1: Experimental setup of an atom-optical billiard [5]. (Copyright 2001 by the American Physical Society)

In 2001, a whole new class of experimental billiards was introduced independently by the groups of Davidson [5] and Raizen [4], the so-called atom-optical billiards. To create an optical billiard, two acousto-optical modulators perpendicular to each other are used. Each of them deflects a laser beam in one of the two orthogonal directions, see Fig. 1.1. The deflection angles are scanned with about 100 kHz synchronously, thus a 2D light pattern is drawn upon a plane being perpendicular to the optical axis. Ultracold atoms ($10\mu K$) travel ballistically between the laser beams and are scattered elastically when reaching them, since the blue detuning of the lasers above the atomic resonance (for example the D_2 line of ^{85}Rb) generates a repulsive force. The corresponding dipole potential is proportional to the laser intensity and inversely proportional to the detuning [51]. Depending on the intensity and the detuning, the potential can be tuned from very soft to almost hard. Because of the fast scanning of the beam, the potential is well approximated by a static potential barrier, the billiard wall. Another blue detuned standing wave along the optical axis confines the motion of the ultracold atoms to a 2D plane. For the atomic densities used in the experiments, the mean collision time between atoms - between one and ten per second - is longer than the experiment time, hence the motion is truly ballistic. Examples for billiard geometries used by experimentalists are for example the circle, the ellipse, the titled Bunimovich stadium and the gravitational wedge [4, 5, 52, 53]. Overall, *"the unique advantage of using ultracold atoms in beams of light as a billiard system is the possibility of creating arbitrary geometries, changing them in time, varying parameters dynamically, introducing noise and decoherence, and study the role of quantum and many-body effects"* [4].

1.2 Time-dependent billiards and Fermi acceleration

Time-dependent billiards are a natural generalization of billiards with static boundaries. By *time-dependent*, we mean that the boundary of the billiard is driven, i.e. the geometry of the billiard changes in time. As a consequence, particles colliding with the moving boundary can loose or gain momentum, the energy is not conserved anymore. This allows the study of non-equilibrium processes such as Fermi acceleration (FA), which is the unbounded energy gain of particles exposed to driving forces. FA was first proposed in 1949 by Enrico Fermi [20] to explain the high energies of cosmic radiation (for a review of FA see [54]). He suggested that charged particles repeatedly interact with time-dependent magnetic fields (originating either from shockwaves of supernovae or from magnetized interstellar clouds) in such a way that on average they gain energy. Nowadays, FA is investigated in a variety of systems belonging to different areas of physics, such as astrophysics [55–57], plasma physics [58, 59], atom optics [60, 61] and has even been used for the interpretation of experimental results in atomic physics [62].

The simplest time-dependent billiards allowing the investigation of FA are the one-dimensional (1D) Fermi-Ulam model (FUM) [63] and the bouncer model [64]. In the FUM, noninteracting particles move freely (i.e. the potential is zero between the walls) in between one fixed and one oscillating wall (assumed to be infinitely heavy). In the bouncer model, particles repeatedly return to an oscillating wall due to gravity. The bouncer model, and even more the FUM and its variants have been the subject of extensive theoretical (see Refs. [65–72] and references therein) and experimental [73–75] studies. It has been proven [66] that the existence of FA in the FUM depends exclusively on the driving law of the oscillating wall: As long as the driving law is sufficiently smooth, invariant spanning curves in phase space prohibit the unlimited energy growth of particles. In contrast, in the bouncer model, already a smooth, in particular a harmonic driving law enables FA. Lichtenberg *et al.* point out [65] that *"The nature of this difference lies in the physical difference between the two problems. The transit time between wall collisions decreases with increasing particle velocity for the FUM configuration and increases with increasing velocity for the bouncer configuration."* In both setups, stochastic driving laws will lead to FA. Note that static 1D billiards (assuming zero potential inside the billiard and no particle-particle interactions) are always integrable, due to energy conservation. This implies that the corresponding static version of the FUM, particles bouncing between two fixed walls, is also integrable. In the following (actually throughout the whole thesis), we will restrict our considerations to billiards with zero potential inside the billiard region, i.e. we will not consider variants of the bouncer model.

In two dimensions (2D), the phase space of static billiards is already much richer than the one for 1D billiards and can range from integrable over mixed to fully chaotic [22]. Concerning 2D time-dependent billiards, this leads to the question how the interplay of the driving law and the phase space of the underlying static billiard determines the existence of FA. Especially, whether already a smooth, for example harmonic, driving law is sufficient to obtain FA in 2D billiards. Note that in the 1D FUM, a smooth driving law will not yield FA. Typical billiard geometries investigated in the literature with respect to FA are shown in Fig. 1.2. In Refs. [76–78], the existence of FA was shown for a harmonically oscillating stadium-like billiard (see Fig. 1.2f) and the authors conjectured that a sufficient condition for the occurrence of FA in a driven 2D billiard is the existence of a chaotic part in the phase space of the corresponding static system ('frozen' billiard). Note that the corresponding static stadium billiard is completely chaotic [22]. This so-called "LRA conjecture" (where the term "LRA" is an acronym for the names of the authors of [76]) is supported by the absence (presence) of FA in the oscillating circular billiard [79, 80], see Fig. 1.2a, (eccentric annular billiard [81, 82], Fig. 1.2d), where the corresponding static system is integrable

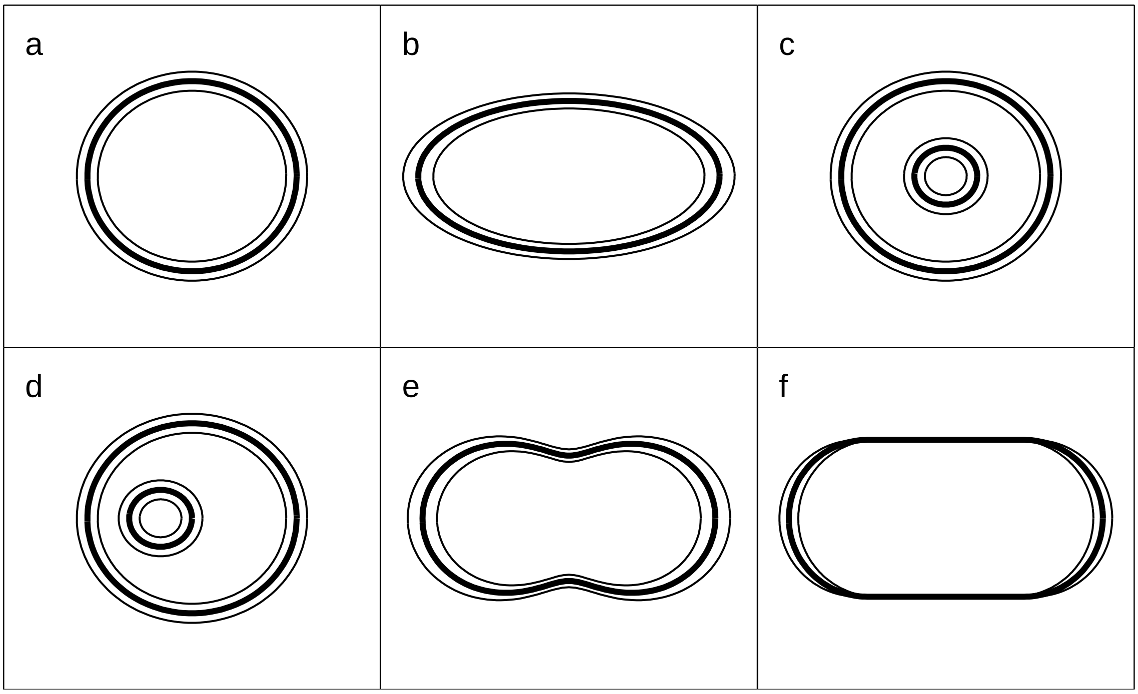

Figure 1.2: Billiard geometries of different driven billiards, thick lines represent the equilibrium position, thin lines are the minimal and maximal extension of the driven billiards, respectively: circle (a), ellipse (b), concentric (c) and eccentric annulus (d), oval (e), stadium (f).

(has a mixed phase space). The absence of FA in the oscillating circle is due to the fact that the angular momentum, which is a constant of motion in the static circular billiard, is still conserved in the driven circle. This allows the construction of invariant hypersurfaces in phase space which eventually bound the energy growth of particles [79]. The same arguments are true for the concentric annular billiard, see Fig. 1.2c, as a consequence, there is no FA in the driven version [81].

The driven elliptical billiard, see Fig.1.2b, is investigated in Refs. [83] and [84], with a focus on the derivation of the corresponding 4D discrete mapping. The authors mention that the energy stays bounded in the time-dependent elliptical billiard, but do not provide any evidence. A certain driven oval-shaped billiard, see Fig.1.2e, shows an ambivalent behavior concerning the existence of FA [85] (note that the static oval billiard possesses a mixed phase space). When driving the oval in such a way that it is a pure scaling ('scaling mode'), no FA is observed, whereas for a shape changing[2] time-dependence of the boundary the oval shows FA. The former finding violates the LRA-conjecture, since according to this conjecture, the driven oval should exhibit FA even in the scaling mode.

An overview concerning FA in 2D time-dependent billiards with a harmonic driving law is shown in Table 1.1. Obviously, the LRA-conjecture cannot be the full story: First of all, the oval in the scaling mode should exhibit FA according to this conjecture, and secondly, the are serious doubts whether the "no" in the case of the elliptical billiard is correct. Even though the existence of FA in the elliptical billiard would not violate the

---

[2] Nevertheless the billiard is at all times still an oval, but with a differently pronounced indentation. For details, see the discussion in section 6.4.

Static counterpart	**FA for harmonic driving?**
integrable	
circle	no
concentric annular	no
ellipse	no?
mixed	
eccentric annular	yes
oval, scaling mode	no
oval, shape changing	yes
chaotic	
stadium	yes

Table 1.1: State of the art of the literature concerning Fermi acceleration (FA) in two-dimensional time-dependent billiards with a harmonic driving law. The geometries of the different billiard systems are shown in Fig. 1.2.

LRA-conjecture, since it states that chaotic parts in the phase space of the underlying static system are a sufficient and not a necessary condition, it would suggest that the LRA-conjecture represents a too crude simplification of the problem. This means, the central question: *Under which conditions will FA arise in 2D billiards?* is still not completely answered.

Except for two studies dealing with resonant phenomena of slowly varying billiards [86,87] and two other works investigating escape rates of driven elliptical billiards [88,89], the focus of the research concerning time-dependent 2D billiards is certainly on FA [76–85]. Apart from whether FA is present in these systems, little is known about 2D driven billiards. One reason is that the phase space of a driven 2D billiard is four-dimensional (4D), making representative visualizations, like the so-called Poincaré surface of sections [34] difficult. Furthermore, the numerical iteration of the corresponding 4D mapping is demanding from a computational point of view [90]. As a consequence, none of the works [76–85] analyzed the full 4D phase space nor addressed the long-term behavior of dynamical quantities in these billiards.

Concerning the quantum dynamics of time-dependent billiards, there are several studies investigating the quantum version of the one-dimensional Fermi-Ulam model (or variants of it) [91–102]. Since the model involves time-dependent Dirichlet boundary conditions which are difficult to treat, both analytically and numerically, most of these works analyze which (non-periodic) movements of the wall allow for exact solutions: Linearly expanding or contracing wall motion is considered in Refs. [91] and [95]. The authors of Refs. [93, 94] find that exact solutions are not only possbible for linear wall motion, but for a time-law of the form $l(t) = \sqrt{at^2 + 2bt + c}$ (with some real constants a, b and c). The same time-law is found from a different perspective in [96, 99] and by means of a supersymmetry formalism in [101]. If additionally a certain electro-magnetic field is superimposed, exact solutions can be obtained for arbitrary time-dependencies of the wall motion [100]. Periodic driving laws are considered in Refs. [92] and [102]. The Floquet or quasienergy spectrum is found to be pure point like for most wall oscillations, resulting in recurrent dynamics and thus to a bounded energy growth [92]. Only certain (non-smooth) driving laws yield a continuous quasienergy spectrum and thus allow for unbounded acceleration via resonance excitations, similarly to the quantum kicked rotator [103]. Very recently, the authors of [102] studied the quantum FUM numerically by expanding the wave function in terms of the instantaneous eigenstates of the corresponding static system. They find that the dynamics of the time-dependent expansion coefficients is chaotic in an intermediate frequency (of the driving) regime, whereas for very low and very high frequencies a periodic behavior of the expansion coefficients is obtained.

For quantum billiards with time-dependent boundaries with dimensions higher than one, there are, to our knowledge, two studies only [104, 105]. In [105], the one-pulse response of a 2D stadium billiard to a deformation of the boundary is studied and the authors find both parametric and stochastic components in the evolving energy distribution. In [104], the radially vibrating 3D spherical billiard is investigated. The authors claim that only superposition states that share the same common rotational symmetry yield chaos, since the orthogonality relations of the instantaneous eigenstates allow in any other case a reduction to a one degree of freedom Hamiltonian which cannot be chaotic. However, their arguments are based on the correspondence between the classical and quantum 3D driven spherical billiard. By doing so, they state that in the classical system, the angular momentum, which is a constant of the motion in the static case, gets destroyed by the driving. This is simply not correct, since it is known, see for example Ref. [79], that in the radially oscillating circular billiard the angular momentum is still conserved and the arguments can be generalized straightforwardly to the 3D spherical billiard. Thus, the results of Ref. [104] have to be treated with caution.

1.3 Objectives of this work

This thesis is divided into two fairly independent parts, the first addressing the classical dynamics and the second the quantum dynamics of driven elliptical billiards, with a focus on the first part.

Classical dynamics

In the first part of the thesis, we aspire a thorough and detailed investigation of the classical dynamics of the time-dependent elliptical billiard. In particular, we study the diffusion in momentum space and show that the mean energy of an ensemble of particles grows over all bounds, i.e. there is Fermi acceleration in the driven elliptical billiard. Furthermore, the transport in momentum space exhibits an unexpected dynamical crossover from sub- to normal diffusion in its long-term evolution. As we will see, the choice of the driving mode influences the diffusion properties and we will thus compare the *breathing mode* to two other representative modes, namely to the *constant eccentricity* and *the quadrupole mode*. We will show that while a crossover from sub- to normal diffusion is also present in the quadrupole mode, the constant eccentricity mode shows exclusively subdiffusion, even asymptotically. For the understanding of these different behaviors, the stickiness properties play a crucial role. In the course of the ensemble's evolution, the mean velocity v increases, the ensemble thus traces different parts (in terms of v) of the phase space. For low v, the phase space consists of a large chaotic sea that contains many small regular islands. For high v, the composition is quite different: Thin channels of chaotic motion are squeezed in between large bulky regular regions. While the stickiness properties are enhanced in the low v regime, they are suppressed for high velocities. As a consequence, as long as the ensemble of particles is predominantly at low v it will exhibit sub-diffusion (all modes, at least for small driving amplitudes), whereas once it is mostly inside the thin channels of chaotic motion located at high v, the diffusion process in momentum space becomes normal (breathing and quadrupole mode).

This first part of the thesis, dealing with the classical dynamics of the driven elliptical billiard, is subdivided into five chapters. In each chapter, the breathing mode is discussed in depth, the two other driving modes (constant eccentricity and quadrupole mode) are considered separately at the end of each chapter.

- First of all, the basic properties of the static elliptical billiard are treated in chapter 2 and especially the role of the second constant of motion F, which is the product of the angular momenta around the two foci, is elucidated. Subsequently, the time-dependent elliptical billiard together with the three different driving modes is introduced. It is shown that a four-dimensional discrete (implicit) mapping is sufficient to completely specify the dynamics and the corresponding preserved measure is derived. Due to the driving, neither the energy nor the quantity F is conserved. As a consequence, transitions via separatrix crossings between rotational and librational motion are now possible. These separatrix crossings will be important when investigating the diffusion in momentum space.

- Chapter 3 is concerned with the examination of the phase space of the driven billiard. Since the phase space is four-dimensional, direct visualizations are impossible. Instead, we let an ensemble of particles propagate and study which parts of phase space it visits by defining appropriate lower-dimensional phase space densities: At low velocities the phase space consists of a large chaotic sea. With increasing velocity, the ensemble is squeezed more and more onto a thin channel, due to the existence of impenetrable bulky regions of regular motion. The origin of these large invariant structures will be illustrated in detail.

- To gain further insight into the properties of phase space, periodic orbits are investigated in chapter 4. The density of periodic orbits inside the low v chaotic sea is considerably higher than the density inside the thin chaotic channels, which are present at high velocities. This will be one of the reasons for the changing stickiness properties, which are described in the next chapter. At the end of this chapter, an intermediate summary will be given in section 4.6, taking into account the results obtained so far.

- Chapter 5 describes stickiness effects. We will show that there is an intermittend interplay of laminar (sticky) and stochastic phases. The stochastic phases are associated with repeated separatrix crossings of the trajectories, whereas the sticky (laminar) phases correspond to pure rotational or pure librational motion. By, among others, investigating the distribution of the length of the laminar phases, we demonstrate that the stickiness properties are enhanced in the low v regime and are suppressed for high velocities

- Finally, the diffusion in momentum space is investigated in chapter 6. The observed crossover from sub- to normal diffusion is related to the phase space and stickiness properties, which are described in the preceding chapters. Based on the results of this work, a general discussion on FA in 2D driven billiards is presented in section 6.4, including a new conjecture concerning the question under which conditions FA arises in time-dependent 2D billiards.

Quantum dynamics

In the second part of the thesis, the quantum version of the time-dependent elliptical billiard is investigated. Since there are no standard methods available to tackle this problem, a numerical procedure for the time-propagation of an arbitrary initial state is developed, tailored to the properties of the driven elliptical billiard. Finally, this procedure is exemplarily applied to the breathing mode of the billiard to obtain the evolution of the energy of various initial states in different frequency regimes of the driving.

- In chapter 7, the standard procedure to solve the stationary Schrödinger equation for the static elliptical billiard is reviewed. The eigenstates are obtained by introducing elliptical coordinates, yielding two coupled Mathieu equations, whose solutions are the ordinary and modified Mathieu functions. Subsequently, the symmetry properties of the eigenstates are discussed.

- The numerical method to propagate an arbitrary initial state in the driven elliptical billiard is developed in chapter 8. To eliminate the time-dependent Dirichlet boundary conditions, a series of transformations is applied. Together with an expansion ansatz into eigenstates of the static circular billiard, this yields eventually a large set of ordinary coupled differential equations, which can be solved by standard techniques. Using the eigenstates of the static circular billiard, which are basically a product of Bessel functions and simple harmonic functions, has the advantage that the Bessel functions, and even more derivatives of Bessel functions are numerically much easier to handle than the (derivatives of) Mathieu functions. Exemplarily, this numerical procedure is used for different frequencies of the driving law to calculate the evolution of the energy of various initial states.

The last chapter summarizes the results of this thesis, both, of the classical and the quantum mechanical part and finally an outlook is given.

Part I

Classical dynamics

2 Basic properties of the elliptical billiard

In this chapter, we introduce the static and the driven elliptical billiard. In the static case, we discuss the phase space, periodic orbits and the product of the angular momenta about the two foci, which is the second constant of motion. In the driven case, the corresponding four-dimensional discrete mapping is derived and the basic properties of the mapping are investigated.

2.1 Static elliptical billiard

2.1.1 Definition

The physical system of a particle inside a two-dimensional elliptical billiard can be rigorously defined by the Lagrangian [106]

$$\mathcal{L} = \frac{m}{2}\left(\dot{x}^2 + \dot{y}^2\right) - V(x,y), \tag{2.1}$$

where m is the mass of the particle and the potential $V(x,y)$ is given by

$$V(x,y) = \left\{ \begin{array}{ll} 0 & \text{if } x^2/a^2 + y^2/b^2 \leq 1 \\ \infty & \text{if } x^2/a^2 + y^2/b^2 > 1. \end{array} \right. \tag{2.2}$$

In other words, the boundary $\mathcal{B}$ of the ellipse is given by

$$\mathcal{B} = \left\{ (x,y)^\top \in \mathbb{R}^2 \middle| \frac{x^2}{a^2} + \frac{y^2}{b^2} = 1 \right\} \tag{2.3}$$

and the potential $V(x,y)$ is zero inside and infinity outside the boundary of the ellipse given by (2.3). We assume $a > b$, which implies that the semi-major axis of the ellipse is given by a and the semi-minor axis by b. The two foci lie at $(\pm e, 0)^\top$, where $f = \sqrt{a^2 - b^2}$ is the linear eccentricity. More common to characterize an ellipse is the dimensionless numerical eccentricity ϵ

$$\epsilon = \frac{f}{a} = \sqrt{1 - \frac{b^2}{a^2}}, \quad 0 \leq \epsilon < 1. \tag{2.4}$$

Throughout the whole thesis, when referring simply to the *eccentricity*, we mean the numerical eccentricity (2.4).

Since $\mathcal{B}$ is a one-dimensional closed curve, it can be characterized by a single, 2π-periodic parameter ϕ, which is more convenient for our purposes:

$$\mathcal{B} = \left\{ \left(\begin{array}{c} a\cos\phi \\ b\sin\phi \end{array} \right) \middle| 0 \leq \phi < 2\pi \right\} \tag{2.5}$$

2.1.2 Mapping

A particle inside the elliptical billiard travels ballistically on straight lines until it will hit the boundary of the ellipse. Upon collisions with the boundary, it is reflected elastically, i.e. the angle of incidence is equal to the angle of reflection. Due to the ballistic motion in between collisions, an orbit of a single particle generated by N collisions with the boundary can be completely specified by the sequence of its positions and directions immediately after each collision with $\mathcal{B}$. The position on $\mathcal{B}$ is parametrized by ϕ and the direction by α, where α is the angle between the forward pointing tangent and the particle's velocity right after the impact. Rather than solving the equations of motion associated with the Lagrangian (2.1), we can use a discrete mapping $\mathcal{M}$ to evolve an initial condition $(\phi_0, \alpha_0)^\top$:

$$\left(\begin{array}{c} \phi_{n+1} \\ \alpha_{n+1} \end{array} \right) = \mathcal{M} \left(\begin{array}{c} \phi_n \\ \alpha_n \end{array} \right), \tag{2.6}$$

where the index n indicates the nth collision with the boundary. Hence, the point set

$$\mathcal{T} = \{(\varphi_n, \alpha_n)^\top | \, i = 0, 1, 2, \dots N\} \tag{2.7}$$

represents a trajectory, with initial condition $(\phi_0, \alpha_0)^\top$, after N collisions with the boundary in the so-called Poincaré surface of section (PSS), see section 2.1.4.

Instead of using $(\phi, \alpha)^\top$ to specify a point in the PSS, we could also use two different variables $(s, p)^\top$, where s is the arclength between, for example, the point $(a, 0)^\top$ and $(a \cos\phi, b \sin\phi)^\top$ and $p = \cos\alpha$. In a sense, the variables s, p represent the canonical choice, since in these variables, the mapping $\mathcal{M}$ is area-preserving [22], i.e.

$$\frac{\partial(s_{n+1}, p_{n+1})}{\partial(s_n, p_0)} = \left| \begin{array}{cc} \partial s_{n+1}/\partial s_n & \partial s_{n+1}/\partial p_n \\ \partial p_{n+1}/\partial s_n & \partial p_{n+1}/\partial p_n \end{array} \right| = 1. \tag{2.8}$$

For a discrete mapping, the area-preserving property (2.8) is the equivalence to the Liouville theorem for Hamiltonian flows [34]. From a practical point of view, the drawback of using s, p instead of ϕ, α is that determining s requires the calculation of elliptical integrals. We will thus use the variables ϕ, α in the following. In terms of ϕ, α, the mapping $\mathcal{M}$ (2.6) is not area-preserving, rather it preserves the invariant measure [84]

$$d\mu = R(\phi) \sin\alpha \, d\alpha d\phi, \tag{2.9}$$

where $R(\phi)$ is the radius of curvature given by

$$R(\phi) = \frac{ab}{\left(a^2 \sin^2\phi + b^2 \cos^2\phi\right)^{\frac{3}{2}}}. \tag{2.10}$$

The mapping $\mathcal{M}$ and the invariant measure $d\mu$ are special cases of the corresponding quantities in the driven elliptical billiard, which will be deduced in detail in sections 2.2.3 and 2.2.4, for that reason they are not shown here.

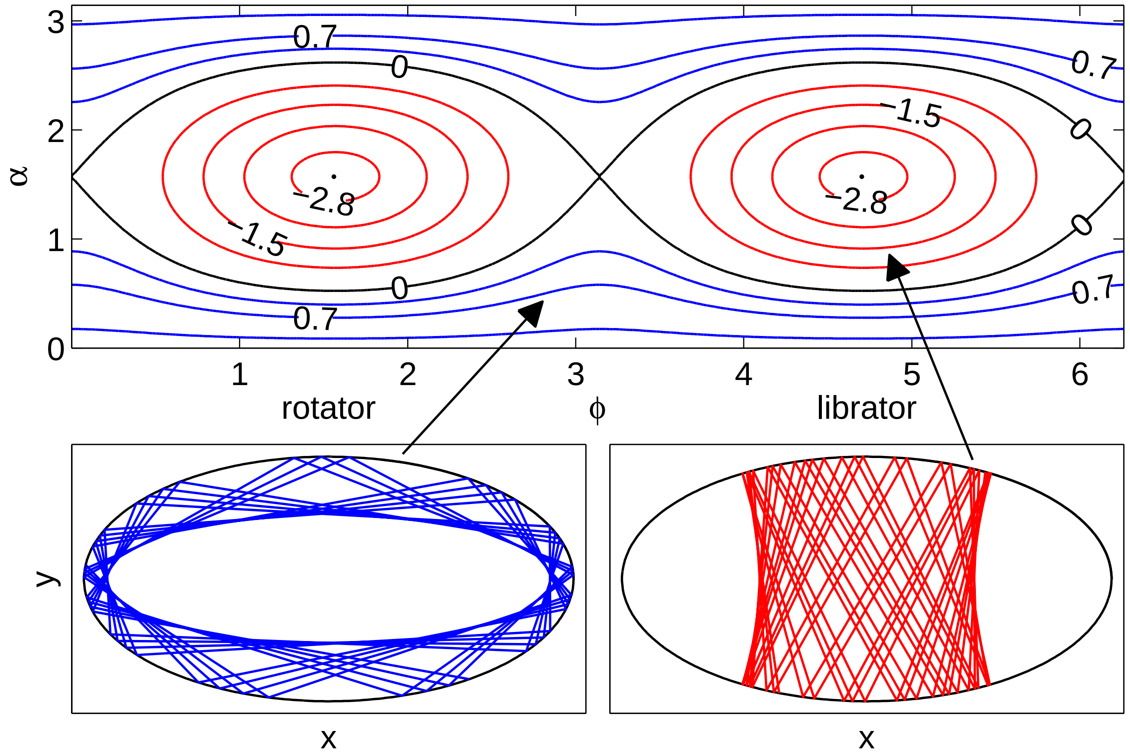

Figure 2.1: Poincaré surface of section of the static elliptical billiard for 8 different initial conditions (upper panel) and typical trajectories in coordinate space (lower panel). The invariant curves in phase space are the $F = const.$ contours. The phase space is divided by the separatrix $F = 0$ into *rotators* (in blue) and *librators* (in red). Rotators have an inner confocal elliptic caustic and librators generate two confocal hyperbolas as caustics.

2.1.3 Constants of motion

The ellipse is an integrable billiard, so there are as many (two) constants of motion as degrees of freedom. The first constant of motion is the energy. This is trivial, since the potential is zero inside the ellipse and particles are reflected elastically upon collisions with the boundary. Besides the energy, the quantity

$$F(\phi, \alpha) = \frac{\cos^2 \alpha \cdot (1 + (1 - \epsilon^2) \cot^2 \phi) - \epsilon^2}{1 + (1 - \epsilon^2) \cot^2 \phi - \epsilon^2} \tag{2.11}$$

is a second constant of motion. It can be physically interpreted as the product of the angular momenta about the two foci [22]. F is restricted to the range $[F_{\min} = -\epsilon^2/(1-\epsilon^2), 1]$. The value of F of an orbit determines the kind of motion that is generated:

1. Orbits with $F(\phi, \alpha) > 0$ correspond to trajectories with a confocal elliptical caustic and are called *rotators*. In the PSS they explore every value of ϕ but are restricted in α. They cross the x-axis always outside the two foci.

2. Orbits with $F(\phi, \alpha) < 0$ are trajectories which always cross the x-axis between the two foci. They generate two caustics in the form of confocal hyperbolas and are called *librators*. They explore a restricted interval in ϕ and α in phase space.

3. The orbit with $F(\phi, \alpha) = 0$ constitutes the separatrix. It crosses the x-axis exactly at the focus points.

2.1.4 Phase space

The phase space associated with the Lagrangian (2.1) is of course four-dimensional (4D), spanned by the variables p_x, p_y, x, y. However, due to energy conservation, any initial conditions will explore a 3D energy shell merely. By specifying points on this energy shell only that correspond to collisions with the boundary, which is equivalent to using the discrete mapping (2.6), the dimension is further reduced by one[1]. This special representation is a Poincaré surface of section (PSS). We will use the terms PSS and phase space interchangeably, since for 2D billiards, all the information contained in the phase space is also contained in the PSS. Note that deducing a PSS, which corresponds always to a discrete mapping, from a continuous trajectory in phase space is not only applicable on billiards, but is a much more general concept [34, 66].

The phase space of the elliptical billiard is given by the rectangle $0 \leq \phi < 2\pi$, $0 \leq \alpha \leq \pi$, but since ϕ is 2π-periodic, the true topology is that of torus [22]. The PSS is shown in Fig. 2.1 (for $a = 2$, $b = 1$). The separatrix $F = 0$ divides the phase space into rotators ($F > 0$) and librators ($F < 0$). The $F = \mathit{const.}$ isolines in phase space are *invariant curves.* Such an invariant curve is mapped by $\mathcal{M}$ onto itself, although this is not true for its individual points. The topology of the PSS is dominated by two period two orbits: Firstly, the one bouncing along the semi-minor axis, with $(\phi_0 = \pi/2, \alpha_0 = \pi/2)$, $(\phi_1 = 3\pi/2, \alpha_1 = \pi/2)$ and $F = F_{\text{min}} = -\epsilon^2/(1 - \epsilon^2) = -3$. Secondly, the diametral orbit along the semi-major axis with $(\phi_0 = 0, \alpha_0 = \pi/2)$, $(\phi_1 = \pi, \alpha_1 = \pi/2)$ and $F = 0$. The stability of these period two orbits can be characterized using the following criterion [22]:

$$\frac{\rho}{2R(\varphi)} - 1 \begin{cases} > 0 & \text{unstable} \\ < 0 & \text{stable,} \end{cases} \tag{2.12}$$

where $R(\varphi)$ is the radius of curvature (2.10) and ρ is the orbit's length in coordinate space. For the trajectory along the semi-major axis $\frac{\rho}{2R} = \frac{1}{1-\epsilon^2} > 1$, thus, this orbit is unstable (hyperbolic fixed point). The orbit along the semi-minor axis obeys $\frac{\rho}{2R} = 1 - \epsilon^2 < 1$ and hence it is stable (elliptic fixed point).

According to Ref. [106], Poncelete's theorem on projective geometry can be applied to the elliptical billiard. It states that all trajectories with the same value of $F(\phi, \alpha)$ share the same caustic and the same dynamics. Hence, if there is a periodic orbit with a certain value of $F(\phi, \alpha) = F_0$, then all trajectories with $F = F_0$ will also be periodic and have the same period. Thus, the only isolated periodic orbits are the two discussed diametral two-bounce orbits. All the other periodic orbits are non-isolated and form families filling up invariant curves.

2.1.5 Periodic orbits

For a later discussion concerning periodic orbits in the driven elliptical billiard, it is instructive to look at the distribution of the periodic orbits in phase space in the static ellipse. The periodic orbits of an integrable system can be found using the fact that the

---

[1] The existence of the second constant of motion F further restricts the motion in the 2D PSS to 1D curves.

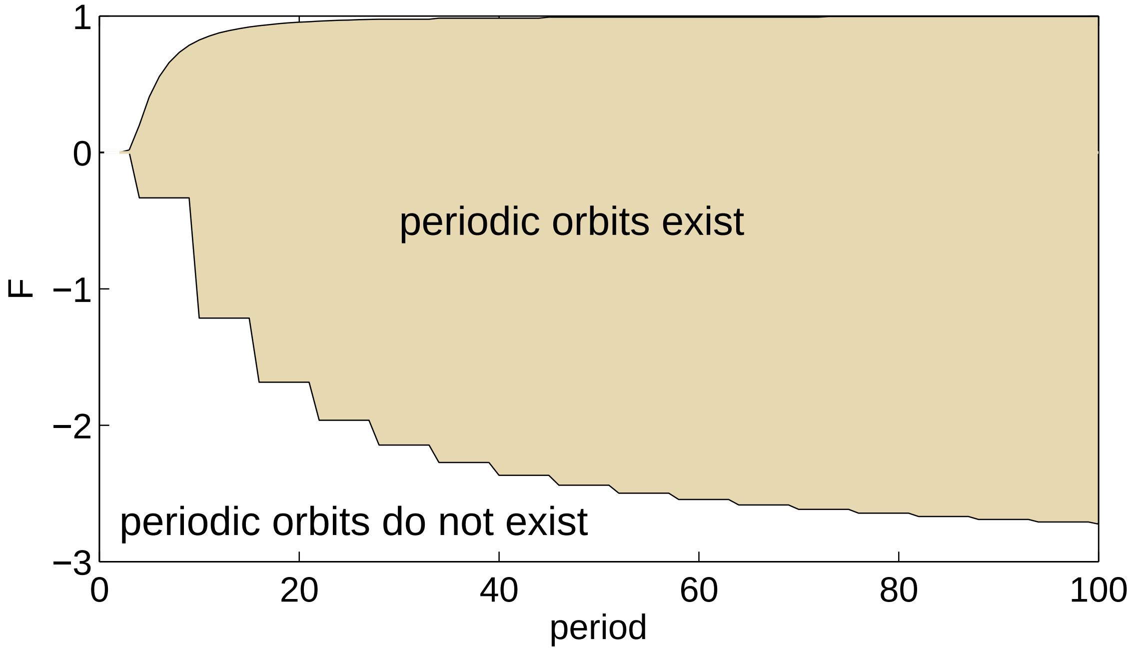

Figure 2.2: Regions in F space that allow for the existence of periodic orbits as a function of the period. The existence of periodic orbits deep in the librator region, i.e. values of F towards -3, requires comparatively large periods. Consequently, periodic orbits with short periods are located around the separatrix ($F = 0$).

winding number w of a torus must be a rational number [107]. The winding number w can be calculated by applying the Hamilton-Jacobi formalism and introducing action-angle variables [108]. This leads to (for a detailed derivation see Appendix A)

$$w_{n,r} = \frac{r}{n} = \frac{F_{el}(\theta_1, \frac{1}{\epsilon_c^2})}{2K(\frac{1}{\epsilon_c^2})} \quad F < 0 \quad \text{librators} \tag{2.13a}$$

$$w_{n,r} = \frac{r}{n} = \frac{F_{el}(\theta_2, \epsilon_c^2)}{2K(\epsilon_c^2)} \quad F > 0 \quad \text{rotators} \tag{2.13b}$$

where the angles θ_1, θ_2 are given by $\sin\theta_1 = 1/\sqrt{1-F}, \sin\theta_2 = \sqrt{1-F}$. $F_{el}(\theta, m)$ is the incomplete elliptic integral of the first kind given by

$$F_{el}(\theta, m) = \int_0^\theta \frac{d\theta}{\sqrt{1 - m\sin^2\theta}} \tag{2.14}$$

and $K(m) = F_{el}(\pi/2, m)$ denotes the corresponding complete integral. The eccentricity of the caustic is $\epsilon_c = 1/\sqrt{1 + Fb^2/f^2}$ and $f = \sqrt{a^2 - b^2}$ is the linear eccentricity of the ellipse. n is the number of bounces at the boundary, i.e. the period of the orbit, r is the rotation number. Equation (2.13) has real solutions for $n \geq 4, r < n/2$, equation (2.13b) for $n \geq 3, r < n/2$. For $F = 0$ the winding number w reaches its maximum and decreases monotonically both with increasing and decreasing F. Hence, the periodic orbits with short periods are located around the separatrix ($F = 0$). The existence of periodic orbits in the librator-region close to the elliptic fixed points and in the rotator-regime close to the whispering-gallery orbits ($F \approx 1$) requires comparably long periods. This behavior can be seen in Fig. 2.2, where those regions (in terms of F) where periodic orbits exist are shown as a function of the period. Note that the periodic orbit along the semiminor axis with $F_{\min} = -\epsilon^2/(1-\epsilon^2) = -3$ exists for all even periods, thus this periodic orbit is not considered in this plot.

2.2 Time-dependent elliptical billiard

2.2.1 Definition

A natural extension of the static elliptical billiard is to apply a driving law to the boundary. In complete analogy to the static case, see section 2.1.1, the physical system of a particle with mass m inside the two-dimensional billiard with a moving boundary is described by the Lagrangian

$$\mathcal{L} = \frac{m}{2}\left(\dot{x}^2 + \dot{y}^2\right) - V(x,y,t), \tag{2.15}$$

where the potential $V(x,y,t)$ is now explicitly time-dependent and given by

$$V(x,y,t) = \begin{cases} 0 & \text{if } x^2/a^2(t) + y^2/b^2(t) \le 1 \\ \infty & \text{if } x^2/a^2(t) + y^2/b^2(t) > 1. \end{cases} \tag{2.16}$$

The functions $a(t)$ and $b(t)$ are the *driving functions* and determine how the shape of the boundary changes in time. We choose $a(t)$ and $b(t)$ to be harmonic functions with period T, which are defined differently by the different driving modes, see the next section 2.2.2.

The boundary $\mathcal{B}(t)$ of the driven elliptical billiard is at a given time t still a one-dimensional closed curve, which depends explicitly on the time t. Like in the static case (2.5), the boundary can be characterized by a single, 2π-periodic parameter ϕ:

$$\mathcal{B}(t) = \left\{ \begin{pmatrix} a(t)\cos\phi \\ b(t)\sin\phi \end{pmatrix} \middle| 0 \le \phi < 2\pi \right\}. \tag{2.17}$$

2.2.2 Driving modes

We still have to specify how the semi-minor and semi-major axes of the billiard change in time, i.e. the functions $a(t)$, $b(t)$ (2.17), this determines the *driving mode*. In this thesis we will focus on the *breathing mode*, but compare the results exemplarily to the ones of the *constant eccentricity* and the *quadrupole mode*. For all modes, $a(t)$ is given by the harmonic function

$$a(t) = a_0 + C\sin(\omega t), \tag{2.18}$$

where C is the driving amplitude and ω the driving frequency. We fix $\omega = 1$ (arbitrary units), since ω just changes the natural momentum scale ωC of the system, but the dynamics is rather controlled by the driving amplitude C, see section 3.5.1.

Breathing mode

$$a(t) = a_0 + C\sin(\omega t) \tag{2.19a}$$
$$b(t) = b_0 + C\sin(\omega t) \tag{2.19b}$$

This choice of $a(t)$ and $b(t)$ corresponds to a concentric mode, see Fig. 2.5a. We fix $a_0 = 2$ and $b_0 = 1$ such that we obtain for $t = 0$ an ellipse with $\epsilon_0 = \sqrt{1 - b_0^2/a_0^2} \approx 0.87$, which is far away from the circle ($\epsilon = 0$). The eccentricity ϵ is time-dependent

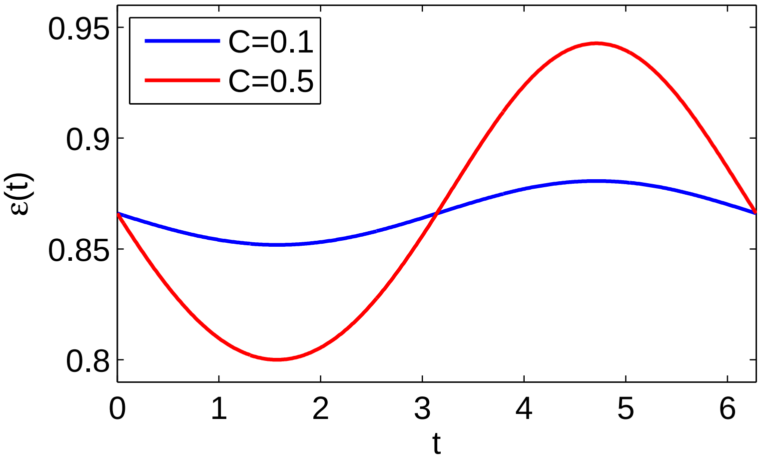

Figure 2.3: Eccentricity $\epsilon(t)$ in the breathing mode as a function of time, for two different driving amplitudes $C = 0.1$ and $C = 0.5$.

$$\epsilon(t) = \sqrt{1 - b^2(t)/a^2(t)}, \tag{2.20}$$

so the billiard actually changes its shape. The breathing mode is not just a scaling of the ellipse corresponding to a_0 and b_0. The eccentricity as a function of time is shown in Fig. 2.3 for two different driving amplitudes $C = 0.1$ and $C = 0.5$. The eccentricity performs a sinusoidally-like oscillation and the amplitude of the oscillation increases with increasing driving amplitude C.

Constant eccentricity mode

$$a(t) = a_0 + C\sin(\omega t) \tag{2.21a}$$
$$b(t) = a(t)\sqrt{1 - \epsilon_0^2} = a(t)\frac{b_0}{a_0} \tag{2.21b}$$

Like in the breathing mode, we fix $a_0 = 2$, $b_0 = 1$. The constant eccentricity mode performs also a concentric oscillation, see Fig. 2.5c. In contrast to the breathing mode, the eccentricity is now constant

$$\epsilon(t) = \sqrt{1 - \frac{b^2(t)}{a^2(t)}} = \sqrt{1 - \frac{b_0^2}{a_0^2}} = \epsilon_0 = \text{const.} \tag{2.22}$$

and also independent of the driving amplitude.

According to the discussion in section 2.1, the structure of the phase space of the static elliptical billiard is completely defined by its eccentricity (it is invariant under a pure scaling transformation). Thus, in the constant eccentricity mode, the phase space of the corresponding frozen billiard[2], is always, i.e. for all phases ξ (where the phase ξ is simply t modulus the driving period T), the same, because the mode performs just a scaling of the ellipse's extension in configuration space. Obviously, this is not true anymore for the breathing mode, since in this case the eccentricity varies with time.

Quadrupole mode

$$a(t) = a_0 + C\sin(\omega t) \tag{2.23a}$$

$$b(t) = b_0 - C\sin(\omega t) \tag{2.23b}$$

We fix $a_0 = b_0 = 1$, so the billiard is a circle at $t = 0$, see Fig. 2.5b. The reason why we choose a_0 differently than in the other modes is the following: If $a_0 \neq b_0$, then (let's assume $a_0 > b_0$) it depends on the driving amplitude whether $\min(a(t)) < \max(b(t))$. In other words, for small amplitudes $a(t)$ is always larger than $b(t)$, whereas for amplitudes larger than a certain critical value, the semi-major and semi-minor axes periodically interchange. The choice $a_0 = b_0$ ensures that this periodic interchange occurs for all amplitudes $C > 0$. Due to this periodic interchange of the semi-major and minor axes, we have to define the eccentricity slightly different, now

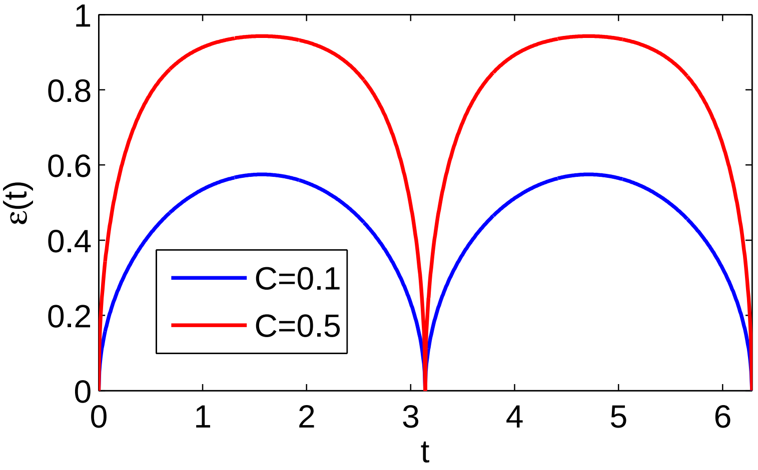

Figure 2.4: Eccentricity $\epsilon(t)$ in the quadrupole mode as a function of time, for two different driving amplitudes $C = 0.1$ and $C = 0.5$.

$$\epsilon(t) = \begin{cases} \sqrt{1 - \frac{b^2(t)}{a^2(t)}} & a(t) \geq b(t) \\ \sqrt{1 - \frac{a^2(t)}{b^2(t)}} & b(t) > a(t). \end{cases} \tag{2.24}$$

The time-dependence of the eccentricity is shown in Fig. 2.4 for two different driving amplitudes. The eccentricity becomes zero twice during one period $T = 2\pi$, each time the semi-major and semi-minor axes are interchanged. The maximum value of ϵ is reached at

---

[2] For the definition of the frozen billiard, see section 2.2.5.

$t = \pi/2$ and $t = 3\pi/2$ and is given by

$$\epsilon_{\max} = \sqrt{1 - \frac{a^2(\pi/2)}{b^2(\pi/2)}} = \frac{2\sqrt{C}}{1+C}. \tag{2.25}$$

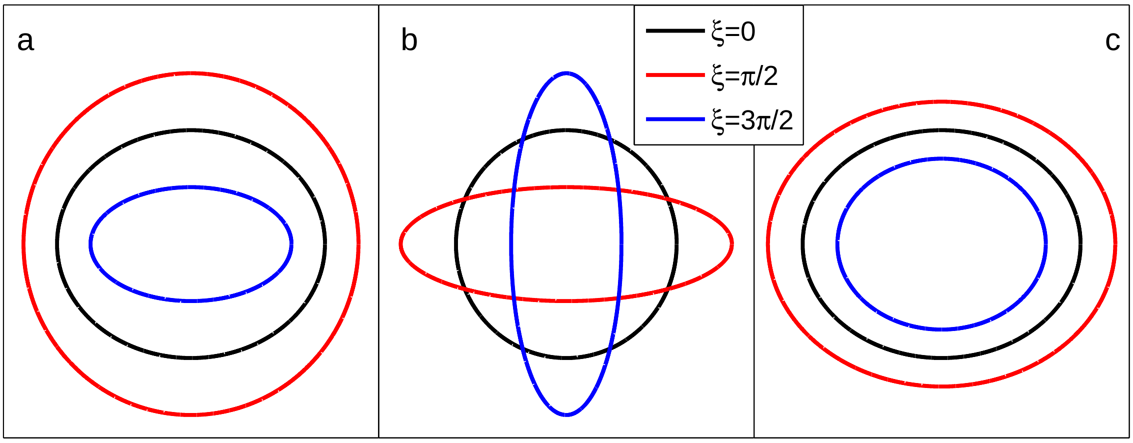

Figure 2.5: Different driving modes of the ellipse in configuration space for three different phases ξ: *breathing mode* (a), *quadrupole mode* (b) and and *constant eccentricity mode* (c).

The boundary of the elliptical billiard for the different driving modes is shown in Fig. 2.5 for three different phases $\xi = 0, \pi/2, 3\pi/2$. The phase $\xi = \pi/2$ ($\xi = 3\pi/2$) corresponds to the maximal (minimal) extension of the billiard and the equilibrium position is reached at $\xi = 0$. Clearly, the breathing and the constant eccentricity mode (Fig. 2.5a,c) are concentric, whereas the quadrupole mode (Fig. 2.5b) is not concentric.

2.2.3 Mapping

Between collisions with the time-dependent boundary, particles move ballistically. It is thus still possible to represent on orbit by the sequence of impacts on the boundary $\mathcal{B}$. However, ϕ and α are not sufficient to specify a point in phase space, since firstly, the position where the collision takes place depends not only on ϕ but also on t and secondly, the energy is not conserved, which means that we have to specify the direction α and the modulus of the velocity right after the impact. This yields a four-dimensional mapping $\mathcal{M}$

$$\begin{pmatrix} \xi_{n+1} \\ \varphi_{n+1} \\ \alpha_{n+1} \\ v_{n+1} \end{pmatrix} = \mathcal{M} \begin{pmatrix} \xi_n \\ \varphi_n \\ \alpha_n \\ v_n \end{pmatrix}, \tag{2.26}$$

where $v_n = |\boldsymbol{v}_n|$ is the modulus of the velocity and $\xi_n = t_n \mod T$ is the phase of the oscillation (T is the period of the driving law). The mapping can be deduced in the following way: Let's assume we have at t_n a particle on the boundary with position

$$\boldsymbol{p}_n = \begin{pmatrix} x_n \\ y_n \end{pmatrix} = \begin{pmatrix} a(t_n)\cos\phi_n \\ b(t_n)\sin\phi_n \end{pmatrix} \in \mathcal{B}(t_n) \tag{2.27}$$

and velocity $\boldsymbol{v}_n = (v_n^x, v_n^y)^\top$. At time $t > t_n$, the particle's position is simply given by (remember the particle moves ballistically in between collisions)

$$\boldsymbol{p}(t) = \boldsymbol{p}_n + (t - t_n)\boldsymbol{v}_n. \tag{2.28}$$

The time t_{n+1} of the next collision can be derived from the condition that the position of the particle at t_{n+1} lies on $\mathcal{B}(t_{n+1})$:

$$\boldsymbol{p}_{n+1} = \begin{pmatrix} x_{n+1} \\ y_{n+1} \end{pmatrix} = \begin{pmatrix} a(t_{n+1}) \cos \phi_{n+1} \\ b(t_{n+1}) \sin \phi_{n+1} \end{pmatrix} \in \mathcal{B}(t_{n+1}) \tag{2.29}$$

On the other hand, we can write $\boldsymbol{p}_{n+1} = \boldsymbol{p}(t_{n+1})$, yielding the set of equations

$$x_{n+1} = x_n + (t_{n+1} - t_n)v_n^x = a(t_{n+1}) \cos \phi_{n+1} \tag{2.30a}$$

$$y_{n+1} = y_n + (t_{n+1} - t_n)v_n^y = b(t_{n+1}) \sin \phi_{n+1}. \tag{2.30b}$$

These are two equations for two unknown variables (t_{n+1} and ϕ_{n+1}). ϕ_{n+1} can be easily eliminated by dividing the left hand side of Eq. (2.30a) by $a(t_{n+1})$ and correspondingly the right hand side of Eq. (2.30b) by $b(t_{n+1})$. Squaring both resulting equations and adding them up yields an implicit equation for t_{n+1}

$$\left(\frac{x_n + v_n^x \cdot (t_{n+1} - t_n)}{a(t_{n+1})}\right)^2 + \left(\frac{y_n + v_n^y \cdot (t_{n+1} - t_n)}{b(t_{n+1})}\right)^2 - 1 = 0 \tag{2.31}$$

where the smallest $t_{n+1} > t_n$ solving Eq. (2.31) has to be taken. Note that in the static elliptical billiard, the denominator does not depend on t_{n+1} and Eq. (2.31) reduces to a quadratic equation in t_{n+1} which can be solved explicitly.

The next phase ξ_{n+1} is given by

$$\xi_{n+1} = t_{n+1} \mod T. \tag{2.32}$$

The position $(x_{n+1}, y_{n+1})^\top \in \mathcal{B}(t_{n+1})$ of the next collision is obtained from Eq. (2.30) and ϕ_{n+1} from Eq. (2.29)

$$\phi_{n+1} = \begin{cases} \arctan\left(\frac{a(t_{n+1})y_{n+1}}{b(t_{n+1})x_{n+1}}\right) & x_{n+1} > 0, y_{n+1} > 0 \\ \arctan\left(\frac{a(t_{n+1})y_{n+1}}{b(t_{n+1})x_{n+1}}\right) + \pi & x_{n+1} < 0 \\ \arctan\left(\frac{a(t_{n+1})y_{n+1}}{b(t_{n+1})x_{n+1}}\right) + 2\pi & x_{n+1} > 0, y_{n+1} < 0 \\ \frac{\pi}{2} & x_{n+1} = 0, y_{n+1} > 0 \\ \frac{3\pi}{2} & x_{n+1} = 0, y_{n+1} < 0. \end{cases} \tag{2.33}$$

A particle with velocity $\boldsymbol{v}_n$ hits the boundary of the elliptical billiard at time t_{n+1} and position ϕ_{n+1}. In the co-moving frame of the boundary (at t_{n+1} and ϕ_{n+1}), the particle undergoes an elastic reflection. This means that the normal component of the velocity of the particle in this frame is reversed. The boundary velocity $\boldsymbol{u}_{n+1}$ right at this point is

$$\boldsymbol{u}_{n+1} = \frac{\partial \mathcal{B}(t)}{\partial t} = \begin{pmatrix} \dot{a}(t_{n+1}) \cos \phi_{n+1} \\ \dot{b}(t_{n+1}) \sin \phi_{n+1} \end{pmatrix}. \tag{2.34}$$

In this moving frame, the particle has a velocity of $\boldsymbol{v}_n - \boldsymbol{u}_{n+1}$ and the normal component is $\langle \boldsymbol{n}_{n+1}, \boldsymbol{v}_n - \boldsymbol{u}_{n+1} \rangle \boldsymbol{n}_{n+1}$, $\langle , \rangle$ denotes the scalar product and $\boldsymbol{n}_{n+1}$ the inward pointing unit normal vector

$$\boldsymbol{n}_{n+1} = \frac{1}{\sqrt{b^2(t_{n+1})\cos^2\phi_{n+1} + a^2(t_{n+1})\sin^2\phi_{n+1}}} \begin{pmatrix} -b(t_{n+1})\cos\phi_{n+1} \\ -a(t_{n+1})\sin\phi_{n+1} \end{pmatrix}. \qquad (2.35)$$

In the static frame of the ellipse, the next velocity is then

$$\boldsymbol{v}_{n+1} = \boldsymbol{v}_n - 2\langle \boldsymbol{n}_{n+1}, \boldsymbol{v}_n - \boldsymbol{u}_{n+1} \rangle \boldsymbol{n}_{n+1} \qquad (2.36)$$

$$v_{n+1} = |\boldsymbol{v}_{n+1}|, \qquad (2.37)$$

where the factor of 2 accounts for the fact that we transform from the static frame to the co-moving one, perform the elastic reflection of the normal component of the relative velocity and then transform back to the static frame.

The final step in deriving the mapping $\mathcal{M}$ (2.26) is to calculate the angle α_{n+1} between the forward pointing tangent vector $\boldsymbol{t}_{n+1}$ and $\boldsymbol{v}_{n+1}$:

$$\alpha_{n+1} = \begin{cases} \arccos\left(\frac{\langle \boldsymbol{v}_{n+1}, \boldsymbol{t}_{n+1} \rangle}{|\boldsymbol{v}_{n+1}|}\right) & \langle \boldsymbol{v}_{n+1}, \boldsymbol{n}_{n+1} \rangle > 0 \\ 2\pi - \arccos\left(\frac{\langle \boldsymbol{v}_{n+1}, \boldsymbol{t}_{n+1} \rangle}{|\boldsymbol{v}_{n+1}|}\right) & \langle \boldsymbol{v}_{n+1}, \boldsymbol{n}_{n+1} \rangle < 0, \end{cases} \qquad (2.38)$$

$$\boldsymbol{t}_{n+1} = \frac{1}{\sqrt{a^2(t_{n+1})\sin^2\phi_{n+1} + b^2(t_{n+1})\cos^2\phi_{n+1}}} \begin{pmatrix} -a(t_{n+1})\sin\phi_{n+1} \\ b(t_{n+1})\cos\phi_{n+1} \end{pmatrix}. \qquad (2.39)$$

The mapping $\mathcal{M}$ is thus given by Eqs. (2.32), (2.33), (2.37), (2.38) together with the auxiliary Eqs. (2.31) and (2.36) and the auxiliary quantities $\boldsymbol{u}_{n+1}$ (2.34), $\boldsymbol{v}_{n+1}$ (2.36), $\boldsymbol{n}_{n+1}$ (2.35) and $\boldsymbol{t}_{n+1}$ (2.39). Due to equation (2.31), which determines the time t_{n+1} of the next collision, $\mathcal{M}$ is an implicit mapping. In general, equation (2.31) can be solved numerically only.

In order to iterate the mapping $\mathcal{M}$, Eq. (2.31) has to be solved numerically. This is actually the key challenge when advancing the mapping, since Eq. (2.31) can have many roots, which can lie arbitrary close to each other. The smallest of these roots which fulfills $t_{n+1} > t_n$ is the one we are searching for (note that t_n is the trivial root of the equation). To resolve the smallest root, we use an advanced bracketing method developed in [90] and decisively improved in [109]. With this very efficient computational scheme, we are able to iterate around 10^6 collisions per second. Nevertheless, when investigation the long-term behavior of dynamical quantities, i.e. going to very large collision numbers (10^{11}), this limits the number of particles that can be iterated, even when using multi processor systems, see also the discussion in section 6.1.

2.2.4 Jacobian and preserved measure

For a mapping $\mathcal{M}$, the determinant of the Jacobian matrix $\mathcal{J}$ (sometimes just called Jacobian) determines the evolution of a differential measure [66], i.e. we can extract the preserved (under $\mathcal{M}$) measure $d\mu$ from the Jacobian [83]. The Jacobian J and the Jacobian matrix $\mathcal{J}$ are given by (for simplicity we use t instead of ξ)

$$J = \det(\mathcal{J}) = \frac{\partial(t_{n+1}, \phi_{n+1}, \alpha_{n+1}, v_{n+1})}{\partial(t_n, \phi_n, \alpha_n, v_n)}, \tag{2.40}$$

$$\mathcal{J} = \begin{pmatrix} \frac{\partial t_{n+1}}{\partial t_n} & \frac{\partial t_{n+1}}{\partial \phi_n} & \frac{\partial t_{n+1}}{\partial \alpha_n} & \frac{\partial t_{n+1}}{\partial v_n} \\ \frac{\partial \phi_{n+1}}{\partial t_n} & \frac{\partial \phi_{n+1}}{\partial \phi_n} & \frac{\partial \phi_{n+1}}{\partial \alpha_n} & \frac{\partial \phi_{n+1}}{\partial v_n} \\ \frac{\partial \alpha_{n+1}}{\partial t_n} & \frac{\partial \alpha_{n+1}}{\partial \phi_n} & \frac{\partial \alpha_{n+1}}{\partial \alpha_n} & \frac{\partial \alpha_{n+1}}{\partial v_n} \\ \frac{\partial v_{n+1}}{\partial t_n} & \frac{\partial v_{n+1}}{\partial \phi_n} & \frac{\partial v_{n+1}}{\partial \alpha_n} & \frac{\partial v_{n+1}}{\partial v_n} \end{pmatrix}. \tag{2.41}$$

The calculation of $\mathcal{J}$ and J is quite tedious, we will thus just briefly sketch the main steps. To obtain the partial derivatives $\frac{\partial t_{n+1}}{\partial t_n}$, $\frac{\partial t_{n+1}}{\partial \phi_n}$, $\frac{\partial t_{n+1}}{\partial \alpha_n}$, $\frac{\partial t_{n+1}}{\partial v_n}$, we rewrite Eq. (2.31) as

$$\begin{aligned} f(t_{n+1}, t_n, \phi_n, \alpha_n, v_n) = \left(\frac{a(t_n)\cos\phi_n + v_n \cos\alpha_n (t_{n+1} - t_n)}{a(t_{n+1})} \right)^2 + \\ \left(\frac{b(t_n)\sin\phi_n + v_n \sin\alpha_n \cdot (t_{n+1} - t_n)}{b(t_{n+1})} \right)^2 - 1 = 0. \end{aligned} \tag{2.42}$$

Now we calculate the total differential of Eq. (2.42)

$$df = \frac{\partial f}{\partial t_{n+1}} dt_{n+1} + \frac{\partial f}{\partial t_n} dt_n + \frac{\partial f}{\partial \phi_n} d\phi_n + \frac{\partial f}{\partial \alpha_n} d\alpha_n + \frac{\partial f}{\partial v_n} dv_n = 0 \tag{2.43}$$

and rewrite it as

$$dt_{n+1} = -\frac{\frac{\partial f}{\partial t_n}}{\frac{\partial f}{\partial t_{n+1}}} dt_n - \frac{\frac{\partial f}{\partial \phi_n}}{\frac{\partial f}{\partial t_{n+1}}} d\phi_n - \frac{\frac{\partial f}{\partial \alpha_n}}{\frac{\partial f}{\partial t_{n+1}}} d\alpha_n - \frac{\frac{\partial f}{\partial v_n}}{\frac{\partial f}{\partial t_{n+1}}} dv_n. \tag{2.44}$$

On the other hand we know that (since $t_{n+1} = t_{n+1}(t_n, \phi_n, \alpha_n, v_n)$)

$$dt_{n+1} = \frac{\partial t_{n+1}}{\partial t_n} dt_n + \frac{\partial t_{n+1}}{\partial \phi_n} d\phi_n + \frac{\partial t_{n+1}}{\partial \alpha_n} d\alpha_n + \frac{\partial t_{n+1}}{\partial v_n} dv_n \tag{2.45}$$

and by comparing the prefactors of the differentials of eqs. (2.44) and (2.45) we get

$$\frac{\partial t_{n+1}}{\partial t_n} = -\frac{\frac{\partial f}{\partial t_n}}{\frac{\partial f}{\partial t_{n+1}}} \qquad \frac{\partial t_{n+1}}{\partial \phi_n} = -\frac{\frac{\partial f}{\partial \phi_n}}{\frac{\partial f}{\partial t_{n+1}}} \tag{2.46}$$

$$\frac{\partial t_{n+1}}{\partial \alpha_n} = -\frac{\frac{\partial f}{\partial \alpha_n}}{\frac{\partial f}{\partial t_{n+1}}} \qquad \frac{\partial t_{n+1}}{\partial v_n} = -\frac{\frac{\partial f}{\partial v_n}}{\frac{\partial f}{\partial t_{n+1}}}. \tag{2.47}$$

To obtain the remaining partial derivatives contained in $\mathcal{J}$, we can use directly the corresponding equations of the mapping $\mathcal{M}$, since they are given in explicit rather than in implicit form. We just have to respect the correct dependencies and accordingly use the chain rule. For example, $\phi_{n+1} = \phi_{n+1}(t_{n+1}, t_n, \phi_n, \alpha_n, v_n)$ and t_{n+1} itself depends on $t_n, \phi_n, \alpha_n, v_n$, so

$$\frac{\partial \phi_{n+1}}{\partial t_n} = \left.\frac{\partial \phi_{n+1}}{\partial t_n}\right|_{t_{n+1}=const.} + \frac{\partial \phi_{n+1}}{\partial t_{n+1}} \frac{\partial t_{n+1}}{\partial t_n}. \tag{2.48}$$

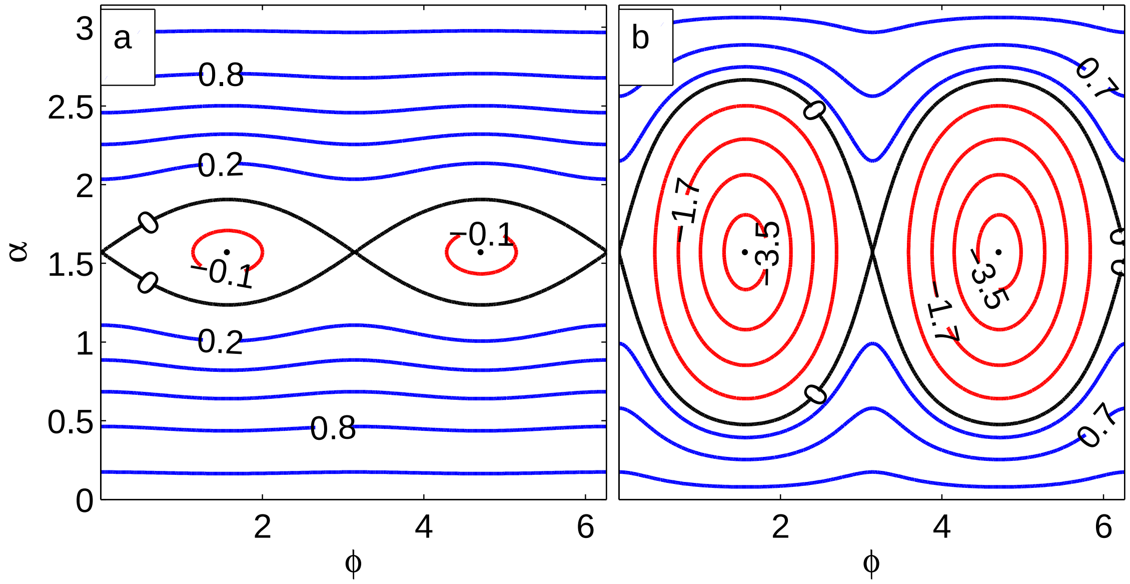

Figure 2.6: Poincaré surface of section of the elliptical billiard for different values of the eccentricity ϵ: (a) $\epsilon = 0.33$ and (b) $\epsilon = 0.89$. The fraction of librators is much higher for $\epsilon = 0.89$ than for $\epsilon = 0.33$. The phase space shown in (a) corresponds to the configuration of the ellipse in the quadrupole mode at $\xi = 0.2$, (b) to the configuration at $\xi = \pi/2$.

Finally, we obtain for the determinant of the Jacobian

$$\det(\mathcal{J}) = \frac{R_n v_n (v_n \sin\alpha_n - u_n)}{R_{n+1} v_{n+1} (v_{n+1} \sin\alpha_{n+1} - u_{n+1})}, \tag{2.49}$$

where R and u are the radius of curvature and the normal boundary velocity at collision n, respectively $n+1$:

$$R(t,\phi) = \frac{a(t)b(t)}{\left(a^2(t)\sin^2\phi + b^2(t)\cos^2\phi\right)^{\frac{3}{2}}} \tag{2.50}$$

$$u(t,\phi) = \langle \boldsymbol{u}(t,\phi), \boldsymbol{n}(t,\phi) \rangle. \tag{2.51}$$

From the form of the determinant of the Jacobian (2.49), we see that the mapping $\mathcal{M}$ preserves the measure

$$d\mu = R(t,\phi) v \left(v \sin\alpha - u(t,\phi)\right) dt d\phi d\alpha dv. \tag{2.52}$$

2.2.5 Concept of the frozen billiard

Even though the boundary $\mathcal{B}^d(\xi)$ (where the index d denotes driven) of the elliptical billiard changes in time, it is at any phase ξ still an ellipse. At some fixed phase ξ_0, we define the boundary $\mathcal{B}^s$ (s stands for static) of a static elliptical billiard as

$$\mathcal{B}^s := \mathcal{B}^d(\xi = \xi_0). \tag{2.53}$$

This is the corresponding *frozen* billiard. The phase space (or PSS) of the frozen billiard is completely determined by the eccentricity $\epsilon(\xi_0)$ of $\mathcal{B}^s$. Since in the breathing and in the quadrupole driving mode the eccentricity ϵ depends on the phase ξ, there is not just one corresponding frozen billiard, but infinitely many different ones. This is exemplarily demonstrated in Fig. 2.6 for the quadrupole mode with amplitude $C = 0.5$. In Fig. 2.6a, the phase space of the corresponding frozen billiard at $\xi_0 = 0.2$ is shown. For this particular phase, the elliptical billiard is very similar to a circle, the eccentricity is $\epsilon(0.2) = 0.33$. As a consequence, there are mainly rotators (blue curves) in the PSS (in a circle there are rotators only). In Fig. 2.6b, the phase space of the corresponding frozen billiard at $\xi_0 = \pi/2$ is shown. The elliptical billiard is maximally deformed at $\xi_0 = \pi/2$, the eccentricity is $\epsilon(\pi/2) = 0.89$ and as a result, the fraction of librators (red curves) is much larger than for $\xi_0 = 0.2$, see also the discussion in section 2.2.7.

In the constant eccentricity mode there is just a single frozen billiard for all phases ξ, since, as the name of the driving mode suggests, the eccentricity is constant and does not depend on the phase.

2.2.6 Momentum transfer

Upon collisions with the moving boundary, the momentum of a particle changes. This can be easily seen from Eq. (2.36). Squaring both sides yields

$$v_{n+1}^2 = v_n^2 - 4\langle \boldsymbol{n}_{n+1}, \boldsymbol{u}_{n+1}\rangle \left[\langle \boldsymbol{n}_{n+1}, \boldsymbol{v}_{n+1}\rangle - \langle \boldsymbol{n}_{n+1}, \boldsymbol{u}_{n+1}\rangle\right] \tag{2.54}$$

and so in general $v_{n+1}^2 \neq v_n^2$. Note that from $\boldsymbol{u}_{n+1} = \boldsymbol{0}$ (static elliptical billiard) it follows immediately that $v_{n+1}^2 = v_n^2$ (elastic collision). As a consequence, in the driven elliptical billiard, the energy is not a constant of motion.

The maximum change of momentum occurs if a particle collides with the boundary at an angle of $\alpha = \pi/2$ and if furthermore $\boldsymbol{n} \parallel \boldsymbol{u}$ ($\Rightarrow \boldsymbol{v} \parallel \boldsymbol{u}$), i.e. the boundary moves in normal direction. Independent of the driving mode, the maximum velocity of the boundary is $\pm\omega C$. For such ($\boldsymbol{n} \parallel \boldsymbol{u}$, $\alpha = \pi/2$) a collision, Eq. (2.54) reduces to

$$v_{n+1}^2 = \left(v_n \pm 2\omega C\right)^2 , \tag{2.55}$$

i.e. the maximal change in momentum upon a single boundary collision is $\pm 2\omega C$.

2.2.7 Product of the angular momenta

In the static elliptical billiard, the product of the angular momenta about the two foci $F(\phi, \alpha)$ (2.11) is preserved, due to this second constant of motion the static ellipse is an integrable billiard. F specifies whether a particle is a librator ($F < 0$) or a rotator ($F > 0$) and more specifically, the exact position of a trajectory in the phase space spanned by ϕ and α. In the driven elliptical billiard, we define in analogy to Eq. (2.11) F as

$$F(\xi, \phi, \alpha) = \frac{\cos^2\alpha \cdot (1 + (1 - \epsilon^2(\xi))\cot^2\phi) - \epsilon^2(\xi)}{1 + (1 - \epsilon^2(\xi))\cot^2\phi - \epsilon^2(\xi)} . \tag{2.56}$$

There is now an additional dependence of F on the phase ξ through the eccentricity ϵ, since ϵ itself depends on ξ, at least in the breathing and quadrupole mode (in the constant eccentricity mode ϵ is of course constant). The definition of Eq. (2.56) is not directly the

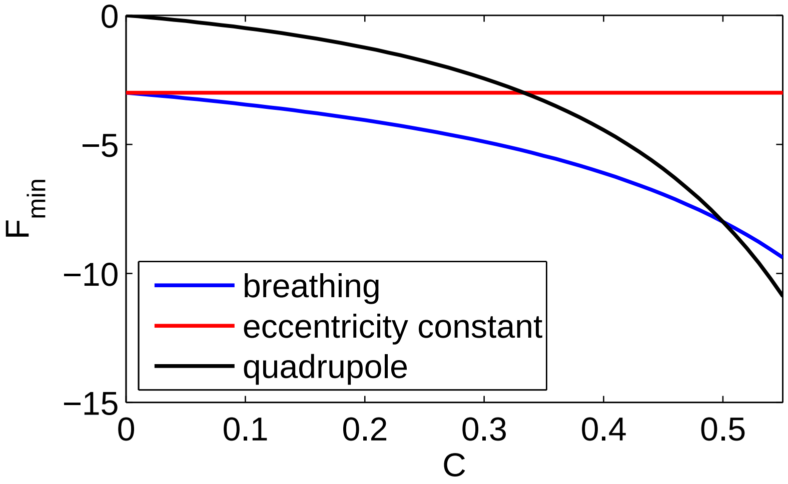

Figure 2.7: Global minimum $F_{\mathrm{min}}^{\mathrm{g}l}$ of F as a function of the driving amplitude C for the different driving modes.

product of the angular momenta about the two foci, since there is no dependence on the velocity v. The definition of (2.56) corresponds to the product of the angular momenta about the two foci for a velocity of $v = 1$.

Like the energy, $F(\xi, \phi, \alpha)$ is not conserved in the driven elliptical billiard. Nevertheless, it is an extremely usefull quantity. For example, the sign of F still specifies whether a particle is a librator ($F < 0$) or a rotator ($F > 0$). As we will see in chapter 3, the phase space of the driven elliptical billiard shows some reminiscence of the phase space of the static billiard. In many cases, especially for high velocities, the $\phi \times \alpha$ subspace of the 4D phase space can be mapped onto F, thereby effectively reducing the dimension by one and enabling representative visualizations of phase space properties.

Fraction of librators and rotators

$F(\xi, \phi, \alpha)$ ranges from

$$F_{\mathrm{min}}(\xi) = \frac{-\epsilon^2(\xi)}{1 - \epsilon^2(\xi)} \tag{2.57}$$

to $F_{\mathrm{max}} = 1$. F_{min} determines how much of the $\phi \times \alpha$-subspace corresponds to librators and how much to rotators. For $F_{\mathrm{min}} = 0$ (this corresponds to a circle), there are no librators present. With increasing eccentricity, the modulus of F_{min} increases and the area in the $\phi \times \alpha$-subspace corresponding to librators (this is the area enclosed by the separatrix $F = 0$) increases as well.

For a fixed amplitude C, $F_{\mathrm{min}}(\xi)$ depends via the eccentricity ϵ on the phase ξ (in the breathing and quadrupole mode). The global minimum $F_{\mathrm{min}}^{\mathrm{g}l}$ is reached at $\xi = 3\pi/2$, since ϵ is maximal at this phase, cf. Figs. 2.3 and 2.4. From these two figures it can also be seen that the maximum value of ϵ varies with the amplitude and with the applied driving mode. Consequently, the global minimum $F_{\mathrm{min}}^{\mathrm{g}l}$ has a dependence on the driving amplitude and mode. $F_{\mathrm{min}}^{\mathrm{g}l}$ as a function of the amplitude for the different driving modes is shown in Fig. 2.7. In the constant eccentricity mode there is no dependence on the amplitude, since the movement of the boundary is a pure scaling it does not change ϵ. In the other two modes, increasing the amplitude leads to a higher maximal eccentricity, which is reached at the extremal configuration of the ellipse at $\xi = 3\pi/2$, and thus to an increase of the modulus

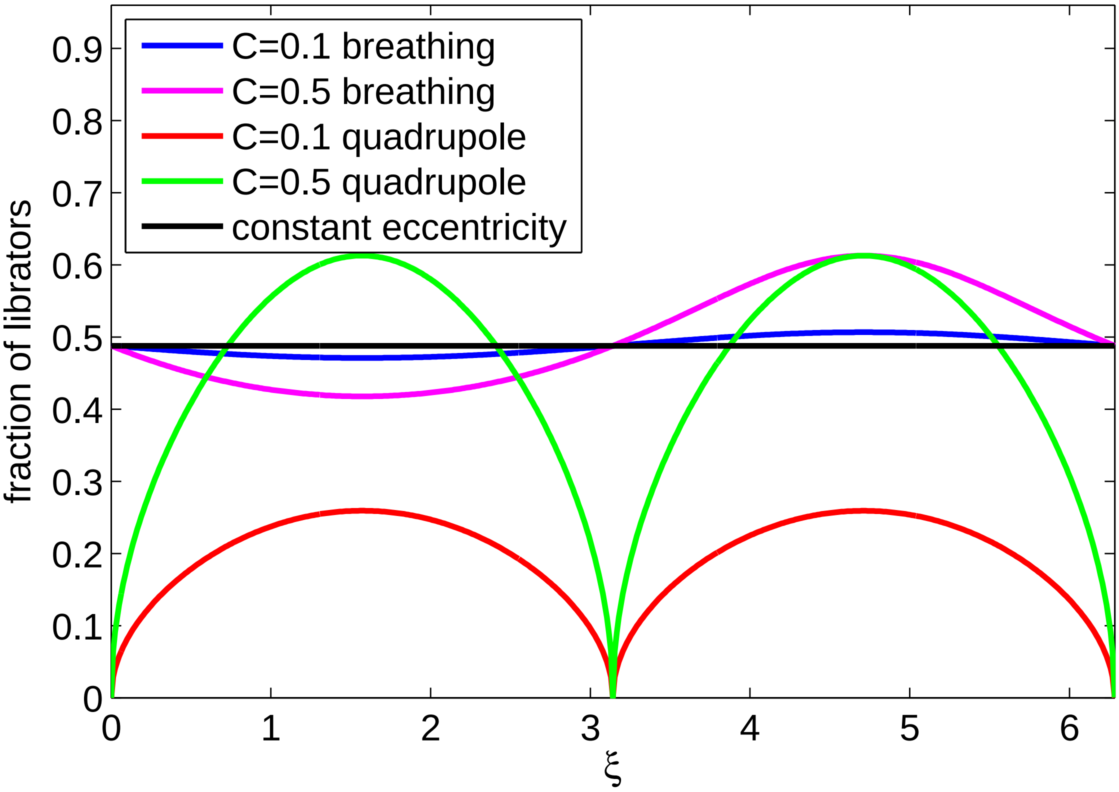

Figure 2.8: Fraction of librators $f_{lib}(\xi)$ in the corresponding frozen billiard for the three different driving modes and two different amplitudes C as a function of the phase ξ. In the constant eccentricity mode, $f_{lib}(\xi)$ is constant, independent of the amplitude. In the breathing mode, $f_{lib}(\xi)$ performs a sinusoidal oscillation whose amplitude increases with increasing C. The strongest oscillation of $f_{lib}(\xi)$ is observed in the quadrupole mode, $f_{lib}(\xi)$ goes to zero once the ellipse becomes a circle, which is the case at $\xi = 0$ and $\xi = \pi$.

of F^{gl}_{min}.

According to the previous discussion, $F_{\text{min}}(\xi)$ determines how much of the $\phi \times \alpha$-subspace corresponds to librators and how much to rotators. To explicitly calculate the fraction of rotators and librators, we use again the concept of the frozen billiard. At a given phase ξ, the corresponding frozen billiard has an eccentricity $\epsilon(\xi)$. The fraction of librators in the PSS of the frozen billiard is given by the area which is enclosed by the separatrix $F(\phi, \alpha) = 0$ divided by the total area of phase space. The total area A_{PSS} of phase space (or PSS) is

$$A_{PSS} = (\phi_{\text{max}} - \phi_{\text{min}})(\alpha_{\text{max}} - \alpha_{\text{min}}) = 2\pi^2. \tag{2.58}$$

The lower half of the separatrix (sx) is obtained by setting the left hand side of Eq. (2.56) to zero and solving for α:

$$\alpha_{sx}(\phi, \epsilon(\xi)) = \arccos \sqrt{\frac{\epsilon^2(\xi)}{1 + (1 - \epsilon^2(\xi)) \cot^2 \phi}}. \tag{2.59}$$

Two times (upper and lower half) the area under $\alpha_{sx}(\phi, \epsilon(\xi))$ divided by A_{PSS} is the fraction of rotators $f_r(\epsilon(\xi))$, thus, the fraction $f_l(\epsilon(\xi))$ of librators is given by (note that $f_l(\epsilon(\xi)) + f_r(\epsilon(\xi)) = 1$)

$$f_l(\epsilon(\xi)) = 1 - \frac{2}{A_{PSS}} \int_0^{2\pi} \alpha_{sx}(\phi, \epsilon(\xi)) d\phi. \tag{2.60}$$

The integral $\int \alpha_{sx}(\phi) d\phi$ cannot be solved analytically, we use a numerical Gauss-Kronrad scheme [110] for its evolution. The fraction of librators $f_l(\epsilon(\xi))$ for different amplitudes and driving modes is shown in Fig. 2.8. In the breathing mode, the dependence of $f_l(\epsilon(\xi))$ is rather weak for $C = 0.1$, since ϵ itself depends barley on the phase ξ, cf. Fig. 2.3. With increasing amplitude, $f_l(\epsilon(\xi))$ oscillates stronger, see the curve $C = 0.5$ for the breathing mode in Fig. 2.8, due to a stronger dependence of ϵ on ξ. In the quadrupole mode, the oscillations of ϵ as a function of ξ are much stronger pronounced and consequently $f_l(\epsilon(\xi))$ shows strong oscillations.

Transitions between librators and rotators

An important implication of the fact that $F(\xi, \phi, \alpha)$ is not conserved in the driven elliptical billiard is that now transitions between librators and rotators are possible [88–90]. Three different effective processes can be identified that lead to these transitions:

1. *Vertical processes*, upon a collision, the angle of incidence is not the angle of reflection angle due to the momentum transferred by the boundary motion. In the $\phi \times \alpha$ subspace, the phase space variable α undergoes a certain change $\triangle\alpha$ compared to a trajectory in the static billiard, so the particle moves vertically in the PSS.

2. *Horizontal processes*, a particle that would hit the boundary at a certain point ϕ in the static billiard, collides with the boundary in the driven case at some ϕ', simply because the boundary of the elliptical billiard has a different shape at the phase when the collisions takes place, so the particle moves horizontally in the PSS.

3. *Eccentricity processes*, the values of F of a particle depend not only on ϕ and α (like in the static billiard), but also on the eccentricity ϵ, which itself depends on the phase ξ. This means the sign of F of a particle can change, simply because the phase ξ changes. In other words, the position of the separatrix, dividing the $\phi \times \alpha$ subspace into rotators and librators, changes with ξ, even though the separatrix has always $F = 0$, see Fig. 2.6. So the particle does not move in the PSS, but the separatrix does.

When we refer to a particle that ‘moves’ in the PSS (or rather the $\phi \times \alpha$ subspace), we mean the following: Let’s assume we have a particle in the static elliptical billiard starting at $(\phi_0, \alpha_0)^\top$. The next collisions takes place at $(\phi_1, \alpha_1)^\top$. Since the product of the angular momenta about the foci is conserved, the F values of the two phase space points are the same, $F(\phi_0, \alpha_0) = F(\phi_1, \alpha_1)$. In the driven billiard, the corresponding particle starts also at $(\phi_0, \alpha_0)^\top$ (with a certain $(\xi_0, v_0)^\top$), but it will hit the boundary at some other position ϕ_1' and the outgoing angle α_1' will be different due to momentum transfer. So the next position in the $\phi \times \alpha$ subspace is given by

$$(\phi_1', \alpha_1')^\top = (\phi_1, \alpha_1)^\top + (\triangle\phi, \triangle\alpha)^\top. \tag{2.61}$$

By ‘moving’ in the PSS we mean the difference vector $(\triangle\phi, \triangle\alpha)^\top$ of a particle is displaced compared to the corresponding position $(\phi_1, \alpha_1)^\top$ of a particle in the static billiard. Now the quantity F is not conserved, i.e. $F(\xi_0, \phi_0, \alpha_0) \neq F(\xi_1', \phi_1', \alpha_1')$.

In general, the processes of the above listing do no appear isolated, but a combination of all three will occur: A particle hits the boundary at a different position φ' compared to the static case (horizontal process), it undergoes a change $\triangle\phi$, additionally the boundary transfers momentum and changes α (vertical process) and finally, the eccentricity at the collision point will be different since the phase ξ has changed (eccentricity process). For a detailed discussion of the vertical and horizontal processes, see Refs. [90] and [89].

The three different processes occur in all the considered driving modes, with one important exception: In the constant eccentricity mode, there are no eccentricity processes, since ϵ stays constant (and does not depend on the phase ξ). This is why the constant eccentricity mode can be viewed as the most ‘regular’ one among the three driving modes.

3 Phase space of the driven elliptical billiard

The objective of this chapter is to describe the topology and composition of the phase space of the driven elliptical billiard. Since the discrete mapping, see Eq. (2.26), is four-dimensional, it is almost impossible to visualize the 4D phase space by means of the standard two-dimensional Poincaré surface of sections, as is it has been done for the static elliptical billiard. Furthermore, the phase space in unbounded in the velocity v. We will thus use other techniques described in the following sections to develop a comprehensive picture of the phase space.

3.1 Global topology

The four-dimensional phase space is spanned by the variables of the mapping (2.26) ξ, ϕ, α, v. The phase ξ ranges from 0 to $2\pi/\omega$, which is 2π for our choice of $\omega = 1$. The position on the boundary is specified by ϕ and varies from 0 to 2π. Unlike in the static elliptical billiard, the angle α is no longer restricted to the interval $[0, \pi]$ but can now range from 0 to 2π [84]. Collisions with $\alpha > \pi$ occur if the ellipse is (locally) expanding and the normal component of the particle's incoming velocity $v_{normal} = \langle \boldsymbol{v}, \boldsymbol{n} \rangle$ is smaller than twice the normal component of the boundary's velocity $u_{normal} = \langle \boldsymbol{u}, \boldsymbol{n} \rangle$, so we have

$$u_{\mathrm{n}ormal} < v_{\mathrm{n}ormal} < 2u_{\mathrm{n}ormal}. \tag{3.1}$$

The normal component of the particle's velocity is of course larger than u_{normal}, which is the precondition for a collision to take place when the ellipse is expanding. As a consequence, the particle does not get reflected in the sense that the sign of the normal component of the velocity of the particle is reversed. Such a particle approaches the boundary comparatively slowly, it looses energy upon the collision but continues to move in the 'same' direction. In other words, if the collision takes place at some t', the particle continues travelling outside of $\mathcal{B}(t')$, but of course still inside $\mathcal{B}(t > t')$.

The modulus of the velocity $v = |\boldsymbol{v}|$ can take any positive value. Whether a particle starting with a small value of v will reach such high values of v is a different question. For the moment it is sufficient that any $v > 0$ can be an initial condition of a particle and hence the phase space is unbounded in v.

Nevertheless, the phase space $\xi \times \phi \times \alpha \times v$ is not just the open 4D cuboid $[0, \frac{2\pi}{\omega}] \times [0, 2\pi] \times [0, 2\pi] \times [0, \infty]$, but possesses a more complicated topology, due to the fact that some parts of this cuboid are physically not accessible (geometrical constraints):

1. There will always be a rebound (i.e. the sign of the normal component of the velocity of a particle is reversed) if a collision occurs when the elliptical billiard is (locally) contracting, which means that for such a collision $\alpha < \pi$. As a consequence, the angle α is restricted to $[0, \pi]$ if $\xi \in [\pi/2, 3\pi/2]$ (breathing and constant eccentricity mode, in the quadrupole mode this depends additionally on ϕ).

2. An implication of the first constraint is that collisions with an outgoing angle of $\alpha \in [\pi, 2\pi]$ can occur only if the ellipse is (locally) expanding ($\xi \in [0, \pi/2] \cup [3\pi/2, 2\pi]$ in the breathing and constant eccentricity mode). For such a collision, there is a further constraint on the outgoing velocity v. The boundary has to expand faster in normal direction than the particle is moving in that direction, so $v_{\mathrm{normal}} < u_{\mathrm{normal}}$. A particle can loose in normal direction maximal $2\omega C$ of momentum, i.e. fast particles, where 'fast' means $v \gg \omega C$, cannot fulfill this condition (unless they hit the boundary almost tangentially).

3. When the ellipse is contracting ($\xi \in [\pi/2, 3\pi/2]$ in the breathing and constant eccentricity mode), the outgoing normal component of the velocity of the particle has to be larger than the normal boundary velocity. As a consequence, there will be no points in phase space of the kind $(\xi \in [\pi/2, 3\pi/2], \phi, \alpha, v < u(\xi, \phi))^{\top}$.

3.2 Phase space density

One of the simplest driven billiard systems is the one-dimensional Fermi-Ulam model (FUM) [66]. In the FUM, particles bounce between one fixed and one oscillating wall, see Fig. 3.5 and the discussion in section 3.3.1. The phase space of the FUM is spanned by ξ and v. At low v, there is a large chaotic sea, whereas at high v there are regular invariant spanning curves, see Fig. 3.5. When comparing the time-dependent ellipse with this prototype driven system, we expect at least some reminiscence of the phase space of the FUM in the phase space of the driven elliptical billiard. This means, we very roughly assume a chaotic sea at low v and more regular structure at high v. To test which parts of phase space are connected, we take an ensemble of particles starting at very low v, let it propagate and examine which parts of phase space it will visit. For this purpose, we define the phase space density of an ensemble of N_p particles at collision n as

$$\rho(\xi, \phi, \alpha, v, n) = \frac{1}{N_p} \sum_{i=1}^{N_p} \delta(\xi - \xi_i^n)\delta(\phi - \phi_i^n)\delta(\alpha - \alpha_i^n)\delta(v - v_i^n), \tag{3.2}$$

where the index i denotes the ith particle. By using the quantity F (2.56) instead of ϕ and α, we can reduce the dimension of the phase space density by one, i.e. we effectively map the $\phi \times \alpha$-supspace onto F:

$$\rho(F, \xi, v, n) = \frac{1}{N_p} \sum_{i=1}^{N_p} \delta(\xi - \xi_i^n)\delta(F - F(\xi,{}_i^n, \phi_i^n, \alpha_i^n))\delta(v - v_i^n). \tag{3.3}$$

The graph of these densities is six-, respectively, five-dimensional. To reduce their dimensionality, we define the velocity resolved phase space densities

$$\rho_{v_1,v_2}(F, \xi) = \frac{1}{N} \int_{v_1}^{v_2} \sum_{n=1}^{N} \rho(F, \xi, v, n) dv, \tag{3.4}$$

$$\rho_{v_1,v_2}(\phi, \alpha) = \frac{1}{N} \int_{0}^{2\pi} d\xi \int_{v_1}^{v_2} \sum_{n=1}^{N} \rho(\xi, \phi, \alpha, v, n) dv, \tag{3.5}$$

$$\rho_{v_1,v_2}(\xi, \alpha) = \frac{1}{N} \int_{0}^{2\pi} d\phi \int_{v_1}^{v_2} \sum_{n=1}^{N} \rho(\xi, \phi, \alpha, v, n) dv. \tag{3.6}$$

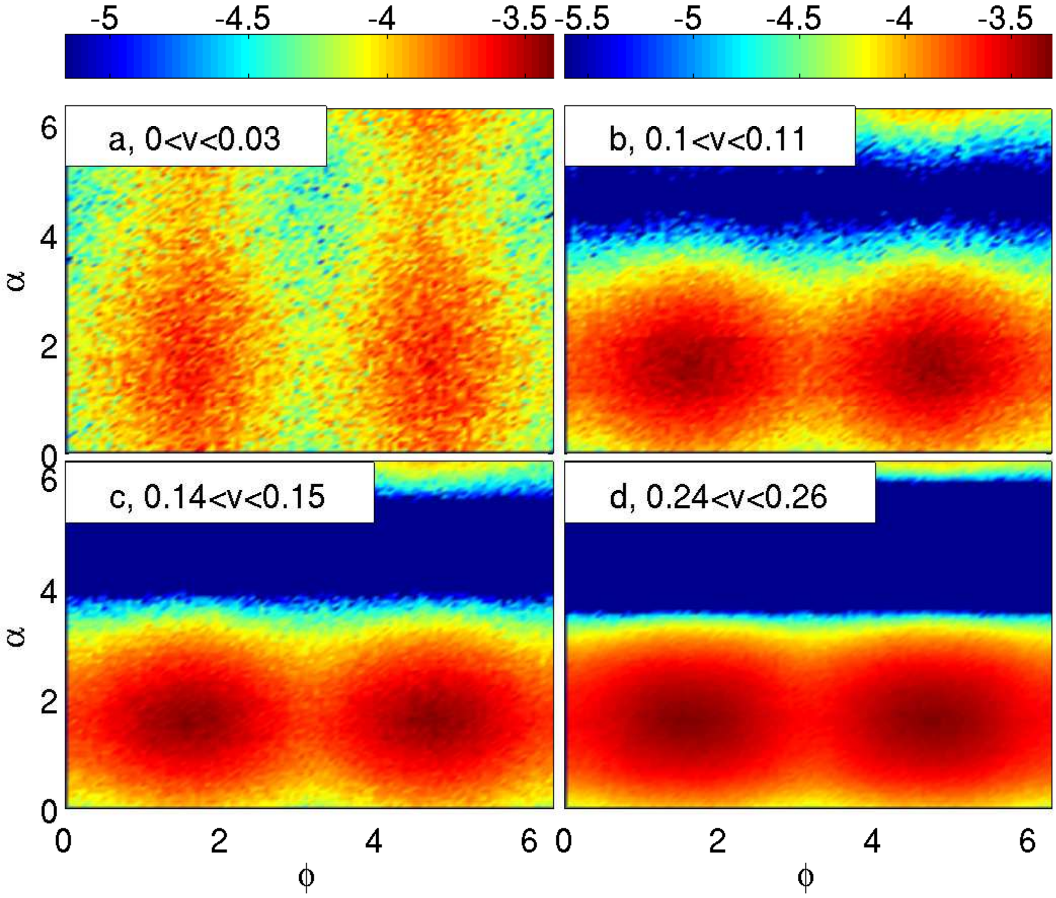

Figure 3.1: Phase space density $\rho_{v_1,v_2}(\phi,\alpha)$ in a low v regime (breathing mode, $C=0.1$). Due to the geometrical constaint number 1, the $\alpha>\pi$ region is populated only for very low velocities (a) and gets depleted more and more with increasing v (b)-(d).

This means all collisions of a simulation between $n=1$ and $n=N$, with $v_1<v<v_2$ are projected onto the $F\times\xi$, the $\phi\times\alpha$-subspace, respectively. In other words, we look at slices of the phase space density with thickness $\triangle v=v_2-v_1$.

3.2.1 Low velocity regime

To probe the low velocity regime, we take an ensemble of $N_p=10^5$ particles with $v_0=0.1$ and ξ_0,ϕ_0,α_0 distributed uniformly and randomly (ξ_0, $\phi_0\in[0,\,2\pi]$, $\alpha_0\in[0,\,\pi]$) and iterate it for 10^4 collisions. In principle, we could also try to use much lower values for the initial velocity, however, the first collision with the boundary would accelerate the particles to velocities of the order of ωC ($=0.1$ for our choice of $\omega=1$ and $C=0.1$), so $v_0=0.1$ is perfectly fine. Similarly, iterating until higher collision numbers is not helpfull when exploring the low velocity regime, since as we will see later, particles will get accelerated when they accumulate more and more collisions. The phase space density $\rho_{v_1,v_2}(\phi,\alpha)$ in the low v regime is shown in Fig. 3.1 in a log-scale colormap (breathing mode, $C=0.1$). The specific velocity slices are: (a) $v_1=0,v_2=0.03$, (b) $v_1=0.1,v_2=0.11$, (c) $v_1=$

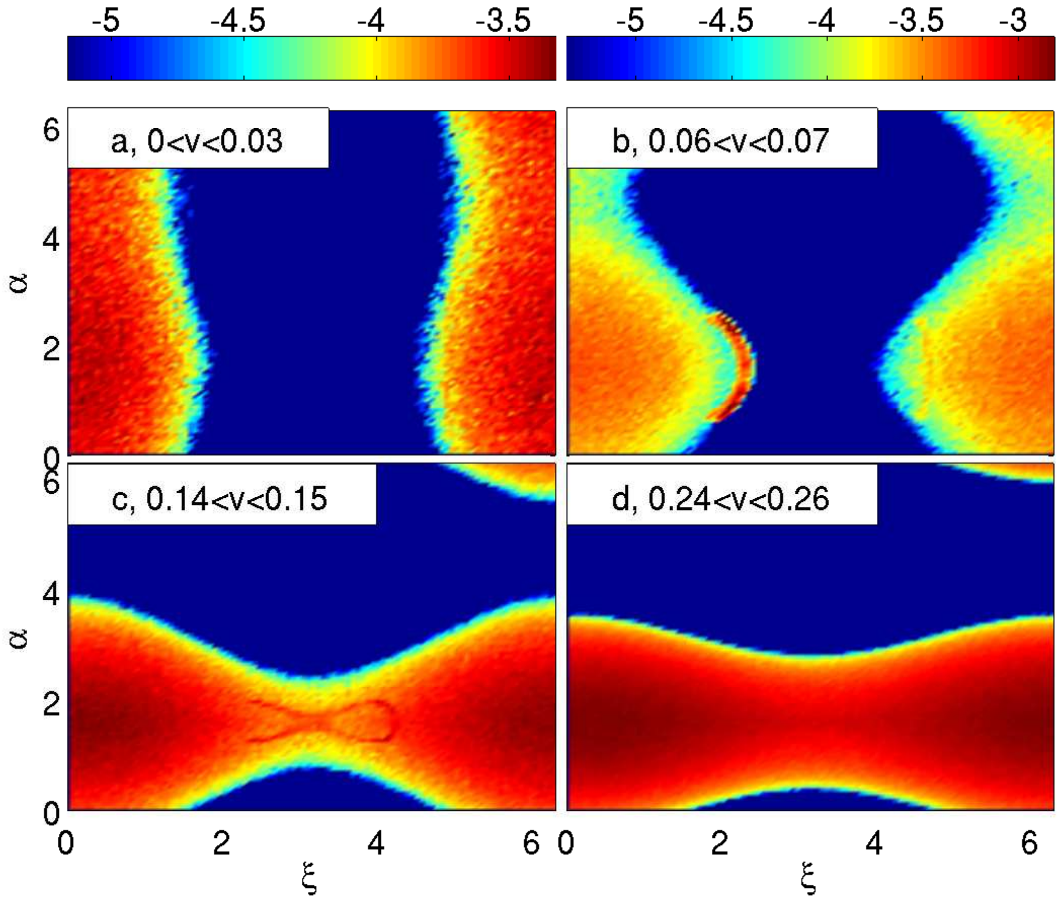

Figure 3.2: Phase space density $\rho_{v_1,v_2}(\xi,\alpha)$ in a low v regime (breathing mode, $C = 0.1$). Angles of $\alpha > \pi$ are only possible when the ellipse is expanding ($\xi \in [0,\pi/2] \cup [3\pi/2, 2\pi]$, geometrical constraint number 1). However, due to the geometrical constraint number 2, collisions with $\alpha > \pi$ occur for very small velocities only, see (a) and (b). When the ellipse is contracting ($\xi \in [\pi/2, 3\pi/2]$), the outgoing velocity has to be roughly larger than the boundary velocity, see (c) and (d) (geometrical constraint number 3).

$0.14, v_2 = 0.15$ and (d) $v_1 = 0.24, v_2 = 0.26$. Note that the lower part of each panel, i.e. the region $0 \leq \phi < 2\pi$, $0 \leq \alpha \leq \pi$ corresponds to the phase space of the static elliptical billiard. The geometrical constraint number 2 described in the previous section 3.1 can be seen in this figure. For $v < 0.03$, see Fig. 3.1a, the full $\alpha \in [0, 2\pi]$ range is accessible. Remember, the condition for a collision with $\alpha > \pi$ is that the normal component of the outgoing velocity of the particle is smaller than the normal component of the velocity of the boundary:

$$v_{normal} < u_{normal} \tag{3.7}$$

Since the maximal (normal) velocity of the boundary is 0.1, condition (3.7) can be fullfiled for every $\alpha \in [\pi, 2\pi]$ in the velocity regime (a). For higher velocities, cf. Fig. 3.1b, condition (3.7) cannot be fulfilled for all $\alpha > \pi$. In particular, particles that are immediately after a collision almost perpendicular to the boundary ($\alpha \approx 3\pi/2$) will have $v_{normal} \approx v > u_{normal}$, leading to the depletion of the $\alpha \approx 3\pi/2$ region. With increasing velocities, cf. Fig. 3.1c,d, the depleted region grows in α, since the condition $v_{normal} = v \sin\alpha > u_{normal}$ is fullfilled for a wider range of α. Once the particles are faster than $10\omega C$, collisions with $\alpha > \pi$ barely occur. If such collisions occur, particles leave the boundary almost tangentially, $\alpha \approx \pi$ or $\alpha \approx 2\pi$. Hence, when investigating the phase space density $\rho(\phi, \alpha)$ for high velocities, we will not show the $\alpha > \pi$ region.

Complementary information about the topology of the phase space in the low velocity regime is provided by the phase space density $\rho_{v_1,v_2}(\xi, \alpha)$, since this quantity explicitly contains the phase ξ. It is shown in Fig. 3.2 in a log-scale colormap (breathing mode, $C = 0.1$). The specific velocity slices are: (a) $v_1 = 0, v_2 = 0.03$, (b) $v_1 = 0.06, v_2 = 0.07$, (c) $v_1 = 0.14, v_2 = 0.15$ and (d) $v_1 = 0.24, v_2 = 0.26$. The geometrical constraint number 1 from section 3.1 implies that there are no collisions with $\alpha > \pi$ when the ellipse is contracing, and Fig. 3.2 shows that $\rho(\xi, \alpha)$ is zero in this particular region $\pi/2 < \xi < 3\pi/2$, $\alpha > 0$, independent of the velocity. Note that due to the logarithmic colormap, it is impossible to have a color corresponding to $\rho = 0$, so we added a small offset to $\rho(\xi, \alpha)$, such that the colorbar is still smooth. Thus, the very left of the colorbar actually corresponds to $\rho(\xi, \alpha) = 0$ and not just to $\rho(\xi, \alpha) \ll 1$. Finally, the geometrical constraint number 3 from section 3.1 states that when the ellipse is contracting, the velocity of the particles right after an impact has to fullfill $v_{normal} > u_{normal}$, so very small values of v are forbidden for $\xi \in [\pi/2, 3\pi/2]$. This can be seen from Fig. 3.2, the region centered around $\xi = \pi$ gets depleted more and more with decreasing velocity of the particles (at $\xi = \pi$ the ellipse is contracting with maximal velocity).

3.2.2 High velocity regime

In the previous section, we investigated the geometrical constraints 'shaping' the phase space in the low velocity regime. For high velocities, the halfspace $\pi > \alpha$ is not accessible (geometrical constraint number 1), apart from that, every point $(\xi, \phi, \alpha, v)^\top$ in the four-dimensional cuboid $[0, \frac{2\pi}{\omega}] \times [0, 2\pi] \times [0, \pi] \times [1, \infty]$ corresponds to a physically allowed collision.

To explore regions in phase space corresponding to higher velocities that are connected with the chaotic sea at low v, we have to iterate an initial ensemble much longer. We take an ensemble of 100 particles and iterate it for 10^9 collisions, again with $v_0 = 0.1$ and ξ_0, ϕ_0, α_0 distributed uniformly randomly. The phase space density $\rho_{v_1,v_2}(F, \xi)$ for different velocity regimes is shown in Fig. 3.3 (breathing mode, $C = 0.1$). The insets show the appendant density $\rho_{v_1,v_2}(\phi, \alpha)$, where the halfspace $\alpha > \pi$ is not shown, since essentially $\rho_{v_1,v_2}(\phi, \alpha)$ is zero for $\alpha > \pi$ due to the geometrical constraint number 1.

For low velocities, $0 < v < 2$ (see Fig. 3.3a), the complete $F \times \xi$ space and thus the complete $\phi \times \alpha$ plane (see the inset where $\rho_{v_1,v_2}(\phi, \alpha)$ is shown) is populated. Already for $2 < v < 4$ (see Fig. 3.3b), no collisions with large negative F values occur, this is exactly the region around the central elliptic fixed points of the corresponding static system, see the inset. With increasing velocity, this effects gets more pronounced, a narrow, sharply bounded region around $F = 0$ is now exclusively populated. In the corresponding frozen billiard, the separatrix is located at $F = 0$, so the ensemble is squeezed with increasing velocity more and more onto the 'separatrix region'. The asymptotic width of the separatrix region is reached at $v \approx 30$, as far as we can tell this region does not shrink any further for $v > 30$, we tested this until $v \approx 600$. Outside this region, no collisional events occur at all, especially the density is zero around the central elliptic fixed point, where we observed the

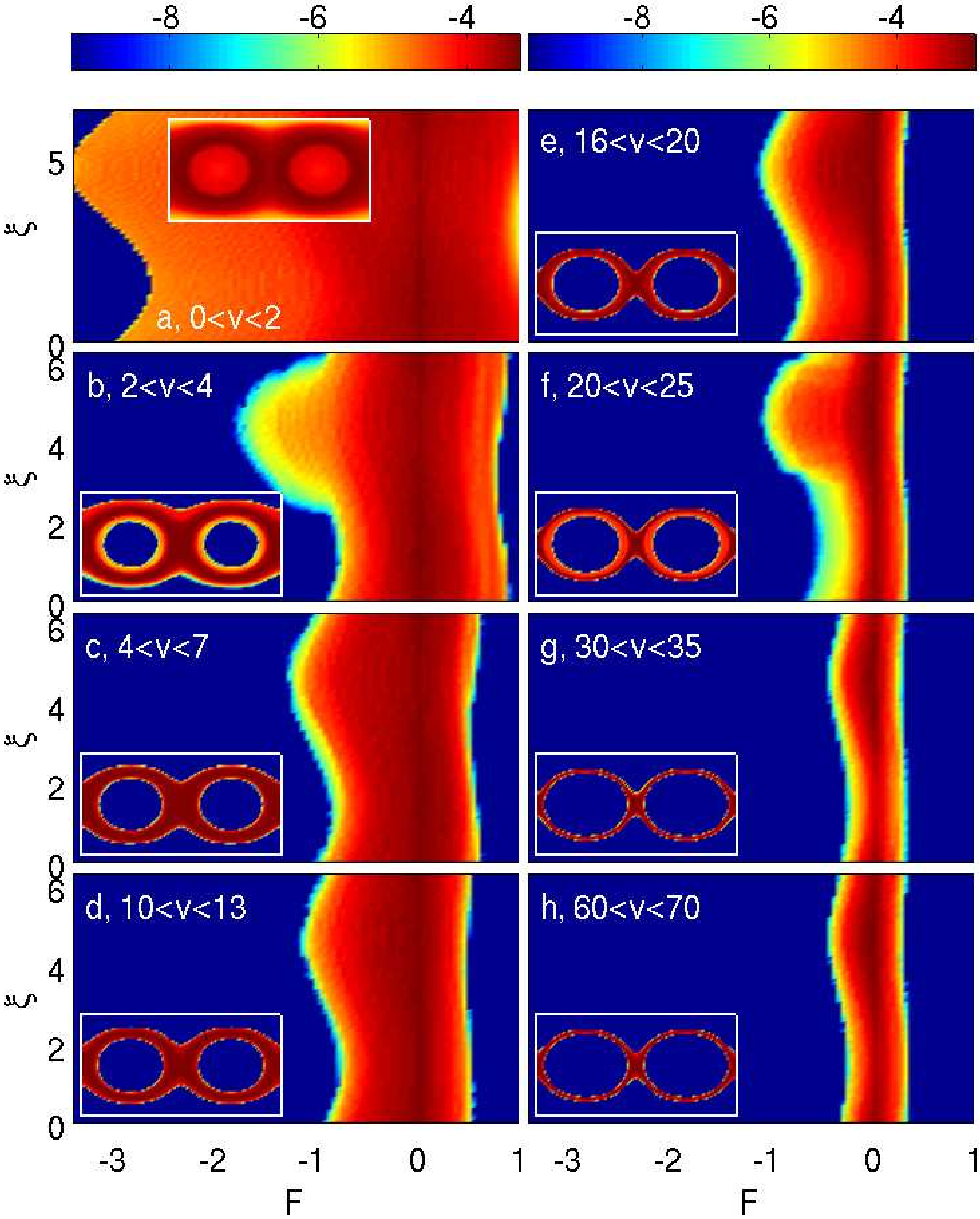

Figure 3.3: Velocity resolved phase space density $\rho_{v_1,v_2}(F,\xi)$ (log-scale colormap, breathing mode, $C = 0.1$). For low velocities (a), the ensemble covers the whole $F \times \xi$ plane. With increasing velocity (b)-(h), it is located in a region around $F(\phi, \alpha) \approx 0$. This region gets thinner and thinner with increasing velocity, until the asymptotic width is reached at around $v \approx 30$. The insets show the corresponding phase space densities $\rho_{v_1,v_2}(\phi, \alpha)$.

highest density for very low velocities, cf. Fig. 3.1. This kind of population of phase space is generic in the sense that it does not depend on the initial ensemble, as long as the initial velocity v_0 is sufficiently small.

The large regions at high v with zero phase space density are not caused by geometrical constraint as it was the case in the low velocity regime, cf. the discussion in section 3.2.1. Rather, there exist bulky regions which are not accessible for an ensemble starting at low v_0. This could either be regions of chaotic motion that are separated from the low v chaotic sea by invariant KAM-tori acting as impenetrable barriers, or regions consisting completely (or mostly, with chaotic layers in between) of invariant KAM-tori, i.e. large islands of integrable motion. In either case, particles starting inside the chaotic sea at low v cannot penetrate into these regions. By placing initial conditions of particles deliberately inside these regions and investigating their dynamics, we can gain further insight into these parts of phase space.

Lyapunov exponents

A quantity that is sensitive to whether a particle moves chaotically and regularly is the Lyapunov exponent σ. It is defined as the mean rate of exponential divergence of nearby trajectories [111]. Suppose we have a reference trajectory $\boldsymbol{x}(t)$ and a neighbor with initial conditions $\boldsymbol{x}(0) + \delta\boldsymbol{x}(0)$. The norm

$$d(t) = \sqrt{\sum_{i=1}^{m} \delta x_i^2(t)} \tag{3.8}$$

is a measure of divergence (m is the dimension of phase space).

The Lyapunov exponent σ is defined as [34]

$$\sigma = \lim_{\substack{t\to\infty \\ d(0)\to 0}} \left(\frac{1}{t}\right) \ln\left(\frac{d(t)}{d(0)}\right) . \tag{3.9}$$

It can be shown that for a system with a m-dimensional phase space there exist m so-called Lyapunov characteristic exponents which can be ordered by size: $\sigma_1 \geq \sigma_2 \geq \cdots \geq \sigma_m$. The Lyapunov exponent σ is the largest of the σ_i and the most important one when characterizing (chaotic) motion. σ is independent of the initial conditions for a connected region of phase space [34]. For a regular trajectory σ is zero, since the distance between between nearby integrable orbits diverges only linearly[1]. Chaotic trajectories have a Lyapunov exponent larger than zero. To determine the Lyapunov exponent numerically, the definition of Eq. (3.9) is not suited, since any finite initial distance $\boldsymbol{d}(t)$ will grow exponentially, however the phase space is bounded in ξ, α and ϕ. More appropriate is a numerical scheme proposed in Refs. [112, 113], which involves a frequent rescaling after some time τ of the acquired distance $\boldsymbol{d}(t)$ back to $\boldsymbol{d}(0)$.

In Fig. 3.4, the Lyapunov exponent σ for particles with $v_0 = 30$ and different initial values of F is shown. At $v = 30$, there are bulky regions which are not accessible for an ensemble starting with $v_0 = 0.1$ inside the low v chaotic sea, cf. Fig. 3.3. Choosing $v_0 = 30$ and F_0 randomly in $F_0 \in [F_{\min}, F_{\max}]$ will place many initial conditions in these regions

---

[1] Note that in general already an algebraic divergence leads to $\sigma = 0$.

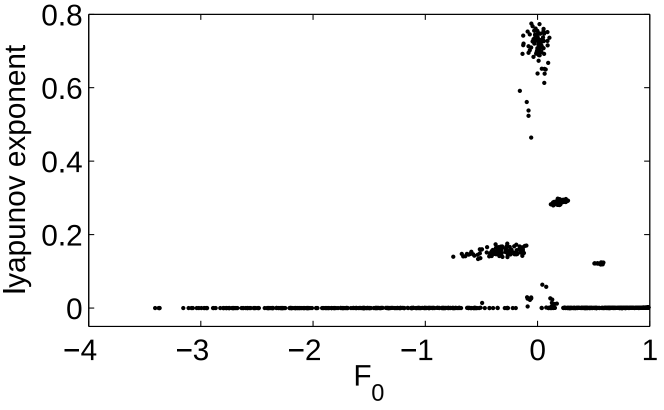

Figure 3.4: Lyapunov exponent σ for particles starting with $v_0 = 30$ and different initial F_0. Particles with $\sigma = 0$ move on invariant KAM-tori, whereas particles with $\sigma > 0$ perform chaotic motion, either inside bounded (especially in v) chaotic layers, or inside chaotic channels which are unbounded in v.

(of course some initial conditions will also be placed in the chaotic regime that is already connected with the low v chaotic sea).

All particles that start with $F_0 < -0.8$ (inside the inaccessible bulky regions) have $\sigma = 0$, they move on librator-type invariant KAM-tori, i.e. their motion is regular and this region is not connected to the chaotic sea at low v. The cloud of particles starting with $F_0 \approx 0$ has $\sigma \approx 0.7$ and corresponds to particles that move chaotically ($\sigma > 0$) in a region that is connected with the chaotic sea at low v, these particles show Fermi acceleration [114]. Particles inside the other clouds with $0 < \sigma < 0.4$ are confined to thin chaotic layers that are enclosed (especially in v) by invariant KAM-tori and are thus not connected to the low v chaotic sea, these particles explore a limited range in v only. Finally, particles with $F > 0$ and $\sigma = 0$ are confined to rotator-type invariant KAM-tori and move regularly. Again, the region with $F > 0$ and $\sigma = 0$ is not connected with the low v chaotic sea and the particles inside this region do not show Fermi acceleration.

The classification of the different clouds in Fig. 3.4 with $\sigma > 0$ into particles moving chaotically in a region in phase space that is connected to the low v chaotic sea at the one hand, and particles inside thin chaotic layers that are confined by invariant KAM-structures on the other hand, is not possible by solely the information provided by the Lyapunov exponent. To distinguish between two different kinds of chaotic motion, we additionally checked the evolution of v (and also the other phase space variables). Whereas particles inside the clouds with $0 < \sigma < 0.4$ explore a very limited range in v only, this is not true for the particles inside the large cloud at $\sigma \approx 0.7$, they exhibit diffusive motion in momentum space. Furthermore, all particles in clouds with $0 < \sigma < 0.4$ have a fixed sign of F, particles in the $\sigma \approx 0.7$ cloud do not have a fixed sign of F.

Overall, we ensured that the regions $\rho_{v_1,v_2}(F,\xi) = 0$ (and $\rho_{v_1,v_2}(\phi,\alpha) = 0$) with no collisional events in Fig. 3.3 are not due to geometrical constraints, but actually correspond to bulky regions of regular motion (and thin layers of chaotic motion layers confined in between such invariant KAM-tori). These regular structures act as impenetrable barriers for particles starting outside of them, for example, for particles starting inside the chaotic sea at low velocities. The origin of these invariant KAM-tori will be investigated in the following section.

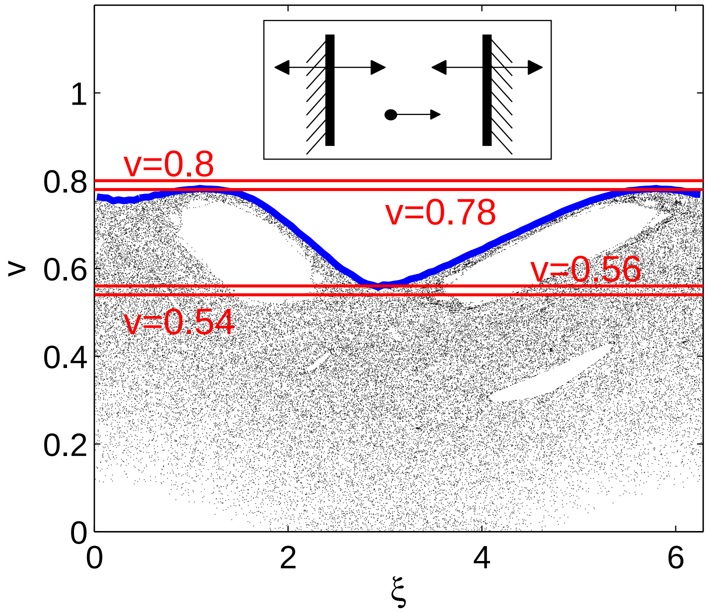

Figure 3.5: Poincaré surface of section of two infinite heavy walls oscillating with opposite phase (variant of the FUM). The first invariant spanning curve (FISC) is shown in blue. The four red lines mark the lower and upper boarder of the FISC. These four values of v are taken to produce the phase space density $\rho(\phi, \alpha)$ shown in Fig. 3.6. Inset: The model in configuration space.

3.3 Origin of the large invariant structures

At low velocities, particles starting with sufficiently small v_0 populate the whole $\xi \times F$-space and thus the whole $\phi \times \alpha$-subspace, see for example Fig. 3.3a. With increasing velocity, the region $F > 0.5$ and $F < -1$ is totally depleted (Fig. 3.3c), due to the presence of impenetrable invariant KAM structures. The origin of these regular islands will be analyzed in the following.

3.3.1 Librator-type invariant structures

To study the "birth" (in terms of v) of the librator-type regular islands ($F < 0$), it is useful to make a small excursion to a variant of the well known Fermi-Ulam model (FUM) [66,68].

Variant of the Fermi-Ulam model

Specifically, we consider the one-dimensional model of a particle moving in between two infinitely heavy walls oscillating harmonically with opposite phase, see the inset of Fig. 3.5. The Poincaré surface of section spanned by v and ξ for a single particle starting with $v_0 = 0.15$ is shown in Fig. 3.5, together with the first invariant spanning curve (FISC) (in blue). The minimum v value of the FISC is approximately 0.55, the maximum v value approximately 0.79. The FISC acts as an impenetrable barrier for particles starting below it. All initial conditions with $v \gg v_{\text{FISC}}$ lead to integrable motion on invariant curves similar to the FISC. For velocities right above the FISC, $v \gtrsim v_{\text{FISC}}$, there are additionally thin layers of chaotic motion, confined in between invariant curves.

Let's consider the motion in the driven elliptical billiard along the semi-minor axis. The central period two orbit with $(\xi_1 = \phi_1 = \alpha_1 = \pi/2, v_1 = 2/\pi)^\top$ and $(\xi_2 = \phi_2 = 3\pi/2, \alpha_2 = \pi/2, v_2 = 2/\pi)^\top$ (and of course the symmetric counterpart) is stable. Small deviations for example in ϕ or α will not get amplified, i.e. the particle will continue to move essentially parallel to the semi-minor axis. The ξ, v dynamics of the full 4D mapping for this kind

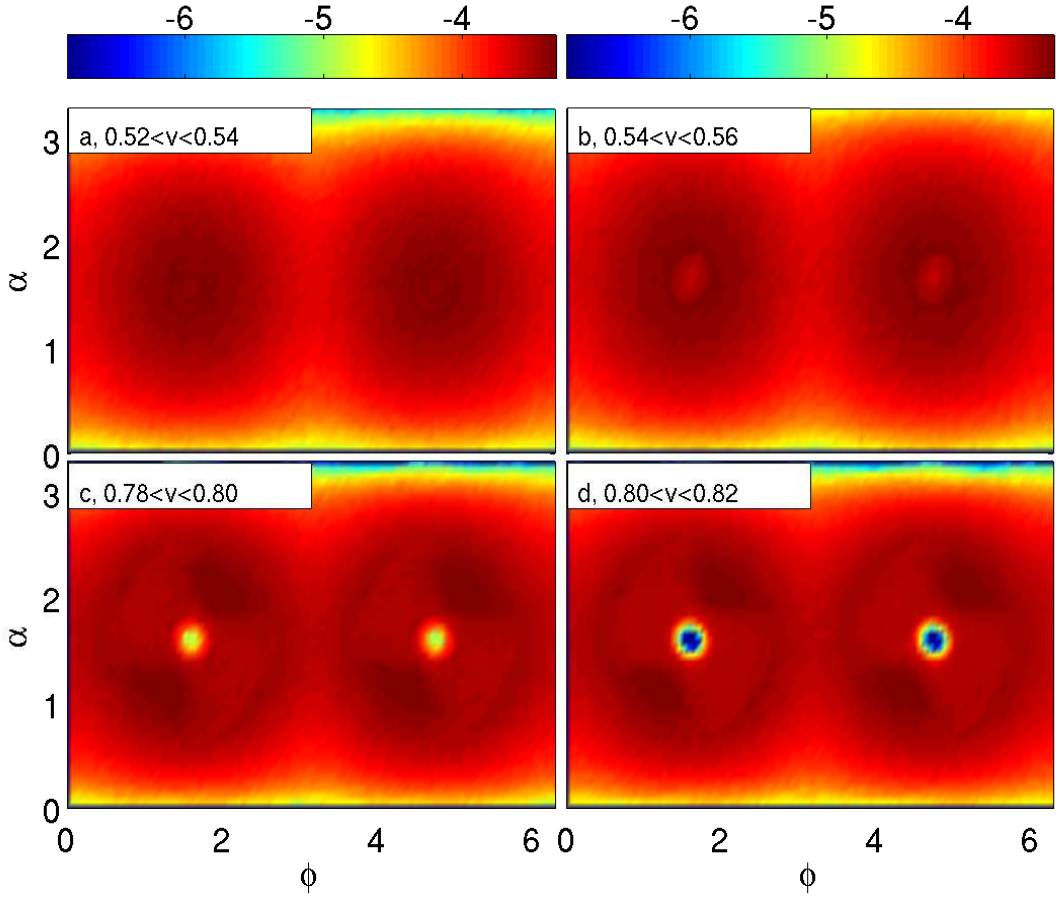

Figure 3.6: Velocity resolved phase space density $\rho_{v_1,v_2}(\phi,\alpha)$ (log-scale colormap, breathing mode, $C = 0.1$). The density is highest around $\phi = \pi/2, 3\pi/2, \alpha = \pi/2$ (a), a weak dip appears in (b) around $\phi = \pi/2, 3\pi/2, \alpha = \pi/2$, gets more pronounced in (c) until $\rho(\phi \approx \pi/2, 3\pi/2, \alpha \approx \pi/2) = 0$ in (d). The velocity regime (a) lies completely below v of the FISC, (b) and (c) are in v regime of the FISC and (d) is slightly above the FISC, cf. Fig. 3.5.

of motion is thus reproduced extremely well by the above described variant of the FUM. As a consequence, particles in the neighborhood of this period two orbit, i.e particles with $\alpha \approx \pi/2, \phi \approx \pi/2$ and $\alpha \approx \pi/2, \phi \approx 3\pi/2$, move mostly on invariant curves if their velocity is larger than $v_{\mathrm{FISC}}(\xi)$. These regular regions are inaccessible from the outside, i.e. particles starting with $v_0 \ll v_{\mathrm{FISC}}$ cannot access them.

The consequences of the analogy between the FUM and the motion along the semi-minor axis in the driven elliptical billiard can be seen in Fig. 3.6, where the phase space density $\rho_{v_1,v_2}(\phi,\alpha)$ is shown for very thin slices of v in a region where the FISC of the associated FUM is located. The density $\rho_{0.52,0.54}(\phi,\alpha)$ (Fig. 3.6 a) is maximal in a rather large region around $\phi = \pi/2, 3\pi/2, \alpha = \pi/2$. This velocity slice is below $v_{\mathrm{FISC}}(\xi)$ for all phases ξ (remember $\min(v_{\mathrm{FISC}}(\xi)) \approx 0.55$). The density $\rho_{0.54,0.56}(\phi,\alpha)$ (Fig. 3.6 b) shows a slight dip around $\phi = \pi/2, 3\pi/2, \alpha = \pi/2$, since there are regular structures associated with the FISC-like motion at these velocities, which are not accessible for the discussed initial ensemble. However, the dip is weakly pronounced due to the fact that the FISC

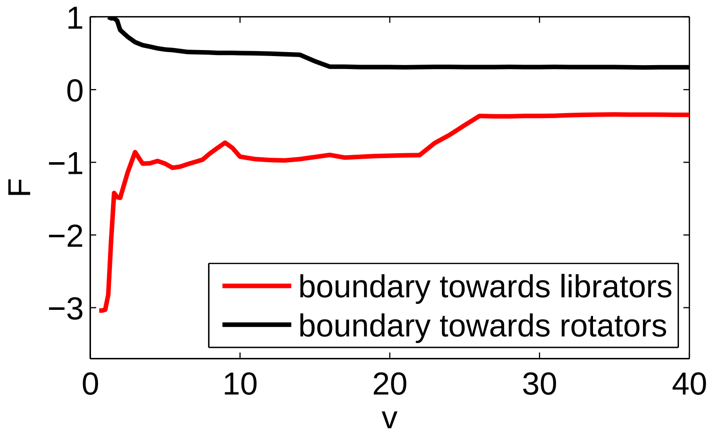

Figure 3.7: Boundaries of the large invariant structures in F space as a function of the velocity v. The chaotic sea (the area between the red and the black curve) is extended over the whole available F range at low v and gets more and more squeezed into a thin channel around $F = 0$ with increasing v.

reaches such low velocities in a very limited ξ range only, see Fig. 3.5. With increasing v, the dip around $\phi = \pi/2, 3\pi/2, \alpha = \pi/2$ gets more and more pronounced, see for example $\rho_{0.78,0.80}(\phi, \alpha)$ in Fig. 3.6 c, since the inaccessible invariant structures are present at these velocities for almost all phases ξ (again compare with Fig. 3.5). Finally, $\rho_{0.80,0.82}(\phi, \alpha)$ (Fig. 3.6 d) is zero around $\phi = \pi/2, 3\pi/2, \alpha = \pi/2$, since the invariant structures cover the whole ξ range for $v > \max(v_{\mathrm{FISC}}(\xi)) \approx 0.79$.

With increasing velocity v, we expect the fingerprints of the emergence of a quasistatic regime for the billiard: The particles are fast enough to experience many collisions with the oscillating walls within a narrow interval of the phase of oscillation. The velocity v of the particles is much larger than the boundary velocity u, i.e. $v \gg \omega C \Rightarrow \boldsymbol{v}_n - \boldsymbol{u}_{n+1} \approx \boldsymbol{v}_n$. The expression for the next velocity (2.36) reduces to $\boldsymbol{v}_{n+1} \approx \boldsymbol{v}_n - 2\langle \boldsymbol{n}_{n+1}, \boldsymbol{v}_n \rangle \boldsymbol{n}_{n+1}$, which is the expression for an elastic reflection, the angle of incidence is almost the angle of reflection. As a result, fast particles trace the orbits of the static system. Thus, the ϕ, α dynamics of (fast) particles in the librator region (at least if they are not too close to the separatrix) can be approximated quite good by the ϕ, α dynamics of a librator in the static elliptical billiard. Concerning the ξ, v dynamics, such particles effectively ‘see’ two oscillating walls, so the variant of the FUM is applicable. As a consequence, the invariant structures grow with increasing v in ϕ and α (and thus also in F), since more and more particles resemble the ϕ, α dynamics of librators in the static elliptical billiard.

The above discussed scenario is valid for the motion along the semi-minor axis, i.e. for $\phi \approx \pi/2, 3\pi/2, \alpha \approx \pi/2$. The motion along the semi-major axis cannot be treated similarly with the variant of the FUM, since the corresponding period two orbit ($\phi_1 = 0, \xi_1 = \alpha_1 = \pi/2, v_1 = 4/\pi$) and ($\phi_2 = \pi, \xi_2 = 3\pi/2, \alpha_2 = \pi/2, v_2 = 4/\pi$) is already unstable. Any small deviation in ϕ or α will get exponentially amplified, such particles move nearly parallel to the semi major axis for very few collisions only.

3.3.2 Rotator-type invariant structures

So far, we discussed invariant structures emanating from librator type orbits ($F < 0$), especially emanating from the central elliptic fixed points at $F = F_{\mathrm{min}}$. In the static ellipse, the other extreme is represented by rotator type orbits with F close to $F_{\mathrm{max}} = 1$. These orbits (they are also called whispering-gallery orbits) skip very close to the boundary of the ellipse, accumulating many collisions during one rotation. When driving the ellipse,

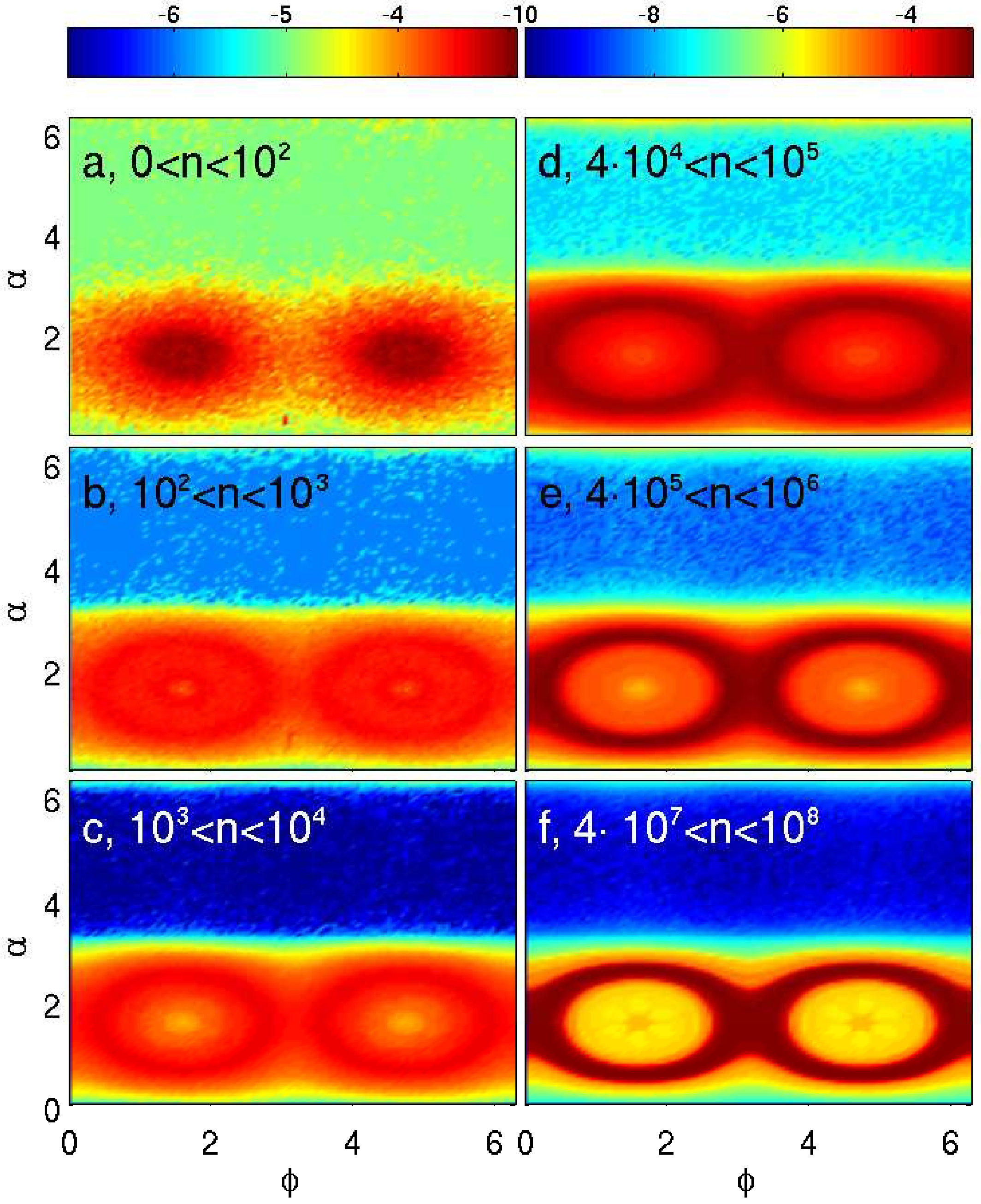

Figure 3.8: Evolution (in terms of the number of collisions n) of the collision resolved phase space density $\rho_{n1,n_2}(\phi,\alpha)$ in the breathing mode ($C = 0.1$, logarithmic colormap). In the beginning (a,b), the ensemble is located around the central fixed point of the corresponding frozen billiard, with increasing number of collisions, $(c) - (f)$, it gets focused more and more onto the region around $F = 0$.

these orbits get destroyed if they have very low ($v < 1$) velocities. With increasing v, we expect that at least the orbits with $F \lessapprox 1$ will get stabilized, i.e. they will follow the boundary of the ellipse adiabatically. Qualitatively, this will be possible when the period $T = 2\pi/\omega$ of the applied driving law of the ellipse and the period T_r of such a whispering-gallery orbit are comparable, i. e. $T \approx T_r$. To estimate the velocity v_r corresponding to T_r, we assume that the length l of such an orbit is given by the mean circumference of the ellipse. For simplicity, we replace the mean circumference by the circumference of the equilibrium configuration of the ellipse at $\xi = 0$, which is given by $4a_0 E_{el}(\epsilon)$, where $E_{el}(\epsilon)$ is the complete elliptic integral of the second kind [115]. With $a_0 = 2, b_0 = 1 \Rightarrow \epsilon = \sqrt{3/4}$ we obtain

$$v_r = \frac{l}{T_r} \approx \frac{8E_{el}(\sqrt{3/4})}{2\pi} \approx 1.54. \tag{3.10}$$

For values of $v > v_r$, stable (integrable) rotator-type motion is possible. In Fig. 3.7, the boundaries in terms of F (actually the mean position of the boundary, averaged over the phase ξ) of the large invariant structures emanating either from librators (red) or rotators (black) are shown as a function of the velocity v. At low v, the chaotic sea (the region between the two curves) covers the whole available range in F. With increasing v, the chaotic sea is squeezed more and more into a thin channel around $F = 0$ until the asymptotic width of the channel is reached at $v \approx 30$. Note that this width of the channel does not decrease any further, we checked this until $v = 600$ in a simulation where we iterated until 10^{11} collisions. The extracted value v_r from Fig. 3.7 for the existence of large invariant structures emanating from rotator-type motion is $v_r \approx 1.4$, which agrees quite well with the approximation $v_r \approx 1.54$ of Eq. (3.10).

3.4 Collision resolved phase space density

In section 3.2, we use the phase space densities $\rho_{v_1,v_2}(F,\xi)$ and $\rho_{v_1,v_2}(\phi,\alpha)$ to explore slices of phase space with thickness $\triangle v = v_2 - v - 1$. Rather than analyzing the phase space densities velocity resolved, it is also instructive to investigate the corresponding collision resolved phase space densities. For that purpose, we define

$$\rho_{n_1,n_2}(F,\xi) = \frac{1}{n_2 - n_1 + 1} \sum_{n=n_1}^{n_2} \int_v \rho(F,\xi,v,n)dv \tag{3.11}$$

$$\rho_{n_1,n_2}(\phi,\alpha) = \frac{1}{n_2 - n_1 + 1} \sum_{n=n_1}^{n_2} \int_0^{2\pi} d\xi \int_v dv\rho(\xi,\phi,\alpha,v,n)dv, \tag{3.12}$$

i.e. all collisions between n_1 and n_2 are projected onto the $\xi \times F$ space, respectively the $\phi \times \alpha$ plane. This allows us to study the evolution of the ensemble in phase space, with respect to the question where it is located with increasing collision number. The phase space density $\rho_{n_1,n_2}(\phi,\alpha)$ for an ensemble starting with $v_0 = 0.1$ is shown in Fig. 3.8 (breathing mode, $C = 0.1$) and the corresponding $\rho_{n_1,n_2}(F,\xi)$ in Fig. 3.9 (both in a log-scale colormap). In the beginning ($n_1 = 0$, $n_2 = 100$) of the evolution, the region around the elliptic fixed points (i.e. at $\alpha = \pi/2$, $\phi = \pi/2, 3\pi/2$ or correspondingly $F_{min}(\xi) = -\epsilon^2(\xi)/(1-\epsilon^2(\xi)))$ of the corresponding frozen billiard possesses the highest visiting probability, see the panels (a). For large collisions numbers ($n_1 = 4 \cdot 10^7$, $n_2 = 10^8$), see Figs. 3.8f and 3.9d, the ensemble

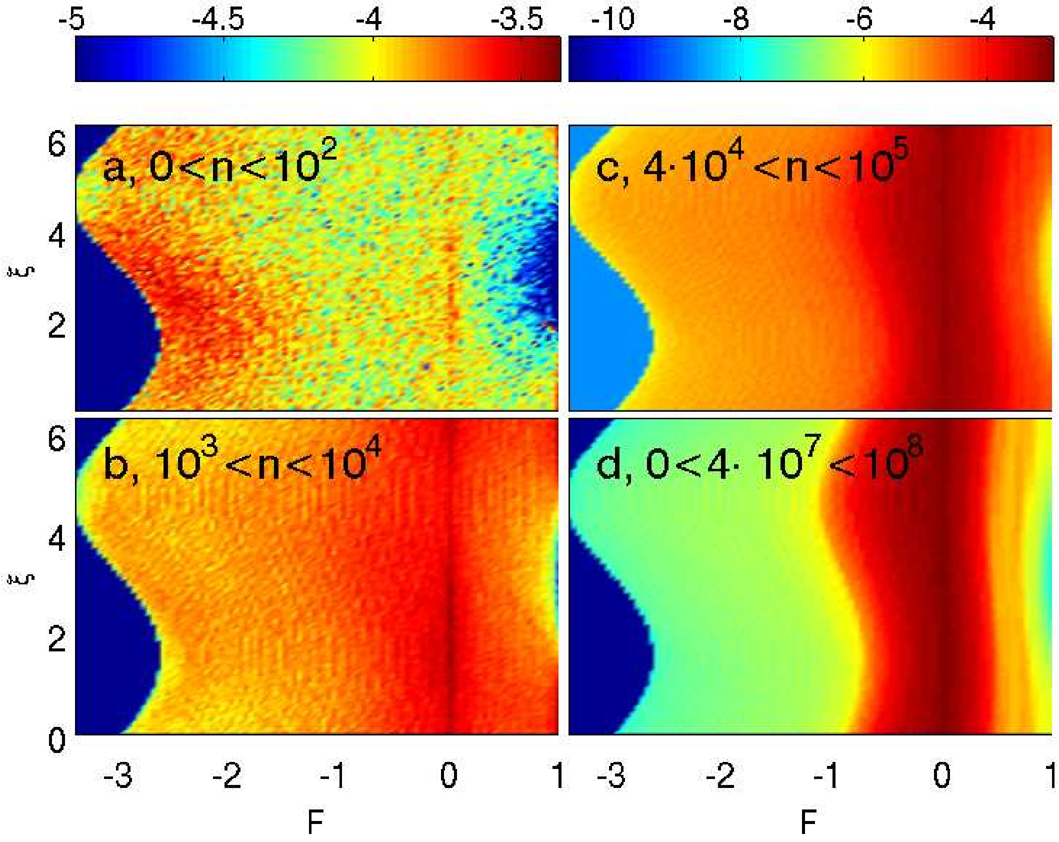

Figure 3.9: Evolution (in terms of the number of collisions n) of the collision resolved phase space density $\rho_{n1,n_2}(F,\xi)$ in the breathing mode ($C = 0.1$, logarithmic colormap). With increasing number of collisions, the ensemble gets focused more and more onto the region around $F = 0$.

is located predominantly in a region around the separatrix ($F = 0$) of the corresponding static system. In other words, with increasing number of collisions, the ensemble gets focused more and more onto the region around $F = 0$.

The evolution (in terms of n) of $\rho_{n_1,n_2}(\phi,\alpha)$ resembles the evolution (in terms of v) of $\rho_{v_1,v_2}(\phi,\alpha)$, the same is true for the corresponding $\rho_{n_1,n_2}(F,\xi)$ and $\rho_{v_1,v_2}(F,\xi)$. However, the collision resolved densities are smeared out, whereas the velocity resolved phase space densities show sharp transition between regions of high and low (actually zero) densities (for intermediate and high velocities). The reason is the following: As we will see in chapter 6, the ensemble shows Fermi acceleration, i.e. the mean velocity of the ensemble increases with increasing number of collisions. But this is true for the mean velocity only, there will always be some particles with low velocities, and these particles will explore the whole $\phi \times \alpha$ plane and not just the region around $F = 0$, like particles with high velocities do.

Combining our knowledge about the collision and the velocity resolved phase space densities and the fact the ensemble averaged modulus of the velocity increases with increasing number of collisions, we can conclude that the ensemble is not only focused onto the $F = 0$ region in its evolution, but it is also squeezed more and more into the thin channels (present at high velocities) of chaotic motion around $F = 0$.

3.5 Other setups

3.5.1 Larger amplitudes in the breathing mode

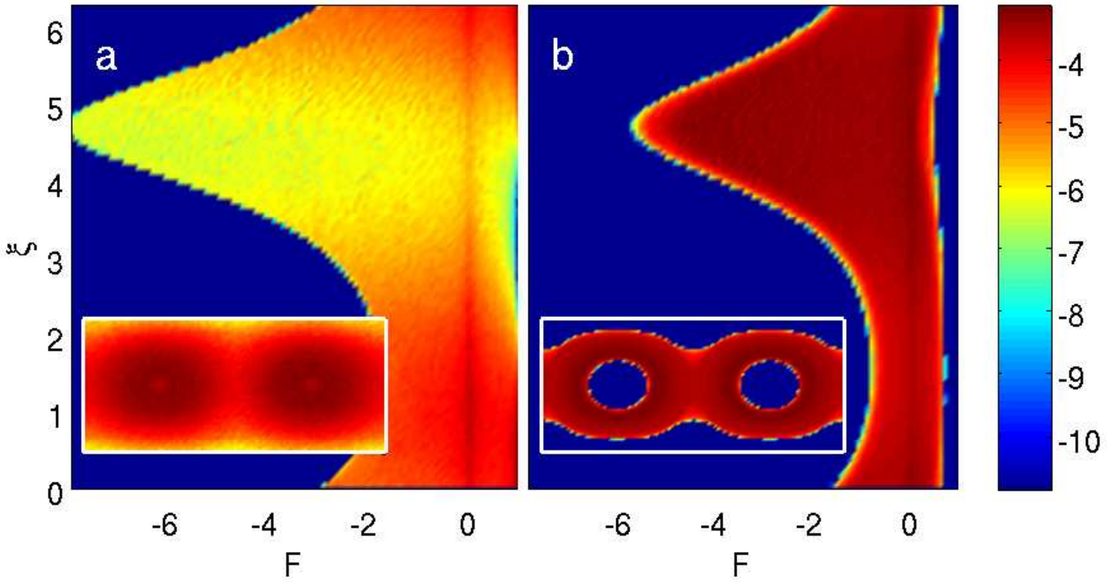

Figure 3.10: Velocity resolved phase space density $\rho_{v_1,v_2}(\xi, F)$ (log-scale colormap) in the breathing mode, now the amplitude $C = 0.5$.

All figures presented so far concerning the phase space analysis show results of the breathing mode with an amplitude of $C = 0.1$. If we increase the amplitude in the breathing mode, we obtain similar results, however there are some differences. Exemplarily, the velocity resolved phase space density $\rho_{v_1,v_2}(\xi, F)$ is shown in Fig. 3.10 for an amplitude of $C = 0.5$ in two different velocity regimes: (a) $0 < v < 2$ and (b) $150 < v < 180$. Due to the larger driving amplitude, the difference between the maximal (reached at $\xi = 3\pi/2$) and minimal (reached at $\xi = \pi/2$) eccentricity is increased. As a consequence, $F_{\text{min}}(\xi)$ performs a strong oscillation and the global minimum $F_{\text{min}}^{gl} = \min(F_{\text{min}}(\xi))$ is shifted towards larger negative values, cf. also Fig. 2.7. The strong oscillation of $F_{\text{min}}(\xi)$ can be seen in Fig. 3.10a, at $\xi = 3\pi/2$ $F_{\text{min}}(3\pi/2) \approx -8$, whereas at $\xi = \pi/2$ $F_{\text{min}}(\pi/2) \approx -2$ (compare with the corresponding Fig. 3.3 for an amplitude of $C = 0.1$, where $F_{\text{min}}(3\pi/2) \approx -3.4$ and $F_{\text{min}}(\pi/2) \approx -2.6$). Since $F_{\text{max}} = 1$ independent of the phase ξ, the fraction of phase space corresponding to librators ($F < 0$) also performs a strong oscillation. The librators which are, at a given phase ξ, rather close to $F_{\text{min}}(\xi)$ actually remain far enough apart from the separatrix $F = 0$ for a full oscillation. Only such librators describe a ξ, v dynamics which is reproduced by the corresponding FUM. The region in F-space in which the FUM is applicable is much narrower than for an amplitude of $C = 0.1$. As a result, the large invariant structures fill out a smaller part of phase space and the region of chaotic motion around F is much larger for $C = 0.5$ compared to $C = 0.1$. This can be seen in Fig. 3.10b and the inset, where $\rho_{v_1,v_2}(\phi, \alpha)$ is shown.

The region in Fig. 3.10b around $F = 0$ with $\rho(\xi, F) \neq 0$ corresponding to chaotic motion does not shrink any further with increasing velocity, so the asymptotic width of this 'chaotic channel' is reached at around $v_{asympt} \approx 150$ for $C = 0.5$. As already indicated, for an amplitude of $C = 0.1$, the asymptotic width is reached already at $v_{asympt} \approx 30$. The natural momentum scale of the driven elliptical billiard is ωC. The ratio of this scale for different amplitudes (for fixed ω) is equal to the ratio of the velocities where the asymptotic width of the chaotic channel is reached:

$$\frac{v_{asympt}(C = 0.1)}{v_{asympt}(C = 0.5)} \approx \frac{30}{150} = \frac{\omega C = 0.1}{\omega C = 0.5} = \frac{1}{5} \tag{3.13}$$

3.5.2 Constant eccentricity mode

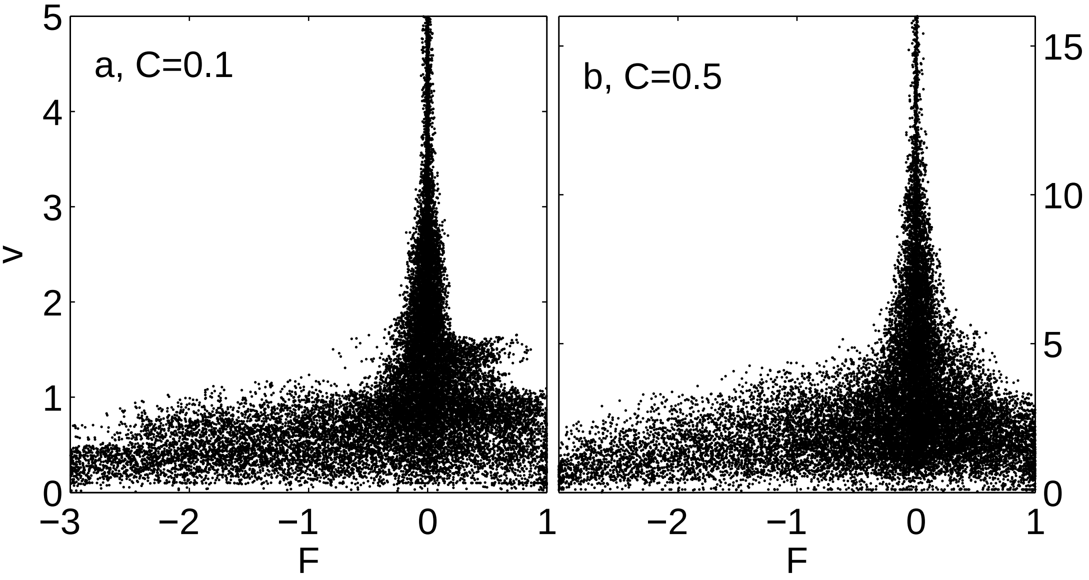

Figure 3.11: Accessible $F \times v$ space for an ensemble starting inside the chaotic sea at low v in the constant eccentricity mode for two different amplitudes C. To generate this plot, the ensembles are propagated for 10^{11} collisions. After certain, logarithmically chosen, iteration numbers, the $F \times v$ values of all particles are plotted. The asymptotic width of the thin channel is approximately the same for both amplitudes, even though it is reached earlier ($v \approx 3.5$) for $C = 0.1$ than for $C = 0.5$ ($v \approx 12$).

In the breathing mode, we observed a change in the composition of phase space with increasing velocity v, from a large chaotic sea at low v, to a thin channel of chaotic motion bounded by large invariant structures at high velocities. This structural change is also present in the constant eccentricity mode. There are some differences between the two driving modes, qualitatively and quantitatively. The minimum of F does neither depend on the phase ξ nor on the amplitude C, see also the discussion in section 2.2.7. As a consequence, the boarder between chaotic and regular motion in the $\xi \times F$-subspace (for high velocities) is not curved, like the one in Figs. 3.3 and 3.10, but is rather a straight line (the ξ dependence of ϵ caused the curved/sinusoidal shape of the boarder between $\rho(F, \xi) = 0$ and $\rho(F, \xi) > 0$ in the breathing mode). Quantitatively, the 'birth' of the large

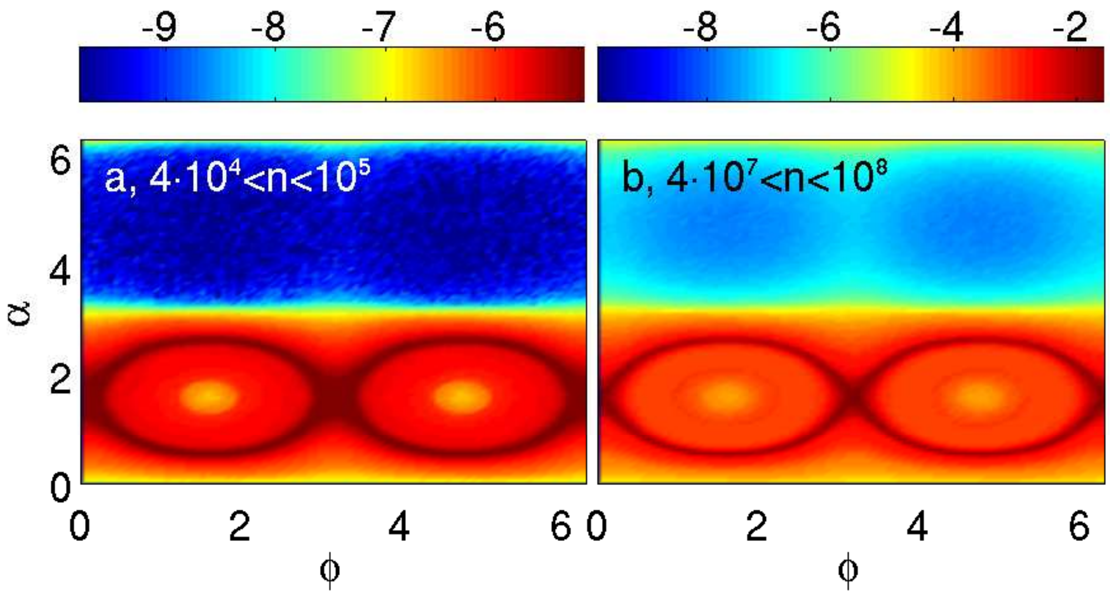

Figure 3.12: Collision resolved phase space density $\rho_{n_1,n_2}(\phi, \alpha)$ (log-scale colormap, $C = 0.1$) in the constant eccentricity mode. Like in the breathing mode, the ensemble gets focused in its evolution more and more onto the region around $F = 0$. The focusing effect is even stronger pronounced in the constant eccentricity mode.

invariant structures emanating from librator-type motion occurs at slightly different values of v, due to following reason: The corresponding FUM is slightly different, since for an amplitude of C, the oscillation amplitude along the semi-minor axis (which has to be taken for the FUM) is not C, but rather Cb_0/a_0 ($= 0.5C$ for our choice of $a_0 = 2, b_0 = 1$). This leads to a different (lower) position of the FISC and in turn, the large regular structures originate at smaller values of v.

An important difference between the two driving modes is the dependence of the asymptotic width of the chaotic channel on the amplitude. In the breathing mode, increasing the amplitude leads to a widening of the chaotic channel due to the larger deformation (in terms of the eccentricity ϵ) of the elliptical billiard. The constant eccentricity driving is a pure scaling and does not deform the elliptical billiard, increasing the amplitude does not change this property, it just changes the natural momentum scale ωC. As a consequence, the asymptotic width of the chaotic channel is independent of the driving amplitude. This can be seen in Fig. 3.11. To generate Fig. 3.11, an ensemble of 100 particles starting with $v_0 = 0.1$ is propagated for 10^{11} collisions. After certain, logarithmically chosen, iteration numbers, the $F \times v$ values of each particle are reported. All such obtained $F \times v$ pairs are plotted in Fig. 3.11 for $C = 0.1$ (a) and $C = 0.5$ (b). In other words, Fig. 3.11 shows the accessible $F \times v$-space for an ensemble starting inside the chaotic sea at low v. Obviously, the asymptotic width is independent of the driving amplitude, although it is reached at different values of v for the different amplitudes (note the different y-scales in the plot).

Compared to the breathing mode, the asymptotic width of the chaotic channel is considerably smaller and is reached at lower values of v. This has to be expected, since the driving law in the breathing mode is a much stronger perturbation than the one in the constant eccentricity mode. On the one hand, already lower velocities in the constant eccentricity mode lead to librator-type motion similar to the orbits in the static elliptical billiard, allowing the application of the FUM for the ξ, v dynamics - the asymptotic width of the chaotic channel is reached earlier (in terms of v). On the other hand, the missing deformation of the billiard ($\epsilon(\xi) = const.$) allows the application of the FUM to particles moving much closer to the separatrix ($F = 0$) than in the breathing mode - the asymptotic width of the chaotic channel is significantly reduced.

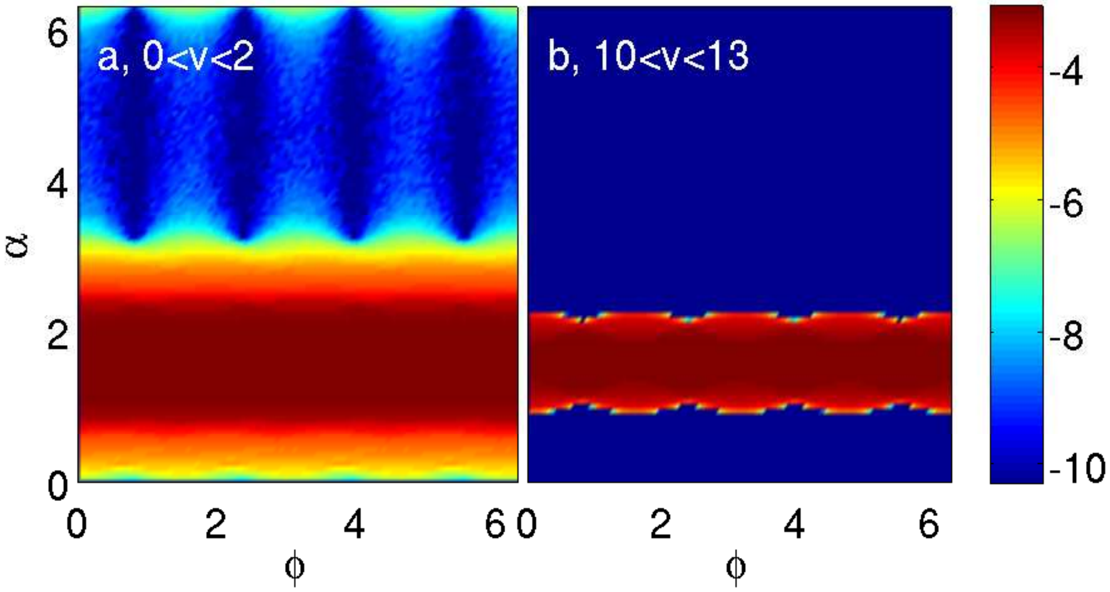

Figure 3.13: Phase space density $\rho(\phi, \alpha)$ in the quadrupole mode ($C = 0.1$) in two different velocity regimes (log-scale colormap). For low velocities (a), the whole $\phi \times \alpha$ space is populated, for higher velocities (b), only a banded region is populated due to emergence of inaccessible rotator-type large regular regions.

Like in the breathing mode, the ensemble is squeezed in its evolution more and more into the thin channels of chaotic motion around $F = 0$. This can be seen in Fig. 3.12, where the collision resolved phase space density $\rho_{n_1,n_2}(\phi, \alpha)$ is shown ($C = 0.1$, logarithmic colormap). Clearly, the high density region around $F = 0$ is considerably thinner than in the case of the breathing mode, since the asymptotic width of the chaotic channel is smaller, i.e. the focusing effect is even more pronounced in the constant eccentricity mode.

3.5.3 Quadrupole mode

In the quadrupole mode the situation is somewhat different. Since the semi-major and semi-minor axes are periodically interchanged, the stability along these axes also changes periodically in time from unstable to stable etc. As a result, there is no stable motion along any of the coordinate axes possible and of course the FUM is not applicable. On the other hand, the whispering-gallery orbits (rotator-type motion with F close to, but smaller than one) are not affected by the periodic interchange of the semi-major and semi-minor axes, since these orbits simply follow the boundary of the elliptical billiard adiabatically. This can be seen in Fig. 3.13, where the phase space density $\rho_{v_1,v_2}(\phi, \alpha)$ for two different velocity regimes is shown, (a) $0 < v < 2$ and (b) $10 < v < 13$ (for an ensemble starting with

$v_0 = 0.1$, $C = 0.1$). Like in other driving modes, the whole $\phi \times \alpha$-space is populated for low velocities, see Fig. 3.13a. At higher velocities, see Fig. 3.13b, the regions with $\rho(\phi, \alpha) = 0$ correspond to inaccessible invariant structures emanating from whispering-gallery orbits. There are no large regular islands emanating from librator-type orbits, thus the phase space density is not depleted around the regions belonging to the motion along the coordinate axes. Going to higher values of v does not lead to a further growth of the regular regions, so the asymptotic width of the chaotic channel, although being quite differently shaped compared to the other driving modes, is reached at $v \approx 10$ for an amplitude of $C = 0.1$.

Like in the breathing mode, increasing the amplitude leads to a widening of the asymptotic width of the chaotic channel and requires higher velocities to reach the asymptotic width of the channel.

4 Periodic Orbits

To gain further insight into the phase space properties, we search for (unstable) periodic orbits in the driven elliptical billiard. This is an intricate task and becomes more difficult with increasing velocity of the orbits, since the typical period grows linearly with v (cf. Eq. (4.11)). Before we discuss the periodic orbits in driven elliptical billiard, we briefly discuss the method we used to detect them in the following section.

4.1 Numerical method

We use a variant of the method developed in Refs. [116, 117] to detect the periodic orbits. The method of Refs. [116, 117] transforms the original dynamical system to a new one which has the same fixed points. The transformation is chosen such, that a certain class of (unstable) periodic orbits gets stabilized, thus enabling their numerical detection.

Suppose we have a N-dimensional discrete dynamical system $\mathcal{U}$ given by

$$\mathcal{U} : \boldsymbol{r}_{i+1} = \boldsymbol{f}(\boldsymbol{r}_i), \quad \boldsymbol{r}_{i+1}, \boldsymbol{r}_i \in \mathbb{R}^N. \tag{4.1}$$

A new dynamical system $\mathcal{S}_k$ is constructed via a linear transformation

$$\mathcal{S}_k : \boldsymbol{r}_{i+1} = \boldsymbol{r}_i + \lambda \boldsymbol{C}_k(\boldsymbol{f}^p(\boldsymbol{r}_i) - \boldsymbol{r}_i), \tag{4.2}$$

where $\boldsymbol{C}_k$ is an orthogonal matrix, λ is a small factor and p is the period of the periodic orbit we want to stabilize. Note that if we have a periodic orbit of period p given by the set $\mathcal{P} = \{\boldsymbol{r}_i, \boldsymbol{r}_{i+1}, \ldots, \boldsymbol{r}_{i+p-1}\}$, then each $\boldsymbol{r} \in \mathcal{P}$ is a fixed point of $\boldsymbol{f}^p$, so $\boldsymbol{f}^p(\boldsymbol{r}) = \boldsymbol{r}$. Obviously, $\boldsymbol{f}^p$ and $\mathcal{S}_k$ have the same fixed points. It can be shown [118] that for every (unstable) fixed point, there exists a suitable orthogonal transformation matrix $\mathcal{C}_k$ together with a small factor λ such that this fixed point is stable under $\mathcal{S}_k$, actually it becomes an attractor. The small factor $\lambda < 1$ has to be chosen in such a way that the modulus of the eigenvalues of the linear stability matrix $\boldsymbol{D}\mathcal{S}_k$ (also called monodromy matrix) is smaller than one, where

$$\boldsymbol{D}\mathcal{S}_k = \mathbf{1} + \lambda \boldsymbol{C}_k(\boldsymbol{D}\boldsymbol{f}^p - \mathbf{1}) \tag{4.3}$$

and $\boldsymbol{D}\boldsymbol{f}^p$ is the linear stability matrix of $\boldsymbol{f}^p$.

The orthogonal matrices $\boldsymbol{C}_k$ correspond to reflections and rotations along the coordinate axes. All entries of $\boldsymbol{C}_k$ are either zero or plus minus one, $C_{ij} \in \{0, \pm 1\}$. Each row and each column contains only one element which is different from zero. In total, there exist $N!2^N$ of such matrices ($= 384$ for $N = 4$) that stabilize different types of periodic orbits. Since some of the transformations are redundant, a much smaller number of different matrices $\mathbf{C}_k$ is sufficient to find all periodic orbits. Now we identify $\boldsymbol{f}$ with the mapping $\mathcal{M}$ (2.26), so $N = 4$. For $N = 4$, no minimal set of $\boldsymbol{C}_k$ has yet been rigorously determined, however a set consisting of 14 different $\boldsymbol{C}_k$ seems to be sufficient to detect all periodic orbits [118].

The advantage of the described method is its global convergence. Any initial conditions, no matter how far they are away from a specific fixed point, will eventually converge if the orthogonal matrix $\boldsymbol{C}_k$ and the small factor λ are chosen appropriately. The drawback is the slow convergence, which depends crucially on λ. On the one hand, λ has to be sufficiently small to ensure that the modulus of all eigenvalues of the matrix $\boldsymbol{D}\mathcal{S}_k$ (4.3) is smaller than one. On the other hand, Eq. (4.2) implies that for very small values of λ, $\boldsymbol{r}_{i+1} \approx \boldsymbol{r}_i$, so the convergence becomes worse with decreasing λ. To circumvent the slow convergence, we use a twofold scheme: Firstly, we use the method based on the linear transformation (4.2) to approach a fixed point, secondly, a Newton-Raphson method [110] is used to obtain the fixed point with high accuracy. The Newton-Raphson method is known to converge very fast, but it requires a good initial guess of the fixed point, this is why we use the linear transformation method first. Applying the Newton-Raphson method requires the Jacobian matrix (2.41), calculated in section 2.2.4.

4.2 Basic properties of periodic orbits in the elliptical billiard

4.2.1 Different types of periodic orbits

Suppose we have a periodic orbit of period p given by the set $\mathcal{P} = \{\boldsymbol{r}_1, \boldsymbol{r}_2, \ldots, \boldsymbol{r}_{p-1}\}$, so $\boldsymbol{r}_i \in \mathcal{P}$ is a fixed point of $\mathcal{M}^p$, $\mathcal{M}^p(\boldsymbol{r}_i) = \boldsymbol{r}_i$ (note that for any $\boldsymbol{r}_i \in \mathcal{P}$, $\boldsymbol{r}_{i+p} = \boldsymbol{r}_i$). To determine the stability of a fixed point, we investigate the linear stability in a small neighborhood around $\boldsymbol{r}_i$, so we expand $\boldsymbol{r} = \boldsymbol{r}_i + \delta\boldsymbol{r}_i$. Linearizing $\mathcal{M}^p(\boldsymbol{r})$ yields

$$\begin{aligned}\mathcal{M}^p(\boldsymbol{r}) = \mathcal{M}^p(\boldsymbol{r}_i + \delta\boldsymbol{r}_i) = \mathcal{M}^p(\boldsymbol{r}_i) + \boldsymbol{D}\mathcal{M}^p(\boldsymbol{r}_i)\delta\boldsymbol{r}_i + \mathcal{O}((\delta\boldsymbol{r}_i)^2) = \\ = \boldsymbol{r}_i + \boldsymbol{D}\mathcal{M}^p(\boldsymbol{r}_i)\delta\boldsymbol{r}_i + \mathcal{O}((\delta\boldsymbol{r}_i)^2). \quad (4.4)\end{aligned}$$

The linearization $\boldsymbol{D}\mathcal{M}^p(\boldsymbol{r}_i)$ is called the monodromy matrix and is of course just the Jacobian matrix $\mathcal{J}$ (2.41). Using the chain rule for differentiation, the monodromy matrix can be written as [111]

$$\boldsymbol{D}\mathcal{M}^p(\boldsymbol{r}_i) = \mathcal{J}(\boldsymbol{r}_{i+p-1}) \cdot \mathcal{J}(\boldsymbol{r}_{i+p-2}) \ldots \mathcal{J}(\boldsymbol{r}_{i+1}) \cdot \mathcal{J}(\boldsymbol{r}_i). \quad (4.5)$$

After one application of $\mathcal{M}^p$, the initial offset $\delta\boldsymbol{r}_i$ is now

$$\delta\boldsymbol{r}_{i+p} = \boldsymbol{D}\mathcal{M}^p(\boldsymbol{r}_i)\delta\boldsymbol{r}_i. \quad (4.6)$$

The (complex) eigenvalues of $\boldsymbol{D}\mathcal{M}^p(\boldsymbol{r}_i)$ are given by $\lambda_1, \lambda_2, \lambda_3$ and λ_4 and in a diagonal representation Eq. (4.6) can be written as

$$\delta\boldsymbol{s}_{i+p} = \mathrm{diag}(\lambda_1, \lambda_2, \lambda_3, \lambda_4)\delta\boldsymbol{s}_i, \quad (4.7)$$

where, with the transformation matrix $\boldsymbol{A}$,

$$\boldsymbol{A}\delta\boldsymbol{r}_i = \delta\boldsymbol{s}_i \quad \text{and } \mathrm{diag}(\lambda_1, \lambda_2, \lambda_3, \lambda_4) = \boldsymbol{A}\boldsymbol{D}\mathcal{M}^p(\boldsymbol{r}_i)\boldsymbol{A}^{-1}. \quad (4.8)$$

The columns of the transformation matrix $\boldsymbol{A}$ are just the eigenvectors of the monodromy matrix $\boldsymbol{D}\mathcal{M}^p(\boldsymbol{r}_i)$. It is easy to see that the stability of the periodic orbit is determined by the eigenvalues of the monodromy matrix, since after n applications of $\mathcal{M}^p$ we obtain

$$\delta \boldsymbol{s}_{i+np} = \mathrm{diag}(\lambda_1^n, \lambda_2^n, \lambda_3^n, \lambda_4^n)\delta \boldsymbol{s}_i. \tag{4.9}$$

The four-dimensional mapping $\mathcal{M}$ (2.26) of the driven elliptical billiard preserves the measure $d\mu = R(\xi,\phi)v(v\sin\alpha - u(\xi,\phi))d\xi d\phi d\alpha dv$ (2.52), where $R(\xi,\phi)$ is the radius of curvature and $u(\xi,\phi)$ is the normal velocity of the ellipse at ϕ and ξ. The existence of a preserved measure ensures that the determinant of the corresponding real monodromy matrix is one

$$\det\left(\boldsymbol{D}\mathcal{M}^p(\boldsymbol{r}_i)\right) = 1. \tag{4.10}$$

Since the monodromy matrix $\boldsymbol{D}\mathcal{M}^p$ (4.5) is real, complex eigenvalues have to come in pairs. The dimension of the monodromy matrix is four, so there are three different combinations of eigenvalues possible (in terms of how many of the eigenvalues are real and how many are complex), corresponding to four different types of fixed points [66]:

1. Four complex eigenvalues ⇒ the $\boldsymbol{r}_i \in \mathcal{P}$ are elliptic fixed points of $\mathcal{M}^p$.
2. Two real and two complex eigenvalues ⇒ the $\boldsymbol{r}_i \in \mathcal{P}$ are loxodromic fixed points of $\mathcal{M}^p$.
3. Four real eigenvalues ⇒ the $\boldsymbol{r}_i \in \mathcal{P}$ are hyperbolic fixed points of $\mathcal{M}^p$.
4. Four real eigenvalues which are exactly one, ⇒ the $\boldsymbol{r}_i \in \mathcal{P}$ are parabolic fixed points of $\mathcal{M}^p$.

The first case corresponds to stable, whereas the subsequent two ones represent unstable periodic orbits. Parabolic fixed points have neutral stability. Practically, parabolic fixed do not occur in the driven elliptical billiard, so we will neglect them in the following.

The direction of the local phase flow around fixed points is determined by the eigenvectors of the corresponding monodromy matrix. The local phase flow around an elliptic fixed point is a pure rotation [111], i.e. small regular islands enclose such stable periodic orbits. For a hyperbolic fixed point, the local flow grows exponentially in two directions (this is the reason why hyperbolic fixed points are unstable) and decays exponentially in the other two directions. The incoming (exponentially decaying) and outgoing directions (exponentially growing) directions are called the stable and unstable manifolds of a fixed point [34]. In terms of the local phase flow, loxodromic fixed points combine the features of elliptic and hyperbolic fixed points. In two directions, the local flow around loxodromic fixed points is elliptic, i.e it is pure rotation. Of the remaining two directions, one grows exponentially and one decays exponentially. Loxodromic periodic orbits are unstable, since the exponential growth of the unstable manifold dominates the local flow.

4.2.2 Velocity dependence of the minimal period

Contrary to the static elliptical billiard, there is a lower bound p_{min} for the period of a periodic orbit in the driven elliptical billiard, which depends on the typical velocity v of such an orbit. The reason for this lower bound is that a periodic orbit has to close in all four phase space variables, i.e. also in the phase ξ. A fast particle exhibits much more collisions within one oscillation of the ellipse than a slow particle, since the area of the ellipse, and thus the maximum path length of a periodic orbit, is bounded. To estimate

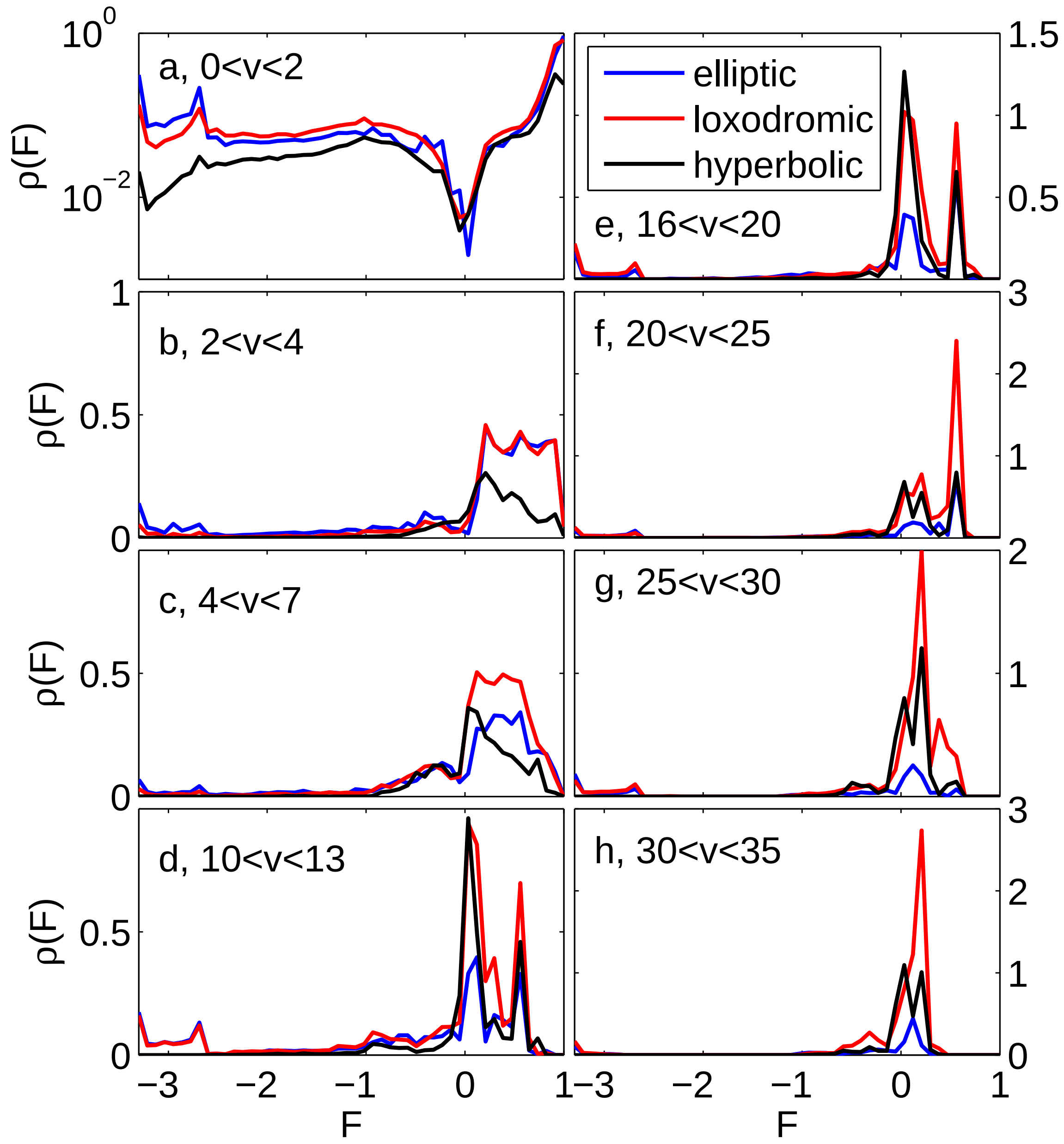

Figure 4.1: Velocity resolved phase space density $\rho_{v_1,v_2}(F,\xi)$ (log-scale colormap, breathing mode, $C = 0.1$). For low velocities (a), the ensemble covers the whole $F \times \xi$ plane. With increasing velocity (b)-(h), it is located in a region around $F(\phi,\alpha) \approx 0$. This region gets thinner and thinner with increasing velocity. The insets show the corresponding $\rho_{v_1,v_2}(\phi,\alpha)$.

$p_{\min}$ as a function of v, we assume a periodic orbit that closes exactly after the shortest possible time, which is one period $T = 2\pi$. For the sake of simplicity, we take v as the mean velocity averaged over the periodic orbit. The minimum period is achieved for such an orbit if the path length l_p gets maximal, which is the case if the particle moves along the semi-major axis (the effective length of the semi major axis is approximately $2a_0$). The minimum period is then given by

$$p_{\min} = \frac{vT}{l_p} = \frac{2\pi v}{2a_0} = \frac{\pi}{a_0} v, \tag{4.11}$$

so $p_{\min}$ depends linearly on v. The relation in Eq. (4.11) can also be interpreted the other way around, for a given period p, the maximal velocity a periodic orbit can have is then

$$v_{max} = \frac{a_0}{\pi} p. \tag{4.12}$$

In chapter 3 we saw that the asymptotic width of the chaotic channel is reached at around $v = 30$ (‘high velocity regime’). An important implication of Eq. (4.12) is that in order to find a representative set of periodic orbits in the high velocity regime, periods up to $p = 100$ have to be used. Note that from Eq. (4.12), $p\text{min} = 47$ for $v = 30$, however, we have to keep in mind that firstly, the relation (4.12) gives the maximal and not the typical velocity and secondly, to explore the high velocity regime, a typical set of periodic orbits in a broader range of velocities, let’s say between $v = 30$ and $v = 40$, is necessary.

4.3 Density of periodic orbits

Density $\rho(F)$

By using the method described in section 4.1, we performed extensive numerical computations and detected periodic orbits up to period 100 in the driven elliptical billiard (breathing mode, $C = 0.1$). In Fig. 4.1, the density $\rho_{v_1,v_2}(F)$ of the periodic orbits with $v_1 < v < v_2$ (where v is the mean velocity of a periodic orbit, i.e. $v = 1/p \sum_{i=1}^{p} v_i$ for an orbit with period p) as a function of F is shown. Just like when analyzing the phase space density, we effectively map the $\phi \times \alpha$ plane onto F, thereby reducing the dimension by one. The different velocity slices are chosen in such a way that they coincide with the corresponding ones of Fig. 3.3.

For small values of v ($0 < v < 2$, see Fig. 4.1a), the periodic orbits cover the whole available F-range, and thus the whole $\phi \times \alpha$ plane, see also Fig. 4.2a where the location of the elliptic (stable) periodic orbits with $0 < v < 2$ in the $\phi \times \alpha$ plane is shown. However, the density $\rho(F)$ is reduced significantly in a narrow region around $F = 0$. Small values of v typically correspond to low periods, cf. the discussion of section 4.2.2. In the corresponding static system, the orbits with low periods are located around the separatrix $F = 0$, see Fig. 2.2, so there is a large discrepancy in the population of periodic orbits in F-space between the static and the driven system. The reason for this discrepancy is that the collisional dynamics in the driven elliptical billiard deviates the most from the dynamics of the corresponding static system for low velocities, mainly because the relative momentum transfer $\triangle v/v$ increases with decreasing v. The region of the separatrix ($F = 0$) is associated with the highest instability and the periodic orbits existing in the static case around $F \approx 0$ have

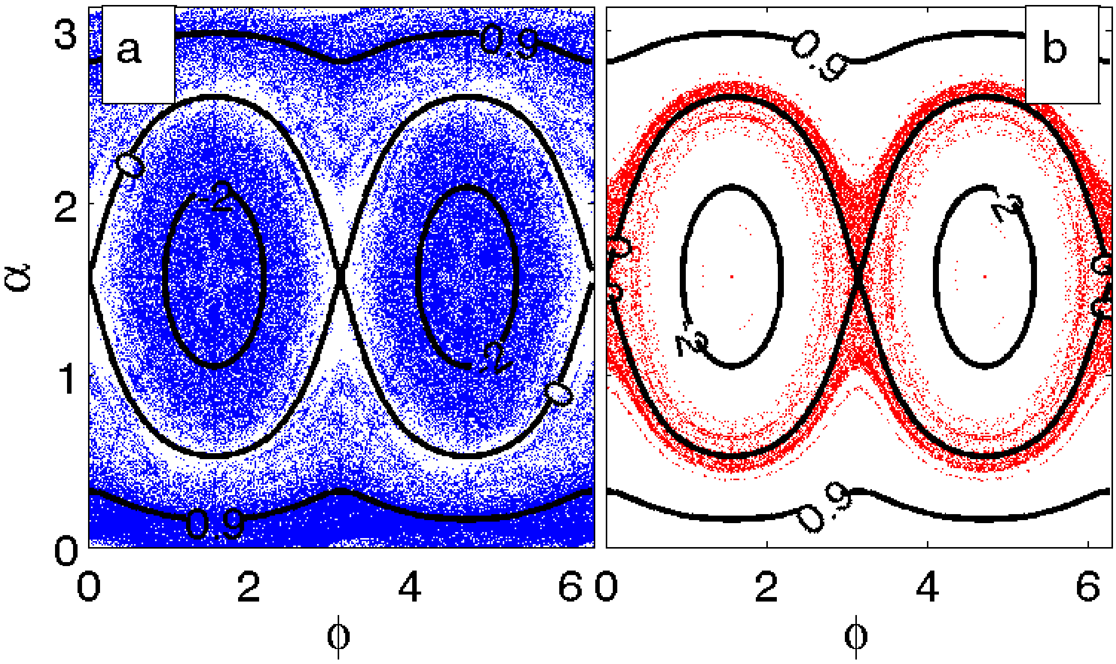

Figure 4.2: Location of periodic orbits in the $\phi \times \alpha$ plane (breathing mode, $C = 0.1$). In (a), the elliptic (stable) periodic orbits with $0 < v < 2$ and in (b) the loxodromic periodic orbits with $30 < v < 35$ are shown.

been destroyed by the driving.

The opposite scenario can be seen for higher values of v, see Fig. 4.1 (b)-(h), see also Fig. 4.2b, where the location of the loxodromic (unstable) periodic orbits with $30 < v < 35$ in the $\phi \times \alpha$ plane is shown. The region $F \approx 0$ possesses the highest density of period orbits, in particular unstable ones (hyperbolic and loxodromic), whereas the librator region around the two central elliptic fixed points is depleted. As we demonstrated in chapter 3, at these velocities, large invariant structures are present, both in the deep librator regime as well as close to the whispering-gallery orbits (rotator regime). The motion inside these bulky invariant structures is mostly regular, with occasionally small layers of chaotic motion enclosed by invariant KAM tori. Even though there are unstable periodic orbits embedded in integrable parts of phase space, for example the two isolated hyperbolic fixed points associated with the period two orbit along the semi-major axis in the static elliptical billiard, this is rather an exception than a rule. In general, unstable periodic orbits, i.e. hyperbolic and loxodromic fixed points, are associated with chaotic motion. For high velocities, the thin channel of chaotic motion, bounded by the mentioned large invariant structures, is located around $F = 0$ and consequently, this where the density $\rho(F)$ of unstable periodic orbits is highest. This does not mean that there are no elliptic periodic orbits in the region of the large invariant structures, but they possess periods larger than 100.

Density $\rho(v)$

A complementary quantity worthwhile to study is the density of periodic orbits $\rho(v)$ as a function of the velocity v, which is shown in Fig. 4.3. The normalization is chosen such

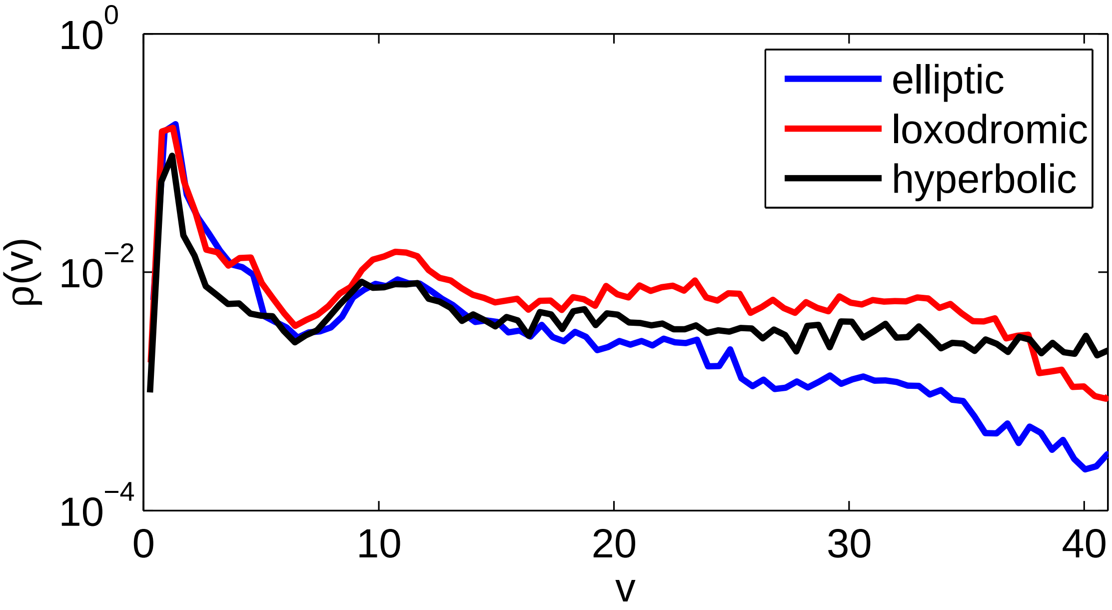

Figure 4.3: Density $\rho(v)$ of periodic orbits up to period 100 in the breathing mode ($C = 0.1$), note the logarithmic scale. The density is highest for low velocities ($0 < v < 3$) and is suppressed significantly for high velocities ($30 < v < 40$). The suppression is particularly pronounced for the density $\rho(v)$ of the elliptic periodic orbits.

that $\int_v \rho(v) = 1$, where $\rho(v) = \rho_{\mathrm{el}}(v) + \rho_{\mathrm{lox}}(v) + \rho_{\mathrm{hyp}}(v)$. The density $\rho(v)$ is highest for low velocities ($0 < v < 3$) for all types of periodic orbits and gets suppressed significantly with increasing velocity, note the logarithmic scale of the ρ-axis. At $30 < v < 40$, the density is roughly 40 times smaller in the case of the loxodromic and hyperbolic and even 300 times smaller for the elliptic periodic orbits, i.e. $\rho_{\mathrm{el}}(v = 1)/\rho_{\mathrm{el}}(v = 35) \approx 300$ and $\rho_{\mathrm{lox}}(v = 1)/\rho_{\mathrm{lox}}(v = 35) \approx \rho_{\mathrm{hyp}}(v = 1)/\rho_{\mathrm{hyp}}(v = 35) \approx 40$. Of course we have to keep in mind that the periodic orbits are located for $30 < v < 40$ in a narrow channel around $F = 0$, whereas at $0 < v < 3$ they cover the whole F space. But even if we account for this narrowing of the region covered with periodic orbits, the effective density $\rho_{\mathrm{lox,hyp}}(v)$ is still a factor of approximately 5 smaller for high compared to low velocities and even a factor of 40 in the case of ρ_{el} (we assume that the narrowing accounts for an factor of roughly 7, cf. Fig. 3.7).

4.4 Statistic of eigenvalues

A quantitative measure for the instability of the loxodromic and hyperbolic fixed points, respectively their stable and unstable manifolds, is the size of the real eigenvalues of the corresponding monodromy matrix. The histogram of the real eigenvalues is shown in Fig. 4.4 for different velocity regimes. There is a large peak around one, which gets more pronounced with increasing velocity. Periodic orbits with eigenvalues very close to one are only marginally unstable, this follows from the discussion in section 4.2.1 and in particular from Eq. (4.9).

Specifically, such marginally unstable periodic orbits do not have eigenvalues λ of exactly

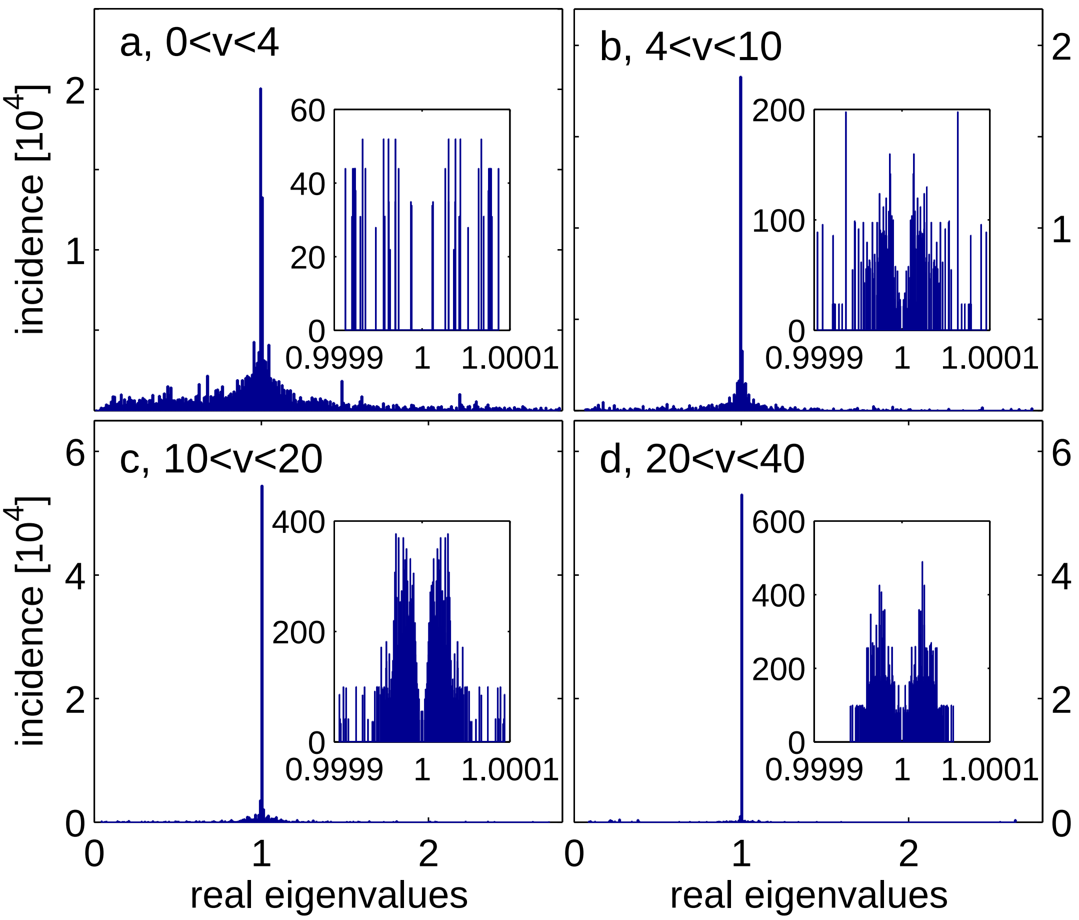

Figure 4.4: Histogram of the real eigenvalues of the loxodromic and hyperbolic periodic orbits in different velocity regimes (a binning of 10^{-2} is used). The peak around 1 gets more pronounced with increasing velocity. The inset shows a magnification of the major peak at 1 (with a binning of $2 \cdot 10^{-7}$).

one, but rather values of λ very close to one. This can be seen in the insets of Fig. 4.4, where a magnification of the peak around one is shown. The symmetry of the eigenvalues very close to one can be understood as follows. Since the real monodromy matrix (4×4) has determinant one (4.10), the eigenvalues λ_i obey

$$\prod_{i=1}^{4} \lambda_i = 1. \tag{4.13}$$

Furthermore, the eigenvalues come in pairs, for example a loxodromic fixed point has $\lambda_{1/2} = a \pm ib$ and $\lambda_3 = 1/\lambda_4$, where $a, b \in \mathbb{R}$ and $|\lambda_{1/2}| = 1$. This means for $\lambda_3 \approx 1$ we can write $\lambda_{3/4} = 1 \pm \epsilon$ ($\epsilon > 0$), so the product $\lambda_3\lambda_4 = 1 - \epsilon^2 \approx 1$ in the first order in ϵ.

The periodic orbits in the static elliptical billiard have all neutral stability, i.e. they have eigenvalues of exactly one, except the isolated elliptic (hyperbolic) fixed point associated with the motion along the semi-minor (semi-major) axis. The occurrence of eigenvalues closer and closer to one with increasing velocity resembles the fact that the particles trace

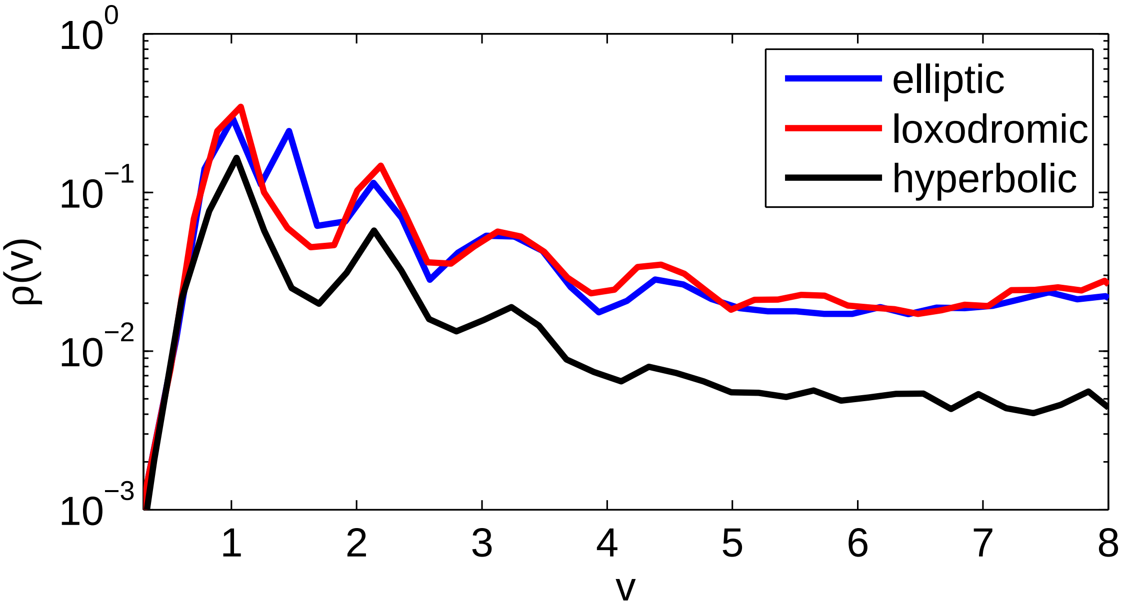

Figure 4.5: Density $\rho(v)$ of periodic orbits up to period 100 in the constant eccentricity mode ($C = 0.1$), note the logarithmic scale. The density is highest for low velocities ($v < 2.5$) and is suppressed significantly for high velocities ($5 < v < 8$). The suppression is particularly pronounced for the density $\rho(v)$ of the hyperbolic periodic orbits.

more and more orbits of the corresponding static billiard and consequently the eigenvalues of many periodic orbits of the driven billiard assimilate to the ones of the static billiard.

Larger amplitudes

When increasing the driving amplitude C, the results concerning the periodic orbits show a similar pattern as for $C = 0.1$. The density of periodic orbits is evenly distributed over F for low v, with a dip around $F = 0$, with increasing velocity, the density of periodic accumulates more and more around the $F = 0$ region. However, for $C = 0.5$ we are not able to obtain representative densities for the velocity regime corresponding to $v_{asymp} \approx 150$ (this is the value where the asymptotic width of the chaotic channel is reached for $C = 0.5$). Since the typical period of periodic orbits grows with increasing velocity, cf. the discussion in section 4.2.2, representative densities for $v_{asymp} \approx 150$ would require to systematically search for periodic orbits up to period 500, this is computationally unfeasible.

4.5 Other driving modes

4.5.1 Constant eccentricity mode

In comparison with the breathing mode, the results concerning the periodic orbits are quite similar in the constant eccentricity mode. The density of the periodic orbits for low values of v ($0 < v < 2$) is evenly distributed over F, with a dip around the separatrix region $F \approx 0$. For higher values of v ($5 < v < 8$), the density of periodic orbits $\rho(F)$ is highest around $F \approx 0$, even though the depletion of the $F \neq 0$ regions is not as pronounced as in the breathing mode. Note that the structural change (from the depletion to the population of $\rho(F)$ in the $F \approx 0$ region) in terms of v happens much faster in the constant eccentricity mode than in the breathing mode. This is in agreement with the results of chapter 3, where we analyzed the growth of large regular regions. The maximal extension of these invariant structures was reached already at roughly $v \approx 4$, whereas in the breathing mode this was the case at $v \approx 30$.

The density of periodic orbits $\rho(v)$ for the constant eccentricity is shown in Fig. 4.5. It is similar to the one of the breathing mode shown in Fig. 4.3, the density is highest for low velocities ($v < 2.5$) and is significantly lower in the high velocity regime ($5 < v < 8$). Whereas in the breathing mode the suppression is strongest for $\rho_{el}(v)$ (elliptic periodic orbits), in the constant eccentricity mode $\rho_{\mathrm{hyp}}(v)$ (hyperbolic periodic orbits) is most suppressed. The ratios $\rho(v=1)/\rho(v=5)$ are significantly smaller now (note that we take again $v = 5$ instead of $v = 30$ for the high velocity regime). Furthermore, if we take into account the narrowing of the region where the periodic orbits are located, the effective ratio of the densities is reduced by a factor of two only.

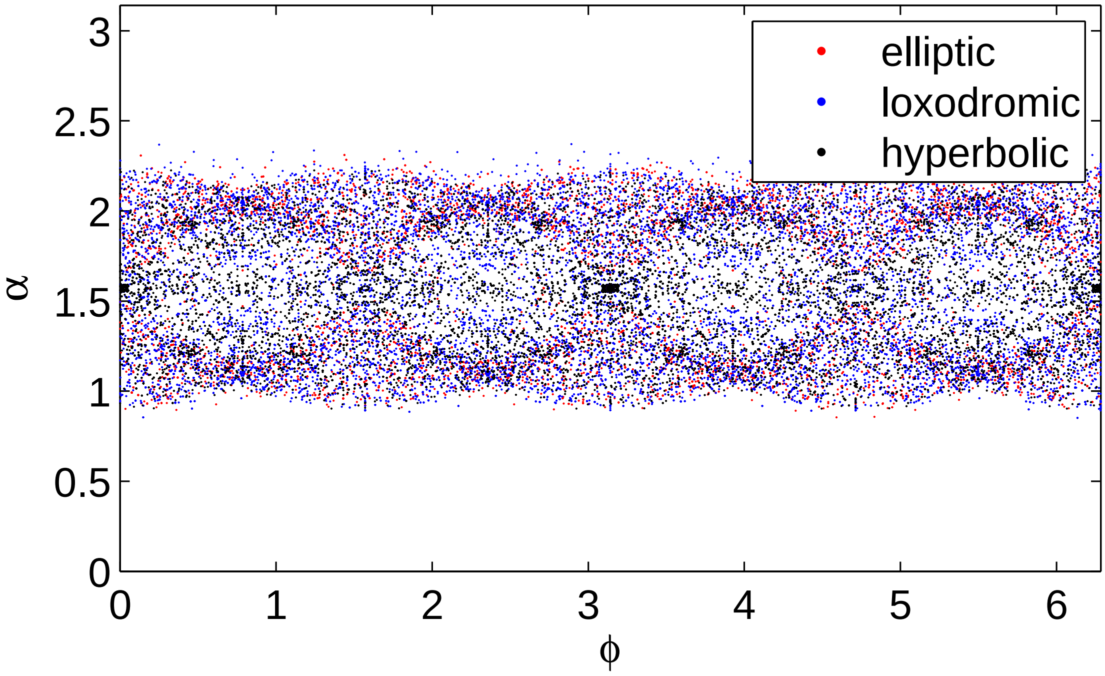

Figure 4.6: Location of periodic orbits up to period 50 in the quadrupole mode for $10 < v < 13$ ($C = 0.1$). Note that the region covered with periodic orbits is the same as the one where the phase space density $\rho_{v_1=10,v_2=13}(\phi, \alpha) \neq 0$, see Fig. 3.13.

4.5.2 Quadrupole mode

Again, the situation is different in the quadrupole mode. For low velocities ($0 < v < 2$), the whole $\phi \times \alpha$ plane is covered with periodic orbits, with the lowest density around $\alpha \approx \pi/2$. For higher velocities ($10 < v < 13$), a banded region with $0 < \phi < 2\pi$ and $0.9 < \alpha < 2.3$ is predominantly populated with periodic orbits, see Fig. 4.6. This is exactly the same

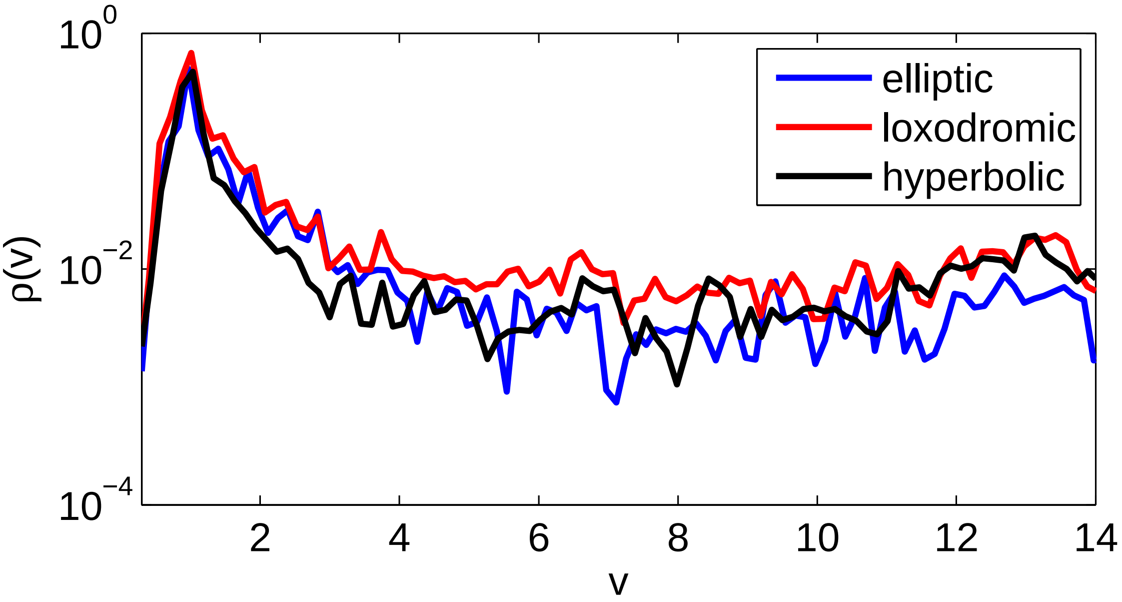

Figure 4.7: Density $\rho(v)$ of periodic orbits up to period 50 in the constant quadrupole mode ($C = 0.1$), note the logarithmic scale. The density is highest for low velocities ($v < 2$) and is suppressed significantly for high velocities ($v > 4$).

region where the phase space density $\rho_{v_1,v_2}(\phi,\alpha)$ is different from zero, see Fig. 3.13, i.e. there are no periodic orbits with periods smaller than 50 in the region of the regular structures emanating from librator-type orbits. Like in the breathing mode, higher periods are necessary for the existence of stable periodic orbits inside the large regular regions.

The density of periodic orbits $\rho(v)$ as a function of the velocity v is shown in Fig. 4.7 for a amplitude of $C = 0.1$. Like in the breathing mode, the density is highest for low ($v < 2$) velocities and decreases significantly with increasing velocity. The asymptotic width of the chaotic channel (even though being differently shaped compared to the other driving modes, see section 3.5.3) is reached at $v \approx 10$. The density $\rho(v = 10)$ is approximately 50 times smaller than the peak density at $v = 1$. If we take into account that the periodic for $v = 10$ do not populate the entire phase space, but a banded region only, cf. Fig. 4.6, the density of periodic orbits inside the channel of chaotic motion (present for $v > 10$) is still a factor of 10 times smaller than the density at low velocities ($v \approx 1$).

Eigenvalues

The accumulation of eigenvalues around one is also observed in the constant eccentricity and in the quadrupole mode. Whereas it is even stronger pronounced in the constant eccentricity mode, it is weakened in the quadruple mode. In both modes, higher velocities of the periodic orbits lead to an enhancement of the central peak around one, just like in the breathing mode. All three modes have in common that with increasing amplitude, the above described effect gets weakened. Summarizing, increasing the velocity and going from the quadrupole to the breathing and further to the constant eccentricity mode leads to more and more eigenvalues very close to one, however increasing the amplitude diminishes this phenomenon. Qualitatively, this can be understood as follows. In the static ellipse, all periodic orbits, except the ones along the semi major and minor axes, have neutral stability, i.e. they have eigenvalues of one. In the driven system, increasing the velocity and going to the constant eccentricity mode resembles more and more the dynamics of the static billiard, whereas increasing the amplitude results in a stronger perturbation and thus to dynamics different from the static system.

4.6 Intermediate summary - velocity resolved composition of phase space

Taking into account the results of chapters 3 and 4, the description of the phase space of the driven elliptical billiard (breathing mode, amplitude $C = 0.1$) can be summarized as follows: For very low velocities ($v < 1$), there is a large chaotic sea extended over the whole $\phi \times \alpha$, and thus over the whole F space (actually $\phi \times \alpha \times \xi$ space, however the phase ξ plays a minor role only, so we will omit ξ in the following discussion). Many periodic orbits are distributed over this chaotic sea, see Fig. 4.3, except for the region around the separatrix $F = 0$ of the corresponding static billiard, where the density of periodic orbits is significantly reduced, see Fig. 4.1a. Small regular islands of varying size enclose the stable (elliptic) periodic orbits. At around $v = 1$, bulky regular islands emanate from the librator-type stable period two orbit along the semi-minor axis. The $\xi \times v$ dynamics of these stable islands is reproduced extremely well by the corresponding one-dimensional Fermi-Ulam model.

The extension of the large invariant structures in F (and in $\phi \times \alpha$) space grows rapidly until $v \approx 3$, see Fig. 3.7. With increasing v, the growth of these regular structures is significantly reduced, but it does not stop until $v \approx 30$ (cf. Fig. 3.7). There are also large regular structures emanating from rotator-type orbits very close to the boundary of the ellipse (also called whispering gallery orbits). These islands appear at $v \approx 1.4$ and grow slowly in F space until $v \approx 15$ (cf. Fig. 3.7). Both types of large regular structures act as impenetrable barriers for particles starting inside the chaotic sea located at low v. Between these bulky regular regions, there is a thin channel of chaotic motion around $F = 0$, which is connected with the low v chaotic sea and is furthermore unbounded in v. The density of periodic orbits, especially the density of stable periodic orbits, inside this chaotic channel is considerably smaller than the density inside the low v chaotic sea. The size of the small invariant KAM tori surrounding the stable periodic orbits inside the thin chaotic channel is also significantly smaller than the corresponding islands around elliptic periodic orbits inside the large chaotic sea located at low v. Enlarging the amplitude does not change the qualitative picture of the phase space, although the asymptotic width of the chaotic channel around $F = 0$ gets wider and the stop of the growth of the large regular structures in F space is shifted towards higher values of the velocity ($v \approx 150$ for an amplitude of $C = 0.5$).

4.6.1 Other driving modes

Constant eccentricity mode

In the constant eccentricity mode, the composition of phase space is very similar to the one of the breathing mode. There is a large chaotic sea at low velocities ($0 < v < 1$), which is squeezed with increasing v more and more into a thin chaotic channel around $F = 0$

due to the emergence of large regular regions at around $v = 1$. The asymptotic width of the thin chaotic channels, and thus the end of the growth in F space of the bulky regular regions, is reached at $v \approx 4$ already, see Fig. 3.11. Like in the breathing mode, the chaotic sea located at low v contains many (stable) periodic orbits, but now the reduction of the density of periodic orbits inside the thin chaotic channels is much less pronounced, see Fig. 4.5. Enlarging the driving amplitude again does not lead to a widening of the chaotic channel, but reaching its asymptotic width at higher values of v, again cf. Fig. 3.11.

Quadrupole mode

As discussed in section 3.5.3, there are no large regular structures emanating from librator-type motion in the quadrupole mode, since semi-minor and semi-major axes, and thus the stability along these axes periodically interchange. Due to this absence of librator-type regular structures, the narrowing of the large chaotic sea at low v is much less pronounced compared to the other driving modes when increasing the velocity v. The narrowing is of course caused by the emergence of bulky regular structures emanating from whispering-gallery orbits, see Fig. 3.13. Like in the breathing mode, increasing the driving amplitude leads to a widening of the chaotic channel and to reaching its asymptotic width at higher values of v.

5 Stickiness

The rich phase space structure, associated with many small regular islands surrounding stable periodic orbits embedded into the low v chaotic sea, causes stickiness of the trajectories [119]. Stickiness describes the phenomenon that particles getting very close to invariant KAM tori spend (extremely) long times in the vicinity of such regular regions, see Ref. [120] and references therein. The motion of such particles becomes for a long time almost regular, they trace the dynamics of the outermost KAM torus of a regular island. Note that this does not mean that particles spend more time in the vicinity of regular islands than in other parts (of equal volume) of the phase space of the same ergodic component [121], they simply visit the vicinity of regular parts very seldom, in accordance with ergodicity. Particles can get also sticky to loxodromic and hyperbolic periodic orbits, or rather to their stable manifolds, especially when the corresponding monodromy matrix has real eigenvalues which are very close to one.

In this chapter, we will firstly investigate single trajectories that get sticky and see that such particles exhibit a certain F dynamics and secondly, we will explore statistical properties describing stickiness, such as the distribution of the length of the stickiness phases.

5.1 Single trajectory

5.1.1 Correlated F and v dynamics

The evolution of a typical trajectory in the driven elliptical billiard starting with a low velocity deep inside the librator regime ($F_0 = -3, v_0 = 0.1$) is shown in Fig. 5.1a for the first three million collisions. The upper curve (blue) shows $F(n)$, the lower curve (red) $v(n)$. According to Fig. 5.1a, $F(n)$ alternates between periods of regular (laminar phases) oscillations (intervals $[0,\ 2.8 \cdot 10^5]$ and $[1.4 \cdot 10^6,\ 1.75 \cdot 10^6]$) and periods of irregular fluctuations (turbulent phases). During these laminar phases, $F(n)$ never crosses the $F = 0$ line (shown in magenta), whereas during the turbulent phases $F(n)$ remains essentially within the zone $[F_{min}, F_{max}] = [-1, 0.4]$, repeatedly crossing the $F = 0$ line associated with the separatrix $F = 0$ of the corresponding frozen billiard. From the magnifications shown in Fig. 5.1b and 5.1c, we see that this structure of alternating laminar and turbulent phases exists on many different scales of n.

Whenever $F(n)$ is in a laminar phase, $v(n)$ oscillates around a fixed central value, whereas during the turbulent $F(n)$ periods, $v(n)$ starts to develop intervals with strong, irregular fluctuations leading to a sudden increase or decrease of its central value. In fact, the increasing parts of the trajectory $v(n)$ prevail such that a net increase of the velocity for longer times can be observed.

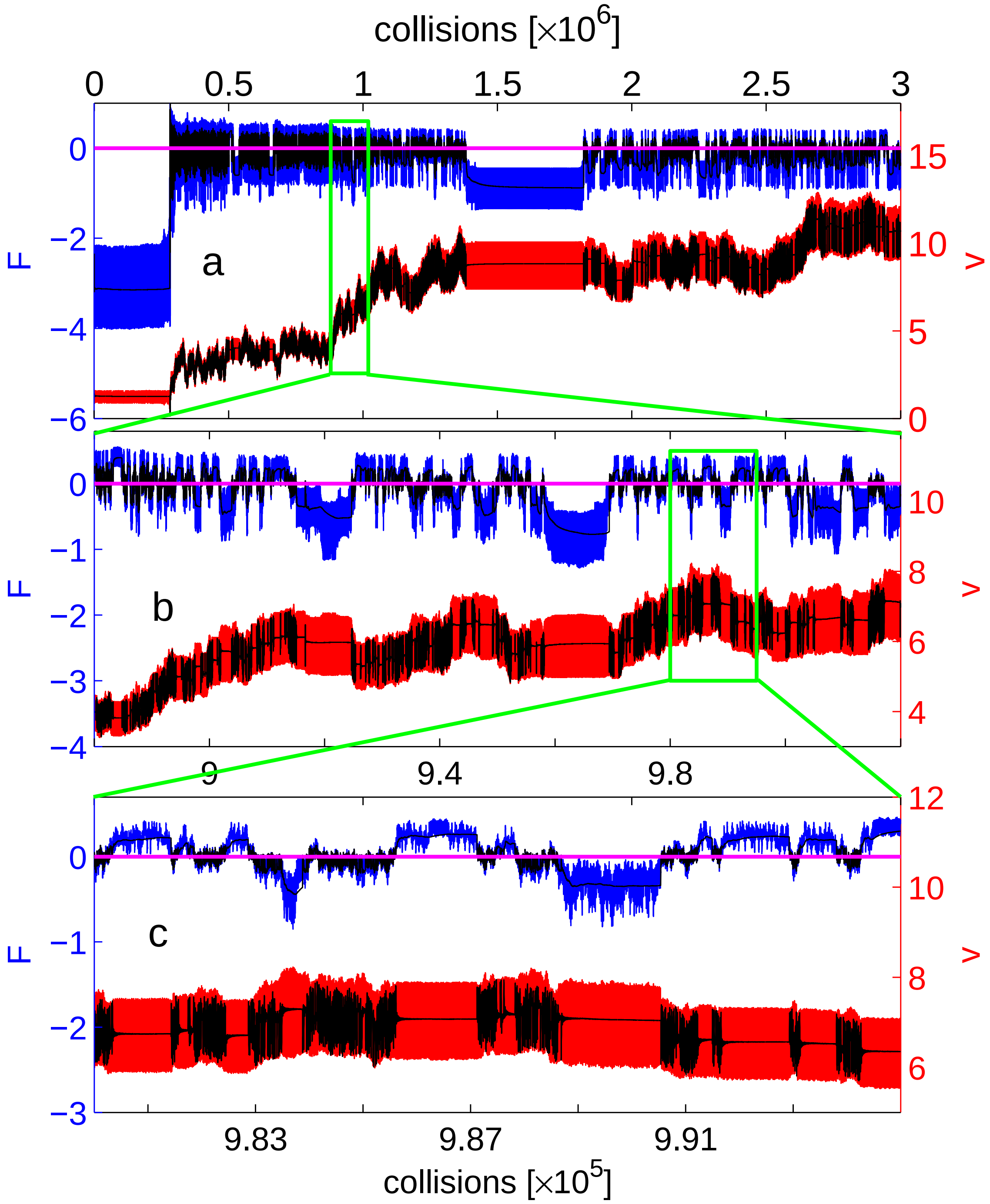

Figure 5.1: The dynamics $F(n)$ (upper curve, blue) and $v(n)$ (lower curve, red) for a single trajectory as a function of the number of collisions (breathing mode, $C = 0.1$). The solid black lines indicate the cumulative mean in each case. The two successive magnifications in (b) and (c) demonstrate that the corresponding fluctuations occur on many scales. The $F = 0$ line is shown in magenta.

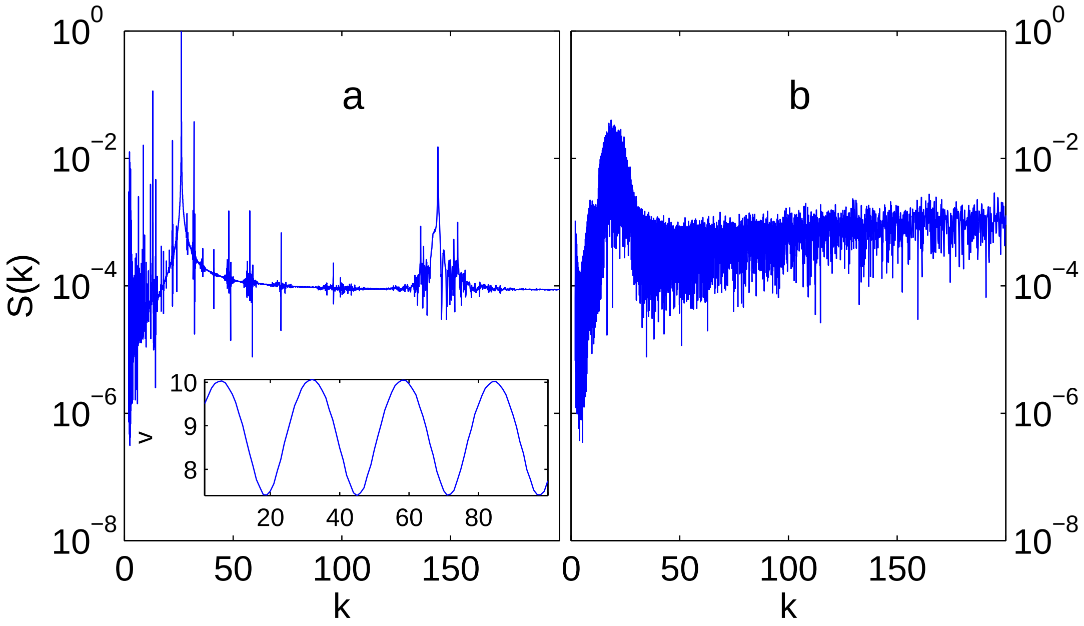

Figure 5.2: Power spectrum $S(k)$ of a typical laminar (a) and turbulent phase (b). The turbulent phase has continuous spectrum, whereas the spectrum of the laminar phase is dominated by isolated peaks. The origin of the major peak at $k \approx 27$ can be seen in the inset, where $v(n)$ for hundred collisions for this laminar phase is shown. Clearly, $v(n)$ has a period of 27.

5.1.2 Power spectrum

The above-observed behavior indicates two important dynamical properties of the driven system: (i) the region around the separatrix is characterized by stochastic dynamics [122] (cf. also with the discussion of chapters 3 and 4 and (ii) the trajectories $F(n)$ and $v(n)$ are strongly correlated (see again Fig. 5.1). The enhanced stochasticity of the dynamics around $F \approx 0$ is also verified by the appearance of the corresponding power-spectrum (the modulus of the discrete Fourier transform)

$$S(k) = \frac{2\pi}{N} \left| \sum_{n=1}^{N} v(n) e^{-\frac{2\pi i (k-1)(n-1)}{N}} \right|, \tag{5.1}$$

presented in Fig. 5.2, where N is the length of the ‘signal’ $v(n)$. For a typical turbulent phase, i.e. motion of $F(n)$ around zero, the continuous part of the spectrum is dominating in this case (Fig. 5.2b). On the contrary, in regions of regular v-oscillations, corresponding to F-dynamics without any zero crossings (typical laminar phases), the power spectrum, shown in Fig. 5.2a, is dominated by isolated peaks, while the continuous background is much less pronounced.

5.1.3 Cumulative mean

To explore the correlated behavior of $v(n)$ and $F(n)$ further, it is necessary to integrate out regular as well as stochastic fluctuations of laminar phases occurring on small time scales. For such an averaging procedure to be successful, we have to efficiently detect the intervals of laminar evolution first. A good estimation of these intervals is obtained by analyzing the timeseries $F(n)$. As 'working intervals' (to calculate the cumulative mean) resembling the laminar phases, we identify the dynamics between two successive zero crossings of F. For a trajectory $F(n)$ with $n \in [1, N]$, this results in M intervals I_j, $j = 1, 2 \dots M$ with associated lengths L_j, such that $N = \sum_{j=1}^{M} L_j$. Then, in each such interval I_j, we calculate the cumulative mean

$$\bar{F}(i)_j = \frac{1}{i} \sum_{q=1}^{i} F(q + \sum_{r=1}^{j-1} L_r), \quad i \in [1, L_j] \tag{5.2}$$

$$\bar{v}(i)_j = \frac{1}{i} \sum_{q=1}^{i} v(q + \sum_{r=1}^{j-1} L_r), \quad i \in [1, L_j]. \tag{5.3}$$

The results for $\bar{F}_j$ and $\bar{v}_j$ of the above-considered trajectory are shown as solid black lines in Fig. 5.1. The similarity of the dynamics of the cumulative mean of F and v with a typical trajectory showing intermittency [123] is remarkable. Additionally, the one-to-one correspondence between periods of stochastic behavior (bursts) of $\bar{F}_j$ and periods of fluctuations of $\bar{v}_j$ is obvious. The intermittent character of the F-dynamics goes along with a specific distribution of the laminar lengths L_j, i.e. the intervals between successive zeros of F, which according to the theory of intermittent maps [124] should obey a power-law. This will be investigated in section 5.2.1.

5.1.4 Stickiness

The origin of the above discussed laminar phases is of course stickiness. Trajectories exhibiting stickiness either get very close to regular structures in phase space and 'stick' for (sometimes extremely) long times to the outermost invariant KAM tori of a regular island, or they approach a loxodromic (or hyperbolic) fixed point very slowly on its incoming (stable) manifold and depart the fixed point very slowly on its outgoing (unstable) manifold. From the discussion of section 4.2.1 it is clear that in the latter case, the time a particle spends near an unstable fixed point depends crucially on the real eigenvalues of corresponding monodromy matrix. The closer the eigenvalues are to one, the longer an approach and the subsequent departure from an unstable fixed will take. In general however, the stickiness properties are dominated by particles approaching invariant KAM tori (regular islands) and not by particles getting close to unstable fixed points [121].

In either case, the motion of 'sticky' particles becomes almost regular, i.e. periodic or quasiperiodic. In particular, any of the phase space variables ξ, ϕ, α and v of a sticky particle performs a pure oscillation, since regular motion in the driven elliptical billiard is always bounded. Depending on the structure of the object a particle gets sticky to, the resulting motion can still be rather complex. Exemplarily, the power spectrum $S(k)$ for $v(n)$ of a sticky particle (actually for the laminar phase from $1.5 \cdot 10^6$ to $1.7 \cdot 10^6$ collisions of Fig. 5.1a) is shown in Fig. 5.2a. There are several distinct peaks in the spectrum, corresponding to different characteristic frequency of the oscillation, the most prominent one at $k \approx 27$. In the inset of Fig. 5.2a, $v(n)$ of this sticky particle for 100 collisions is shown. The mean velocity of this sticky particle is $\bar{v} = 8.8$ and it moves on a librator-type orbit. The mean distance of a librator-type orbit between two collisions is, as a first approximation, given by $2b_0 = 2$. The number of collisions n_c with the boundary the sticky particle experiences

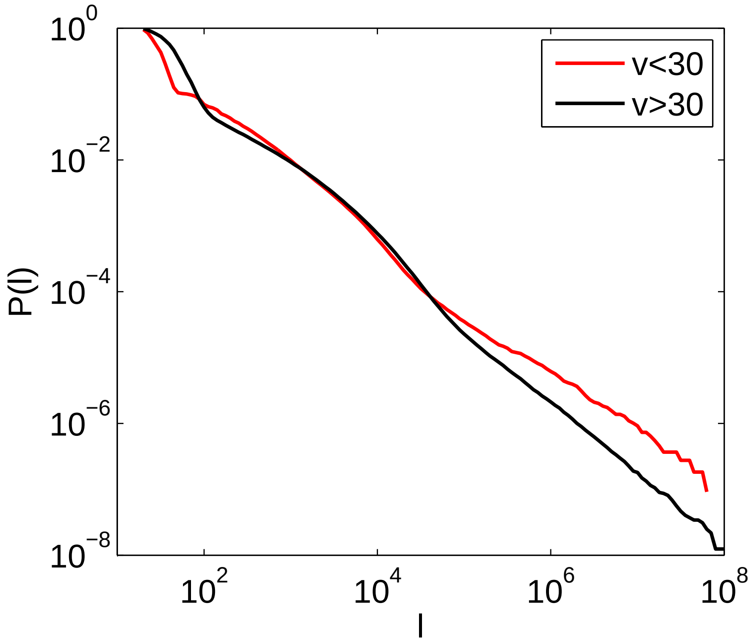

Figure 5.3: Propability $P(l)$ (cumulative distribution) that a laminar phase has a length of greater than or equal to l, in two different velocity regimes (breathing mode, $C = 0.1$). The distribution $P_{v>30}(l)$ decays faster than $P_{v<30}(l)$ for $l > 10^5$, whereas for $l < 10^5$ both distributions are very similar.

within one period $T = 2\pi$ of the driving law is given by $n_c = \bar{v}T/(2b_0) = 8.8\pi = 27.4$, which agrees very well with the position of the major peak in the power spectrum. In other words, since the particle probes the motion of the boundary regularly, the most prominent peak of the power spectrum resembles the period of the driving law. The existence of the other distinct peaks, for example at $k = 13, 22, 32, 48, 56, 72, 96, 136, 144, 153$, indicates that the particle is not sticky to a single periodic orbit, but to a more complicated regular structure.

5.2 Distribution of laminar phases

5.2.1 Distribution of the length of laminar phases

The ultimate quantity to characterize stickiness is the distribution of the length of laminar phases $\tilde{p}(l)$. It is known that the distribution $\tilde{p}(l)$ relates to many dynamical properties of the system, such as transport and decay of correlations [121]. Unfortunately, in the driven elliptical billiard it is very difficult to extract the true distribution $\tilde{p}(l)$ for mainly two reasons: Firstly, the tail and not the short time behavior of the distribution (i.e. $\tilde{p}(l)$ for very large l) determines the relevant dynamical properties. Since $\tilde{p}(l)$ is typically a power law, laminar phases lasting for a very large number of collisions l occur very rarely, so the statistics of $\tilde{p}(l)$ naturally gets worse for large l. Secondly, it is a very intricate task to actually determine the length of a laminar phase: There is no typical scale of the length of a laminar phase since power laws are scale free. Due to the very rich structure of the four-dimensional phase space it is unfeasible to determine to which particular non-hyperbolic structure a certain trajectory got sticky, so we cannot use e.g. the distance to an island as a criterion whether a particle is sticky or not. However, we can use a peculiarity of the driven ellipse: As already described in the previous section 5.1, particles that are in a laminar phase are typically confined either to pure rotator or to pure librator type motion, in the sense that the sign of F does not change during such a phase. By exploiting this fact, we define in complete analogy with section 5.1 $p(l)$ as a 'working distribution', where now the length l of a laminar phase is simply given by the number of consecutive collisions without a change in the sign of F (we consider laminar phases with $l \geq 20$ only).

To circumvent the problem of bad statistics in the tail of $p(l)$ at least partially, we use for representation purposes the cumulative distribution

$$P(l) = \int_l^\infty p(l')dl'. \tag{5.4}$$

$P(l)$ is the probability that a laminar phase has a length greater than or equal to l. If $p(l)$ follows a power law of the form $p(l) = cl^{-\alpha}$ (where c is a normalization constant and we assume $\alpha > 1$), then

$$P(l) = \int_l^\infty l'^{-\alpha}dl' = \frac{c}{\alpha - 1} l^{-(\alpha-1)} \tag{5.5}$$

is also a power law, but with an exponent of $\alpha - 1$ [125]. A further advantage of using $P(l)$ instead of $p(l)$ is that no binning of the data is necessary for a graphical representation. As already indicated, the tail of $p(l)$ strongly influences dynamical quantities, such as the transport in momentum space. We thus have to determine the exponent α for values of l larger than some l_{min}. The best method to extract the exponent α for $l \geq l_{\text{min}}$ is not to apply a least square fit to either $p(l)$ or to $P(l)$, but rather to use the formula [126]

$$\alpha = 1 + M \left[\sum_{i=1}^{M} \ln \frac{l_i}{l_{\text{min}}} \right]^{-1}, \tag{5.6}$$

with the original data, where l_i, $i = 1 \ldots M$ are the observed lengths of the laminar phases with $l_i \geq l_{min}$.

The cumulative distribution $P(l)$ for two different velocity regimes (breathing mode, $C = 0.1$) is shown in Fig. 5.3. The two distributions are chosen in a way that $P_{v>30}(l)$ corresponds to particles that are inside the thin chaotic channels around $F = 0$ and $P_{v<30}(l)$ to particles that are not yet in this regime. In the tail ($l > 10^5$), the distribution $P_{v>30}(l)$ decays faster than $P_{v<30}(l)$, whereas for $n < 10^5$ both distributions are very similar. Applying Eq. (5.6) with $l_{min} = 6 \cdot 10^4$, we obtain $\alpha_{v<30} = 1.85 \pm 0.03$ and $\alpha_{v>30} = 2.20 \pm 0.01$, so there is a significant difference between the two exponents. For an amplitude of $C = 0.5$, the distributions $p(l)$ look very similar to the ones corresponding to $C = 0.1$, now $\alpha = 2.34 \pm 0.02$ once the particles are inside the channel of chaotic motion around $F = 0$ and $\alpha = 1.92 \pm 0.02$ for low velocities.

5.2.2 Fraction of laminar phases

The distribution $p(l)$ quantifies the frequency of the length of the laminar phases. However, it does not provide an information about how many particles are actually sticky at a given collision number n. Thus, a complementary quantity concerning stickiness is the fraction $f_{\text{l}am}(n)$ of particles of an ensemble that are sticky as a function of n. This quantity is shown in Fig. 5.4 for the breathing mode ($C = 0.1$). $f_{\text{l}am}(n)$ increases until $n \approx 10^6$, stays constant until $n \approx 10^8$ and decreases slowly from then on.

The distribution $f_{\text{l}am}(n)$ for larger amplitudes corresponds qualitatively to the one of

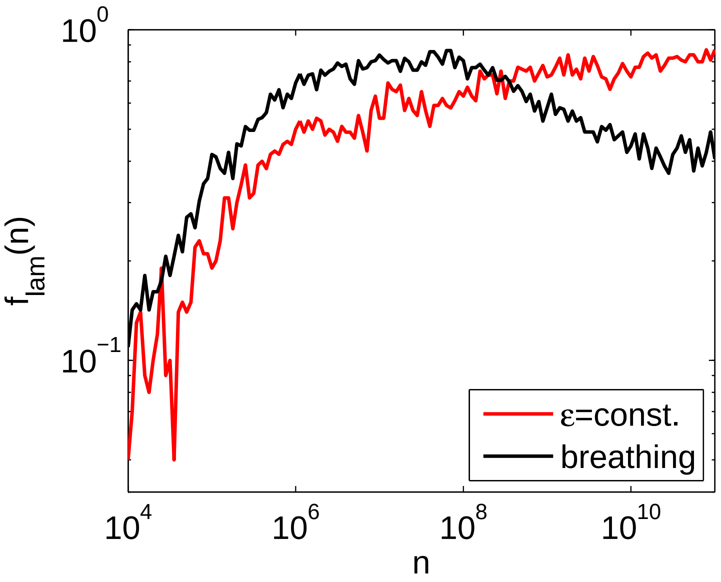

Figure 5.4: The fraction of particles that are in a laminar phase $f_{lam}(n)$ (i.e. they are sticky) as a function of the number of collisions for the breathing and constant eccentricity mode ($C = 0.1$). In the breathing mode, the fraction of particles that are sticky reaches a maximum shortly before $n = 10^8$ and decreases for larger n, whereas in the constant eccentricity mode the fraction almost saturates at roughly $n = 10^9$.

$C = 0.1$, i.e. $f_{lam}(n)$ shows a local maximum and a subsequent decrease. Overall, $f_{lam}(n)$ becomes smaller with increasing amplitude, i.e. $f_{\mathrm{lam},C>0.1}(n) < f_{\mathrm{lam},C=0.1}(n)$ for all values of n, which agrees with the intuitive picture that a larger driving amplitude introduces more chaoticity and thus less stickiness in the system.

Discussion

Taking into account the results presented in sections 3 and 4, the quantities $f_{lam}(n)$ and $p(l)$ describing stickiness effects reflect the change (in terms of v) in the composition of phase space described in section 4.6. The large chaotic sea at low v and the subsequent region (in terms of v) where the bulky regular islands grow further and further in F space, are characterized by enhanced stickiness, due to the following two reasons: Firstly, the enhanced stickiness is caused by the high density of (stable) periodic orbits in this region. Regular islands of various size enclose the stable periodic orbits and represent a large 'sticky' surface. Furthermore, particles get sticky to unstable periodic orbits (loxodromic and hyperbolic fixed points), or rather their incoming (stable) manifold, especially when the eigenvalues of the corresponding monodromy matrix are close to one. Secondly, the region associated with the growth of the bulky regular regions emanating from librator- and rotator-type motion, i.e. the parts of phase space with velocities smaller than 30, naturally exhibits enhanced stickiness: The growth of the large regular region can be viewed as a destruction of invariant structures when analyzing the phase space from high to low velocities (rather than from low to high v). At high velocities, there is a thin channel of chaotic motion around $F = 0$, bounded in ξ, ϕ and α (but not in v) by impenetrable invariant structures. In terms of KAM theory [34, 66, 111], decreasing the velocity can be effectively interpreted as increasing the perturbation strength (if we take the static elliptical billiard as the unperturbed system). At some perturbation strength, the outermost invariant KAM tori (i.e. the one actually bounding the chaotic motion) will get destroyed. The structure resulting from the destroyed torus is called *cantorus* [127, 128] (the name cantorus comes from *cantor set* and *torus*). These cantori have a fractal structure similar to a cantor set and act as bottlenecks for the transport in phase space, i.e these structures cause stickiness [129]. With increasing perturbation strength, i.e. with decreasing velocity, more and more of the invariant tori break open and are turned into cantori, the channel of chaotic motion gets wider. The stickiness is reduced inside the thin chaotic channel around $F = 0$ present at $v > 30$, since the density of periodic orbits, especially the one of the stable periodic orbits, is considerably smaller than the density of periodic orbits inside the large low v chaotic sea. Furthermore, once the asymptotic width of the chaotic channel is reached at $v \approx 30$, the invariant structures do not grow any further, i.e. the mechanism of generating cantori (which cause stickiness) is stopped.

5.3 Other setups

5.3.1 Constant eccentricity mode

In the constant eccentricity mode, the distribution of the length of the laminar phases $p(l)$ follows a power law for $l > 10^2$ with an exponent right below 2, specifically $\alpha = 1.97 \pm 0.01$, independent of the amplitude. Unlike in the breathing mode, the power law exponent is independent of the velocity regime, i.e the stickiness (at least in terms of $p(l)$) is not reduced inside the thin chaotic channels. This is supported also by the fraction $f_{\mathrm{l}am}(n)$ of particles that are in a laminar phase. With increasing number of collisions n, $f_{\mathrm{l}am}(n)$ increases as well, until it approximately saturates at $n \approx 10^9$, see Fig. 5.4. In contrast to the breathing mode, this plateau is not followed by a subsequent decrease.

This qualitatively different behavior can be understood if we take into account the result of section 4.5.1. Even though the density of periodic orbits $\rho(v)$ is lower at high v than at low v, see Fig. 4.5, the density of periodic orbits inside the chaotic channel is only slightly reduced compared to the large chaotic sea at low v. This means that, unlike in the breathing mode, there are still ‘enough’ (especially stable) periodic orbits inside the thin chaotic channel around $F = 0$ to cause stickiness such that the exponent α of the distribution of the length of the laminar phases is still below the critical exponent of $\alpha_c = 2$ (see the discussion in section 6.3.1).

5.3.2 Quadrupole mode

In the quadrupole mode, the quantity F can hardly be interpreted as the (normalized) product of the angular momenta around the two foci, since the two foci do not always lie on the same coordinate axis, but rather periodically switch between the x- and the y-axis. Nevertheless, we can define F according to Eq. (2.56) and use it to identify the length of the laminar phases. The result for the two characteristic velocity regimes is shown in Fig. 5.5 (for $C = 0.1$), where actually the cumulative distribution $P(l)$ instead of $p(l)$ is presented. Neither of the two distributions $P_{v<10}(l)$ and $P_{v>10}(l)$ follows a pure power law, so extracting a power law exponent makes no sense. Furthermore, the statistics of $P_{v<10}(l)$ for large values of l is very poor. Nevertheless, we can tentatively assume that $P_{v<10}(l)$ decays for large l slower than $P_{v>10}(l)$, i.e. the region $v < 10$ exhibits enhanced stickiness. This is supported by the fraction of particles $f_{\mathrm{l}am}(n)$ that are sticky. Like in the breathing mode, $f_{\mathrm{l}am}(n)$ shows a plateau-like structure followed by a decrease, where the decrease now sets in at already $\approx 10^7$ collisions.

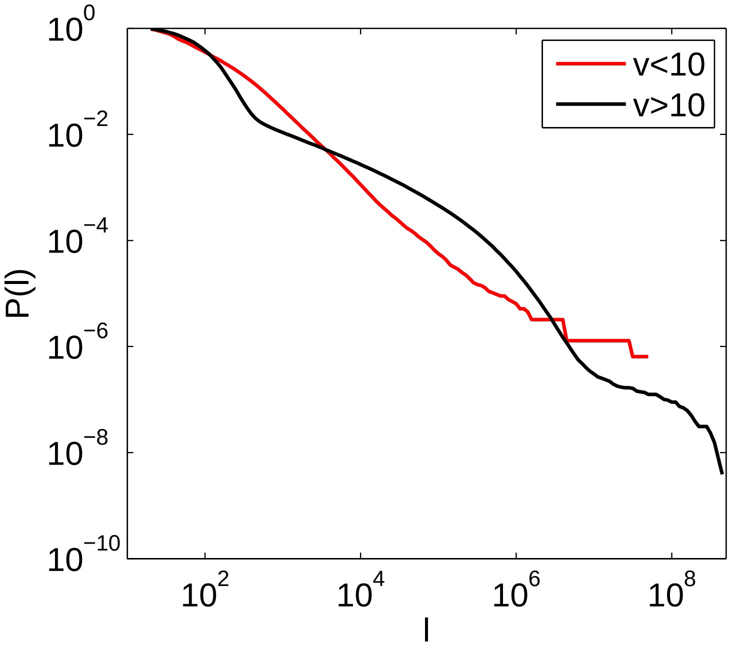

Figure 5.5: Propability $P(l)$ (cumulative distribution) that a laminar phase has a length of greater than or equal to l, in two different velocity regimes in the quadrupole mode ($C = 0.1$). The distribution $P_{v>10}(l)$ decays faster than $P_{v<10}(l)$ for $l > 10^5$, whereas for $l < 10^5$ both distributions are very similar.

The origin of the reduced stickiness in the region $v > 10$ is the same as the corresponding one in the breathing mode: The density of periodic orbits $\rho(v)$ inside the channel of chaotic motion (i.e. the banded region with $\rho(\phi, \alpha) > 0$ in Fig. 3.13) is significantly smaller than $\rho(v)$ for the large low v chaotic sea, see Fig. 4.7.

6 Diffusion in momentum space

In this chapter, we study the long time evolution of the energy of an ensemble of particles inside the driven ellipse, especially with respect to the question how the different modes influence the asymptotic behavior of the diffusion in momentum space. We will use the results accumulated in the previous sections to provide a qualitative understanding of the diffusion process in momentum space.

6.1 Validity of the results

When investigating the long-term behavior of dynamical quantities in the driven elliptical billiard, there are two computational issues that need to be addressed. Firstly, we have to ensure that statistical quantities, like the ensemble averaged energy, are converged. Secondly, we have to deal with errors arising from the finite numerical precision when iterating the mapping $\mathcal{M}$. Both aspects will be discussed in the following.

6.1.1 Statistical convergence

Addressing the long-term behavior, requires the iteration of the implicit mapping $\mathcal{M}$ (2.26) for many collisions. As we will see in this section, an ensemble of particle has to be iterated for $N_c = 10^{11}$ collisions in the driven elliptical billiard to resolve the phenomenon of a dynamical crossover in the diffusion process. As a consequence, the number of particles N_p of a specific ensemble is rather small $(100 - 200)$, since the total number of collisions N_{tot} that can be iterated within a feasible time (even when using large scale multi-processor computing facilities) is of the order of 10^{13} and is simply the product of the number of particles and the number of collisions each particle is iterated, so $N_{tot} = N_p \cdot N_c$. To ensure the convergence of quantities such as the ensemble averaged velocity $\langle v\rangle(n)$, we used different combinations of N_p and N_c with better statistics in the number of particles, such as $N_p = 10^4, N_c = 10^8$ and found perfect agreement. A drawback of this method is that we cannot address the long-term evolution of the higher moments such as the standard deviation or the skewness of $\langle v\rangle(n)$, since for $N_c = 10^{11}$, at least $N_p = 10^3$ would be necessary to obtain acceptable statistics.

6.1.2 Finite numerical precision

When solving a (partly) chaotic system numerically, the main issue we have to deal with is the following: Trajectories exhibiting chaotic motion have a positive Lyapunov exponent, see section 3.2.2. The meaning of a positive Lyapunov exponent is that such particles are sensitive to a change of the initial conditions, i.e. any small deviation of an initial condition will get amplified exponentially when iterating the mapping. The mapping is iterated numerically with double-precision, i.e. given a phase space point $\boldsymbol{x}_n = (\xi_n, \phi_n, \alpha_n, v_n)^\top$, the next phase space point $\boldsymbol{x}_{n+1}$ is obtained with an accuracy of circa 10^{-16}. Even though this is a very small deviation from the 'true' phase space point $\tilde{\boldsymbol{x}}_{n+1}$ only, it will get amplified exponentially. By 'true' we mean the point $\tilde{\boldsymbol{x}}_{n+1}$ that is obtained from $\boldsymbol{x}_n$ by applying the mapping $\mathcal{M}$ assuming infinite numerical precision, i.e. $\tilde{\boldsymbol{x}}_{n+1}$ it is the exact next phase space point. Already after 46 iterations of the mapping, the resulting $\boldsymbol{x}_{n+46}$ deviates from the exact point $\tilde{\boldsymbol{x}}_{n+46}$ by a distance of the order of one (if we assume a Lyapunov exponent of $\sigma = 0.8$). This means after comparatively few collisions, the trajectory deviates macroscopically from the exact one. We can thus asked ourselves whether a numerically (with finite precision) obtained orbit still reflects a physical trajectory.

Fortunately, physical meaningfull results are ensured by the concept of 'shadowing' or 'shadowability' [130–134]. It states that an orbit $\mathcal{O} = \{\boldsymbol{x}_0, \boldsymbol{x}_1, \boldsymbol{x}_2, \dots \boldsymbol{x}_N\}$, obtained from numerically iterating the initial condition $\boldsymbol{x}_0$, represents a physical trajectory, even though a 'different' one. The exact orbit, generated by advancing $\boldsymbol{x}_0$ assuming infinite precision, is denoted by $\mathcal{O}^e = \{\boldsymbol{x}_0, \tilde{\boldsymbol{x}}_1, \tilde{\boldsymbol{x}}_2, \dots \tilde{\boldsymbol{x}}_N\}$. Now, 'different' means, that the orbit $\mathcal{O}$ does not represent the exact orbit $\mathcal{O}^e$, but it 'shadows' a different orbit $\mathcal{O}^d = \{\boldsymbol{y}_0, \tilde{\boldsymbol{y}}_1, \tilde{\boldsymbol{y}}_2, \dots \tilde{\boldsymbol{y}}_N\}$ in the sense that the difference between $\boldsymbol{x}_i \in \mathcal{O}$ and $\tilde{\boldsymbol{y}}_i \in \mathcal{O}^d$ is small, $|\boldsymbol{x}_i - \tilde{\boldsymbol{y}}_i| \ll 1$. The orbit $\mathcal{O}^d$ is the exact orbit corresponding to a slightly different initial condition, i.e. $\boldsymbol{y}_0 = \boldsymbol{x}_0 + \delta\boldsymbol{x}_0$, where $|\delta\boldsymbol{x}_0| \ll 1$ is a very small deviation.

Overall, iterating the mapping $\mathcal{M}$ with finite numerical precision reproduces physical trajectories, even though corresponding to slightly perturbed initial conditions. This is not a drawback since we are interested in statistical properties, like the ensemble averaged energy, or the distribution of the length of laminar phases. To obtain such statistical quantities, it is important to use a representative ensemble of particles, but the *exact* initial conditions of the ensemble do not play a role. Actually, quantities like the distribution of the length of laminar phases $\rho(l)$ are independent of the initial conditions, as long as the initial conditions lie within the same connected ergodic component of the phase space [121].

Furthermore, we exemplarily used both single and double precision (both on 32 and 64-bit machines) in our simulations and found no differences in the relevant quantities. Additionally, we applied two different numerical schemes to solve the implicit mapping, especially for the bracketing of the first root with $t_{n+1} > t_n$ of Eq. (2.31), again leading to the same results.

6.2 Evolution of the energy

The initial conditions of an ensemble of $N_p = 160$ particles are uniformly distributed in the variables ξ_0, $\phi_0 \in [0, 2\pi]$, $\alpha_0 \in [0, \pi]$. The modulus of the initial velocity $v_0 = 0.1$ is chosen in a way that all initial conditions lie inside the large chaotic sea located at low v. The ensemble averaged velocity

$$\langle v \rangle(n) = 1/N_p \sum_{i=1}^{N_p} v_n(i), \tag{6.1}$$

(or mean velocity, we will use these two terms interchangeably, i stands for the i-th particle) as a function of the collision number n is shown for two different amplitudes ($C = 0.1$ and $C = 0.5$) in Fig. 6.1 (breathing mode). The breathing mode shows Fermi acceleration (FA), i.e. the energy grows with increasing v infinitely. Specifically, the mean velocity grows asymptotically according to a power law, i.e $\langle v \rangle(n) \sim n^{\gamma}$ for large n. The diffusion

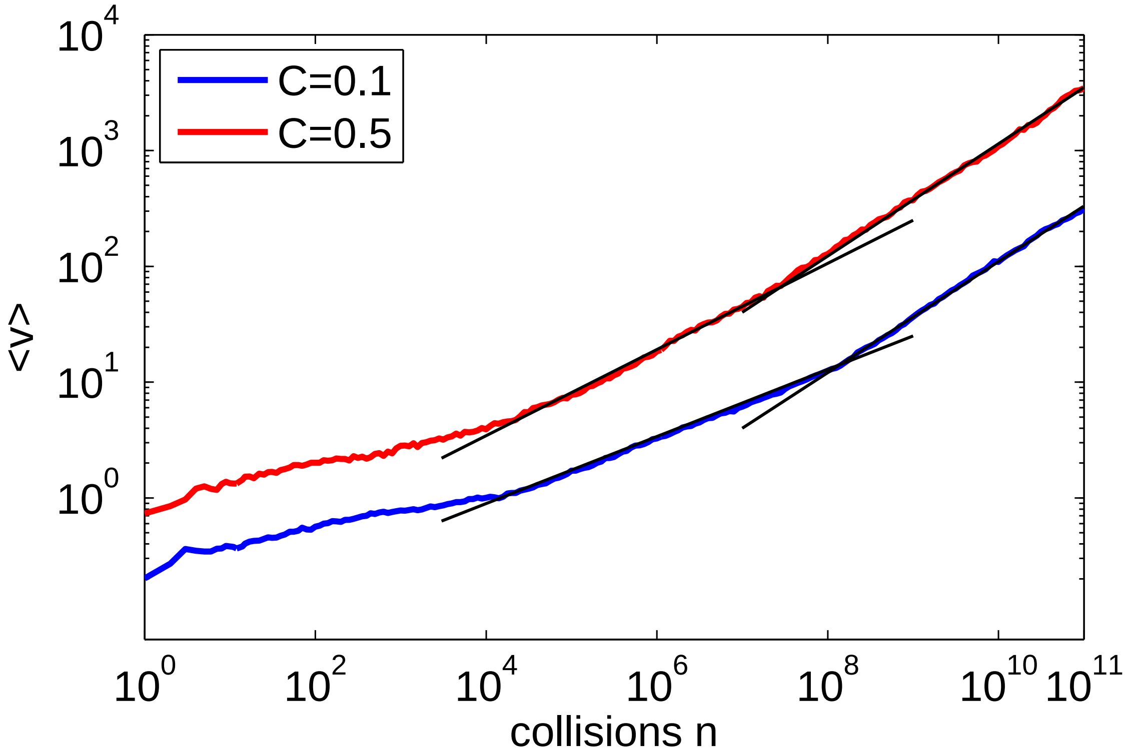

Figure 6.1: The ensemble averaged modulus of the velocity $\langle v\rangle(n)$ as a function of the number of collisions n for two different amplitudes C (breathing mode). Asymptotically, i.e. for $n > 10^8$, the mean velocity exhibits normal diffusion, $v \sim n^{1/2}$, whereas in the transient regime $10^4 < n < 10^8$ the transport in momentum space is subdiffusive, $v \sim n^{\gamma(C)}$, with $\gamma(C) < 1/2$.

exponent γ is approximately 1/2 for large n, independent of the amplitude. Asymptotically, the breathing modes exhibits normal diffusion in momentum space. Note that in energy space, this corresponds to $\langle E\rangle(n) \sim n$, since $E \sim v^2$ (all particles have the same mass and the potential is zero inside the ellipse).

Yet there is an intermediate regime, in which the mean velocity obeys over several (roughly four) decades a powerlaw $\langle v\rangle(n) \sim n^{\gamma}$, where the exponent γ depends on the amplitude and is smaller than 1/2. This transient regime lasts from approximately 10^4 to 10^8 collisions. The diffusion exponents γ obtained from a power law fit in this transient regime are shown in Table 6.1 (actually for all three driving modes). In this regime (see also Ref. [135]), γ grows monotonically with increasing amplitude (breathing mode), but is always smaller than 1/2. Subsequently to the transient regime, the breathing mode exhibits normal diffusion ($\gamma = 1/2$) independent of the amplitude, so there is a crossover in the diffusion exponent γ from sub- to normal diffusion after roughly 10^8 collisions. Contrary to many other systems [136], this crossover in the diffusion in momentum space is not induced by the change of an external parameter, but rather occurs dynamically during the evolution of the ensemble.

Before we provide a qualitative explanation of the dynamical crossover from sub- to normal diffusion, we briefly discuss the initial transient, i.e. the region from 1 to approximately 10^4 collisions, before the power law sets in, see Fig. 6.1.

Table 6.1: Diffusion exponent $\gamma(C)$ for $\langle v\rangle(n) \sim n^{\gamma(C)}$ for different values of the amplitude C and the different driving modes. In the breathing and in the quadruple mode the diffusion exponent in the transient regime between 10^4 and 10^8 collisions (breathing mode), 10^4 and $8 \cdot 10^7$ collisions (quadrupole mode) is shown, whereas in the constant eccentricity mode $\langle v\rangle(n) \sim n^{\gamma(C)}$ is a power law for $n > 10^4$.

C	0.10	0.20	0.30	0.40	0.50
$\gamma_{br}(C)$	0.28	0.34	0.36	0.39	0.40
$\gamma_{quad}(C)$	0.23	0.38	0.45	0.45	0.46
$\gamma_{ecc}(C)$	0.09	0.09	0.09	0.09	0.09

6.2.1 Initial transient

Suppose that after the initial transient of $\mathcal{O}(10^4)$, the ensemble averaged modulus of the velocity exhibits a power law of the form $v_l(n_l) = \delta \cdot n_l^\gamma$ (for convenience we write v_l instead of $\langle v_l\rangle$). In a double logarithmic representation, this is simply a straight line with slope β which would intersect the y-axis at $\ln\delta$, since with $v = \ln v_l$, $n = \ln n_l$ we have $v(n) = \ln\delta + \beta\cdot n$ (in the discussion of the initial transient, the index l refers to quantities in a linear-linear representation, in contrast to quantities without an index, which correspond to a double-logarithmic representation). To enhance the duration of the power law, naively we could try to simply wait until a power law is observed, let's say after e.g. $n_0 = 10^5$ collisions, take the ensemble at this point and use the corresponding values of ξ_i, ϕ_i, α_i and v_i as new initial conditions and restart the simulation. However, this will not work, the whole described procedure corresponds to the transformation

$$\tilde{v}_l(n_l) = v_l(n_l + n_0) = \delta(n_l + n_0)^\gamma \tag{6.2}$$

$$\tilde{v}(n) = \ln\delta + \gamma\ln(e^n + n_0) \tag{6.3}$$

which is obviously not a power law for small values of n. This can be easily seen by comparing the slope of the original power law $v(n) = \ln\delta + \gamma n$, which is of course always γ, to the slope $\tilde{v}'(n) = \gamma e^n/(e^n + n_0)$ of the modified power law of Eq. (6.3) in the double logarithmic representation for three different regimes:

$n_l = 1 \Leftrightarrow n = 0$: $\tilde{v}'(0) = \frac{\gamma}{1+n_0} \approx \frac{\beta}{n_0}$, so in the beginning we observe a nearly straight line, where the slope β of the original power law is suppressed by a factor of n_0.

$n_l = n_0 \Leftrightarrow n = \ln n_0$: $\tilde{v}'(\ln n_0) = \frac{\gamma e^{\ln n_0}}{e^{\ln n_0}+n_0} = \frac{\gamma n_0}{2n_0} = \gamma/2$, so the slope is suppressed by a factor of 2.

$n_l = 10n_0 \Leftrightarrow n = \ln 10 + \ln n_0$: $\tilde{v}'(\ln 10 + \ln n_0) = \frac{10\beta}{11} \approx \beta$, so after $n_l = 10n_0$, we are back in the power law regime.

In other words, applying the transformation (6.2) results in a transient of the order of $10n_0$. Effectively, the transformation (6.2) corresponds to starting with higher initial velocity $\tilde{v}_0 := \tilde{v}_l(0) = \delta n_0^\gamma$ of the ensemble. We can thus conclude, that increasing v_0 results in a longer initial transient. This can be seen in Fig 6.2, where the mean velocity $\langle v\rangle(n)$ for different initial v_0 is shown. To ensure that the particles start inside the chaotic sea, the

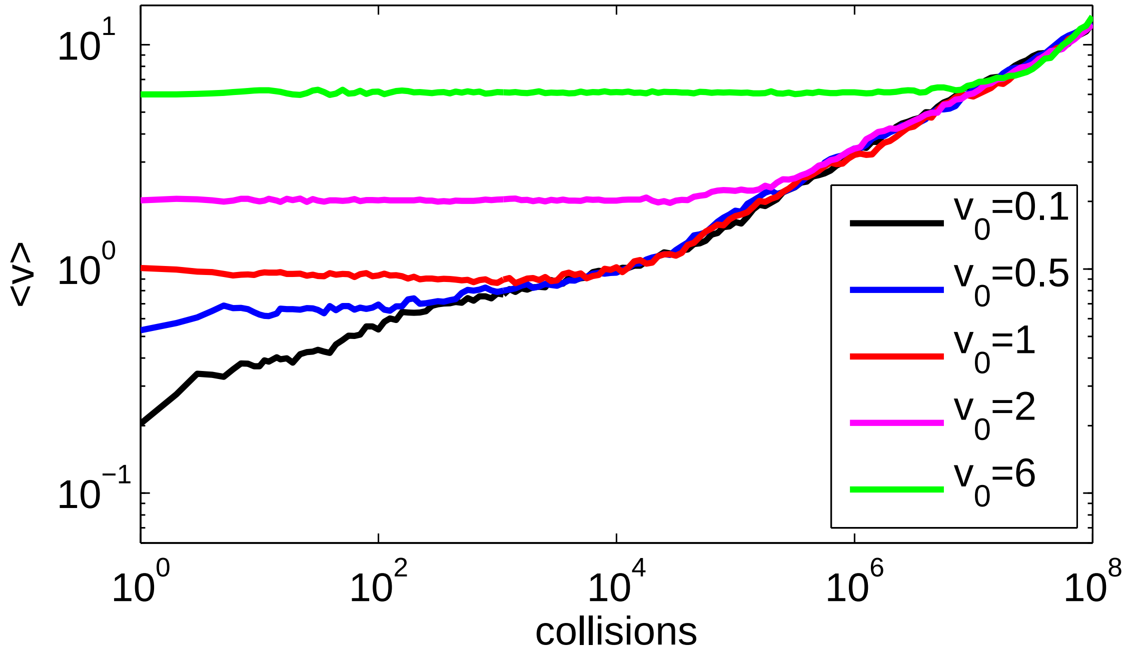

Figure 6.2: The initial transient for different values v_0 of the initial velocity in the breathing mode ($C = 0.1$). The duration of the initial transient increases with increasing v_0.

initial conditions are chosen in such that $|F_0| < 0.1$. Clearly, the duration of the initial transient increases with increasing v_0, but eventually all curves follow the same power law, independent of v_0

In the sense of the above discussion, the value $v_0 = 0.1$ we used in our simulation is already too high, it will lead to a transient of $\mathcal{O}(10^3 - 10^4)$, ideal would be an initial velocity of $v_0 = \delta \approx 0.04$ (breathing mode). However, starting with $v_0 = \delta$ would again yield a similar transient, since after a few collisions the velocity of the ensemble would be of the order of a few $\omega C > \delta$ due to the momentum transferred upon collisions with the moving boundary.

6.2.2 Crossover from sub- to normal diffusion

Subsequent to the initial transient of the order of 10^4 collisions, the driven ellipse in the breathing mode shows sub-diffusion ($\gamma < 1/2$) in momentum space for roughly four decades, see Fig. 6.1 and Table 6.1, cf. also Refs. [114,135]. Between laminar phases corresponding to sticky motion, chaotic phases of the trajectories associated with many separatrix ($F = 0$) crossings [122] lead to stochastic fluctuations of v and thus to a net increase of the mean velocity $\langle v \rangle$. It is known, for example from continuous time random walks [137], that such an intermittent [124] interplay of laminar and chaotic phases can lead to the appearance of subdiffusion, if the expectation value $\langle l \rangle = \int_{l_0}^{\infty} l p(l) dl$ of the waiting times (laminar phases) $p(l)$ diverges. For a power law $p(l) \sim l^{-\alpha}$, we have

$$\langle l \rangle = \int_{l_0}^{\infty} l p(l) dl = \int_{l_0}^{\infty} l^{-\alpha+1} dl = \frac{1}{-\alpha+2} l^{-\alpha+2} \Big|_{l_0}^{\infty}, \qquad (6.4)$$

so $\langle l \rangle$ diverges if $\alpha \leq \alpha_c = 2$.

In the breathing elliptical billiard, we observe subdiffusion in momentum space in the transient regime from 10^4 to 10^8 collisions. The mean velocity $\langle v \rangle(n)$ of the ensemble in this regime is smaller than 30, so the ensemble is not yet located in the thin chaotic channel around $F = 0$ which is present for $v > 30$, cf. Fig. 3.7. The part of phase space with $v < 30$ is characterized by enhanced stickiness, cf. the discussion in chapter 5. The ensemble probes for $10^4 < n < 10^8$ exactly this 'sticky' part of phase space. Two effective quantities support this observation: Firstly, the fraction $f_{\text{lam}}(n)$ of an ensemble that is actually sticky at a given collision number n increases until 10^8 collisions and secondly, the distribution of the length l of laminar phases $p_{v<30}(l) \sim l^{-\alpha}$ decays rather slowly for large l, with an exponent of $\alpha_{v<30} = 1.85$ for $l > 6 \cdot 10^4$. According to continuous time random walk theory (CTRW) [137], subdiffusive transport requires an exponent α less than two, and $\alpha_{v<30} < \alpha_c = 2$, so the appearance of subdiffusion is in agreement with CTRW theory.

The quantities $f_{\text{lam}}(n)$ and $p(l)$ depend on the driving amplitude C in a way that the stickiness is reduced with increasing amplitude, for example, $p(l)$ decays for $C = 0.5$ faster than for $C = 0.1$, cf. the discussion in chapter 5. As a result, the diffusion exponent γ in the transient regime, see Table 6.1, increases with increasing amplitude.

The regime of sub-diffusion ($n < 10^8$) is followed by normal diffusion in momentum space ($n > 10^8$), cf. Fig. 6.1. The mean velocity $\langle v \rangle(n)$ is now larger than 30, so the particles are for $n > 10^8$ predominantly inside the thin channel of chaotic motion around $F = 0$ ('acceleration channel'). The stickiness effects in this channel of chaotic motion are less pronounced: Firstly, the fraction of particles $f_{\text{lam}}(n)$ that are sticky decreases for $n > 10^8$. Secondly, the distribution of waiting times $p_{v>30}(l) \sim l^{-\alpha}$ decays for $l > 10^5$ faster than $p_{v<30}(l)$, hence $\alpha_{v>30} = 2.20 > \alpha_{v<30} = 1.85$. In particular $\alpha_{v>30} > \alpha_c$, so the expectation value $\langle l \rangle$ is finite and in agreement with CTRW theory this results in normal diffusion. In other words, there are fewer and shorter laminar phases once the ensemble is predominantly located in the narrow acceleration channel around $F = 0$.

The crossover from sub- to normal diffusion in momentum space persists when increasing the amplitude. For $C = 0.5$ the power law exponent of $p(l)$ corresponding to the sub-diffusive regime is $\alpha = 1.92 < \alpha_c$ and $\alpha = 2.34 > \alpha_c$ in the regime of normal diffusion, so just like for $C = 0.1$, the crossover can be traced back to a change of the stickiness properties of the phase space in the different velocity regimes.

Summarizing, the breathing mode shows Fermi acceleration, i.e. the mean velocity $\langle v \rangle$ grows with increasing number of collisions n over all bounds. For low values of $\langle v \rangle$ (corresponding to a small number of collisions), the ensemble fills out a large chaotic sea, with increasing n, and thus increasing $\langle v \rangle$, it is squeezed more and more into the thin channel of chaotic motion round $F = 0$. In its evolution, the ensemble probes dynamically different parts (in terms of v) of phase space and the different parts have different (stickiness) properties, which influence the kind of transport (either sub- or normal diffusion) that occurs in momentum space.

6.3 Other modes

6.3.1 Constant eccentricity mode

The evolution of ensemble averaged modulus of the velocity $\langle v \rangle(n)$ as a function of the number of collisions in the constant eccentricity mode is shown in Fig. 6.3 for two different amplitudes ($C = 0.1$ and $C = 0.5$). The mean velocity $\langle v\rangle(n)$ follows a power law $\langle v\rangle(n) \sim n^{\gamma}$ for $n > 10^3$. The power law exponent γ is equal to 0.09 independent of the amplitude, see Table 6.1. This means the transport in momentum space is subdiffusive throughout the whole evolution (at least until 10^{11} collisions, which is the maximum we are able to iterate) and we do not observe a crossover in the diffusion process from sub- to normal diffusion in the constant eccentricity mode.

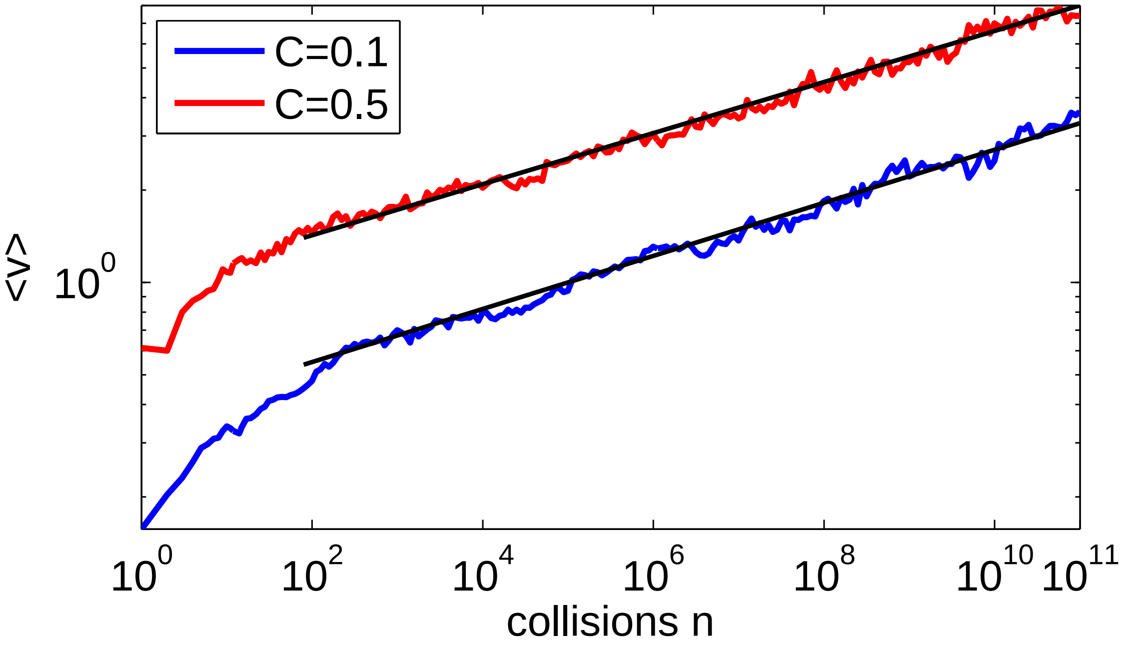

Figure 6.3: The ensemble averaged modulus of the velocity $\langle v\rangle(n)$ as a function of the number of collisions n for two different amplitudes C in the constant eccentricity mode. The diffusion in momentum space is subdiffusive throughout the whole evolution, $\langle v\rangle(n) \sim n^{\gamma}$ follows a power (for $n > 10^3$) law with an exponent of $\gamma = 0.09$ independent of the amplitude.

The driving law in the constant eccentricity mode is a pure scaling, in particular it is the only driving mode that leaves, as the name suggest, the eccentricity ϵ constant. In the corresponding frozen billiard, ϵ exclusively determines the phase space properties. In particular, the eccentricity ϵ determines the minimum value of F, namely $F_{\text{min}} = -\epsilon^2/(1-\epsilon)$ (remember $F_{\text{max}} = 1$ independent of ϵ in all driving modes) and F_{min} determines the measure of rotators and librators in the phase space of the frozen billiard, cf. the discussion in section 2.2.7. At any given phase ξ the phase space of the corresponding frozen billiard is the same: The driving does not induce any deformation (in terms of ϵ) of the billiard. As a consequence, there are no transitions from librators to rotators and vice versa caused by the deformation of the phase space of the corresponding frozen billiard. Note that there are of course transitions from librators to rotators and vice versa due to the momentum transfer upon boundary collisions. Transitions between librators and rotators are always associated with separatrix ($F = 0$) crossings and as we saw in section 5.1, separatrix crossings lead to stochastic fluctuations in v and eventually to Fermi acceleration. In this sense, the constant eccentricity mode can be viewed as the most ‘regular’ perturbation of the static billiard among the considered driving modes.

The comparatively small diffusion exponent $\gamma = 0.09$ is a result of this 'regular' character of the constant eccentricity mode. Even though we observe, similar to the breathing mode, the emergence of large invariant structures from librator- and rotator-type motion, squeezing the ensemble with increasing velocity into thin channels around $F = 0$, this is not accompanied by a change of the stickiness properties, cf. the discussion in section 5.3.1. As a result, the diffusion exponent γ is independent of the velocity regime and does not show a crossover like the one in the breathing mode. Specifically, two stickiness properties support this observation: Firstly, the fraction of particles that are laminar (sticky) $f_{\mathrm{lam}}(n)$ continuously increases with increasing n and does not drop down as it is the case in the breathing mode, cf. Fig. 5.4. Secondly, the distribution of the length of the laminar phases $p(l)$ decays independently of the velocity (and amplitude) with an exponent $\alpha < \alpha_c$, which according to CTRW theory allows for subdiffusive transport.

Increasing the driving amplitude C does not change any of the above discussed properties, it just changes the natural momentum scale ωC of the system, resulting in higher mean velocities, but not in different diffusion exponents, see Fig. 6.3 and Table 6.1.

Finally a short remark to the initial transient. The slope of $\langle v\rangle(n)$ for $n < 10^3$ is higher than the asymptotical value, in the sense of the discussion in section 6.2.1, this means we used a too small value of v_0. The reason why we used such a small v_0 is that all initial conditions lie inside the chaotic sea located at low v, independent of ϕ_0, α_0, ξ_0 and not 'accidentally' inside a regular structure.

6.3.2 Quadrupole mode

The evolution of ensemble averaged modulus of the velocity $\langle v\rangle(n)$ as a function of the number of collisions in the quadrupole mode is shown in Fig. 6.4 for two different amplitudes ($C = 0.1$ and $C = 0.5$). The mean velocity $\langle v\rangle(n)$ follows asymptotically ($n > 5 \cdot 10^7$) a power law with an diffusion exponent of one half, i.e. the quadrupole mode exhibits normal diffusion. Like in the breathing mode, there is a transient regime in which the mean velocity obeys over several (roughly four) decades a powerlaw $\langle v\rangle(n) \sim n^\gamma$, where the exponent γ depends on the amplitude and is smaller than $1/2$ (at least for small amplitudes). This transient regime lasts from approximately 10^4 to $5 \cdot 10^7$ collisions. The diffusion exponents γ obtained from a power law fit in this transient regime are shown in Table 6.1. For $C = 0.3, 0.4, 0.5$, the diffusion exponent γ has values of ≈ 0.45, within in the uncertainty of the power law fit, these values are not significantly different from the asymptotic value $\gamma = 1/2$. This means the quadrupole mode shows a crossover in the diffusion process after roughly $5 \cdot 10^7$ collision (at least for small amplitudes), similar to the breathing mode. This is supported by the fact that the fraction $f_{\mathrm{lam}}(n)$ of sticky particles decreases for $n > 10^7$, so the crossover should set in earlier than in the breathing mode, which is the case ($5 \cdot 10^7$ compared to 10^8). For larger amplitudes ($C \geq 0.3$), the diffusion exponent γ in the transient regime ($10^4 < n < 5 \cdot 10^7$) is already close to the asymptotic ($n > 5 \cdot 10^7$) exponent of $\gamma = 1/2$, so there is no crossover in the diffusion for amplitudes with $C \geq 0.3$.

The quadrupole mode can be viewed as a stronger perturbation than the breathing mode, since the stability of the motion along the coordinate axes changes periodically between stable and unstable, making the existence of large regular islands of stable librator-type motion impossible, even for large velocities. In that sense, it is surprising at first sight that the diffusion exponent γ for an amplitude of $C = 0.1$ is smaller in the quadrupole than in the breathing mode ($\gamma_{quad}(C = 0.1) = 0.23 < \gamma_{br}(C = 0.1) = 0.28$). However,

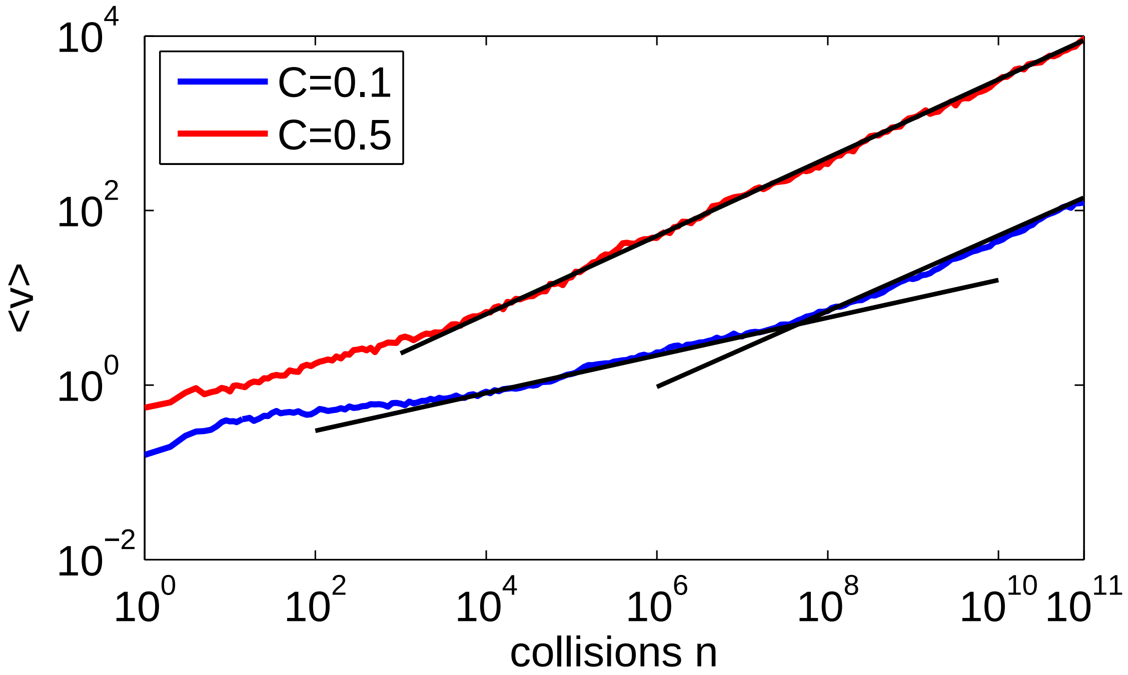

Figure 6.4: The ensemble averaged modulus of the velocity $\langle v\rangle(n)$ as a function of the number of collisions n for two different amplitudes C in the quadrupole mode. Asymptotically, i.e. for $n > 10^8$, the mean velocity exhibits normal diffusion, $v \sim n^{1/2}$, independent of the amplitude. In the transient regime $10^4 < n < 5 \cdot 10^7$ the transport in momentum space is subdiffusive for $C = 0.1$, whereas for $C = 0.5$ the diffusion process is normal.

we have to keep in mind that for our choice of a_0 and b_0 the equilibrium position of the quadrupole mode is a circle (i.e. $\epsilon_{\text{min}} = 0$) and the maximal deformation corresponds to $\epsilon_{\text{max}} = 0.58$ only, whereas in the breathing mode the boundary is always an ellipse with $\epsilon_{\text{min}} = 0.85$ and $\epsilon_{\text{max}} = 0.88$. The time-dependent breathing circular billiard does not show Fermi acceleration [79] and an amplitude of $C = 0.1$ is a rather weak perturbation only, so a rather small power law exponent has to be expected. With increasing amplitude, the equilibrium configuration of the quadrupole mode is of course still a circle, but the maximal eccentricity that is reached increases rapidly, see for example Fig. 2.4, resulting in larger diffusion exponents.

6.4 Discussion: Fermi acceleration in driven billiards

Concerning the question under which conditions FA will arise in 2D driven billiards, see also the discussion in section 1.2, the LRA-conjecture states that a sufficient condition for the occurrence of FA in a driven 2D billiard is the existence of a chaotic part in the phase space of the corresponding static system [76, 138, 139]. Our discovery of FA in the driven elliptical billiard [114, 135, 140, 141] shows that this is not a necessary condition (note again that the static counterpart of the driven elliptical billiard is integrable, i.e. there are no chaotic parts in phase space). Actually, the time-dependent elliptical billiard is the first[1] billiard with an integrable static counterpart that shows FA for a harmonic driving law[2].

Colloquially speaking, the LRA-conjecture states that the stochasticity necessary for FA, which in the 1D Fermi-Ulam model (FUM) can be achieved only by randomizing the driving law itself[3], can be assured in 2D billiards by the existence of chaotic parts in the phase space of the corresponding static system. In other words, in 2D billiards, the stochastic component of the driving law can be 'replaced' by chaotic dynamics of the frozen billiards. In the harmonically driven elliptical billiard, both ingredients (driving law and frozen phase space) are regular, i.e. the stochasticity is caused by the interplay of the driving law and the corresponding static phase space, but not by any of them on its own.

In contrast to the driven elliptical billiard, the oscillating circular billiard does not show FA. So a legitimate question is why is there no FA in the driven circular billiard, while there is FA in the time-dependent elliptical billiard, even though in both cases the corresponding static system is integrable. The answer is that in the circular billiard, the angular momentum is conserved even when driving the billiard [79], whereas the product of the angular momenta about the foci is not conserved when driving the elliptical billiard. Already the structure of the phase space of the static circular billiard is much simpler than the one of the elliptical billiard: It consists exclusively of invariant curves corresponding to rotational motion[4], actually straight lines in the $\phi \times \alpha$ Poincaré surface of section, in particular there are neither any hyperbolic fixed points, nor there is a separatrix.

One remaining puzzle is the absence of FA for a certain driving mode of an oval [85]. The time-dependent boundary of this oval is given by

$$\mathcal{B}(t) = \left\{ \left(\begin{array}{c} \cos\phi\,[1+\eta_2\cos t + \epsilon(1+\eta_1\cos t)\cos 2\phi] \\ \sin\phi\,[1+\eta_2\cos t + \epsilon(1+\eta_1\cos t)\cos 2\phi] \end{array} \right) \middle| 0 \le \phi < 2\pi \right\}. \tag{6.5}$$

For $\eta_1 = \eta_2 = 0$ the static oval is recovered and the geometry can be described in polar coordinates by $r(\phi) = 1 + \epsilon\cos 2\phi$. The parameter $\epsilon \in [0, 1)$ controls the amount of chaos in phase space (for $\epsilon = 0$ the integrable circle is obtained). In the driven case, $\eta_1 = \eta_2$ corresponds to a pure scaling mode, since Eq. (6.5) reduces to $r(t, \phi) = [1 + \eta_1 \cos t](1 + \epsilon\cos 2\phi)$, whereas for $\eta_1 \neq \eta_2$ the billiard changes its shape. The extension of the oval (scaling mode) in configuration space is shown in Fig. 1.2e.

The authors of Ref. [85] find that FA exists in the driven oval for $\eta_1 \neq \eta_2$, but claim that the energy stays bounded for the scaling mode ($\eta_1 = \eta_2$). We rechecked the results of Ref. [85] by numerically simulating an ensemble of particles in the driven oval [140], with the parameters specified in Ref. [85]. While we are able to reproduce the results in the $\eta_1 \neq \eta_2$ case, we did find FA even in the scaling ($\eta_1 = \eta_2$), see Fig. 6.5. Possibly, the long transient of the order of 10^7 collisions ($v_0 = 5$) has been misinterpreted by Kamphorst et al. [85] as the absence of FA. As it can be seen from Fig.6.5, the ensemble averaged velocity will eventually, after a transient, follow a power law $\langle v\rangle(n) \sim n^\gamma$, where the exponent γ is independent of v_0. Actually, our results are confirmed by a very recent publication [142]

---

[1] Here, we consider only billiards in the original sense of Birkhoff [21] in which particles move freely in between boundary collisions, i.e. we dot not consider billiards with an additional potential like the bouncer model [64].

[2] Note that for a stochastic driving law, any billiard geometry will show FA.

[3] More precisely: making the driving law sufficiently non-smooth

[4] There are additionally the diametral periodic two orbits, which can be viewed as librator-type motion, however, they have measure zero.

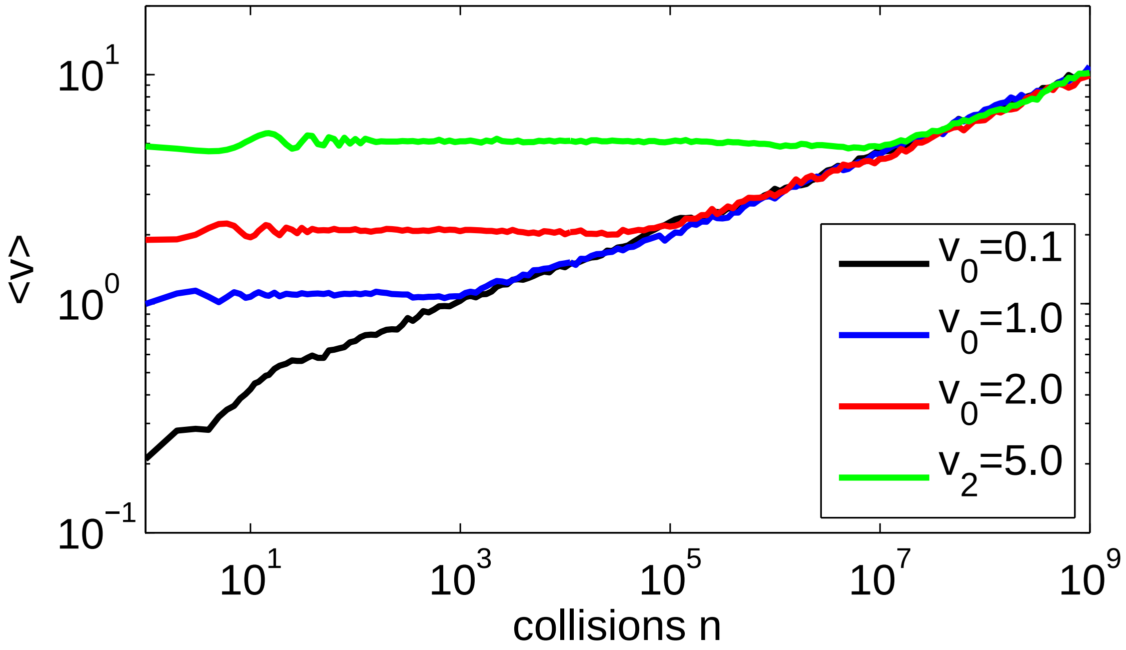

Figure 6.5: Ensemble averaged velocity $\langle v\rangle(n)$ as a function of n (collisions) in the driven oval (scaling mode) for different initial velocities v_0. Clearly, the oval shows FA. Just like in the elliptical billiard, the length of the initial transient increases with increasing v_0.

Static counterpart	**FA for harmonic driving?**
integrable	
circle	no
concentric annular	no
ellipse	yes
mixed	
eccentric annular	yes
oval, scaling mode	yes
oval, shape changing	yes
chaotic	
stadium	yes

Table 6.2: State of the art of the literature concerning Fermi acceleration (FA) in two-dimensional time-dependent billiards with a harmonic driving law. The geometries of the different billiard systems are shown in Fig. 1.2. The double horizontal line indicates the 'boarder' of FA.

(partly the same authors as in Ref. [85]), where the existence of FA is demonstrated even in the case of the scaling mode of the oval.

An overview concerning FA in 2D time-dependent billiards with a harmonic driving law including the results of this thesis is given in Table 6.4 (compare with Table 1.1, where the state of the art without the results of this thesis is shown). The 'boarder' of systems exhibiting FA goes right through the systems with integrable static counterparts, as explained in the beginning of this section. Furthermore, the systems where the frozen billiards have mixed dynamics all show FA. We thus conjecture that a necessary and sufficient condition for the presence of FA in a smoothly driven billiard is the existence of at least one hyperbolic fixed point in the phase space of the corresponding static counterpart.

Part II

Quantum dynamics

7 Static elliptical billiard

To find the quantum mechanical eigenstates $\Psi_n(x,y)$ of a static elliptical billiards, we have to solve the corresponding stationary Schrödinger equation

$$H(x,y)\Psi_n(x,y) = E_n\Psi_n(x,y) \tag{7.1}$$

where E_n is the energy of $\Psi_n(x,y)$ and the Hamiltonian $H(x,y)$ is given by

$$H(x,y) = -\frac{\hbar^2}{2\mu}\left(\frac{\partial^2}{\partial x^2} + \frac{\partial^2}{\partial y^2}\right) + V(x,y). \tag{7.2}$$

The potential $V(x,y)$ is zero inside and infinity outside the static elliptical billiard:

$$V(x,y) = \left\{ \begin{array}{ll} 0 & \text{if } \frac{x^2}{a^2} + \frac{y^2}{b^2} \le 1 \\ \infty & \text{if } \frac{x^2}{a^2} + \frac{y^2}{b^2} > 1. \end{array} \right. \tag{7.3}$$

This means the eigenvalue equation (7.1) has to be solved under Dirichlet boundary conditions

$$\Psi(x,y) = 0 \quad \text{for} \quad \left\{ (x,y)^\top \in \mathbb{R}^2 \middle| \frac{x^2}{a^2} + \frac{y^2}{b^2} = 1 \right\}, \tag{7.4}$$

where a and b are the semi-major and semi-minor axis of the ellipse.

Due to the boundary condition of Eq. (7.4), solving the eigenvalue equation (7.1) is actually not trivial and involves some subtleties [108,143–148]. Here, we follow the discussion given in Ref. [108] and additionally use results presented in Refs. [148] and [147]. We start by changing from Cartesian to elliptic coordinates:

$$x = f\cosh\xi\cos\eta, \quad 0 \le \xi \le \xi_0 \tag{7.5a}$$

$$y = f\sinh\xi\sin\eta, \quad 0 \le \phi < 2\pi, \tag{7.5b}$$

where $f = \sqrt{a^2 - b^2}$ is half the distance between the foci of an ellipse with semi-major axes a and semi-minor axes b and $\xi_0 = \operatorname{arctanh}(b/a)$. The stationary Schrödinger equation reads

$$H(\xi,\eta)\varphi(\xi,\eta) = E\varphi(\xi,\eta), \tag{7.6}$$

where $\varphi(\xi,\eta)$ is an eigenfunction with energy E and $H(\xi,\eta)$ is the Hamiltonian:

$$\hat{H}(\xi,\eta) = -\frac{\hbar^2}{2\mu} \triangle (\xi,\eta) + V(\xi,\eta) \tag{7.7}$$

The potential energy $V(\xi,\eta)$ in elliptic coordinates is now

$$V(\xi,\eta) = \left\{ \begin{array}{ll} 0 & \text{if } \xi \le \xi_0 \\ \infty & \text{if } \xi > \xi_0, \end{array} \right.$$

As a consequence, the eigenfunctions $\varphi(\xi, \eta)$ have to satisfy the Dirichlet boundary condition $\varphi(\xi_0, \eta) = 0$ and also the periodicity condition $\varphi(\xi, \eta) = \varphi(\xi, \eta + 2\pi)$. The Laplacian operator in elliptic coordinates is given by

$$\triangle(\xi, \eta) = \frac{2}{f^2(\cosh 2\xi - \cos 2\eta)} \left(\frac{\partial^2}{\partial \xi^2} + \frac{\partial^2}{\partial \eta^2} \right) \tag{7.8}$$

The two-dimensional (2D) Schrödinger equation inside the elliptical billiard (i.e. $\xi \leq \xi_0$) then simplifies to

$$\left[\frac{\partial^2}{\partial \xi^2} + \frac{\partial^2}{\partial \eta^2} + \frac{k^2 f^2}{2} (\cosh 2\xi - \cos 2\eta) \right] \varphi(\xi, \eta) = 0, \tag{7.9}$$

with $k^2 = 2\mu E/\hbar^2$. Obviously, $\varphi(\xi, \eta)$ can be separated with the standard ansatz

$$\varphi(\xi, \eta) = R(\xi)\Theta(\eta) \tag{7.10}$$

into a radial ($R(\xi)$) and an angular ($\Theta(\eta)$) part. Plugging this separation ansatz in the Schrödinger equation (7.9), we obtain two ordinary differential equations:

$$R''(\xi) - (\alpha - 2q \cosh 2\xi) R(\xi) = 0, \tag{7.11a}$$

$$\Theta''(\eta) + (\alpha - 2q \cos 2\eta) \Theta(\eta) = 0, \tag{7.11b}$$

where α is the separation constant and q is the dimensionless, rescaled energy

$$q = \frac{k^2 f^2}{4} = \frac{\mu f^2}{2\hbar^2} E. \tag{7.12}$$

Equations (7.11a), (7.11b) are the standard form of the Mathieu equations, Eq. (7.11b) is the ordinary Mathieu equation (OME) and Eq. (7.11a) is the modified Mathieu equation (MME). The corresponding solutions are the ordinary and modified Mathieu functions (OMF, MMF), respectively. Note that the change of variables $\eta = i\xi$ transforms the OME into the MME. Even though the ansatz (7.10) decouples the Schrödinger equation (7.9), yielding two ordinary differential equations, one depending on ξ, the other depending on η only, the separation constants α and q to not decouple [149], as we will see in the following.

Let's discuss the solutions of the OME first. The physical solutions of the OME have to be periodic, i.e. they can be expanded in a Fourier series (actually, Floquet theory guarantees the existence of periodic solutions [147])

$$\Theta_l(\eta) = \begin{cases} ce_l(\eta, q) = \sum_{k=0}^{\infty} A_k(l, q) \cos(k\eta) \\ se_l(\eta, q) = \sum_{k=1}^{\infty} B_k(l, q) \sin(k\eta) \end{cases} \tag{7.13}$$

For a fixed q, it is known that only certain values of α admit for periodic solutions. These eigenvalues are called the characteristic values α_l and β_l, where l is the order ($l \geq 0$ for $ce_l(\eta)$ and $l \geq 1$ for $se_l(\eta)$). Since the Mathieu equation is of Sturm-Liouville type, all eigenvalues are real, positive and can be ordered $\alpha_0 < \beta_1 < \alpha_1 < \beta_2 \ldots$. In the $q \times \alpha$ plane, the functions $\alpha_l(q)$ and $\beta_l(q)$ are curves that do not intersect. The $ce_l(\eta, q)$ and $se_l(\eta, q)$ with even order have a period of π, the ones with odd order have a period of 2π. The order l specifies the number of zeros of $ce_l(\eta, q)$ and $se_l(\eta, q)$ in the interval $\eta \in [0, \pi]$. The expansion coefficients $A_k(l,q)$ and $B_k(l,q)$ are determined by the recurrence relations for the Mathieu equations [115].

The solutions of the MME Eq. (7.11a), i.e. the radial part, can be obtained from the solutions of the OME by the mentioned change of variable $\eta = i\xi$, yielding

$$R_l(\xi) = \begin{cases} Ce_l(\xi, q_l) = \sum_{k=0}^{\infty} A_k(l, q_l)\cosh(k\xi) \\ Se_l(\xi, q_l) = \sum_{k=1}^{\infty} B_k(l, q_l)\sinh(k\xi). \end{cases} \tag{7.14}$$

Note that the expansion coefficients $A_k(l,q)$ and $B_k(l,q)$ are the same as the ones in the solutions (7.13) of the OME. In the case of the OME, the eigenvalues α and β are determined by the condition that the solutions are periodic. The solutions of the MME can also be viewed as an independent eigenvalue problem for the q's (with fixed α and β), now the condition is that $R_l(\xi)$ has to the satisfy the Dirichlet boundary condition (remember $\xi_0 = \mathrm{arctanh(b/a)}$)

$$R_l(\xi_0) = \begin{cases} Ce_l(\xi_0, q) = 0 \\ Se_l(\xi_0, q) = 0. \end{cases} \tag{7.15}$$

The eigenvalues associated to α and β are denoted by $q_r^e(\alpha)$ and $q_r^o(\beta)$, where the index o, e refers to the even and odd MMF and $r \geq 1$ is the rth zero of the MMF, not counting a possible root at $\xi = 0$. In the $q \times \alpha$ plane, the functions $q_r^e(\alpha)$ and $q_r^o(\beta)$ are curves that again do not intersect. The solution $\varphi(\xi,\eta)$ of the Schrödinger equation (7.9) is the product (7.10) of the OMF and MMF, both eigenvalue problems have to be solved simultaneously, since α (or β) and q in the OMF and MMF of the solution $\varphi(\xi,\eta)$ cannot be chosen independently. The pairs (α, q) (or (β, q)) that satisfy both eigenvalue problems simultaneously are of course the crossing points of the family of curves $\alpha_l(q)$ and $\beta_l(q)$ with the $q_r^e(\alpha)$ and $q_r^o(\beta)$. Thus, there are two types of crossing points that correspond to solutions of the simultaneous eigenvalues problem:

1. $\alpha_r(q)$ with $q_m^e(\alpha)$ (even modes)

2. $\beta_r(q)$ with $q_m^o(\beta)$ (odd modes)

As we will see later, these two types of crossing points are related to the symmetries of the solution $\varphi(\xi,\eta)$.

The eigenfunction $\varphi_{l,r}(\xi,\eta)$ can be split into even $(\varphi_{l,r}^e(\xi,\eta))$ and odd $(\varphi_{l,r}^e(\xi,\eta))$ modes (expect for $l = 0$):

$$\varphi_{l,r}^e(\xi,\eta) = Ce_l(\xi, q_{l,r}^e)ce_l(\eta, q_{l,r}^e) \tag{7.16a}$$

$$\varphi_{l,r}^o(\xi,\eta) = Se_l(\xi, q_{l,r}^o)se_l(\eta, q_{l,r}^o) \tag{7.16b}$$

By writing that q depends on l and r, we mean of course $q_{l,r}^e = q_r^e(\alpha_l)$ and correspondingly $q_{l,r}^o = q_r^o(\beta_l)$. The indices l and r are the angular and radial quantum number. l is the order of the OMF and r specifies the number of zeros of the MMF in the interval $\xi \in [0, \xi_0]$, not counting the zeros at the origin i.e. $q_{l,r}^{e,o}$ is the r-th zero of the MMF of order l. Since the MMF has to be zero at ξ_0, it follows that r is greater or equal to one. According to Eq. (7.12), the separation constant q is directly proportional to the energy and the energy eigenvalues $E^{e,o}_{l,r}$ corresponding to the eigenfunctions $\varphi^{e,o}_{l,r}(\xi,\eta)$ can be written as

$$E^{e,o}_{l,r} = \frac{2\hbar^2}{\mu f^2} q^{e,o}_{l,r} = \frac{2\hbar^2}{\mu a^2 \epsilon^2} q^{e,o}_{l,r}, \tag{7.17}$$

where ϵ is the eccentricity of the ellipse.

In elliptical coordinates, the second constant of motion (the product of the angular momenta around the two foci) is given by (for a derivation see Appendix A)

$$\tilde{F} = \mu^2 f^2 h^2 \left(\dot{\eta}^2 \sinh^2 \xi - \dot{\xi}^2 \sin^2 \eta\right), \tag{7.18}$$

or in terms of the canonical momenta (see Eq. (A.5) of Appendix A)

$$\tilde{F} = \frac{f^2}{h^2} \left(p_\eta^2 \sinh^2 \xi - p_\xi^2 \sin \eta\right), \tag{7.19}$$

where h is the metric factor (Eq. (A.4) of Appendix A) resulting from the transformation from Cartesian to elliptic coordinates. The definition of $\tilde{F}$ is slightly different from the one of $F(\phi,\alpha)$ in Eq. (2.11) for the discrete mapping. According to the definition of Eq. (7.19), $\tilde{F}$ is energy dependent, whereas $F(\phi,\alpha)$ in Eq. (2.11) is independent of the energy. Actually, $F(\phi,\alpha)$ can be obtained from $\tilde{F}$ by scaling out the energy, see Appendix A for details:

$$F = \frac{\tilde{F}}{2\mu E b^2} \tag{7.20}$$

The eigenvalue equation corresponding to the second constant of motion $\tilde{F}$ is obtained by substituting the momentum operators $p_\xi = -i\hbar\partial/\partial\xi$ and $p_\eta = -i\hbar\partial/\partial\eta$ in Eq. (7.19), this yields

$$\frac{f^2\hbar^2}{h^2}\left(\sin^2\eta \frac{\partial^2}{\partial\xi^2} - \sinh^2\xi \frac{\partial^2}{\partial\eta^2}\right)\varphi(\xi,\eta) = f'\varphi(\xi,\eta), \tag{7.21}$$

where f' is the corresponding eigenvalue. The separation ansatz $\varphi(\xi,\eta) = R(\xi)\Theta(\eta)$ (7.10) again results in two Mathieu equations (7.11), where the necessary separation constant C is related to the α and q by $\alpha = f'/\hbar^2 - C/2$ and $q = -C/4$. The eigenvalue equation for the Hamiltonian $H(\xi,\eta)$ (7.6) and the one for $\tilde{F}$ (7.21) are completely equivalent if f' is chosen such that $f' = (\alpha - 2q)\hbar^2$.

In other words, solving the coupled (via the separation constants α and q) Mathieu equations (7.11) corresponds to diagonalizing the Hamiltonian (7.6) and $\tilde{F}$ (7.19) simultaneously.

7.1 Symmetries

The symmetries of the eigenstates $\Psi^{e,o}_{l,r}(x,y)$ of the elliptical billiard are determined by the OMF $\Theta_l(\eta)$ (7.13) [147]. For an even OMF, i.e. for $ce_l(\eta)$, the wavefunction $\Psi^{e}_{l,r}(x,y)$ is symmetric with respect to the x-axis ($\Psi^{e}_{l,r}(x,y) = \Psi^{e}_{l,r}(x,-y)$), this symmetry is denoted by $\pi_y = +1$. Odd OMF $se_{l+1}(\eta)$ imply an antisymmetric eigenstate $\Psi^{o}_{l,r}(x,y)$ with respect to the x-axis ($\Psi^{e}_{l,r}(x,y) = -\Psi^{e}_{l,r}(x,-y)$), denoted by $\pi_y = -1$. The symmetry of $\Psi^{e,o}_{l,r}(x,y)$ with respect to the y-axis is fixed by the angular quantum number l, which is the order of

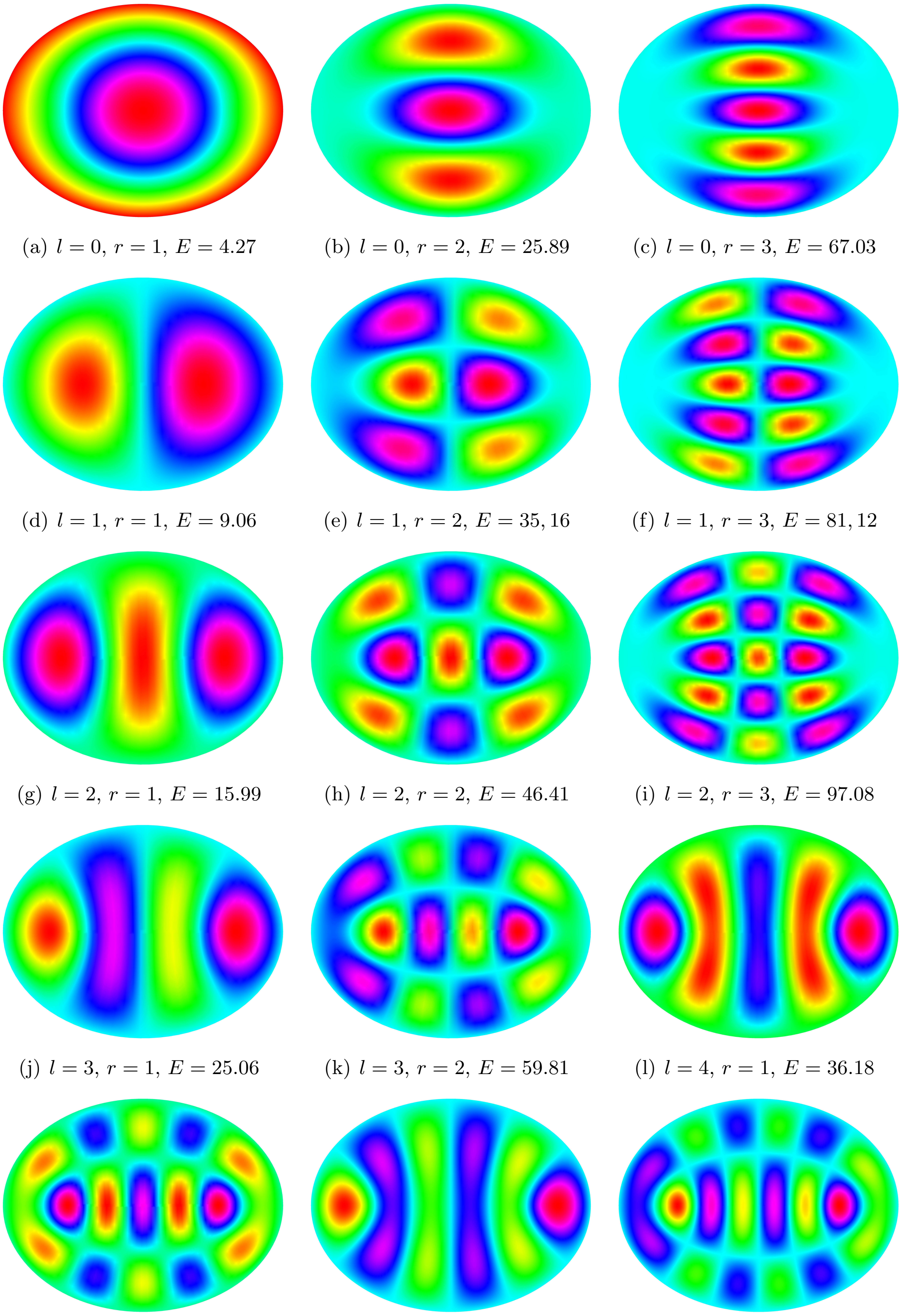

(a) $l = 0,\ r = 1,\ E = 4.27$ (b) $l = 0,\ r = 2,\ E = 25.89$ (c) $l = 0,\ r = 3,\ E = 67.03$

(d) $l = 1,\ r = 1,\ E = 9.06$ (e) $l = 1,\ r = 2,\ E = 35,16$ (f) $l = 1,\ r = 3,\ E = 81,12$

(g) $l = 2,\ r = 1,\ E = 15.99$ (h) $l = 2,\ r = 2,\ E = 46.41$ (i) $l = 2,\ r = 3,\ E = 97.08$

(j) $l = 3,\ r = 1,\ E = 25.06$ (k) $l = 3,\ r = 2,\ E = 59.81$ (l) $l = 4,\ r = 1,\ E = 36.18$

(m) $l = 4,\ r = 2,\ E = 75,53$ (n) $l = 5,\ r = 1,\ E = 49.20$ (o) $l = 5,\ r = 2,\ E = 93,66$

Figure 7.1: The first fifteen even eigenstates $\Psi^{e}_{l,r}(x, y)$ of the elliptical billiard (eccentricity $\epsilon = 0.7$) with energies smaller than 100 (in units of $\hbar^2/\mu$). The eigenstates are ordered according to l and r.

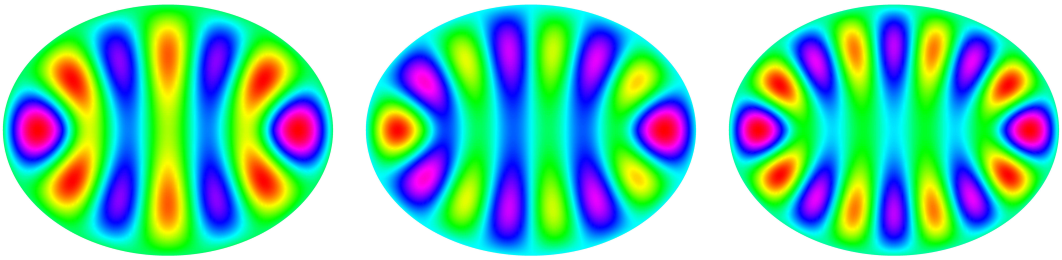

(a) $l = 6,\ r = 1,\ E = 63.95$ (b) $l = 7,\ r = 1,\ E = 80,29$ (c) $l = 8,\ r = 1,\ E = 98,14$

Figure 7.2: The subsequent three (compare with Fig. 7.1) even eigenstates $\Psi^e_{l,r}(x,y)$ of the elliptical billiard (eccentricity $\epsilon = 0.7$) with energies smaller than 100 (in units of $\hbar^2/\mu$). The eigenstates are ordered according to l and r.

the OMF. For even Mathieu functions, $\Psi^e_{l,r}(x,y)$ is symmetric to the y-axis ($\Psi^o_{l,r}(x,y) = \Psi^o_{l,r}(-x,y)$) if l is even and antisymmetric ($\Psi^o_{l,r}(x,y) = -\Psi^o_{l,r}(-x,y)$) if l is odd. Naturally, this symmetry is denoted by π_x. For odd Mathieu functions, it is just the other way around, $\Psi^o_{l,r}(x,y)$ is symmetric to the y-axis if l is odd and antisymmetric if l is even. Overall, this yields four possible combinations concerning the parity of the eigenstates $\Psi^{e,o}_{l,r}(x,y)$, which are summarized in the following list:

1. $\pi_y = +1,\ \pi_x = +1 \Rightarrow \Psi^e_{l,r}(x,y) = \Psi^e_{l,r}(-x,-y)$ even solutions with even l
2. $\pi_y = +1,\ \pi_x = -1 \Rightarrow \Psi^e_{l,r}(x,y) = -\Psi^e_{l,r}(-x,-y)$ even solutions with odd l
3. $\pi_y = -1,\ \pi_x = +1 \Rightarrow \Psi^o_{l,r}(x,y) = -\Psi^o_{l,r}(-x,-y)$ odd solutions with odd l
4. $\pi_y = -1,\ \pi_x = -1 \Rightarrow \Psi^o_{l,r}(x,y) = \Psi^o_{l,r}(-x,-y)$ odd solutions with even l

The four parity combinations correspond to the characterization of the symmetry reduced quarter elliptic billiard. However, the boundary conditions along the coordinate axes of the quarter billiard have to be adjusted according to the different parities: Dirichlet boundary conditions are required along the x-axis (y-axis) for $\pi_y = -1$ ($\pi_x = -1$) and Neumann boundary conditions along the x-axis (y-axis) for $\pi_y = +1$ ($\pi_x = +1$).

The first 31 eigenstates (in terms of the energy) $\varphi^{e,o}_{l,r}(\xi,\eta)$, or rather the corresponding $\Psi^{e,o}_{l,r}(x,y)$ are shown in Figs. 7.1-7.4. Figures 7.1 and 7.2 show the even solutions $\Psi^e_{l,r}(x,y)$, Figs. 7.3 and 7.4 the odd solutions $\Psi^o_{l,r}(x,y)$. Exemplarily, a pseudo 3D plot of $\Psi^o_{8,1}(x,y)$ is shown in Fig. 7.4b. A summary of all eigenstates with energies smaller than 100 (in units of $\hbar^2/\mu$) is provided in Table 7.1, together with the corresponding parities π_x and π_y, in perfect agreement with the results of Ref. [147].

Changing the eccentricity

Let's suppose we have solved the eigenvalue problem for a certain elliptical billiard with some a and b and obtained the corresponding energies $E^{e,o}_{l,r}$ associated with the eigenfunctions $\varphi^{e,o}_{l,r}(\xi,\eta)$. Now we can ask the question, if we take a different elliptical billiard with some a' and b', can we construct the solutions for this new billiard in a simple way from the solutions $\varphi^{e,o}_{l,r}(\xi,\eta)$ corresponding to the original billiard? Unfortunately, the answer is in general *no*, for the following reason. The eigenvalue condition for the MMF is determined

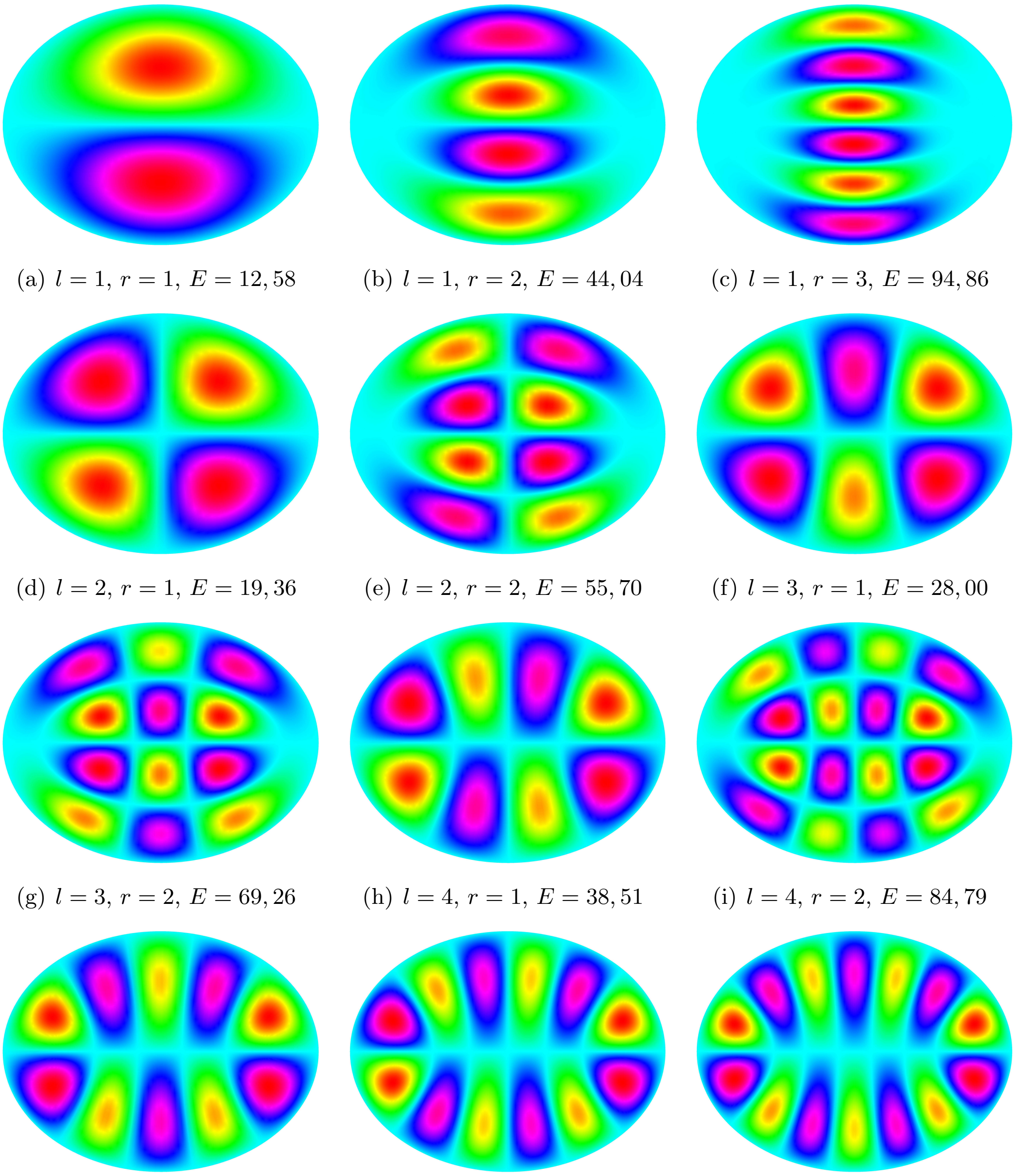

(a) $l = 1,\ r = 1,\ E = 12,58$ (b) $l = 1,\ r = 2,\ E = 44,04$ (c) $l = 1,\ r = 3,\ E = 94,86$

(d) $l = 2,\ r = 1,\ E = 19,36$ (e) $l = 2,\ r = 2,\ E = 55,70$ (f) $l = 3,\ r = 1,\ E = 28,00$

(g) $l = 3,\ r = 2,\ E = 69,26$ (h) $l = 4,\ r = 1,\ E = 38,51$ (i) $l = 4,\ r = 2,\ E = 84,79$

(j) $l = 5,\ r = 1,\ E = 50,87$ (k) $l = 6,\ r = 1,\ E = 65,02$ (l) $l = 7,\ r = 1,\ E = 80,91$

Figure 7.3: The first twelve odd eigenstates $\Psi^{o}_{l,r}(x, y)$ of the elliptical billiard (eccentricity $\epsilon = 0.7$) with energies smaller than 100 (in units of $\hbar^2/\mu$). The eigenstates are ordered according to l and r.

Table 7.1: All eigenstates $\Psi^{e,o}_{l,r}(x,y)$ of the elliptical billiard ($a = 1$, $b = \sqrt{0.51} \Rightarrow$ eccentricity $\epsilon = 0.7$) with $E < 100$ (in units of $\hbar^2/\mu$). The eigenstates are ordered according to the energy. π_y denotes the symmetry of $\Psi^{e,o}_{l,r}(x,y)$ with respect to the x-axis, π_x the symmetry with respect to the y-axis.

Nr.	$E[\hbar^2/\mu]$	l	r	even/odd	π_y	π_x
1	4,26746467296841	0	1	e	$+$	$+$
2	9,05833743989127	1	1	e	$+$	$-$
3	12,5767716183027	1	1	o	$-$	$+$
4	15,9932956100182	2	1	e	$+$	$+$
5	19,3575699486713	2	1	o	$-$	$-$
6	25,0613040235925	3	1	e	$+$	$-$
7	25,8946835562053	0	2	e	$+$	$+$
8	27,9978909472761	3	1	o	$-$	$+$
9	35,1559767684275	1	2	e	$+$	$-$
10	36,1778674132568	4	1	e	$+$	$+$
11	38,5107744066434	4	1	o	$-$	$-$
12	44,0403038439535	1	2	o	$-$	$+$
13	46,4063392523710	2	2	e	$+$	$+$
14	49,1994183129200	5	1	e	$+$	$-$
15	50,8690169646518	5	1	o	$-$	$+$
16	55,6991458568600	2	2	o	$-$	$-$
17	59,8105839847306	3	2	e	$+$	$-$
18	63,9521752887384	6	1	e	$+$	$+$
19	65,0221182986808	6	1	o	$-$	$-$
20	67,0300646884918	0	3	e	$+$	$+$
21	69,2568647336151	3	2	o	$-$	$+$
22	75,5269941628273	4	2	e	$+$	$+$
23	80,2913751675629	7	1	e	$+$	$-$
24	80,9097977192208	7	1	o	$-$	$+$
25	81,1161254257784	1	3	e	$+$	$-$
26	84,7927265920939	4	2	o	$-$	$-$
27	93,6561344912959	5	2	e	$+$	$-$
28	94,8599289049241	1	3	o	$-$	$+$
29	97,0765686826710	2	3	e	$+$	$+$
30	98,1446114315661	8	1	e	$+$	$+$
31	98,4730020452241	8	1	o	$-$	$-$

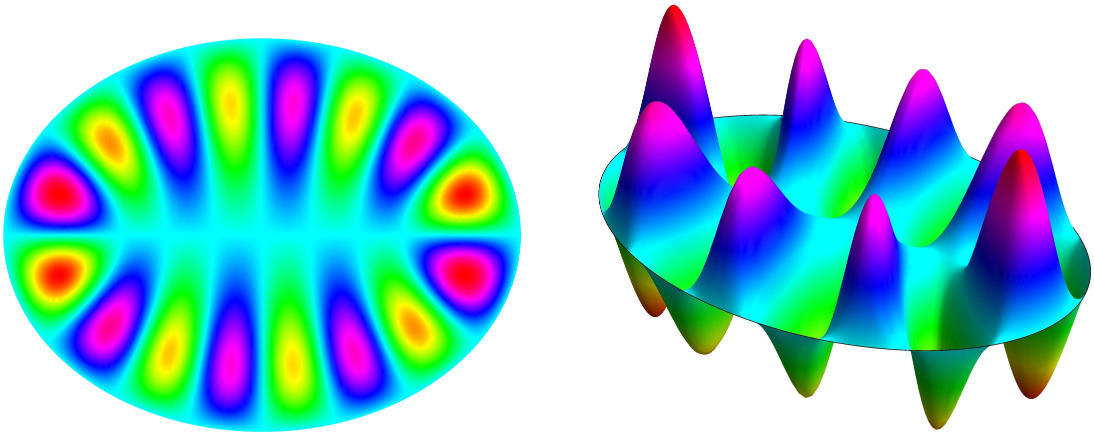

(a) $l = 8,\ r = 1,\ E = 98,47$ (b) $l = 8,\ r = 1,\ E = 98,47$

Figure 7.4: The remaining (compare with Fig. 7.3) odd eigenstate $\Psi^{o}_{8,1}(x,y)$ of the elliptical billiard with $E < 100$ (a). In (b), a pseudo 3D plot of $\Psi^{o}_{8,1}(x,y)$ is shown.

by the Dirichlet boundary condition $R_l(\xi_0) = 0$ (7.15) and $\xi_0 = \text{arctanh(b/a)}$. This means changing a and b results in a different ξ_0 and thus to a new eigenvalue problem. However, when a' and b' are chosen such that ratio of the axes stays constant, i.e. $a'/b' = a/b$, which is equivalent to leaving the eccentricity ϵ constant, the new eigenfunctions and energies are obtained from the old ones simply by replacing the semifocal distance $f = \sqrt{a^2 - b^2}$ by $\sqrt{a'^2 - b'^2}$.

8 Development of the numerical method for the driven elliptical billiard

To study the time evolution of a quantum mechanical initial state $\Psi_0(x,y) := \Psi(x,y,t=0)$ propagating in the harmonically oscillating elliptical billiard, we have to solve the time-dependent Schrödinger equation

$$i\hbar \frac{\partial \Psi(x,y,t)}{\partial t} = H(x,y,t)\Psi(x,y,t), \tag{8.1}$$

where the Hamiltonian $H(x,y,t)$ is given by

$$H(x,y,t) = -\frac{\hbar^2}{2\mu}\left(\frac{\partial^2}{\partial x^2} + \frac{\partial^2}{\partial y^2}\right) + V(x,y,t) \tag{8.2}$$

and the potential $V(x,y,t)$ is zero inside and infinity outside the time-dependent elliptical billiard:

$$V(x,y,t) = \begin{cases} 0 & \text{if } \frac{x^2}{a^2(t)} + \frac{y^2}{b^2(t)} \leq 1 \\ \infty & \text{if } \frac{x^2}{a^2(t)} + \frac{y^2}{b^2(t)} > 1. \end{cases} \tag{8.3}$$

This means the Schrödinger equation (8.1) has to be solved under Dirichlet boundary conditions

$$\Psi(x,y,t) = 0 \quad \text{for} \quad \left\{ (x,y)^\top \in \mathbb{R}^2 \middle| \frac{x^2}{a^2(t)} + \frac{y^2}{b^2(t)} = 1, \, \forall t \right\}, \tag{8.4}$$

where $a(t)$ and $b(t)$ are determined by the driving law of the elliptical billiard. Here, the geometry of the ellipse comes into play, the wave function Ψ has to vanish on the boundary of the time-dependent ellipse.

8.1 Transformations

8.1.1 Time-dependent coordinate transformation

The explicit time-dependence of the boundary conditions is very difficult, if not impossible to treat with standard numerical techniques. To remove the explicit time-dependence of the boundary conditions, we apply the following time-dependent coordinate transformation, whose 1D variant has been successfully used to remove time-dependent boundary conditions [91, 93–95, 99–102] in 1D systems

$$\eta = \frac{x}{a(t)}, \quad \xi = \frac{y}{b(t)} \Rightarrow \Psi(\eta,\xi,t) = 0 \text{ for } \left\{ (\eta,\xi)^\top \in \mathbb{R}^2 \middle| \eta^2 + \xi^2 = 1, \, \forall t \right\}, \tag{8.5}$$

yielding the time-dependent Schrödinger equation

$$i\hbar\frac{\partial\Psi(\eta(t),\xi(t),t)}{\partial t} = H(\eta(t),\xi(t),t)\Psi(\eta(t),\xi(t),t). \tag{8.6}$$

The advantage of applying this time-dependent coordinate transformation is that the boundary condition in the new coordinates η, ξ is extremely simple, the wave function $\Psi(\eta,\xi,t)$ has to vanish on the circle given by $\eta^2+\xi^2=1$. The prize we have to pay for is that now the coordinates themselves are time-dependent, $\eta=\eta(t)$ and $\xi=\xi(t)$, i.e. the wave function is of the form $\Psi(\eta(t),\xi(t),t)$. This has to be taken into account when applying the differential operator $\partial/\partial t$ on $\Psi(\eta(t),\xi(t),t)$ in the time-dependent Schrödinger equation (8.6). This can be done by writing

$$\frac{\partial\Psi(\eta(t),\xi(t),t)}{\partial t} = \frac{\partial\Psi}{\partial\eta}\frac{\partial\eta(t)}{\partial t} + \frac{\partial\Psi}{\partial\xi}\frac{\partial\xi(t)}{\partial t} + \left.\frac{\partial\Psi(\eta,\xi,t)}{\partial t}\right|_{\eta,\xi=const.} \tag{8.7}$$

With Eq. (8.5) we have

$$\frac{\partial\eta(t)}{\partial t} = \frac{\partial}{\partial t}\frac{x}{a(t)} = -\frac{x\dot{a}(t)}{a^2(t)} = -\eta(t)\frac{\dot{a}(t)}{a(t)} \tag{8.8}$$

and correspondingly $\partial\xi(t)/\partial t = -\xi(t)\dot{b}(t)/b(t)$. With the coordinate transformation given by (8.5), we can define the effective Hamiltonian as

$$H^e(\eta,\xi,t) = -\frac{\hbar^2}{2\mu}\left(\frac{1}{a^2(t)}\frac{\partial^2}{\partial\eta^2} + \frac{1}{b^2(t)}\frac{\partial^2}{\partial\xi^2}\right) + i\hbar\left(\frac{\dot{a}(t)}{a(t)}\eta\frac{\partial}{\partial\eta} + \frac{\dot{b}(t)}{b(t)}\xi\frac{\partial}{\partial\xi}\right). \tag{8.9}$$

and the corresponding time-dependent Schrödinger equation is

$$i\hbar\left.\frac{\partial\Psi(\eta,\xi,t)}{\partial t}\right|_{\eta,\xi=const.} = H^e(\eta,\xi,t)\Psi(\eta,\xi,t). \tag{8.10}$$

We call the Hamiltonian (8.9) *effective*, since it absorbs the additional terms, see Eq. (8.7) and (8.8), resulting from the time-dependence of η and ξ when applying the partial derivative $\partial/\partial t$ to the left hand side of Eq. (8.6). This is why in the 'new' Schrödinger equation (8.10), containing the effective Hamiltonian H^e, the coordinates η and ξ can be treated as constant when calculating the partial derivative $\partial/\partial t$ on the left hand side of Eq. (8.10).

These additional terms make the effective Hamiltonian H^e non-Hermitian. This can be easily seen, we just have to calculate whether $\langle f|\,\hat{A}\,|g\rangle = \langle g|\,\hat{A}\,|f\rangle^*$, where $\hat{A} = i\hbar x\frac{\partial}{\partial x}$ with arbitrary test functions f and g (the first part of the Hamiltonian (8.9) is Hermitian and $\dot{a}/a$ and $\dot{b}/b$ are just real numbers, so the above defined $\hat{A}$ is the only part that needs to be investigated):

$$\begin{aligned}\langle f|\,\hat{A}\,|g\rangle &= \int f^*\hat{A}g dx = \int f^* i\hbar x\frac{\partial}{\partial x}g dx = i\hbar f^*g\Big|_{x_1}^{x_2} - i\hbar\int g\frac{\partial}{\partial x}\left(f^*x\right)dx = \\ &= -i\hbar\int gx\frac{\partial}{\partial x}f^*dx - i\hbar\int gf^*dx = \left(i\hbar\int g^*x\frac{\partial}{\partial x}f dx\right)^* + \left(i\hbar\int g^*f dx\right)^*\end{aligned} \tag{8.11}$$

$$\Rightarrow \langle f|\,\hat{A}\,|g\rangle = \langle g|\,\hat{A}\,|f\rangle^* + \langle g|f\rangle\,, \tag{8.12}$$

where we assume that the boundary term $i\hbar f^* g\big|_{x_1}^{x_2}$ vanishes.

8.1.2 Unitary transformation

To remove the terms $i\hbar\eta\frac{\partial}{\partial\eta}$ and $i\hbar\xi\frac{\partial}{\partial\xi}$ and at the same time make the effective Hamiltonian Hermitian, we apply the following time-dependent unitary transformation

$$\Psi(\eta,\xi,t) = \Omega(\eta,t)\cdot\Upsilon(\xi,t)\cdot\Lambda(\eta,\xi,t) \tag{8.13}$$

$$\Omega(\eta,t) = \sqrt{\frac{2}{a(t)}}\exp\left(\frac{i\mu}{2\hbar}\dot{a}(t)a(t)\eta^2\right) \tag{8.14}$$

$$\Upsilon(\xi,t) = \sqrt{\frac{2}{b(t)}}\exp\left(\frac{i\mu}{2\hbar}\dot{b}(t)b(t)\xi^2\right) \tag{8.15}$$

$$\Rightarrow \Psi(\eta,\xi,t) = \frac{2}{\sqrt{ab}}\exp\left(\frac{i\mu}{2\hbar}(\dot{a}a\eta^2+\dot{b}b\xi^2)\right)\cdot\Lambda(\eta,\xi,t). \tag{8.16}$$

With this transformation we finally obtain the Schrödinger equation

$$i\hbar\frac{\partial\Lambda(\eta,\xi,t)}{\partial t} = \mathcal{H}(\eta,\xi,t)\Lambda(\eta,\xi,t), \tag{8.17}$$

with the effective Hamiltonian

$$\mathcal{H}(\eta,\xi,t) = -\frac{\hbar^2}{2\mu}\left(\frac{1}{a^2(t)}\frac{\partial^2}{\partial\eta^2}+\frac{1}{b^2(t)}\frac{\partial^2}{\partial\xi^2}\right)+\frac{1}{2}\mu a(t)\ddot{a}(t)\eta^2+\frac{1}{2}\mu b(t)\ddot{b}(t)\xi^2 \tag{8.18}$$

and the time-independent boundary conditions of Eq. (8.5). This Hamiltonian can be interpreted as a two-dimensional anisotropic harmonic oscillator with time-dependent frequencies and time-dependent masses whose wave function has to vanish on the unit circle.

8.1.3 Transformation to polar coordinates

Since the wave function $\Lambda(\eta,\xi,t)$ has to vanish on the unit circle $\eta^2+\xi^2=1$, we expand $\Lambda(\eta,\xi,t)$ in terms of the eigenfunctions $\Phi_{n,m}$ of the (unit) static circular billiard, then we automatically fullfill this boundary condition. The eigenfunctions $\Phi_{n,m}$ of the static circular billiard are best described in polar coordinates, so we transform η and ξ to polar coordinates:

$$\eta = r\cos\phi \qquad \xi = r\sin\phi \quad \Rightarrow \Lambda(r,\phi,t) = 0 \text{ for } r=1, \tag{8.19}$$

yielding the extremely simple boundary condition $\Lambda(r=1,\phi,t)=0$, $\forall\phi,t$. To obtain the Hamiltonian (8.18) in polar coordinates, we cannot simply use the standard expression for the Laplacian in polar coordinates, since $\partial^2/\partial\eta^2$ and $\partial^2/\partial\xi^2$ have different prefactors, so e.g. the mixed terms $\partial^2/\partial\xi\partial\eta$ do not cancel. The inverse of the transformation (8.19) is of course

$$r = \sqrt{\eta^2+\xi^2}, \quad \phi = \arctan\frac{\xi}{\eta}. \tag{8.20}$$

For an arbitrary function $f(r,\phi)=f(r(\eta,\xi),\phi(\eta,\xi))$, the partial derivatives $\partial/\partial\eta$ and $\partial/\partial\xi$ are calculated using the chain rule

$$\begin{aligned}\frac{\partial f(r,\phi)}{\partial\eta}&=\frac{\partial f(r,\phi)}{\partial r}\frac{\partial r}{\partial\eta}+\frac{\partial f(r,\phi)}{\partial\phi}\frac{\partial\phi}{\partial\eta}\\ \frac{\partial f(r,\phi)}{\partial\xi}&=\frac{\partial f(r,\phi)}{\partial r}\frac{\partial r}{\partial\xi}+\frac{\partial f(r,\phi)}{\partial\phi}\frac{\partial\phi}{\partial\xi}\end{aligned}$$

and

$$\begin{aligned}\frac{\partial r}{\partial\eta}&=\cos\phi & \frac{\partial\phi}{\partial\eta}&=-\frac{\sin\phi}{r}\\ \frac{\partial r}{\partial\xi}&=\sin\phi & \frac{\partial\phi}{\partial\xi}&=\frac{\cos\phi}{r},\end{aligned}$$

yielding

$$\frac{\partial}{\partial\eta}=\cos\phi\frac{\partial}{\partial r}-\frac{\sin\phi}{r}\frac{\partial}{\partial\phi} \tag{8.21}$$

$$\frac{\partial}{\partial\xi}=\sin\phi\frac{\partial}{\partial r}+\frac{\cos\phi}{r}\frac{\partial}{\partial\phi}. \tag{8.22}$$

Accordingly, the second derivatives $\partial^2/\partial\eta^2$ and $\partial^2/\partial\xi^2$ can be obtained and the Hamiltonian (8.18) in polar coordinates then reads

$$\begin{aligned}\mathcal{H}(r,\phi,t)=&-\frac{\hbar^2}{2\mu a^2(t)}\left(\sin^2\phi\frac{\partial^2}{\partial r^2}-\frac{2\sin\phi\cos\phi}{r^2}\frac{\partial}{\partial\phi}+\frac{2\sin\phi\cos\phi}{r}\frac{\partial^2}{\partial r\partial\phi}\right.\\ &\left.+\frac{\cos^2\phi}{r}\frac{\partial}{\partial r}+\frac{\cos^2\phi}{r^2}\frac{\partial^2}{\partial\phi^2}\right)-\frac{\hbar^2}{2\mu b^2(t)}\left(\cos^2\phi\frac{\partial^2}{\partial r^2}+\frac{2\sin\phi\cos\phi}{r^2}\frac{\partial}{\partial\phi}\right.\\ &\left.-\frac{2\sin\phi\cos\phi}{r}\frac{\partial^2}{\partial r\partial\phi}+\frac{\sin^2\phi}{r}\frac{\partial}{\partial r}+\frac{\sin^2\phi}{r^2}\frac{\partial^2}{\partial\phi^2}\right)+\frac{1}{2}\mu a(t)\ddot{a}(t)r^2\cos^2\phi+\frac{1}{2}\mu b(t)\ddot{b}(t)r^2\sin^2\phi\end{aligned} \tag{8.23}$$

and the corresponding Schrödinger equation is

$$i\hbar\frac{\partial\Lambda(r,\phi,t)}{\partial t}=\mathcal{H}(r,\phi,t)\Lambda(r,\phi,t). \tag{8.24}$$

Ansatz

Since the boundary conditions of Eq. (8.19) correspond to Dirichlet boundary conditions on a circle, we make an ansatz and expand the wave function in terms of the eigenfunctions $\Phi_{n,m}(r,\phi)$ of the static circular billiard:

$$\Lambda(r,\phi,t)=\sum_{n=1}^{N}\sum_{m=-M}^{M}c_{n,m}(t)\Phi_{n,m}(r,\phi), \tag{8.25}$$

with time-dependent expansion coefficients $c_{n,m}(t)$, where n is the radial and m the azimuthal quantum number. The time-independent eigenfunctions $\Phi_{n,m}(r,\phi)$ of the static circular billiard factorize

$$\Phi_{n,m}(r,\phi) = R_{n,m}(r) \cdot \Theta_m(\phi) \tag{8.26}$$

and the normalized radial and azimuthal (angular) functions are given by [150, 151]

$$R_{n,m}(r) = \frac{\sqrt{2}}{J_{m+1}(k_{n,m})} J_m(k_{m,n}r) \tag{8.27}$$

$$\Theta_m(\phi) = \frac{1}{\sqrt{2\pi}} e^{im\phi} \tag{8.28}$$

$$\Rightarrow \Phi_{n,m}(r,\phi) = \frac{1}{\sqrt{\pi} J_{m+1}(k_{m,n})} J_m(k_{m,n}r) e^{im\phi}, \tag{8.29}$$

where J_m is the Bessel function of the first kind of order m and $k_{m,n}$ is the nth zero of J_m.

To determine the time-dependent expansion coefficients $c_{n,m}(t)$, we insert the ansatz (8.25) into the time-dependent Schrödinger equation (8.24), project it on the bra $\langle\Lambda|$ and thus obtain a set of coupled differential equations for the $c_{n,m}(t)$

$$\langle\Lambda| i\hbar \frac{\partial}{\partial t} |\Lambda\rangle = \langle\Lambda| \mathcal{H}(t) |\Lambda\rangle . \tag{8.30}$$

We first calculate the left hand side of Eq. (8.30) in the r, ϕ representation and get

$$\begin{aligned}\langle\Lambda| i\hbar \frac{\partial}{\partial t} |\Lambda\rangle &= i\hbar \int_0^1 rdr \int_0^{2\pi} d\phi \sum_{n,m,n',m'} c^*_{n,m}(t)\dot{c}_{n',m'}(t)\Phi^*_{n,m}(r,\phi)\Phi_{n',m'}(r,\phi) \\ &= i\hbar \sum_{n,m,n',m'} c^*_{n,m}(t)\dot{c}_{n',m'}(t) \int_0^1 rdr \int_0^{2\pi} d\phi \Phi^*_{n,m}(r,\phi)\Phi_{n',m'}(r,\phi) = \\ &= i\hbar \sum_{n,m,n',m'} c^*_{n,m}(t)\dot{c}_{n',m'}(t)\delta_{nn'}\delta_{mm'} = i\hbar \sum_{n,m} c^*_{n,m}(t)\dot{c}_{n,m}(t),\end{aligned} \tag{8.31}$$

where $\dot{c}$ denotes the derivative with respect to t and we have used the orthogonality relation for Bessel functions

$$\int_0^1 J_m(k_{m,n}r)J_m(k_{m,n'}r)rdr = \frac{\delta_{n,n'}}{2}[J_{m+1}(k_{m,n}r)]^2 \tag{8.32}$$

and the orthogonality relation for the angular part

$$\int_0^{2\pi} e^{im\phi}e^{im'\phi} = 2\pi\delta_{m,m'}. \tag{8.33}$$

Calculating the right hand side of Eq. (8.30), i.e. $\langle\Lambda| \mathcal{H}(t) |\Lambda\rangle$, is much more involved. To make the procedure clearly arranged, we first split the Hamiltonian into parts

$$\mathcal{H}(r,\phi,t) = \sum_{i=1}^{12} \mathcal{H}_i(r,\phi,t), \tag{8.34}$$

where the $\mathcal{H}_i(r,\phi,t)$ are given by

$$\begin{aligned}
\mathcal{H}_1(r,\phi,t) &= -\frac{\hbar^2}{2\mu a^2(t)}\sin^2\phi\frac{\partial^2}{\partial r^2} && (8.35a)\\
\mathcal{H}_2(r,\phi,t) &= \frac{\hbar^2}{2\mu a^2(t)}\frac{2\sin\phi\cos\phi}{r^2}\frac{\partial}{\partial\phi} && (8.35b)\\
\mathcal{H}_3(r,\phi,t) &= -\frac{\hbar^2}{2\mu a^2(t)}\frac{2\sin\phi\cos\phi}{r}\frac{\partial^2}{\partial r\partial\phi} && (8.35c)\\
\mathcal{H}_4(r,\phi,t) &= -\frac{\hbar^2}{2\mu a^2(t)}\frac{\cos^2\phi}{r}\frac{\partial}{\partial r} && (8.35d)\\
\mathcal{H}_5(r,\phi,t) &= -\frac{\hbar^2}{2\mu a^2(t)}\frac{\cos^2\phi}{r^2}\frac{\partial^2}{\partial\phi^2} && (8.35e)\\
\mathcal{H}_6(r,\phi,t) &= -\frac{\hbar^2}{2\mu b^2(t)}\cos^2\phi\frac{\partial^2}{\partial r^2} && (8.35f)\\
\mathcal{H}_7(r,\phi,t) &= -\frac{\hbar^2}{2\mu b^2(t)}\frac{2\sin\phi\cos\phi}{r^2}\frac{\partial}{\partial\phi} && (8.35g)\\
\mathcal{H}_8(r,\phi,t) &= \frac{\hbar^2}{2\mu b^2(t)}\frac{2\sin\phi\cos\phi}{r}\frac{\partial^2}{\partial r\partial\phi} && (8.35h)\\
\mathcal{H}_9(r,\phi,t) &= -\frac{\hbar^2}{2\mu b^2(t)}\frac{\sin^2\phi}{r}\frac{\partial}{\partial r} && (8.35i)\\
\mathcal{H}_{10}(r,\phi,t) &= -\frac{\hbar^2}{2\mu b^2(t)}\frac{\sin^2\phi}{r^2}\frac{\partial^2}{\partial\phi^2} && (8.35j)\\
\mathcal{H}_{11}(r,\phi,t) &= \frac{1}{2}\mu a(t)\ddot{a}(t)r^2\cos^2\phi && (8.35k)\\
\mathcal{H}_{12}(r,\phi,t) &= \frac{1}{2}\mu b(t)\ddot{b}(t)r^2\sin^2\phi. && (8.35l)
\end{aligned}$$

The right hand side of Eq. (8.30) then also splits into parts

$$\langle\Lambda|\,\mathcal{H}(t)\,|\Lambda\rangle = \sum_{i=1}^{12}\langle\Lambda|\,\mathcal{H}_i(t)\,|\Lambda\rangle\,. \tag{8.36}$$

Now, we exemplarily calculate $\langle\Lambda|\,\mathcal{H}_1(t)\,|\Lambda\rangle$, the other matrix elements are given in Appendix B.1

$$\begin{aligned}
&\langle\Lambda|\,\mathcal{H}_1\,|\Lambda\rangle = \\
&\frac{-\hbar^2}{2\mu a^2(t)}\int_0^1 rdr\int_0^{2\pi}d\phi\sum_{n,n'=1}^{N}\sum_{m,m'=-M}^{M}c^*_{n,m}(t)c_{n',m'}(t)\Phi^*_{n,m}(r,\phi)\sin^2\phi\frac{\partial^2}{\partial r^2}\Phi_{n',m'}(r,\phi)\\
&\qquad = \frac{-\hbar^2}{\mu a^2(t)}\sum_{n,m,n',m'}\frac{c^*_{n,m}(t)c_{n',m'}(t)}{J_{m+1}(k_{m,n})J_{m'+1}(k_{m',n'})}\int J_m(k_{m,n}r)J''_{m'}(k_{m',n'}r)rdr\\
&\qquad\qquad\qquad\qquad \frac{1}{2\pi}\int\sin^2\phi\, e^{i\phi(m'-m)}d\phi = \ldots\int J_m(k_{m,n}r)J''_{m'}(k_{m',n'}r)rdr
\end{aligned}$$

$$\begin{aligned}\left(\frac{1}{2}\delta_{m',m}-\frac{1}{4}\delta_{m'+2,m}-\frac{1}{4}\delta_{m'-2,m}\right) &= \frac{-\hbar^2}{2\mu a^2(t)}\sum_{n,m,n'}\frac{c^*_{n,m}(t)}{J_{m+1}(k_{m,n})}\\ &\int\left(\frac{c_{n',m}(t)J_m(k_{m,n}r)J''_m(k_{m,n'}r)}{2J_{m+1}(k_{m,n'})}-\frac{c_{n',m+2}(t)J_m(k_{m,n}r)J''_{m+2}(k_{m+2,n'}r)}{4J_{m+1}(k_{m+2,n'})}\right.\\ &\left.-\frac{c_{n',m-2}(t)J_m(k_{m,n}r)J''_{m-2}(k_{m-2,n'}r)}{4J_{m-1}(k_{m-2,n'})}\right)rdr,\end{aligned} \tag{8.37}$$

where the double prime denotes the derivative with respect to r, i.e. $J''(r) = \partial^2 J(r)/\partial r^2$. The radial integrals appearing in the matrix element (8.37) cannot be calculated analytically. Overall, the following 12 integrals occur when considering all 12 matrix elements of Eq. (8.36):

$$I^1_{nmn'} := \int_0^1 J_m(k_{m,n}r)J''_m(k_{m,n'}r)rdr \qquad I^2_{nmn'} := \int_0^1 J_m(k_{m,n}r)J''_{m+2}(k_{m+2,n'}r)rdr \tag{8.38}$$

$$I^3_{nmn'} := \int_0^1 J_m(k_{m,n}r)J''_{m-2}(k_{m-2,n'}r)rdr \qquad I^4_{nmn'} := \int_0^1 J_m(k_{m,n}r)J_m(k_{m,n'}r)r^{-1}dr \tag{8.39}$$

$$I^5_{nmn'} := \int_0^1 J_m(k_{m,n}r)J_{m-2}(k_{m-2,n'}r)\frac{dr}{r} \qquad I^6_{nmn'} := \int_0^1 J_m(k_{m,n}r)J_{m+2}(k_{m+2,n'}r)\frac{dr}{r} \tag{8.40}$$

$$I^7_{nmn'} := \int_0^1 J_m(k_{m,n}r)J'_m(k_{m,n'}r)dr \qquad I^8_{nmn'} := \int_0^1 J_m(k_{m,n}r)J'_{m+2}(k_{m+2,n'}r)dr \tag{8.41}$$

$$I^9_{nmn'} := \int_0^1 J_m(k_{m,n}r)J'_{m-2}(k_{m-2,n'}r)dr \qquad I^{10}_{nmn'} := \int_0^1 J_m(k_{m,n}r)J_m(k_{m,n'}r)r^3dr \tag{8.42}$$

$$I^{11}_{nmn'} := \int_0^1 J_m(k_{m,n}r)J_{m+2}(k_{m+2,n'}r)r^3dr \qquad I^{12}_{nmn'} := \int_0^1 J_m(k_{m,n}r)J_{m-2}(k_{m-2,n'}r)r^3dr. \tag{8.43}$$

Since we have to evaluate these integrals numerically, it is convenient to eliminate the derivatives $J'(r)$, $J''(r)$ and the $1/r$ singularity. This can be done by using the following basic relations for Bessel functions:

$$J'_p(r) = J_{p-1}(r) - \frac{p}{r}J_p(r) \tag{8.44}$$

$$\frac{1}{r}J_p(r) = \frac{1}{2p}\left(J_{p-1}(r) + J_{p+1}(r)\right). \tag{8.45}$$

Combining these two relations and using the chain rule we obtain:

$$J'_p(kr) = \frac{k}{2}\left(J_{p-1}(kr) - J_{p+1}(kr)\right) \tag{8.46}$$

$$J_p''(kr) = \frac{k^2}{4}\left(J_{p-2}(kr) - 2J_p(kr) + J_{p+2}(kr)\right) \tag{8.47}$$

$$\frac{1}{r}J_p(kr) = \frac{k}{2p}\left(J_{p-1}(kr) + J_{p+1}(kr)\right). \tag{8.48}$$

With these three relations, the integrals in Eqs. (8.38)-(8.43) can be written as

$$\begin{aligned}
I^1_{nmn'} &= \frac{k^2_{n',m}}{4}\int_0^1 J_m(k_{m,n}r)\left[J_{m-2}(k_{m,n'}r) - 2J_m(k_{m,n'}r) + J_{m+2}(k_{m,n'}r)\right] rdr\\
I^2_{nmn'} &= \frac{k^2_{n',m+2}}{4}\int_0^1 J_m(k_{m,n}r)\left[J_{m}(k_{m+2,n'}r) - 2J_{m+2}(k_{m+2,n'}r) + J_{m+4}(k_{m+2,n'}r)\right] rdr\\
I^3_{nmn'} &= \frac{k^2_{n',m-2}}{4}\int_0^1 J_m(k_{m,n}r)\left[J_{m-4}(k_{m-2,n'}r) - 2J_{m-2}(k_{m-2,n'}r) + J_{m}(k_{m-2,n'}r)\right] rdr\\
I^4_{nmn'} &= \frac{k_{m,n'}}{2m}\int_0^1 J_m(k_{m,n}r)\left[J_{m-1}(k_{m,n'}r) + J_{m+1}(k_{m,n'}r)\right] dr\\
I^5_{nmn'} &= \frac{k_{m-2,n'}}{2(m-2)}\int_0^1 J_m(k_{m,n}r)\left[J_{m-3}(k_{m-2,n'}r) + J_{m-1}(k_{m-2,n'}r)\right] dr\\
I^6_{nmn'} &= \frac{k_{m+2,n'}}{2(m+2)}\int_0^1 J_m(k_{m,n}r)\left[J_{m+1}(k_{m+2,n'}r) + J_{m+3}(k_{m+2,n'}r)\right] dr\\
I^7_{nmn'} &= \frac{k_{m,n'}}{2}\int_0^1 J_m(k_{m,n}r)\left[J_{m-1}(k_{m,n'}r) - J_{m+1}(k_{m,n'}r)\right] dr\\
I^8_{nmn'} &= \frac{k_{m+2,n'}}{2}\int_0^1 J_m(k_{m,n}r)\left[J_{m+1}(k_{m+2,n'}r) - J_{m+3}(k_{m+2,n'}r)\right] dr\\
I^9_{nmn'} &= \frac{k_{m-2,n'}}{2}\int_0^1 J_m(k_{m,n}r)\left[J_{m-3}(k_{m-2,n'}r) - J_{m-1}(k_{m-2,n'}r)\right] dr\\
I^{10}_{nmn'} &= \int_0^1 J_m(k_{m,n}r)J_m(k_{m,n'}r)r^3dr\\
I^{11}_{nmn'} &= \int_0^1 J_m(k_{m,n}r)J_{m+2}(k_{m+2,n'}r)r^3dr\\
I^{12}_{nmn'} &= \int_0^1 J_m(k_{m,n}r)J_{m-2}(k_{m-2,n'}r)r^3dr
\end{aligned}$$

With the following abbreviations, we have to calculate effectively 18 different basic integrals numerically:

$$\begin{aligned}
L^1_{nmn'} &:= \int_0^1 J_m(k_{m,n}r)J_{m-2}(k_{m,n'}r)rdr & L^2_{nmn'} &:= \int_0^1 J_m(k_{m,n}r)J_{m}(k_{m,n'}r)rdr\\
L^3_{nmn'} &:= \int_0^1 J_m(k_{m,n}r)J_{m+2}(k_{m,n'}r)rdr & L^4_{nmn'} &:= \int_0^1 J_m(k_{m,n}r)J_{m}(k_{m+2,n'}r)rdr\\
L^5_{nmn'} &:= \int_0^1 J_m(k_{m,n}r)J_{m+2}(k_{m+2,n'}r)rdr & L^6_{nmn'} &:= \int_0^1 J_m(k_{m,n}r)J_{m+4}(k_{m+2,n'}r)rdr\\
L^7_{nmn'} &:= \int_0^1 J_m(k_{m,n}r)J_{m-4}(k_{m-2,n'}r)rdr & L^8_{nmn'} &:= \int_0^1 J_m(k_{m,n}r)J_{m-2}(k_{m-2,n'}r)rdr
\end{aligned}$$

$$
\begin{aligned}
L^9_{nmn'} &:= \int_0^1 J_m(k_{m,n}r)J_m(k_{m-2,n'}r)rdr & L^{10}_{nmn'} &:= \int_0^1 J_m(k_{m,n}r)J_{m-1}(k_{m,n'}r)dr\\
L^{11}_{nmn'} &:= \int_0^1 J_m(k_{m,n}r)J_{m+1}(k_{m,n'}r)dr & L^{12}_{nmn'} &:= \int_0^1 J_m(k_{m,n}r)J_{m-3}(k_{m-2,n'}r)dr\\
L^{13}_{nmn'} &:= \int_0^1 J_m(k_{m,n}r)J_{m-1}(k_{m-2,n'}r)dr & L^{14}_{nmn'} &:= \int_0^1 J_m(k_{m,n}r)J_{m+1}(k_{m+2,n'}r)dr\\
L^{15}_{nmn'} &:= \int_0^1 J_m(k_{m,n}r)J_{m+3}(k_{m+2,n'}r)dr & L^{16}_{nmn'} &:= \int_0^1 J_m(k_{m,n}r)J_m(k_{m,n'}r)r^3dr\\
L^{17}_{nmn'} &:= \int_0^1 J_m(k_{m,n}r)J_{m+2}(k_{m+2,n'}r)r^3dr & L^{18}_{nmn'} &:= \int_0^1 J_m(k_{m,n}r)J_{m-2}(k_{m-2,n'}r)r^3dr.
\end{aligned}
$$

How the $L^i_{nmn'}$ are related to the $I^i_{nmn'}$, see Appendix B.2.

With the definition of the $I^i_{nmn'}$, the matrix elements of Eq. (8.36) can be written considerably shorter, for example the matrix element $\langle\Lambda|\,\mathcal{H}_1\,|\Lambda\rangle$ reads

$$
\begin{aligned}
\langle\Lambda|\,\mathcal{H}_1\,|\Lambda\rangle = \frac{-\hbar^2}{\mu a^2(t)}\sum_{n,m,n'}\frac{c^*_{nm}(t)}{J_{m+1}(k_{m,n})}\Bigg(&\frac{c_{n'm}(t)}{2J_{m+1}(k_{n'm})}I^1_{nmn'}\\
&-\frac{c_{n',m-2}(t)}{4J_{m-1}(k_{m-2,n'})}I^3_{nmn'}-\frac{c_{n',m+2}(t)}{4J_{m+3}(k_{m+2,n'})}I^2_{nmn'}\Bigg). \qquad (8.49)
\end{aligned}
$$

The other matrix elements are given in appendix B.3.

Now back to the system of the coupled ordinary differential equations (ODE) (8.30) for the time-dependent expansion coefficients $c_{n,m}(t)$. The left hand side of Eq. (8.30), which is given by Eq. (8.31), contains a double sum over n and m, the right hand side of Eq. (8.30) a sum over m, n and n'. Since all the $c_{n,m}(t)$ are independent and the relation in Eq. (8.30) holds for all times t, Eq. (8.30) has to be valid not only for the sum, but for a fixed pair of m and n already. The system of coupled ODEs for the $c_{n,m}(t)$ can then be written as:

$$
i\hbar\dot{c}_{n,m}(t) = \sum_{n'}\left\{c_{n',m}(t)d^1_{nmn'}(t) + c_{n',m-2}(t)d^2_{nmn'}(t) + c_{n',m+2}(t)d^3_{nmn'}(t)\right\} \qquad (8.50)
$$

where the $d^j_{nmn'}$, $j = 1, 2, 3$ are time-dependent real coefficients given by

$$
\begin{aligned}
d^1_{nmn'} = \frac{1}{J_{m+1}(k_{m,n})J_{m+1}(k_{m,n'})}\Bigg[&\left(-\frac{\hbar^2}{\mu a^2(t)}-\frac{\hbar^2}{\mu b^2(t)}\right)\\
&\left(\frac{k^2_{m,n'}}{8}(L^1_{nmn'}-2L^2_{nmn'}+L^3_{nmn'})-\frac{k_{m,n'}(m-1)}{4}L^{10}_{nmn'}-\frac{k_{m,n'}(m+1)}{4}L^{11}_{nmn'}\right)\\
&+\frac{\mu L^{16}_{nmn'}}{2}\left(a(t)\ddot{a}(t)+b(t)\ddot{b}(t)\right)\Bigg] \qquad (8.51)
\end{aligned}
$$

$$d^2_{nmn'} = \frac{1}{J_{m+1}(k_{m,n})J_{m-1}(k_{m-2,n'})}\Bigg[\left(\frac{\hbar^2}{\mu a^2(t)} - \frac{\hbar^2}{\mu b^2(t)}\right)$$
$$\left(\frac{k^2_{m-2,n'}}{16}(L^7_{nmn'} - 2L^8_{nmn'} + L^9_{nmn'}) + \frac{3k_{m-2,n'}(m-1)}{8}L^{13}_{nmn'} - \frac{k_{m-2,n'}(m-3)}{8}L^{12}_{nmn'}\right)$$
$$+\frac{\mu L^{18}_{nmn'}}{4}\left(a(t)\ddot{a}(t) - b(t)\ddot{b}(t)\right)\Bigg] \tag{8.52}$$

$$d^3_{nmn'} = \frac{1}{J_{m+1}(k_{m,n})J_{m+3}(k_{m+2,n'})}\Bigg[\left(\frac{\hbar^2}{\mu a^2(t)} - \frac{\hbar^2}{\mu b^2(t)}\right)$$
$$\left(\frac{k^2_{m+2,n'}}{16}(L^4_{nmn'} - 2L^5_{nmn'} + L^6_{nmn'}) + \frac{3k_{m+2,n'}(m+1)}{8}L^{14}_{nmn'} - \frac{k_{m+2,n'}(m+3)}{8}L^{15}_{nmn'}\right)$$
$$+\frac{\mu L^{17}_{nmn'}}{4}\left(a(t)\ddot{a}(t) - b(t)\ddot{b}(t)\right)\Bigg]. \tag{8.53}$$

(For a detailed derivation see Appendix B.4.)

8.2 Numerical integration of the system of ODEs

A typical d-dimensional system of coupled first-order differential equations is given by

$$\frac{dy_i(t)}{dt} = f_i(t, y_1(t), y_2(t), \dots y_n(t)), \tag{8.54}$$

where $i = 1, 2, \dots d$. Standard routines for solving such a system additionally require the Jacobian $\mathbf{J}$ (the vector $Y(t)$ contains all the $y_i(t)$)

$$J_{ij} = \frac{\partial f_i(t, Y(t))}{\partial y_j} \tag{8.55}$$

and the partial derivatives

$$\frac{\partial f_i(t, Y(t))}{\partial t}. \tag{8.56}$$

To put the system of ODEs (8.50) into the standard form of Eq. (8.54), we have to assign a linear index to the $c_{n,m}$. This can be done in the following fashion

$$\begin{array}{cccc}
c_{1,-M} = c_1 & c_{2,-M} = c_2 & \cdots & c_{N,-M} = c_N \\
c_{1,-M+1} = c_{N+1} & c_{2,-M+1} = c_{N+2} & \cdots & c_{N,-M+1} = c_{2N} \\
\vdots & \vdots & & \vdots \\
c_{1,0} = c_{NM+1} & c_{2,0} = c_{MN+2} & \cdots & c_{N,0} = c_{N(M+1)} \\
\vdots & \vdots & & \vdots \\
c_{1,M} = c_{2NM+1} & c_{2,M} = c_{2MN+2} & \cdots & c_{N,0} = c_{N(2M+1)}
\end{array}$$

or, in short form (n ranges from $1, 2, \dots, N$ and m from $-M, -M+1, \dots, -1, 0, 1, \dots, M$)

$$c_{n,m} = c_{N(M+m)+n}. \tag{8.57}$$

Now if C is a vector containing the $c_i(t)$, with $i = 1, 2, \dots N(2M+1)$, then the system of differential equations (8.50) can be written as

$$\dot{C}(t) = \frac{1}{i\hbar}\mathbf{X}(t)C(t), \tag{8.58}$$

where $\mathbf{X}$ is a $N(2M+1) \times N(2M+1)$ matrix of the following form, where ■ denote $N \times N$ matrices and the rest is filled with zeros:

$$\mathbf{X} = \left(\begin{array}{ccccccccccc}
\ddots & & \ddots & & \ddots & & & & & & \\
& \ddots & & \ddots & & \ddots & & & & & \\
& & \blacksquare & & \blacksquare & & \blacksquare & & & & \\
& & & \blacksquare & & \blacksquare & & \blacksquare & & & \\
& & & & \blacksquare & & \blacksquare & & \blacksquare & & \\
& & & & & \ddots & & \ddots & & \ddots & \\
& & & & & & \ddots & & \ddots & & \ddots
\end{array}\right) \tag{8.59}$$

For the $d^i_{nmn'}$, with $i = 1, 2, 3$, we use a similar convention, i.e. the index pair n, m is replaced with a linear index in the same way as for $c_{n,m}$, but n' remains unchanged, so we have $d^i_{j,n'}$, with $j = 1, 2, \dots N(2M+1)$ and $n' = 1, 2, \dots N$. With this convention, the matrix $\mathbf{X}$ is shown in a more detailed fashion in Fig. 8.1.

The matrix (8.58) form of the ODEs is of the standard form of eq. (8.54), since it can be written as

$$\frac{dc_i(t)}{dt} = \frac{1}{\iota\hbar}\sum_{l=1}^{(2M+1)N} X_{il}(t)c_l(t), \tag{8.60}$$

i.e. we identify $c_i(t) = y_i(t)$ and

$$f_i(t, y_1(t), y_2(t), \dots y_n(t)) = \frac{1}{\iota\hbar}\sum_{l=1}^{(2M+1)N} X_{il}(t)c_l(t). \tag{8.61}$$

Now we have to keep in mind that the $c_i(t)$ are complex, whereas the $X_{il}(t)$ are real. We thus write (we use ι instead of i for the imaginary unit in order to not confuse it with the index i)

$$\frac{d(\mathrm{Re}(c_i) + \iota\mathrm{Im}(c_i))}{dt} = \frac{1}{\iota\hbar}\sum_{l=1}^{(2M+1)N} X_{il}(\mathrm{Re}(c_l) + \iota\mathrm{Im}(c_l)). \tag{8.62}$$

Equating powers of ι we get

$$\frac{d(\mathrm{Re}(c_i))}{dt} = \frac{1}{\hbar}\sum_{l=1}^{(2M+1)N} X_{il}\mathrm{Im}(c_l) \tag{8.63}$$

$$\frac{d(\mathrm{Im}(c_i))}{dt} = -\frac{1}{\hbar}\sum_{l=1}^{(2M+1)N} X_{il}\mathrm{Re}(c_l). \tag{8.64}$$

Since $\mathrm{Re}(c_i)$ and $\mathrm{Im}(c_i)$ are independent variables, we can just use a single linear index

$$
\begin{pmatrix}
\ddots & & & & & \ddots & & & & & & & & & \\
d^1_{(m-2)N+1,1} & \cdots & d^1_{(m-2)N+1,N} & & & & d^3_{(m-2)N+1,1} & \cdots & d^3_{(m-2)N+1,N} & & & & & & \\
d^1_{(m-2)N+2,1} & \cdots & d^1_{(m-2)N+2,N} & & & & d^3_{(m-2)N+2,1} & \cdots & d^3_{(m-2)N+1,N} & & & & & & \\
\vdots & & \vdots & & & & \vdots & & \vdots & & & & & & \\
d^1_{(m-2)N+N,1} & \cdots & d^1_{(m-2)N+N,N} & & & & d^3_{(m-2)N+N,1} & \cdots & d^3_{(m-2)N+N,N} & & & & & & \\
& & & d^1_{(m-1)N+1,1} & \cdots & d^1_{(m-1)N+1,N} & & & & d^3_{(m-1)N+1,1} & \cdots & d^3_{(m-1)N+1,N} & & & \\
& & & d^1_{(m-1)N+2,1} & \cdots & d^1_{(m-1)N+2,N} & & & & d^3_{(m+1)N+2,1} & \cdots & d^3_{(m-1)N+1,N} & & & \\
& & & \vdots & & \vdots & & & & \vdots & & \vdots & & & \\
\ddots & & & d^1_{(m-1)N+N,1} & \cdots & d^1_{(m-1)N+N,N} & & & & d^3_{(m+1)N+N,1} & \cdots & d^3_{(m-1)N+N,N} & & & \\
d^2_{mN+1,1} & \cdots & d^2_{mN+1,N} & & & & d^1_{mN+1,1} & \cdots & d^1_{mN+1,N} & & & & d^3_{mN+1,1} & \cdots & d^3_{mN+1,N} \\
d^2_{mN+2,1} & \cdots & d^2_{mN+2,N} & & & & d^1_{mN+2,1} & \cdots & d^1_{mN+2,N} & & & & d^3_{mN+2,1} & \cdots & d^3_{mN+2,N} \\
\vdots & & \vdots & & & & \vdots & & \vdots & & & & \vdots & & \vdots \\
d^2_{mN+N,1} & \cdots & d^2_{mN+N,N} & & & & d^1_{mN+N,1} & \cdots & d^1_{mN+N,N} & & & & d^3_{mN+N,1} & \cdots & d^3_{mN+N,N} \\
& & & & & & & & & & & & & & \ddots \\
& & & d^2_{(m+1)N+1,1} & \cdots & d^2_{(m+1)N+1,N} & & & & d^1_{(m+1)N+1,1} & \cdots & d^1_{(m+1)N+1,N} & & & \\
& & & d^2_{(m+1)N+2,1} & \cdots & d^2_{(m+1)N+2,N} & & & & d^1_{(m+1)N+2,1} & \cdots & d^1_{(m+1)N+1,N} & & & \\
& & & \vdots & & \vdots & & & & \vdots & & \vdots & & & \\
& & & d^2_{(m+1)N+N,1} & \cdots & d^2_{(m+1)N+N,N} & & & & d^1_{(m+1)N+N,1} & \cdots & d^1_{(m+1)N+N,N} & & & \\
& & & & & & d^2_{(m+2)N+1,1} & \cdots & d^2_{(m+2)N+1,N} & & & & d^1_{(m+2)N+1,1} & \cdots & d^1_{(m+2)N+1,N} \\
& & & & & & d^2_{(m+2)N+2,1} & \cdots & d^2_{(m+2)N+2,N} & & & & d^1_{(m+2)N+2,1} & \cdots & d^1_{(m+2)N+1,N} \\
& & & & & & \vdots & & \vdots & & & & \vdots & & \vdots \\
& & & & & & d^2_{(m+2)N+N,1} & \cdots & d^2_{(m+2)N+N,N} & & & & d^1_{(m+2)N+N,1} & \cdots & d^1_{(m+2)N+N,N} \\
& & & & & & & & & \ddots & & & & & \ddots
\end{pmatrix}
$$

Figure 8.1: The composition of the matrix $\boldsymbol{X}$ is shown. Overall, there are three bands, corresponding to d^1, d^2, d^3 each consisting of blocks with dimension $N \times N$. Each block has an associated index m (columns) and m' (rows), both ranging from $-M$ to M.

going from 1 to $2N(2M+1)$ and order them in the following way:

$$\begin{array}{rcr}
\mathrm{Re}(c_1) = c'_1 & \ldots & \mathrm{Re}(c_N) = c'_N \\
\mathrm{Im}(c_1) = c'_{N+1} & \ldots & \mathrm{Im}(c_N) = c'_{2N} \\
\vdots & & \vdots \\
\mathrm{Re}(c_{2NM+1}) = c'_{4NM+1} & \ldots & \mathrm{Re}(c_{N(2M+1)}) = c'_{N(4M+1)} \\
\mathrm{Im}(c_{2NM+1}) = c'_{N(4M+1)+1} & \ldots & \mathrm{Im}(c_{N(2M+1)}) = c'_{2N(2M+1)}
\end{array}$$

The matrix $\mathbf{X}'/(\iota\hbar)$ is now $2N(2M+1) \times 2N(2M+1)$ and in the sense of Eq. (8.59) given by

$$\mathbf{X}' = \left(\begin{array}{cccccccccccccc}
\ddots & & & \ddots & & & & \ddots & & & & & & \\
 & \mathbf{0} & \blacksquare & & & \mathbf{0} & \blacksquare & & & \mathbf{0} & \blacksquare & & & \\
 & -\blacksquare & \mathbf{0} & & & -\blacksquare & \mathbf{0} & & & -\blacksquare & \mathbf{0} & & & \\
 & & & \mathbf{0} & \blacksquare & & & \mathbf{0} & \blacksquare & & & \mathbf{0} & \blacksquare & \\
 & & & -\blacksquare & \mathbf{0} & & & -\blacksquare & \mathbf{0} & & & -\blacksquare & \mathbf{0} & \\
 & & & & & \ddots & & & & \ddots & & & & \ddots
\end{array} \right) . \tag{8.65}$$

The Jacobian (8.55) can be easily calculated:

$$J_{ij} = \frac{1}{\iota\hbar} \sum_i X_{il}(t) \frac{\partial c_l}{\partial c_j} = \frac{1}{\iota\hbar} \sum_i X_{il}(t) \delta_{lj} = \frac{1}{\iota\hbar} X_{ij} \quad \Leftrightarrow \quad \mathbf{J} = \frac{1}{\iota\hbar} \mathbf{X} \tag{8.66}$$

The partial derivatives $\partial f_i / \partial t$ (8.56) are obtained by replacing in the definition (8.61) the $d^i_{nmn'}(t)$ contained in $\mathbf{X}$ by $\dot{d}^i_{nmn'}(t)$

$$\begin{aligned}
\dot{d}^1_{nmn'} = {} & \frac{1}{J_{m+1}(k_{m,n}) J_{m+1}(k_{m,n'})} \Bigg[\left(\frac{\hbar^2 \dot{a}(t)}{\mu a^3(t)} + \frac{\hbar^2 \dot{b}(t)}{\mu b^3(t)} \right) \\
& \left(\frac{k^2_{m,n'}}{4} (L^1_{nmn'} - 2L^2_{nmn'} + L^3_{nmn'}) - \frac{k_{m,n'}(m-1)}{4} L^{10}_{nmn'} - \frac{k_{m,n'}(m+1)}{4} L^{11}_{nmn'} \right) \\
& + \frac{\mu L^{16}_{nmn'}}{2} \left(a \dddot{a} + \dot{a}\ddot{a} + b \dddot{b} + \dot{b}\ddot{b} \right) \Bigg]
\end{aligned} \tag{8.67}$$

$$\begin{aligned}
\dot{d}^2_{nmn'} = {} & \frac{1}{J_{m+1}(k_{m,n}) J_{m-1}(k_{m-2,n'})} \Bigg[\left(\frac{\hbar^2 \dot{b}(t)}{\mu b^3(t)} - \frac{\hbar^2 \dot{a}(t)}{\mu a^3(t)} \right) \\
& \left(\frac{k^2_{m-2,n'}}{8} (L^7_{nmn'} - 2L^8_{nmn'} + L^9_{nmn'}) + \frac{3k_{m-2,n'}(m-1)}{8} L^{13}_{nmn'} - \frac{k_{m-2,n'}(m-3)}{8} L^{12}_{nmn'} \right) \\
& + \frac{\mu L^{18}_{nmn'}}{4} \left(a \dddot{a} + \dot{a}\ddot{a} - b \dddot{b} - \dot{b}\ddot{b} \right) \Bigg]
\end{aligned} \tag{8.68}$$

$$\dot{d}^3_{nmn'} = \frac{1}{J_{m+1}(k_{m,n})J_{m+3}(k_{m+2,n'})}\Bigg[\left(\frac{\hbar^2\dot{b}(t)}{\mu b^3(t)} - \frac{\hbar^2\dot{a}(t)}{\mu a^3(t)}\right)$$

$$\left(\frac{k^2_{m+2,n'}}{8}(L^4_{nmn'} - 2L^5_{nmn'} + L^6_{nmn'}) + \frac{3k_{m+2,n'}(m+1)}{8}L^{14}_{nmn'} - \frac{k_{m+2,n'}(m+3)}{8}L^{15}_{nmn'}\right)$$

$$+ \frac{\mu L^{17}_{nmn'}}{4}\left(a\dddot{a} + \dot{a}\ddot{a} - b\dddot{b} - \dot{b}\ddot{b}\right)\Bigg]. \quad (8.69)$$

For efficient numerical computations it is reasonable to divide the $d^i_{nmn'}(t)$ into time-dependent and time-independent parts. The time-dependent parts are simple analytic functions that exclusively depend on time. The time-independent parts need to be computed only once but in turn depend on the indices n, m, n':

$$d^1_{nmn'}(t) = g_1(t)f^1_{nmn'} + g_2(t)f^2_{nmn'} \quad (8.70a)$$
$$d^2_{nmn'}(t) = g_3(t)f^3_{nmn'} + g_4(t)f^4_{nmn'} \quad (8.70b)$$
$$d^3_{nmn'}(t) = g_3(t)f^5_{nmn'} + g_4(t)f^6_{nmn'}. \quad (8.70c)$$

And correspondingly for the partial derivatives $\partial f_i/\partial t$ (8.56):

$$\dot{d}^1_{nmn'}(t) = \dot{g}_1(t)f^1_{nmn'} + \dot{g}_2(t)f^2_{nmn'} \quad (8.71a)$$
$$\dot{d}^2_{nmn'}(t) = \dot{g}_3(t)f^3_{nmn'} + \dot{g}_4(t)f^4_{nmn'} \quad (8.71b)$$
$$\dot{d}^3_{nmn'}(t) = \dot{g}_3(t)f^5_{nmn'} + \dot{g}_4(t)f^6_{nmn'} \quad (8.71c)$$

The functions g_i and $\dot{g}_i$ explicitly depend on time, and are determined by the driving law of the elliptical billiard, i.e by the functions $a(t)$ and $b(t)$:

$$g_1(t) = -\frac{\hbar^2}{\mu a^2(t)} - \frac{\hbar^2}{\mu b^2(t)} \quad (8.72a)$$
$$g_2(t) = \mu\left(a(t)\ddot{a}(t) + b(t)\ddot{b}(t)\right) \quad (8.72b)$$
$$g_3(t) = \frac{\hbar^2}{\mu a^2(t)} - \frac{\hbar^2}{\mu b^2(t)} \quad (8.72c)$$
$$g_4(t) = \mu\left((a(t)\ddot{a}(t) - b(t)\ddot{b}(t)\right), \quad (8.72d)$$

$$\dot{g}_1(t) = \frac{2\hbar^2\dot{a}(t)}{\mu a^3(t)} + \frac{2\hbar^2\dot{b}(t)}{\mu b^3(t)} \quad (8.73a)$$
$$\dot{g}_2(t) = \mu\left(a\dddot{a} + \dot{a}\ddot{a} + b\dddot{b} + \dot{b}\ddot{b}\right) \quad (8.73b)$$
$$\dot{g}_3(t) = -\frac{2\hbar^2\dot{a}(t)}{\mu a^3(t)} + \frac{2\hbar^2\dot{b}(t)}{\mu b^3(t)} \quad (8.73c)$$
$$\dot{g}_4(t) = \mu\left(a\dddot{a} + \dot{a}\ddot{a} - b\dddot{b} - \dot{b}\ddot{b}\right). \quad (8.73d)$$

The functions $f^i_{nmn'}$ depend the the indices n, m, n' only (and not on the time t) and need to be computed only once:

$$f^1_{nmn'} := \frac{k^2_{m,n'}(L^1_{nmn'} - 2L^2_{nmn'} + L^3_{nmn'}) - 2k_{m,n'}(m-1)L^{10}_{nmn'}}{8J_{m+1}(k_{m,n})J_{m+1}(k_{n'm})} - \frac{2k_{m,n'}(m+1)L^{11}_{nmn'}}{8J_{m+1}(k_{m,n})J_{m+1}(k_{n'm})} \tag{8.74a}$$

$$f^2_{nmn'} := \frac{L^{16}_{nmn'}}{2J_{m+1}(k_{m,n})J_{m+1}(k_{n'm})} \tag{8.74b}$$

$$f^3_{nmn'} := \frac{k^2_{m-2,n'}(L^7_{nmn'} - 2L^8_{nmn'} + L^9_{nmn'}) + 6k_{m-2,n'}(m-1)L^{13}_{nmn'}}{16J_{m+1}(k_{m,n})J_{m-1}(k_{m-2,n'})} - \frac{2k_{m-2,n'}(m-3)L^{12}_{nmn'}}{16J_{m+1}(k_{m,n})J_{m-1}(k_{m-2,n'})} \tag{8.74c}$$

$$f^4_{nmn'} := \frac{L^{18}_{nmn'}}{4J_{m+1}(k_{m,n})J_{m-1}(k_{m-2,n'})} \tag{8.74d}$$

$$f^5_{nmn'} := \frac{k^2_{m+2,n'}(L^4_{nmn'} - 2L^5_{nmn'} + L^6_{nmn'}) + 6k_{m+2,n'}(m+1)L^{14}_{nmn'}}{16J_{m+1}(k_{m,n})J_{m+3}(k_{m+2,n'})} - \frac{2k_{m+2,n'}(m+3)L^{15}_{nmn'}}{16J_{m+1}(k_{m,n})J_{m+3}(k_{m+2,n'})} \tag{8.74e}$$

$$f^6_{nmn'} := \frac{L^{17}_{nmn'}}{4J_{m+1}(k_{m,n})J_{m+3}(k_{m+2,n'})}. \tag{8.74f}$$

8.2.1 Symmetries

To numerically solve the system of ODEs (8.50), we have to fix N and M, specify the initial expansion coefficients $c_{n,m}(t)$ and calculate the $f^i_{nmn'}$. The $f^i_{nmn'}$ (8.74) are composed by the integrals $L^i_{nmn'}$. These 18 different integrals types cannot be calculated analytically (except $L^2_{nmn'}$ which is just the orthogonality relation for the Bessel functions), so we have to evaluate them numerically. This is done with very high numerical precision by utilizing an adaptive Gauss-Kronrad scheme [110] using the implementation of the GSL (GNU Scientific Library) [152]. Overall $17N^2(2M+1)$ integrals have to be evaluated. To reduce the numerical effort, we can exploit certain symmetries, especially the $m \to -m$ symmetry (note that m goes from $-M$ to M). The basic relation we need is the following one for Bessel functions [115]:

$$J_{-m}(r) = (-1)^m J_m(r) \qquad m > 0. \tag{8.75}$$

An important consequence of Eq. (8.75) is that the zeros of the Bessel functions are invariant under $m \to -m$, $k_{n,-m} = k_{n,m}$. Exemplarily, we show how the $m \to -m$ transformation affects $L^{12}_{nmn'}$:

$$L^{12}_{n,-m,n'} = \int_0^1 J_{-m}(k_{n,-m}r)J_{-m-3}(k_{n',-m-2}r)dr =$$

$$= (-1)^{2m+3} \int_0^1 J_m(k_{n,-m}r) J_{m+3}(k_{n',-(m+2)}r)dr = \\ - \int_0^1 J_m(k_{n,m}r) J_{m+3}(k_{m+2,n'}r)dr = -L^{15}_{n,m,n'}. \quad (8.76)$$

This yields for the $L^i_{nmn'}$

$$\begin{array}{lll}
L^1_{n,-m,n'} = L^3_{n,m,n'} & L^2_{n,-m,n'} = L^2_{n,m,n'} & L^3_{n,-m,n'} = L^1_{n,m,n'} \\
L^4_{n,-m,n'} = L^9_{n,m,n'} & L^5_{n,-m,n'} = L^8_{n,m,n'} & L^6_{n,-m,n'} = L^7_{n,m,n'} \\
L^7_{n,-m,n'} = L^6_{n,m,n'} & L^8_{n,-m,n'} = L^5_{n,m,n'} & L^9_{n,-m,n'} = L^4_{n,m,n'} \\
L^{10}_{n,-m,n'} = -L^{11}_{n,m,n'} & L^{11}_{n,-m,n'} = -L^{10}_{n,m,n'} & L^{12}_{n,-m,n'} = -L^{15}_{n,m,n'} \\
L^{13}_{n,-m,n'} = -L^{14}_{n,m,n'} & L^{14}_{n,-m,n'} = -L^{13}_{n,m,n'} & L^{15}_{n,-m,n'} = -L^{12}_{n,m,n'} \\
L^{16}_{n,-m,n'} = L^{16}_{n,m,n'} & L^{17}_{n,-m,n'} = L^{18}_{n,m,n'} & L^{18}_{n,-m,n'} = L^{17}_{n,m,n'}
\end{array}$$

and for the $I^i_{nmn'}$

$$\begin{array}{lll}
I^1_{n,-m,n'} = I^1_{n,m,n'} & I^2_{n,-m,n'} = I^3_{n,m,n'} & I^3_{n,-m,n'} = I^2_{n,m,n'} \\
I^4_{n,-m,n'} = I^4_{n,m,n'} & I^5_{n,-m,n'} = I^6_{n,m,n'} & I^6_{n,-m,n'} = I^5_{n,m,n'} \\
I^7_{n,-m,n'} = I^7_{n,m,n'} & I^8_{n,-m,n'} = I^9_{n,m,n'} & I^9_{n,-m,n'} = I^8_{n,m,n'} \\
I^{10}_{n,-m,n'} = I^{10}_{n,m,n'} & I^{11}_{n,-m,n'} = I^{12}_{n,m,n'} & I^{12}_{n,-m,n'} = I^{11}_{n,m,n'}.
\end{array}$$

This means we do not have to evaluate the $L^i_{nmn'}$ with $m < 0$ but can instead use the above shown symmetry relations. To investigate the symmetries of the $f^i_{n,m,n'}$ and eventually of the $d^i_{n,m,n'}$, we need a further relation for the Bessel functions [115]:

$$J_{m+1}(k_{m,n}) = -J_{m-1}(k_{m,n}). \quad (8.77)$$

This relation is valid at the point $k_{m,n}$ only, so at the n-th zero of the Bessel function of order m. Now we immediately see (cf. Appendix B.5 for the definition of the $f^1_{n,-m,n'}$)

$$\begin{array}{lll}
f^1_{n,-m,n'} = f^1_{n,m,n'} & f^2_{n,-m,n'} = f^2_{n,m,n'} & f^3_{n,-m,n'} = f^5_{n,m,n'} \\
f^4_{n,-m,n'} = f^6_{n,m,n'} & f^5_{n,-m,n'} = f^3_{n,m,n'} & f^6_{n,-m,n'} = f^4_{n,m,n'}.
\end{array}$$

This gives for the $d^i_{n,m,n'}$

$$\begin{array}{lll}
d^1_{n,-m,n'} = d^1_{n,m,n'} & d^2_{n,-m,n'} = d^3_{n,m,n'} & d^3_{n,-m,n'} = d^2_{n,m,n'}
\end{array}$$

and

$$\begin{array}{lll}
d^1_{n,m,n'} = d^1_{n',m,n} & d^2_{n,m,n'} = d^2_{n',-m+2,n} & d^3_{n,m,n'} = d^3_{n',-m-2,n}.
\end{array}$$

These symmetries can be exploited to reduce the ODE system, which originally has a dimension of $2N(2M+1)$. Since the matrix $\mathbf{X}$ (8.65) is composed exclusively of the $d^i_{nmn'}$, the following symmetry relation holds for $\mathbf{X}$:

$$X_{n,m;n',m'} = X_{n,-m;n',-m'}, \tag{8.78}$$

where $\mathbf{X} = (X_{i;j})$ and $i, j = 1, 2, \ldots 2N(2M+1)$ and in the sense of Eq. (8.57) the pair n, m stands for the linear index i and n', m' for j. With the notation of Eq. (8.78) the ODE system can be written as (where summation of repeated indices is assumed)

$$\dot{c}_{n,m}(t) = \frac{1}{i\hbar} X_{n,m;n',m'} c_{n',m'}(t). \tag{8.79}$$

Now we assume that our initial state has a certain symmetry, i.e. the expansions coefficients $c_{n,m}$ of the circular billiard basis obey

$$c_{n,-m}(t=0) = c_{n,m}(t=0). \tag{8.80}$$

It is important to note that all eigenstates of the static elliptical billiard possess this symmetry and choosing such an eigenstate as the initial state is reasonable. Now, the formal solution of Eq. (8.79) is given by [153]

$$c_{n,m}(t) = \left[T\left(e^{\frac{-i}{\hbar}\int_0^t \mathbf{X}(\tau)d\tau}\right)\right]_{n,m;n',m'} c_{n',m'}(0), \tag{8.81}$$

where T stands for the time-ordered product, since in general $\mathbf{X}(t)$ and $\mathbf{X}(t')$ do not commute. The time-ordering does not affect the symmetry properties of $\mathbf{X}$, since it is exclusively related to the time-dependence and the symmetry (8.78) is independent of time. At every instance t, $\mathbf{X}(t)$ has the property (8.78) and the evolution matrix in Eq. (8.81) then also possesses this property, since it is basically an (infinite) product of matrices $\mathbf{X}(t)$ at different times t, i.e.

$$\left[T\left(e^{\frac{-i}{\hbar}\int_0^t \mathbf{X}(\tau)d\tau}\right)\right]_{n,m;n',m'} = \left[T\left(e^{\frac{-i}{\hbar}\int_0^t \mathbf{X}(\tau)d\tau}\right)\right]_{n,-m;n',-m'}. \tag{8.82}$$

As a consequence, the symmetry of the initial state (8.80) will be preserved for all times:

$$c_{n,-m}(t) = c_{n,m}(t). \tag{8.83}$$

We thus have to consider positive values of m only, i.e. effectively we now have to solve a system of dimension $2N(M+1)$ instead of $2N(2M+1)$ (we still have to consider the blocks in $\mathbf{X}$ with $m=0$, this is why $M+1$ and not just M appears in the dimension).

Another property of the ODE (8.50) system is that it can be decoupled into two smaller subsystems which can be solved independently: For all times, all $\dot{c}_{n,m}(t)$ with even m depend on $c_{n,m}$ with even m only, and all $\dot{c}_{n,m}(t)$ with odd m depend exclusively on coefficients $c_{n,m}$ with odd m. This means we can set up one system containing all the even $c_{n,m}(t)$ and one system containing all the odd $c_{n,m}(t)$ and solve them independently of each other. If M is even, we have one system with $m = 0, 2, 4 \ldots M$ ($\#\{m\} = M/2+1$) and one with $m = 1, 3, 5 \ldots M-1$ ($\#\{m\} = M/2$). If M is odd, we have one system with $m = 0, 2, 4 \ldots M-1$ ($\#\{m\} = (M+1)/2$) and one with $m = 1, 3, 5 \ldots M$ ($\#\{m\} = (M+1)/2$). The dimensions are shown in the following table:

If the coefficients $c_{n,m}(t)$ of the initial state do not have the symmetry of Eq. (8.80), we

	M even	M odd
Dimension of system 1 ($m = 0, 2, 4 \dots$)	$N(M+2)$	$N(M+1)$
Dimension of system 2 ($m = 1, 3, 5 \dots$)	NM	$N(M+1)$

can still apply the procedure described above and split the system into two smaller ones, now we get:

	M even	M odd
Dimension of system 1 ($m = \dots -2, 0, 2, \dots$)	$2N(M+1)$	$2NM$
Dimension of system 2 ($m = \dots -3, -1, 1, 3, \dots$)	$2NM$	$2N(M+1)$

The numerical integration of the reduced ODE systems is done by using either an embedded Runge-Kutta Price-Dormand, or an implicit 4th order Runge-Kutta at Gaussian points method [110] or an implicit Burlirsch-Stoer method of Bader and Deuflhard [154], all of them implemented in the GSL [152] with adaptive step-size control.

8.3 Calculating observables

The numerical integration of the ODE system is carried out after applying a series of transformations described in section 8.1. If we want to calculate physical observables like the energy $E(t)$, we have to invert all transformations and calculate the observables using the wavefunction and the Hamiltonian specified in Eqs. (8.1) and (8.2). The reason why we cannot directly use the wavefunction and the Hamiltonian for example of Eqs. (8.23) and (8.25) is due to the fact that this is an effective or working Hamiltonian only and not one in the usual sense. When the time-dependent coordinate transformation of Eq. (8.5) is applied to the time-dependent Schrödinger equation, we get additional terms from the time derivative $i\hbar\partial/\partial t$. These additional terms are absorbed by the effective Hamiltonian, which means that using the wavefunction and the Hamiltonian of Eqs. (8.23) and (8.25) would lead to unphysical results for the energy.

8.3.1 Energy

The time-dependent energy is given by

$$E(t) = \langle \Psi(x,y,t) | \, H(x,y,t) \, | \Psi(x,y,t) \rangle \tag{8.84}$$

and the wavefunction $\Psi(x,y,t)$ is obtained by inverting the three transformations of section 8.1

$$\Psi(x,y,t) = \frac{2}{\sqrt{ab}} e^{\frac{i\mu}{2\hbar}\left(\frac{\dot{a}}{a}x^2 + \frac{\dot{b}}{b}y^2\right)} \sum_{n,m} c_{n,m}(t) \Phi_{n,m}\left(\sqrt{\frac{x^2}{a^2} + \frac{y^2}{b^2}}, \arctan\left(\frac{ay}{bx}\right)\right). \tag{8.85}$$

The wave function $\Psi(x, y, t)$ vanishes outside the time-dependent elliptical billiard, i.e.

$$E(t) = \iint_{\frac{x^2}{a^2}+\frac{y^2}{b^2}\leq 1} \Psi^*(x, y, t) H(x, y, t) \Psi(x, y, t) dx dy, \tag{8.86}$$

where of course $a = a(t)$ and $b = b(t)$. Since the integral has to be evaluated over the area of the elliptical billiard $\frac{x^2}{a^2} + \frac{y^2}{b^2} \leq 1$ and the functional form of Ψ in Eq. (8.85) is somewhat complicated, we will again apply a series of transformations to simplify the equations. First we apply the same transformation as given in Eq. (8.5), but now as a time-independent coordinate transformation, which just depends parametrically on the time t:

$$\eta = \frac{x}{a}, \quad \xi = \frac{y}{b} \tag{8.87}$$

The wavefunction and the Hamiltonian are then given by

$$\Psi(\eta, \xi, t) = 2e^{\frac{i\mu}{2\hbar}\left(\dot{a}a\eta^2+\dot{b}b\xi^2\right)} \sum_{n,m} c_{n,m}(t) \Phi_{n,m}\left(\sqrt{\eta^2+\xi^2}, \arctan\left(\frac{\xi}{\eta}\right)\right), \tag{8.88}$$

$$H(\eta, \xi, t) = -\frac{\hbar^2}{2\mu}\left(\frac{1}{a^2(t)}\frac{\partial^2}{\partial\eta^2} + \frac{1}{b^2(t)}\frac{\partial^2}{\partial\xi^2}\right). \tag{8.89}$$

With $\eta = r\cos\phi$ and $\xi = r\sin\phi$ we transform again to polar coordinates and get

$$\Psi(r, \phi, t) = 2e^{\frac{i\mu}{2\hbar}r^2\left(\dot{a}a+\sin^2\phi(\dot{b}b-\dot{a}a)\right)} \sum_{n,m} c_{n,m}(t) \Phi_{n,m}(r, \phi) \tag{8.90}$$

and the corresponding Hamiltonian is given by Eq. (8.23). Note that we have inverted two of the three transformations, yielding the same Hamiltonian but the wave function $\Psi(r, \phi, t)$ has now a time and coordinate dependent phase factor. Due to this time and coordinate dependent prefactor, applying the Hamiltonian (8.23) on $\Psi(r, \phi, t)$ (8.90) is tedious, the derivation can be found in Appendix B.6. The Energy can then be written as

$$\begin{aligned} E(t) = \langle\Psi|\,\mathcal{H}(t)\,|\Psi\rangle = \sum_{m',n',m,n} \int_0^1 \int_0^{2\pi} \Phi^*_{n'm'}(r, \phi) \mathcal{H}(r, \phi, t) \Phi_{nm}(r, \phi) dr d\phi = \\ \sum_{m,n,n'} c^*_{m,n'}(t)\Big[c_{m,n}(t)s^1_{n,m,n'}(t) + c_{m-2,n}(t)s^2_{n,m,n'}(t) + c_{m+2,n}(t)s^3_{n,m,n'}(t)\Big], \end{aligned} \tag{8.91}$$

where the $s^i_{nmn'}$ are now complex and they are defined similarly to the $d^i_{nmn'}$:

$$\mathrm{Re}(s^1_{nmn'}(t)) = g_1(t) f^1_{nmn'} + g_5(t) f^2_{nmn'} \tag{8.92a}$$

$$\mathrm{Im}(s^1_{nmn'}(t)) = g_6(t) f^7_{nmn'} \tag{8.92b}$$

$$\mathrm{Re}(s^2_{nmn'}(t)) = g_3(t) f^3_{nmn'} + g_7(t) f^4_{nmn'} \tag{8.92c}$$

$$\mathrm{Im}(s^2_{nmn'}(t)) = g_8(t) f^8_{nmn'} \tag{8.92d}$$

$$\mathrm{Re}(s^3_{nmn'}(t)) = g_3(t) f^5_{nmn'} + g_7(t) f^6_{nmn'} \tag{8.92e}$$

$$\mathrm{Im}(s^3_{nmn'}(t)) = g_8(t) f^9_{nmn'}. \tag{8.92f}$$

Just like for the $d^i_{nmn'}$, the $s^i_{nmn'}$ can be divided into simple time-dependent functions and time-independent parts, where the latter ones depend on the indices n, m, n':

$$f^7_{nmn'} := \frac{2k_{mn'}\left(L^{19}_{nmn'} - L^{20}_{nmn'}\right) + 4L^2_{nmn'}}{J_{m+1}(k_{mn})J_{m+1}(k_{mn'})} \tag{8.93a}$$

$$f^8_{nmn'} := \frac{k_{m-2,n'}(L^{23}_{nmn'} - L^{24}_{nmn'}) - 2(m-2)L^8_{nmn'}}{J_{m+1}(k_{mn})J_{m-1}(k_{m-2,n'})} \tag{8.93b}$$

$$f^9_{nmn'} := \frac{k_{m+2,n'}(L^{21}_{nmn'} - L^{22}_{nmn'}) + 2(m+2)L^5_{nmn'}}{J_{m+1}(k_{mn})J_{m+3}(k_{m+2,n'})}, \tag{8.93c}$$

$$g_5(t) = \frac{\mu\left(\dot{a}^2(t)a^4(t) + b^4(t)\dot{b}^2(t)\right)}{a^2(t)b^2(t)} \tag{8.94a}$$

$$g_6(t) = -\frac{\hbar\left(\dot{a}(t)a^3(t) + b^3(t)\dot{b}(t)\right)}{a^2(t)b^2(t)} \tag{8.94b}$$

$$g_7(t) = \frac{\mu\left(\dot{a}^2(t)a^4(t) - b^4(t)\dot{b}^2(t)\right)}{a^2(t)b^2(t)} \tag{8.94c}$$

$$g_8(t) = -\frac{\hbar\left(\dot{a}(t)a^3(t) - b^3(t)\dot{b}(t)\right)}{a^2(t)b^2(t)} \tag{8.94d}$$

and the additional integrals $L^{19}_{nmn'}$ until $L^{24}_{nmn'}$ are given by

$$L^{19}_{nmn'} := \int_0^1 J_m(k_{n,m}r)J_{m-1}(k_{m,n'}r)r^2dr \tag{8.95a}$$

$$L^{20}_{nmn'} := \int_0^1 J_m(k_{n,m}r)J_{m+1}(k_{m,n'}r)r^2dr \tag{8.95b}$$

$$L^{21}_{nmn'} := \int_0^1 J_m(k_{n,m}r)J_{m+1}(k_{m+2,n'}r)r^2dr \tag{8.95c}$$

$$L^{22}_{nmn'} := \int_0^1 J_m(k_{n,m}r)J_{m+3}(k_{m+2,n'}r)r^2dr \tag{8.95d}$$

$$L^{23}_{nmn'} := \int_0^1 J_m(k_{n,m}r)J_{m-3}(k_{m-2,n'}r)r^2dr \tag{8.95e}$$

$$L^{24}_{nmn'} := \int_0^1 J_m(k_{n,m}r)J_{m-1}(k_{m-2,n'}r)r^2dr. \tag{8.95f}$$

The symmetries of the $L^{19}_{nmn'}$ until $L^{24}_{nmn'}$ and the resulting symmetries of $f^7_{nmn'}$, $f^8_{nmn'}$, $f^9_{nmn'}$ and of the $s^i_{nmn'}$ are given in Appendix B.7.

8.3.2 Population analysis

In the previous section we described how to calculate the energy $E(t)$ for a wavefunction $\Psi(x, y, t)$, but this does not provide any information about the spectral decomposition of the energy. It is convenient to analyze the spectral composition of the energy in terms of the population of the instantaneous eigenstates of the elliptical billiard. By 'instantaneous eigenstates' we mean the following: At a given time t, the boundary of the elliptical billiard has a certain configuration. If we now take this particular configuration, treat it as a static ellipse and calculate the corresponding eigenstates (as done in the previous chapter) assuming Dirichlet boundary conditions, we obtain the instantaneous eigenstates.

To determine the eigenstates of the static elliptical billiard, the natural way is to use the procedure described in the previous chapter, i.e. solving the corresponding Mathieu equation. The eigenstates $|t_i(t)\rangle$ (we assume a single linear index in the sense of Eq. (8.57)) can then be written in terms of Mathieu functions. To obtain the population of each eigenstate, we expand the wave function $\Psi(x, y, t)$ in terms of the $|t_i(t)\rangle$

$$|\Psi(t)\rangle = \sum_i \langle t_i \,|\, \Psi(t)\rangle \, |t_i\rangle = \sum_i d_i \, |t_i\rangle \, , \tag{8.96}$$

i.e. the population of the eigenstates is given by the expansion coefficients d_i, which are the of course just the projection of $|\Psi(t)\rangle$ on $\langle t_i(t)|$, $d_i = \langle t_i \,|\, \Psi(t)\rangle$. However, if the eigenstates $|t_i(t)\rangle$ are given by Mathieu function, calculating this projection can be quite tedious, thus we choose a different way.

For the static elliptical billiard, we apply the transformations given in Eqs. (8.5) and (8.19), i.e. now the transformation (8.5) is a time-independent coordinate transformation (the semi-major and semi-minor axis a and b are fixed). The resulting Hamiltonian is given by Eq. (8.23) if we set $\ddot{a} = \ddot{b} = 0$. To find the eigenstates, we have to diagonalize this Hamiltonian. This is done by choosing the ansatz (8.25), i.e. we expand the wave function in terms of the eigenstates $|u_i\rangle$ (again we use a single linear index in the sense of Eq. (8.57)) of the circular billiard, which are much easier to handle than the Mathieu functions.

$$|\Psi(t)\rangle = \sum_i \langle u_i \,|\, \Psi(t)\rangle \, |u_i\rangle = \sum_i c_i \, |u_i\rangle \tag{8.97}$$

In this representation, the Hamiltonian is simply given by the matrix $\tilde{\mathbf{X}}$, which is given by $\mathbf{X}$ Eq. (8.59) (see also Fig. 8.1) if we again set $\ddot{a} = \ddot{b} = 0$. Since $\mathbf{X}$ is exclusively composed of the $d^i_{nmn'}$, setting $\ddot{a} = \ddot{b} = 0$ corresponds to $g_1 = g_4 = 0$ in the definition (8.72) of the $d^i_{nmn'}$. Since $\tilde{\mathbf{X}}$ is real and symmetric, it can be diagonalized, yielding

$$\mathbf{V}^{-1}\tilde{\mathbf{X}}\mathbf{V} = \mathrm{diag}(\lambda_1, \lambda_2, \ldots \lambda_D), \tag{8.98}$$

where $D = N(2M + 1)$ is the dimension of $\tilde{\mathbf{X}}$. The columns of the matrix $\mathbf{V}$ are of course the eigenvectors $\mathbf{e}^i, i = 1, 2, \ldots D$ of $\tilde{\mathbf{X}}$. This means that the jth elliptical eigenstate $|t_j(t)\rangle$ in terms of the circular eigenstates $|u_i(t)\rangle$ is given by

$$|t_j(t)\rangle = \sum_k e^j_k \, |u_k(t)\rangle \, , \tag{8.99}$$

where e^j_k denotes the kth component of $\mathbf{e}^j$. Now the projection $|\Psi(t)\rangle$ on the ith eigenstate $\langle t_i(t)|$ is given by (note that $\sum_i |u_i\rangle \langle u_i| = \mathbf{1}$)

$$\langle t_k \,|\, \Psi(t)\rangle = \sum_i \langle t_i \,|\, u_i\rangle \langle u_i \,|\, \Psi(t)\rangle = \sum_i S^{+}_{ki} c_i. \tag{8.100}$$

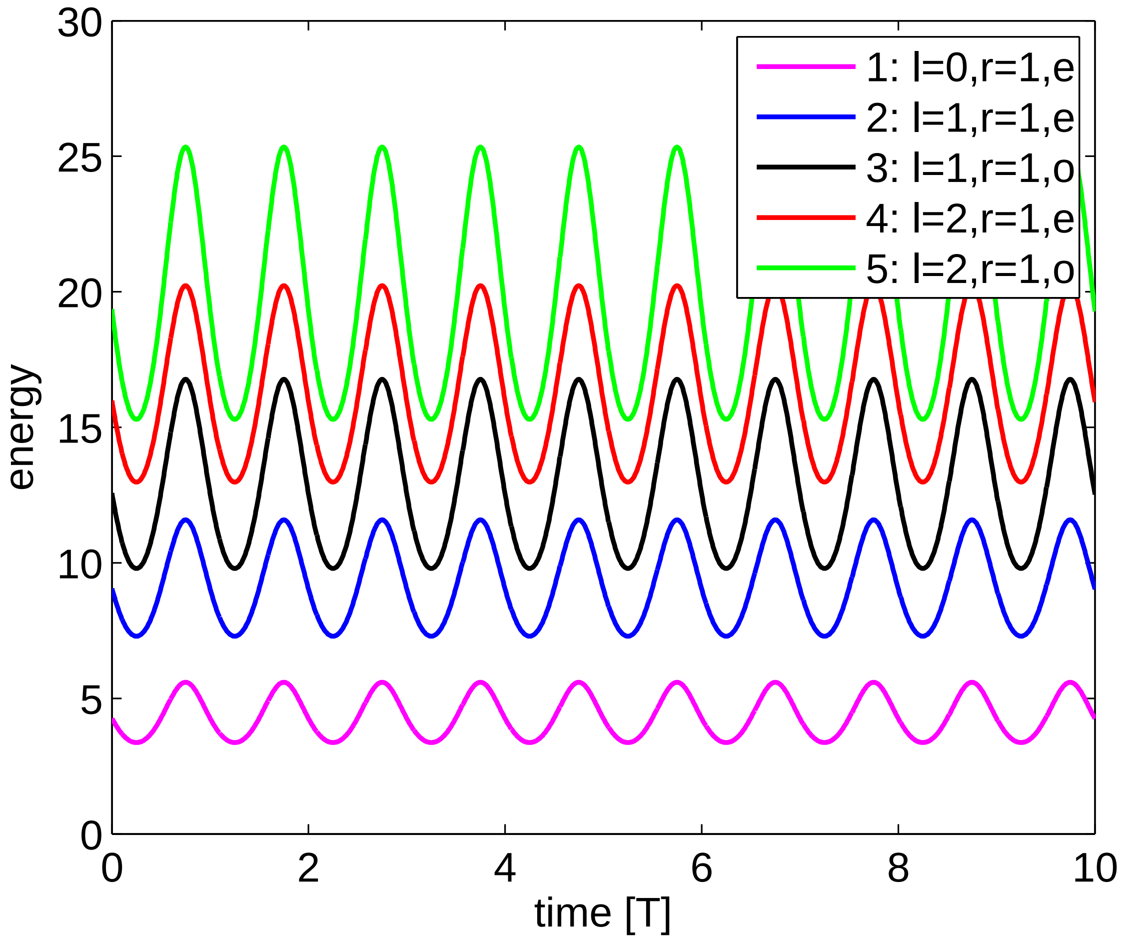

Figure 8.2: The evolution of the energy (in units of $\hbar^2/\mu$) for different initial states $\Psi^{e,o}_{l,r}(t=0)$ as a function of time ($\omega = 1$, $C = 0.1$, $T = 2\pi/\omega$). The number in the legend refers to the linear index when ordering the eigenstates of the static elliptical billiard in terms of their energy, see Table 7.1.

The basis transformation matrix (between the elliptic and circular eigenstates) $S_{ik} = \langle u_i \,|\, t_k \rangle$ is of course just the matrix $\mathbf{V}$. Thus, the population p_k of the kth instantaneous eigenstate $\langle t_k(t)|$ is just the modulus of the scalar product between the kth eigenvector $\mathbf{e}^k$ and the coefficient vector $\mathbf{c}$ (i.e. the vector containing all the $c_i = \langle u_i \,|\, \Psi(t)\rangle$)

$$p_k = |\, \langle t_k \,|\, \Psi(t) \rangle \,| = |\mathbf{e}^k \cdot \mathbf{c}|. \tag{8.101}$$

8.4 Results

In this section, we apply the developed numerical procedure for the propagation of an arbitrary initial state in the driven elliptical billiard. As already done in chapter 7, we use for the equilibrium positions of the semi-major and semi-minor axes $a_0 = 1$, $b_0 = \sqrt{0.51}$, resulting in an eccentricity of $\epsilon_0 = 0.7$. These values of a_0 and b_0 are used to validate the energies for the eigenstates of the static elliptical billiard with the results of Ref. [147], where the same values for the axes are used. The driving amplitude C is set to 0.1 and we

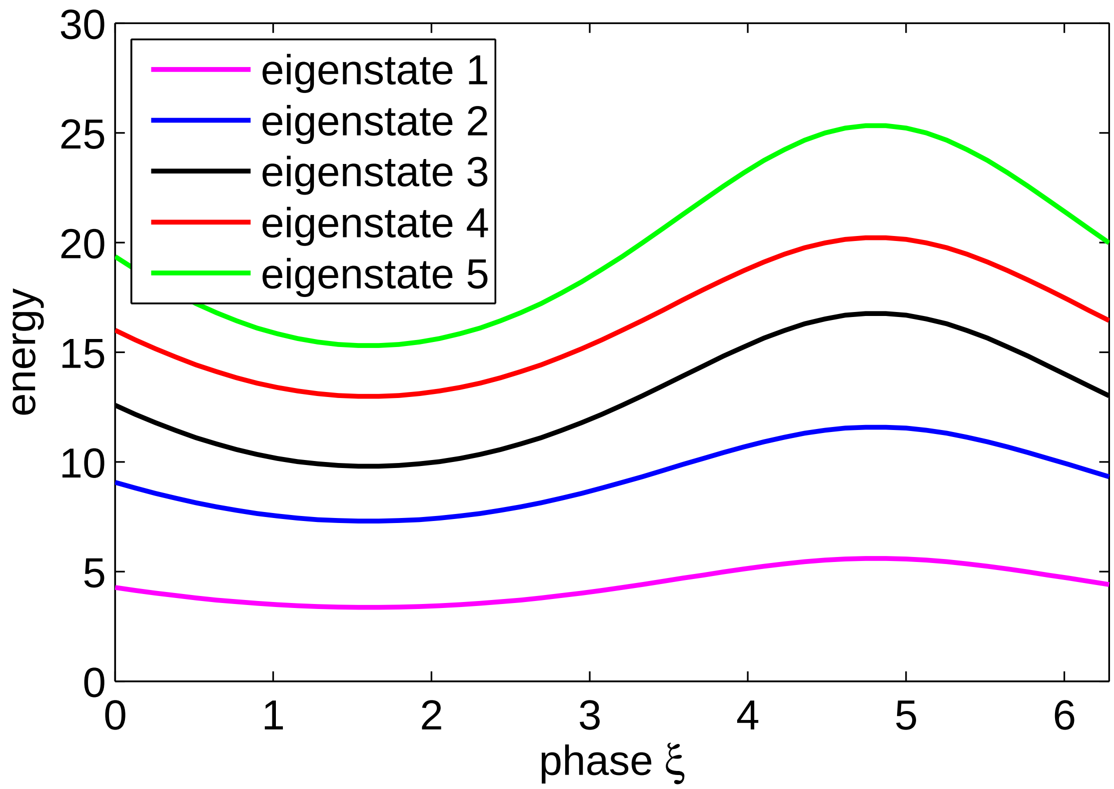

Figure 8.3: Energies of the first five eigenstates, see Table 7.1, of the static elliptical billiard for different configurations of the boundary $\mathcal{B}(\xi)$.

will exclusively consider the breathing mode. The wave function $\Lambda(r, \phi, t)$, see Eq. (8.24), is expanded according to the ansatz (8.25) into the eigenstates $\Phi_{n,m}(r, \phi)$ of the static circular billiard:

$$\Lambda(r, \phi, t) = \sum_{n=1}^{N} \sum_{m=-M}^{M} c_{n,m}(t) \Phi_{n,m}(r, \phi). \tag{8.102}$$

We set $M = 90$ and $N = 40$, i.e. $\Lambda(r, \phi, t)$ is expanded into $N(2M + 1) = 7240$ circular eigenstates. For the initial state $\Psi_0(x, y) = \Psi(x, y, t = 0)$, we chose an eigenstate of the static elliptical billiard, either the groundstate or one of the first four excited states, cf. Table 7.1. The evolution of the energy and the population of the instantaneous eigenstates are calculated according to the procedure described in section 8.3.

The energy (measured in units of $\hbar^2/\mu$)

$$E(t) = \langle \Psi(x, y, t) | \, H(x, y, t) \, | \Psi(x, y, t) \rangle \tag{8.103}$$

as a function of time (in units of the driving period $T = 2\pi/\omega$) for five different initial states and a frequency of $\omega = 1$ is shown in Fig. 8.2. Note that just the first 10 periods are shown, since the next 990 periods (this is how long we iterated) look absolutely the same. The energy performs a sinusoidal-like oscillation, where the amplitude of this oscillation increases with increasing energy of the initial state. Actually, the initial eigenstates follow for this frequency of $\omega = 1$ adiabatically the motion of the boundary. This is confirmed by

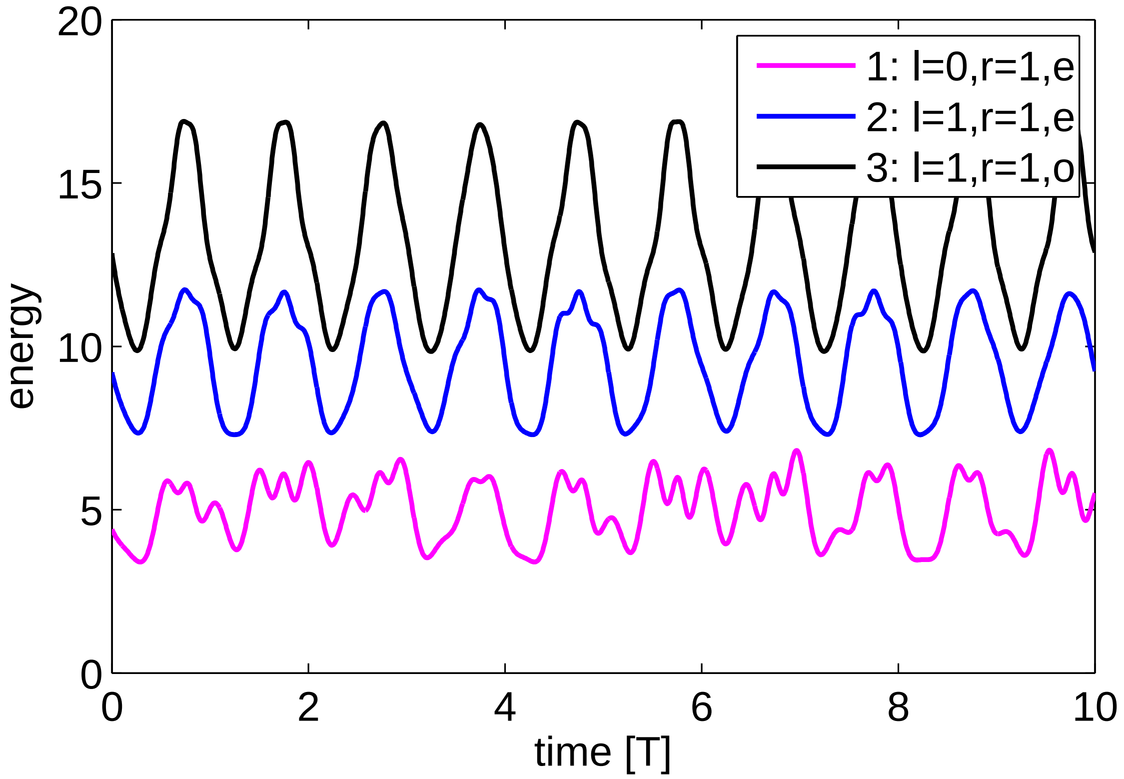

Figure 8.4: The evolution of the energy (in units of $\hbar^2/\mu$) for three different initial states $\Psi^{e,o}_{l,r}(t=0)$ as a function of time, now for a driving frequency of $\omega = 10$. Unlike for $\omega = 1$ (see Fig. 8.2), the evolution of the energy is not purely adiabatic.

two observations: Firstly, the population analysis, cf. section 8.3.2, of the instantaneous eigenstates shows that the initial state is the only one that stays populated throughout the evolution of the wave function. If we denote the population of the ith (ordered by the energy) instantaneous eigenstate by $p_i(t)$, then we get $p_i(t) = const. = 1$ (note that for our choice of the initial state $p_i(t=0) = 1$). Secondly, the evolution of the energy coincides perfectly with the energies of the instantaneous eigenstates at the corresponding configuration of the elliptical billiard. The energies for the first five instantaneous eigenstates as a function of the phase $\xi \in [0, 2\pi]$ are shown in Fig. 8.3. Since the x-axis of Fig. 8.2 is expressed in units of the period $T = 2\pi/\omega$, one oscillation between k and $k+1$ ($k = 1, 2 \ldots 9$) in Fig. 8.2 corresponds to the oscillation between 0 and 2π in Fig. 8.3, yielding perfect agreement.

Whether a certain initial state will follow the motion of the elliptic boundary adiabatically can be roughly estimated in the following way. We assign to an initial state with energy E_0 a typical frequency ω_0 simply by writing $E_0 = \hbar\omega_0$ and compare it with the frequency ω of the driving. It is known from linear stability analysis that the first shape changing response (the quadrupole response) of a pertubed eigenstate will have a frequency of $2\omega_0$, i.e. actually we have to compare ω with $2\omega_0$. The ground state of the static elliptical billiard has $E_0 = 4.27$, which results in $\omega_0 \approx 9.5$ (with $\hbar = 1$). When the driving frequency ω is comparable to ω_0, we expect effects of the driving, i.e. the initial state will not remain

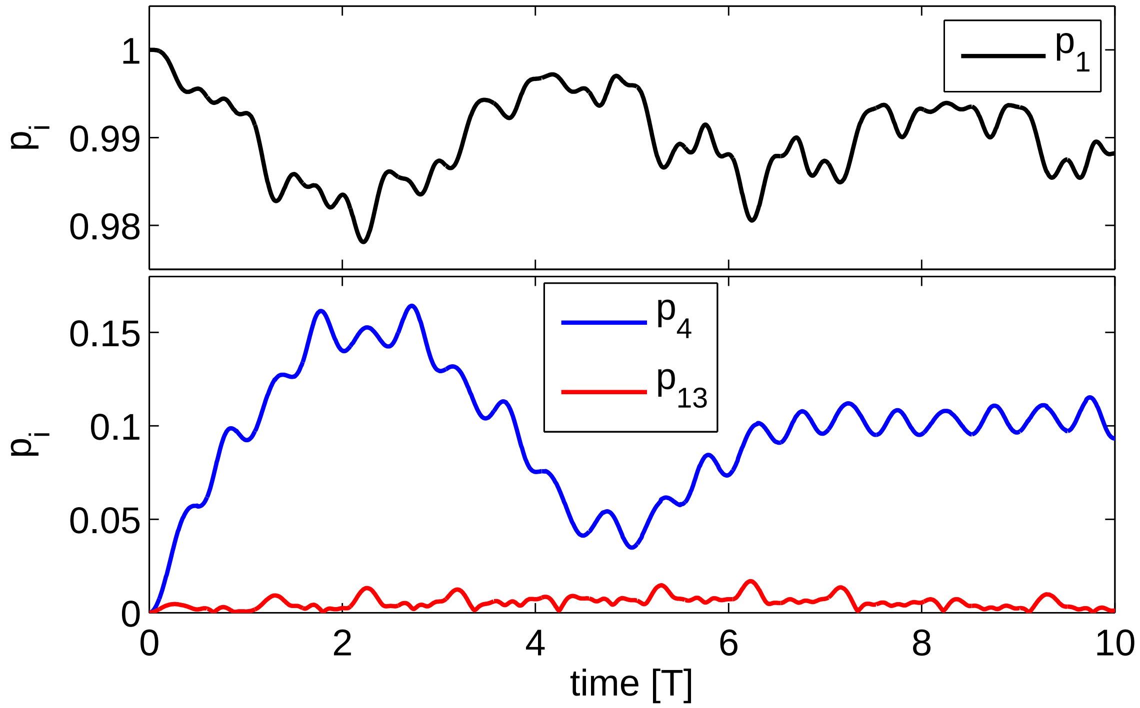

Figure 8.5: The population p_i of certain instantaneous eigenstates for the case $\omega = 10$ and $\Psi_0 = \Psi^e_{0,1}$ (ground state) as a function of time is shown. The coefficient p_1 corresponding to the instantaneous ground state is still dominant, however there are other coefficients which are considerably different from zero (also p_7 and p_{10} which are not shown here).

purely adiabatically in the instantaneous ground state.

The results for a driving frequency of $\omega = 10$, i.e. $\omega_0 \approx \omega$ for the ground state of the static billiard, are shown in Fig. 8.4, where the energy as a function of time for three (for better visibility) different initial states is plotted. Clearly, the evolution of the energy is not a pure oscillation like for $\omega = 1$ (see Fig. 8.4), there are some additional fluctuations. However, the energy $E(t)$ stays bounded, for example, $E(t)$ remains still in the region $3 < E(t) < 7$ for $\Psi_0 = \Psi^e_{0,1}$, even in the long-term evolution (not shown here). With increasing energy of the initial state, the adiabatic behavior is more and more recovered, since the typical frequencies of these states increase as well.

The population analysis yields that due to the higher driving frequency, higher excited instantaneous eigenstates are now populated. Exemplarily, this is shown in Fig. 8.5, where the initial state is chosen to be the instantaneous ground state, i.e. $\Psi_0 = \Psi^e_{0,1}(t = 0) \Rightarrow p_1(0) = 1$. Beside the coefficient p_1 corresponding to the initial state, the coefficients p_4 and p_{13} (also p_7 and p_{10} and some higher p_i, not shown here) get populated. The initial state $\Psi^e_{0,1}(t = 0)$ has the symmetries $\pi_x = \pi_y = +1$ and from Table 7.1 we see that instantaneous eigenstates associated with p_4, p_7, p_{10}, p_{13} have exactly the same symmetry properties. This suggests that preferably instantaneous eigenstates with the same symmetries as the initial state will get excited.

Finally, we use a very high driving frequency of $\omega = 100$. The evolution of the energy for three different initial states is shown in Fig. 8.6. The energy shows irregular fluctuations

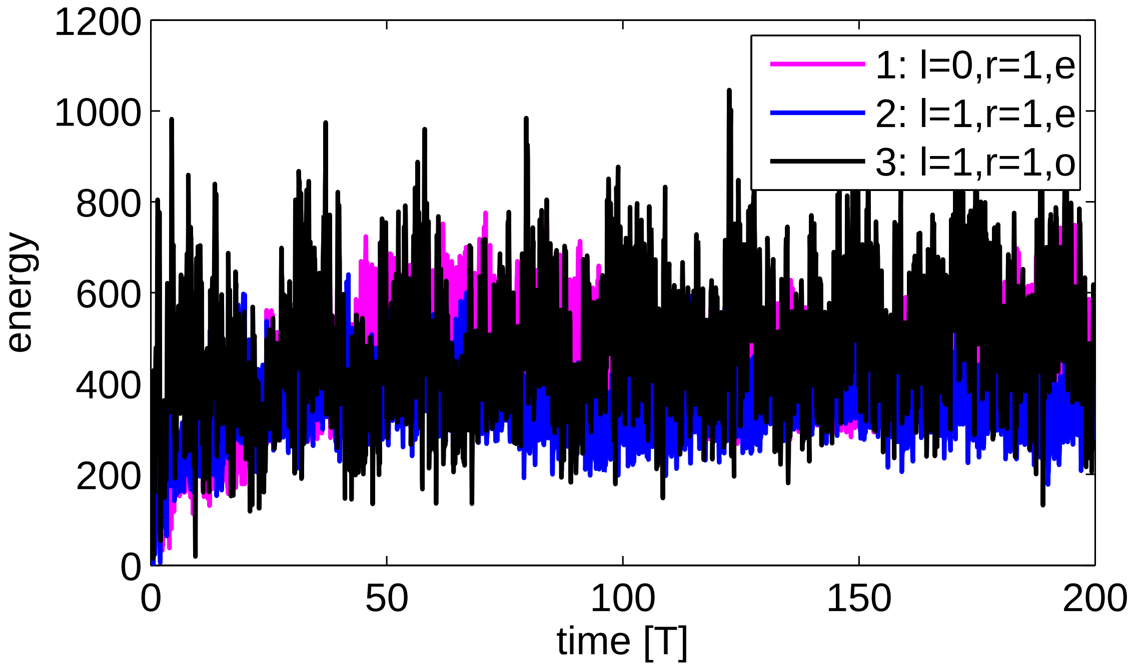

Figure 8.6: The evolution of the energy (in units of $\hbar^2/\mu$) for three different initial states $\Psi_{l,r}^{e,o}(t = 0)$ as a function of time, now for a driving frequency of $\omega = 100$. The energy shows irregular fluctuations, but stays bounded.

and is much higher than for $\omega = 1$ or for $\omega = 10$, but stays bounded. In particular, the energy grows diffusively until $T \approx 50$ and subsequently saturates. The driving frequency ω is now much higher than the frequency ω_0 associated with the initial states. As a consequence, the evolution of the energy depends barely on the initial state, i.e. all three curves in Fig. 8.6 show strong oscillations but stay approximately in the same energy regime.

The fact that the energy saturates and does not grow over all bounds is a well-known phenomenon in driven quantum systems. It is known as *dynamical localization* and was first observed in the case of the quantum kicked rotator [155–157]. Even though there is no simple quantitative explanation, qualitatively, dynamical localization can be interpreted as an interference phenomenon, i.e. destructive interference leads to a suppression of the growth of the energy. Dynamical localization can be viewed as a special case of Anderson localization [158]. Anderson localization (or strong localization) is the absence of diffusion of waves in random media, for example wave functions get exponentially localized in a certain media once the disorder exceeds a critical value. Whereas Anderson localization refers to the (diffusion in) configuration space, dynamical localization describes the same phenomenon in momentum space, actually they are completely equivalent from a mathematical point of view [1].

Whether the phenomenon observed in Fig. 8.6 actually corresponds to dynamical localization is still under investigation.

9 Conclusion and Outlook

9.1 Classical dynamics

Our investigation of three different driving modes of the driven elliptical billiard shows that all three modes exhibit Fermi acceleration (FA). However, whereas we observe subdiffusive transport in momentum space throughout the whole evolution in the *constant eccentricity mode*, the *breathing* and *quadrupole mode* show a crossover from sub- to normal diffusion after a very large number of collisions. All three modes have in common that the characteristic composition of the four-dimensional phase space changes with increasing velocity v. At low v, there is a large chaotic sea containing many small regular islands that enclose stable periodic orbits. With increasing v, bulky regular regions rapidly grow towards the separatrix, until for high v only small channels of chaotic motion are present around the separatrix region. The large regular structures act as impenetrable barriers for particles starting inside the low v chaotic sea. The bulky regular regions emanate from librator-type orbits on the one hand and from whispering-gallery orbits on the other hand. The origin of the large librator-type regular structures can be traced back to the existence of the well-known first invariant spanning curve in the corresponding one-dimensional Fermi-Ulam model. The stickiness properties are enhanced in the low v regime for all driving modes and reduced in the case of the breathing and quadrupole mode inside the thin channels of chaotic motion at high v, but not in the case of the constant eccentricity mode. This observation coincides with the density of the periodic orbits, which decreases significantly with increasing v in the case of the breathing and quadrupole mode but not in the case of the constant eccentricity mode. The enhancement and reduction of the stickiness properties are reflected in the distribution $\rho(l)$ of the length of the laminar (sticky) phases, which eventually determines whether the transport process in momentum space will be normal or subdiffusive: $\rho(l)$ is quantitatively different in the low and in the high v regime, in particular it decays for large l in the high v regime faster than in the low v regime. Since the particles show FA, the mean velocity of the propagating ensemble grows with increasing number of collisions. As a consequence, the ensemble probes in its evolution dynamically different parts of phase space (all modes) associated with varying stickiness properties (breathing and quadrupole mode), which induces the crossover from sub- to normal diffusion (breathing and quadrupole mode).

Concerning the question under which conditions FA will arise in two-dimensional (2D) driven billiards, the "LRA-conjecture" states that a sufficient condition for the occurrence of FA in a smoothly driven 2D billiard is the existence of a chaotic part in the phase space of the corresponding static system. Our discovery of FA in the driven elliptical billiard [114, 135, 141] shows that this is not a necessary condition (note that the static counterpart of the driven elliptical billiard is integrable, i.e. there are no chaotic parts in phase space). Meanwhile, the absence of FA in the a certain mode of an oval-shaped billiard [85] seemed to disprove the LRA-conjecture. We could resolve this contradiction by showing that the scaling mode of the oval does exhibit FA [140], however after a very long transient (this has been confirmed independently very recently in Ref. [142]). In this thesis we demonstrated that the driven elliptical billiard shows FA even in the constant eccentricity mode, which can be viewed as the most regular time-dependent perturbation of the static elliptical billiard, since it is a pure scaling. We thus conjecture, thereby augmenting the LRA-conjecture, that a necessary and sufficient condition for the presence of FA in a smoothly driven 2D billiard is the existence of at least one hyperbolic fixed point in the phase space of the corresponding static counterpart.

9.2 Quantum dynamics

The quantum version of the static elliptical billiard is solved by the well-known standard procedure based on the introduction of elliptical coordinates. The eigenstates are then the solutions of two Mathieu equations. However, there are some subtleties involved in this procedure: Even though the original differential equation decouples into two Mathieu equations, the separation constants do not decouple, i.e. effectively there are two eigenvalue problems that have to be solved simultaneously. Changing the eccentricity of the elliptical billiard results in a completely new eigenvalue problem. This is one of the reasons why in the driven billiard, in order to propagate an arbitrary initial state, the straightforward ansatz (which would automatically satisfy the time-dependent Dirichlet boundary conditions) of expanding the wave function in terms of the instantaneous eigenstates is not appropriate. Instead, we apply a series of transformations yielding a system with time-independent boundary conditions: Now, the wave function has to vanish on the unit circle. We thus expand the wave function of this new system into the eigenfunctions of the static circular billiard, which are (especially their derivatives) numerically much easier to handle than the Mathieu functions. Eventually, we obtain a (large) system of coupled ordinary differential equations for the time-dependent expansion coefficients which are numerically solved either by a Runge-Kutta Price-Dormand or an implicit Burlirsch-Stoer scheme.

The developed numerical method is successfully applied to propagate different initial states for the breathing mode of the elliptical billiard. As initial states, the first (in terms of the energy) eigenstates of the corresponding static billiard are used. While for low driving frequencies the evolution of the energy is purely adiabatic, with increasing frequency more and more higher excited states with the same symmetry properties as the initial state get populated. For high frequencies, the energy performs irregular fluctuations, independent of the initial state, but stays bounded. Whether this saturation of the energy is due to dynamical localization will be investigated in the future.

An interesting perspective is the possibility of Landau-Zener tunnelling [159, 160] in the driven elliptical billiard. As we saw in section 8.4 (in particular cf. Fig. 8.3), the energies of the instantaneous eigenstates vary when the shape of the elliptical billiard is changed. The main contribution of this energy variation is simply due to fact that the area of the elliptical billiard changes. Additionally, there is a contribution which is due to the varying eccentricity. In the case of the lowest eigenstates, see Fig. 8.3, this effect is neglegible and the energy levels remain well separated. However for higher excited states, this can lead to avoided crossings, as it is shown in Fig. 9.1. In principle, such avoided crossings can lead to population transfer between two such neighboring instantaneous eigenstates in the driven elliptical billiard. For even higher excited eigenstates, there are also multiple avoided crossings, coupling three or more states.

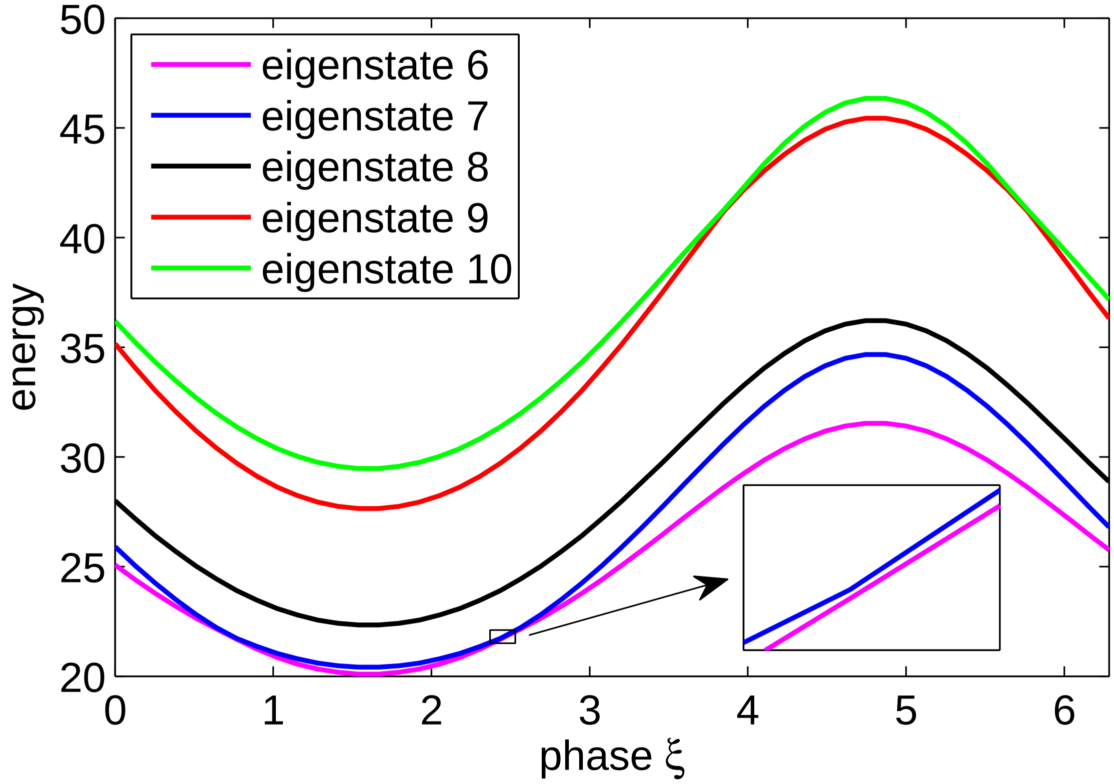

Figure 9.1: Energies (in units of $\hbar^2/\mu$) of five different eigenstates of the static elliptical billiard for different configurations of the boundary $\mathcal{B}(\xi)$. All the close approaches of two neighboring energy levels correspond to avoided crossings, exemplarily this is shown by magnifying one of them.

The key ingredient for the existence of these avoided crossings is the dependence of the eccentricity on the phase ξ of the oscillation. This leads, for example, to the interesting question whether the driving law can be adjusted in such a way that there is a cascade of avoided crossings, triggering the population of higher and higher excited states, even for comparatively low driving frequencies.

A Hamilton-Jacobi formalism of the static elliptical billiard

To derive the action-angle variables for the static elliptical billiard, we follow the discussion given in Ref. [108]. For a nice introduction to action-angle variables (Hamilton-Jacobi theory) see for example Ref. [34].

We start by changing form cartesian to elliptic coordinates:

$$x = f \cosh \xi \cos \eta, \quad 0 \le \xi \le \xi_0 \tag{A.1a}$$

$$y = f \sinh \xi \sin \eta, \quad 0 \le \phi < 2\pi, \tag{A.1b}$$

where $f = \sqrt{a^2 - b^2}$ is half the distance between the foci of an ellipse with semi-major axes a and semi-minor axes b and $\xi_0 = \operatorname{arctanh}(b/a)$. The eccentricity $\epsilon = \sqrt{1 - b^2/a^2}$ can be written as

$$\epsilon = \frac{f}{a} = \frac{1}{\cosh \xi_0}. \tag{A.2}$$

This means the generalized coordinates are $q_1 = \xi$ and $q_2 = \eta$. The Lagrangian in elliptic coordinates reads

$$\mathcal{L} = \frac{\mu h^2}{2} \left(\dot{\xi}^2 + \dot{\eta}^2 \right), \tag{A.3}$$

where μ is the mass of the particle and h is the metric factor

$$h^2 = \frac{f^2}{2} (\cosh 2\xi - \cos 2\eta). \tag{A.4}$$

The canonical momenta p_ξ and p_η are obtained in the standard way:

$$p_\xi = \frac{\partial \mathcal{L}}{\partial \dot{\xi}} = \mu h^2 \dot{\xi} \tag{A.5a}$$

$$p_\eta = \frac{\partial \mathcal{L}}{\partial \dot{\eta}} = \mu h^2 \dot{\eta}. \tag{A.5b}$$

A Legendre-tranformation of the Langrangian yields the classical Hamiltonian:

$$\mathcal{H} = \frac{p_\xi^2 + p_\eta^2}{2\mu h^2}, \tag{A.6}$$

which is of course equal to the total energy E, since the static elliptical billiard is a conservative system. Beside the energy, the product of the angular momenta around the foci is also conserved:

$$\Lambda = \mathbf{L}_1 \cdot \mathbf{L}_2 = (\mathbf{r}_1 \times \mu \mathbf{v}) \cdot (\mathbf{r}_2 \times \mu \mathbf{v}), \tag{A.7}$$

where

$$\mathbf{r}_1 = (x - f)\hat{\mathbf{x}} + y\hat{\mathbf{y}} \tag{A.8a}$$
$$\mathbf{r}_2 = (x + f)\hat{\mathbf{x}} + y\hat{\mathbf{y}} \tag{A.8b}$$

with the unit cartesian vectors $\hat{\mathbf{x}}$ and $\hat{\mathbf{y}}$. The velocity in elliptic coordinates is

$$\mathbf{v} = h\dot{\xi}\hat{\boldsymbol{\xi}} + h\dot{\eta}\hat{\boldsymbol{\eta}} \tag{A.9}$$

and the unit vectors $\hat{\boldsymbol{\xi}}$ and $\hat{\boldsymbol{\eta}}$ in elliptic coordinates are given by $\boldsymbol{\eta}$

$$\begin{pmatrix} \hat{\mathbf{x}} \\ \hat{\mathbf{y}} \end{pmatrix} = \frac{f}{h} \begin{pmatrix} \sinh \sin \cos \eta & -\cosh \xi \sin \eta \\ \cosh \xi \sin \eta & \sinh \xi \cos \eta \end{pmatrix} \begin{pmatrix} \hat{\boldsymbol{\xi}} \\ \hat{\boldsymbol{\eta}} \end{pmatrix}. \tag{A.10}$$

In elliptical coordinates, the conserved quantity λ (A.7) can be written as

$$\Lambda = \mu^2 f^2 h^2 \left(\dot{\eta}^2 \sinh^2 \xi - \dot{\xi}^2 \sin^2 \eta \right), \tag{A.11}$$

or in terms of the canonical momenta (A.5)

$$\Lambda = \frac{f^2}{h^2} \left(p_\eta^2 \sinh^2 \xi - p_\xi^2 \sin^2 \eta \right). \tag{A.12}$$

The range of Λ depends on the energy

$$\Lambda \in [-2\mu E f^2, 2\mu E b^2]. \tag{A.13}$$

It is usefull to scale this energy dependence out, i.e. we define

$$\gamma = \frac{\Lambda}{2\mu E b^2} \in \left[-\frac{f^2}{b^2}, 1 \right]. \tag{A.14}$$

This conicides with our definition of $F(\phi, \alpha)$ (2.11) for the corresponding mapping (note that $\gamma_{\text{min}} - f^2/b^2 = -\epsilon^2/(1-\epsilon^2) = F_{\text{min}}$). The canonical momenta (A.5) can be expressed in terms of the two constants of motion γ and E, a tedious calculation yields

$$p_\xi^2 = 2\mu E f^2 \left(\sinh^2 \xi - \frac{b^2}{f^2}\gamma \right) \tag{A.15a}$$
$$p_\eta^2 = 2\mu E f^2 \left(\sin^2 \eta + \frac{b^2}{f^2}\gamma \right). \tag{A.15b}$$

For generalized coordinates q_i and momenta p_i, the action variables J_i are given by [34]

$$J_i = \frac{1}{2\pi} \oint p_i dq_i \tag{A.16}$$

and the frequencies ω_i associated to the angle variables Θ_i by

$$\omega_i = \dot{\Theta}_i = \frac{\partial \mathcal{H}(J_i, \Theta_i)}{\partial J_i}. \tag{A.17}$$

By using the canonical momenta of Eq. (A.15), this yields

$$J_\xi = 2\sqrt{\frac{\mu E f^2}{2\pi^2}} \int_{\xi_c}^{\xi_0} \sqrt{\sinh^2 \xi - \frac{b^2}{f^2}\gamma} d\xi \tag{A.18a}$$

$$J_\eta = 4\sqrt{\frac{\mu E f^2}{2\pi^2}} \int_{\eta_c}^{\pi/2} \sqrt{\sin^2 \eta + \frac{b^2}{f^2}\gamma} d\eta. \tag{A.18b}$$

The lower integration limit depends on whether the trajectory is a librator or a rotator. For rotators, $\xi_c = \operatorname{arccosh}(1/\epsilon_c)$ and $\eta_c = 0$, for librators, $\xi_c = 0$ and $\eta_c = \operatorname{arccosh}(1/\epsilon_c)$. ϵ_c is the eccentricity of the caustic (confocal ellipse for rotators or two confocal hyperbolae for librators) and is

$$\epsilon_c = \frac{1}{\sqrt{1 + b^2\gamma^2/f^2}}. \tag{A.19}$$

The condition for periodic orbits is that the ratio of the frequencies (A.17) is a rational number:

$$\frac{\omega_\xi}{\omega_\eta} = \frac{\frac{\partial \mathcal{H}}{\partial J_\xi}}{\frac{\partial \mathcal{H}}{\partial J_\eta}} = \frac{\partial J_\eta}{\partial J_\xi} = \frac{\frac{\partial J_\eta}{\gamma}}{\frac{\partial J_\xi}{\partial \gamma}} = \frac{n}{r}, \tag{A.20}$$

where n is the number of bounces of a periodic orbit and r is the rotation number. Carrying out the differentiations in Eq. (A.20) finally yields the result of Eq. (2.13).

B Details of the quantum mechanical derivations

B.1 Matrix elements

Exemplarily, the matrix element $\langle\Lambda|\,\mathcal{H}_2\,|\Lambda\rangle$ is calculated in the text, see Eq. (8.37), the other matrix elements are presented here:

$$\begin{aligned}
&\langle\Lambda|\,\mathcal{H}_2\,|\Lambda\rangle = \\
&\quad \frac{\hbar^2}{\mu a^2(t)} \iint \frac{1}{r} dr d\phi \sum_{n,m,n',m'} c^*_{n,m}(t) c_{n',m'}(t) \Phi^*_{n,m}(r,\phi) \sin\phi\cos\phi \frac{\partial}{\partial\phi} \Phi_{n',m'}(r,\phi) \\
&\quad = \frac{2\hbar^2}{\mu a^2(t)} \sum_{n,m,n',m'} \frac{c^*_{nm}(t) c_{n'm'}(t)}{J_{m+1}(k_{m,n}) J_{m'+1}(k_{n'm'})} \int J_m(k_{m,n}r) J_{m'}(k_{n'm'}r) \frac{1}{r} dr \\
&\quad \frac{im'}{2\pi} \int \sin\phi\cos\phi\, e^{i\phi(m'-m)} d\phi = \ldots \int J_m(k_{m,n}r) J_{m'}(k_{n'm'}r) \frac{dr}{r} \\
&\left(\frac{m'}{4}\delta_{m,m'+2} - \frac{m'}{4}\delta_{m,m'-2}\right) = \cdots \sum_{n,m,n'} \cdots \int \left(\frac{m-2}{4} J_m(k_{m,n}r) J_{m-2}(k_{m-2,n'}r)\right. \\
&\qquad\qquad \left. - \frac{m+2}{4} J_m(k_{m,n}r) J_{m+2}(k_{m+2,n'}r)\right) \frac{dr}{r}
\end{aligned} \tag{B.1}$$

$$\begin{aligned}
&\langle\Lambda|\,\mathcal{H}_3\,|\Lambda\rangle = \\
&\quad \frac{-\hbar^2}{\mu a^2(t)} \iint dr d\phi \sum_{n,m,n',m'} c^*_{n,m}(t) c_{n',m'}(t) \Phi^*_{n,m}(r,\phi) \sin\phi\cos\phi \frac{\partial^2}{\partial\phi\partial r} \Phi_{n',m'}(r,\phi) \\
&\quad = \frac{-2\hbar^2}{\mu a^2(t)} \sum_{n,m,n',m'} \frac{c^*_{nm}(t) c_{n'm'}(t)}{J_{m+1}(k_{m,n}) J_{m'+1}(k_{n'm'})} \int J_m(k_{m,n}r) J'_{m'}(k_{n'm'}r) dr \\
&\quad \frac{im'}{2\pi} \int \sin\phi\cos\phi\, e^{i\phi(m'-m)} d\phi = \ldots \int J_m(k_{m,n}r) J'_{m'}(k_{n'm'}r) dr \\
&\left(\frac{m'}{4}\delta_{m,m'+2} - \frac{m'}{4}\delta_{m,m'-2}\right) = \cdots \sum_{n,m,n'} \cdots \int \left(\frac{m-2}{4} J_m(k_{m,n}r) J'_{m-2}(k_{m-2,n'}r)\right. \\
&\qquad\qquad \left. - \frac{m+2}{4} J_m(k_{m,n}r) J'_{m+2}(k_{m+2,n'}r)\right) dr \\
&\qquad\qquad \langle\Lambda|\,\mathcal{H}_4\,|\Lambda\rangle = \\
&\quad \frac{-\hbar^2}{2\mu a^2(t)} \iint dr d\phi \sum_{n,m,n',m'} c^*_{n,m}(t) c_{n',m'}(t) \Phi^*_{n,m}(r,\phi) \cos^2\phi \frac{\partial}{\partial r} \Phi_{n',m'}(r,\phi)
\end{aligned} \tag{B.2}$$

$$
\begin{aligned}
&= \frac{-\hbar^2}{\mu a^2(t)} \sum_{n,m,n',m'} \frac{c^*_{nm}(t)c_{n'm'}(t)}{J_{m+1}(k_{m,n})J_{m'+1}(k_{n'm'})} \int J_m(k_{m,n}r)J'_{m'}(k_{n'm'}r)dr \\
&\qquad \frac{1}{2\pi}\int \cos^2\phi\, e^{i\phi(m'-m)}d\phi = \dots \int J_m(k_{m,n}r)J'_{m'}(k_{n'm'}r)dr \\
&\left(\frac{1}{4}\delta_{m,m'+2}+\frac{1}{4}\delta_{m,m'-2}+\frac{1}{2}\delta_{mm'}\right) = \dots \frac{1}{4}\int \Big(J_m(k_{m,n}r)J'_{m-2}(k_{m-2,n'}r) \\
&\qquad + J_m(k_{m,n}r)J'_{m+2}(k_{m+2,n'}r) + 2J_m(k_{m,n}r)J'_m(k_{m,n'}r)\Big)dr
\end{aligned}
\tag{B.3}
$$

$$
\begin{aligned}
&\langle\Lambda|\,\mathcal{H}_5\,|\Lambda\rangle = \\
&\quad \frac{-\hbar^2}{2\mu a^2(t)} \iint \frac{dr}{r}d\phi \sum_{n,m,n',m'} c^*_{n,m}(t)c_{n',m'}(t)\Phi^*_{n,m}(r,\phi)\cos^2\phi\frac{\partial^2}{\partial\phi^2}\Phi_{n',m'}(r,\phi) \\
&= \frac{-\hbar^2}{\mu a^2(t)} \sum_{n,m,n',m'} \frac{c^*_{nm}(t)c_{n'm'}(t)}{J_{m+1}(k_{m,n})J_{m'+1}(k_{n'm'})} \int J_m(k_{m,n}r)J_{m'}(k_{n'm'}r)\frac{dr}{r}\left(\frac{-m'^2}{2\pi}\right) \\
&\qquad \int \cos^2\phi\, e^{i\phi(m'-m)}d\phi = \dots \frac{-m'^2}{4}\int J_m(k_{m,n}r)J_{m'}(k_{n'm'}r)\frac{dr}{r} \\
&\big(\delta_{m,m'+2}+\delta_{m,m'-2}+2\delta_{mm'}\big) = \dots \left(-\frac{1}{4}\right)\int \Big((m-2)^2J_m(k_{m,n}r)J_{m-2}(k_{m-2,n'}r) \\
&\qquad + (m+2)^2J_m(k_{m,n}r)J_{m+2}(k_{m+2,n'}r) + 2m^2J_m(k_{m,n}r)J_m(k_{m,n'}r)\Big)\frac{dr}{r}
\end{aligned}
\tag{B.4}
$$

$$
\begin{aligned}
&\langle\Lambda|\,\mathcal{H}_6\,|\Lambda\rangle = \\
&\quad \frac{-\hbar^2}{2\mu b^2(t)} \iint rdrd\phi \sum_{n,m,n',m'} c^*_{n,m}(t)c_{n',m'}(t)\Phi^*_{n,m}(r,\phi)\cos^2\phi\frac{\partial^2}{\partial r^2}\Phi_{n',m'}(r,\phi) \\
&= \frac{-\hbar^2}{\mu b^2(t)} \sum_{n,m,n',m'} \frac{c^*_{nm}(t)c_{n'm'}(t)}{J_{m+1}(k_{m,n})J_{m'+1}(k_{n'm'})} \int J_m(k_{m,n}r)J''_{m'}(k_{n'm'}r)rdr \\
&\qquad \frac{1}{2\pi}\int \cos^2\phi\, e^{i\phi(m'-m)}d\phi = \dots \int J_m(k_{m,n}r)J''_{m'}(k_{n'm'}r)rdr \\
&\left(\frac{1}{2}\delta_{m',m}+\frac{1}{4}\delta_{m'+2,m}+\frac{1}{4}\delta_{m'-2,m}\right) = \cdots \sum_{n,m,n'} \cdots \int \Big(\frac{1}{2}J_m(k_{m,n}r)J''_m(k_{n'm}r) \\
&\qquad + \frac{1}{4}J_m(k_{n'm}r)J''_{m+2}(k_{n,m+2}r) + \frac{1}{4}J_m(k_{n'm}r)J''_{m-2}(k_{n,m-2}r)\Big)rdr
\end{aligned}
\tag{B.5}
$$

$$
\begin{aligned}
&\langle\Lambda|\,\mathcal{H}_7\,|\Lambda\rangle = \\
&\quad \frac{-\hbar^2}{\mu b^2(t)} \iint \frac{1}{r} dr d\phi \sum_{n,m,n',m'} c^*_{n,m}(t) c_{n',m'}(t) \Phi^*_{n,m}(r,\phi) \sin\phi\cos\phi \frac{\partial}{\partial\phi}\Phi_{n',m'}(r,\phi) \\
&\quad = \frac{-2\hbar^2}{\mu b^2(t)} \sum_{n,m,n',m'} \frac{c^*_{nm}(t)c_{n'm'}(t)}{J_{m+1}(k_{m,n})J_{m'+1}(k_{n'm'})} \int J_m(k_{m,n}r)J_{m'}(k_{n'm'}r)\frac{1}{r}dr \\
&\qquad \frac{im'}{2\pi}\int \sin\phi\cos\phi\, e^{i\phi(m'-m)}d\phi = \dots \int J_m(k_{m,n}r)J_{m'}(k_{n'm'}r)\frac{dr}{r} \\
&\left(\frac{m'}{4}\delta_{m,m'+2} - \frac{m'}{4}\delta_{m,m'-2}\right) = \cdots \sum_{n,m,n'} \cdots \int \Bigg(\frac{m-2}{4} J_m(k_{m,n}r)J_{m-2}(k_{m-2,n'}r) \\
&\qquad\qquad - \frac{m+2}{4}J_m(k_{m,n}r)J_{m+2}(k_{m+2,n'}r)\Bigg)\frac{dr}{r}
\end{aligned}
\tag{B.6}
$$

$$
\begin{aligned}
&\langle\Lambda|\,\mathcal{H}_8\,|\Lambda\rangle = \\
&\quad \frac{\hbar^2}{\mu b^2(t)} \iint dr d\phi \sum_{n,m,n',m'} c^*_{n,m}(t) c_{n',m'}(t) \Phi^*_{n,m}(r,\phi) \sin\phi\cos\phi \frac{\partial^2}{\partial\phi\partial r}\Phi_{n',m'}(r,\phi) \\
&\quad = \frac{2\hbar^2}{\mu b^2(t)} \sum_{n,m,n',m'} \frac{c^*_{nm}(t)c_{n'm'}(t)}{J_{m+1}(k_{m,n})J_{m'+1}(k_{n'm'})} \int J_m(k_{m,n}r)J'_{m'}(k_{n'm'}r)dr \\
&\qquad \frac{im'}{2\pi}\int \sin\phi\cos\phi\, e^{i\phi(m'-m)}d\phi = \dots \int J_m(k_{m,n}r)J'_{m'}(k_{n'm'}r)dr \\
&\left(\frac{m'}{4}\delta_{m,m'+2} - \frac{m'}{4}\delta_{m,m'-2}\right) = \cdots \sum_{n,m,n'} \cdots \int \Bigg(\frac{m-2}{4} J_m(k_{m,n}r)J'_{m-2}(k_{m-2,n'}r) \\
&\qquad\qquad - \frac{m+2}{4}J_m(k_{m,n}r)J'_{m+2}(k_{m+2,n'}r)\Bigg)dr
\end{aligned}
\tag{B.7}
$$

$$
\begin{aligned}
&\langle\Lambda|\,\mathcal{H}_9\,|\Lambda\rangle = \\
&\quad \frac{-\hbar^2}{2\mu b^2(t)} \iint dr d\phi \sum_{n,m,n',m'} c^*_{n,m}(t) c_{n',m'}(t) \Phi^*_{n,m}(r,\phi) \sin^2\phi \frac{\partial}{\partial r}\Phi_{n',m'}(r,\phi) \\
&\quad = \frac{-\hbar^2}{\mu b^2(t)} \sum_{n,m,n',m'} \frac{c^*_{nm}(t)c_{n'm'}(t)}{J_{m+1}(k_{m,n})J_{m'+1}(k_{n'm'})} \int J_m(k_{m,n}r)J'_{m'}(k_{n'm'}r)dr \\
&\qquad \frac{1}{2\pi}\int \sin^2\phi\, e^{i\phi(m'-m)}d\phi = \dots \int J_m(k_{m,n}r)J'_{m'}(k_{n'm'}r)dr \\
&\left(-\frac{1}{4}\delta_{m,m'+2} - \frac{1}{4}\delta_{m,m'-2} + \frac{1}{2}\delta_{mm'}\right) = \dots \frac{1}{4}\int \Big(- J_m(k_{m,n}r)J'_{m-2}(k_{m-2,n'}r) \\
&\qquad\qquad - J_m(k_{m,n}r)J'_{m+2}(k_{m+2,n'}r) + 2J_m(k_{m,n}r)J'_m(k_{m,n'}r)\Big)dr
\end{aligned}
\tag{B.8}
$$

$$
\begin{aligned}
&\langle\Lambda|\,\mathcal{H}_{10}\,|\Lambda\rangle = \\
&\quad \frac{-\hbar^2}{2\mu b^2(t)} \iint \frac{dr}{r} d\phi \sum_{n,m,n',m'} c^*_{n,m}(t) c_{n',m'}(t) \Phi^*_{n,m}(r,\phi) \sin^2\phi \frac{\partial^2}{\partial\phi^2} \Phi_{n',m'}(r,\phi) \\
&= \frac{-\hbar^2}{\mu b^2(t)} \sum_{n,m,n',m'} \frac{c^*_{nm}(t) c_{n'm'}(t)}{J_{m+1}(k_{m,n}) J_{m'+1}(k_{n'm'})} \int J_m(k_{m,n}r) J_{m'}(k_{n'm'}r) \frac{dr}{r} \left(\frac{-m'^2}{2\pi}\right) \\
&\qquad \int \sin^2\phi\, e^{i\phi(m'-m)} d\phi = \ldots \frac{m'^2}{4} \int J_m(k_{m,n}r) J_{m'}(k_{n'm'}r) \frac{dr}{r} \\
&\big(\delta_{m,m'+2} + \delta_{m,m'-2} - 2\delta_{mm'}\big) = \cdots \sum_{n,m,n'} \ldots \frac{1}{4} \int \Bigg((m-2)^2 J_m(k_{m,n}r) J_{m-2}(k_{m-2,n'}r) \\
&\qquad + (m+2)^2 J_m(k_{m,n}r) J_{m+2}(k_{m+2,n'}r) - 2m^2 J_m(k_{m,n}r) J_m(k_{m,n'}r) \Bigg) \frac{dr}{r} \qquad \text{(B.9)}
\end{aligned}
$$

$$
\begin{aligned}
&\langle\Lambda|\,\mathcal{H}_{11}\,|\Lambda\rangle = \\
&\quad \frac{\mu}{2} a(t)\ddot{a}(t) \iint r^3 dr d\phi \sum_{n,m,n',m'} c^*_{n,m}(t) c_{n',m'}(t) \Phi^*_{n,m}(r,\phi) \cos^2\phi \Phi_{n',m'}(r,\phi) \\
&= \mu a(t)\ddot{a}(t) \sum_{n,m,n',m'} \frac{c^*_{nm}(t) c_{n'm'}(t)}{J_{m+1}(k_{m,n}) J_{m'+1}(k_{n'm'})} \int J_m(k_{m,n}r) J_{m'}(k_{n'm'}r) r^3 dr \\
&\qquad \frac{1}{2\pi} \int \cos^2\phi\, e^{i\phi(m'-m)} d\phi = \ldots \frac{1}{4} \int J_m(k_{m,n}r) J_{m'}(k_{n'm'}r) r^3 dr \\
&\big(\delta_{m,m'+2} + \delta_{m,m'-2} + 2\delta_{mm'}\big) = \cdots \sum_{n,m,n'} \ldots \frac{1}{4} \int \Bigg(J_m(k_{m,n}r) J_{m-2}(k_{m-2,n'}r) \\
&\qquad + J_m(k_{m,n}r) J_{m+2}(k_{m+2,n'}r) + 2 J_m(k_{m,n}r) J_m(k_{m,n'}r) \Bigg) r^3 dr \qquad \text{(B.10)}
\end{aligned}
$$

$$
\begin{aligned}
&\langle\Lambda|\,\mathcal{H}_{12}\,|\Lambda\rangle = \\
&\quad \frac{\mu}{2} b(t)\ddot{b}(t) \iint r^3 dr d\phi \sum_{n,m,n',m'} c^*_{n,m}(t) c_{n',m'}(t) \Phi^*_{n,m}(r,\phi) \sin^2\phi \Phi_{n',m'}(r,\phi) \\
&= \mu b(t)\ddot{b}(t) \sum_{n,m,n',m'} \frac{c^*_{nm}(t) c_{n'm'}(t)}{J_{m+1}(k_{m,n}) J_{m'+1}(k_{n'm'})} \int J_m(k_{m,n}r) J_{m'}(k_{n'm'}r) r^3 dr \\
&\qquad \frac{1}{2\pi} \int \sin^2\phi\, e^{i\phi(m'-m)} d\phi = \ldots \frac{1}{4} \int J_m(k_{m,n}r) J_{m'}(k_{n'm'}r) r^3 dr \\
&\big(-\delta_{m,m'+2} - \delta_{m,m'-2} + 2\delta_{mm'}\big) = \cdots \sum_{n,m,n'} \ldots \frac{1}{4} \int \Bigg(- J_m(k_{m,n}r) J_{m-2}(k_{m-2,n'}r) \\
&\qquad - J_m(k_{m,n}r) J_{m+2}(k_{m+2,n'}r) + 2 J_m(k_{m,n}r) J_m(k_{m,n'}r) \Bigg) r^3 dr. \qquad \text{(B.11)}
\end{aligned}
$$

B.2 Relations betwenn the $I^i_{nmn'}$ and the $L^i_{nmn'}$

$$\begin{aligned}
I^1_{nmn'} &= \frac{k^2_{n',m}}{4}\left(L^1_{nmn'} - 2L^2_{nmn'} + L^3_{nmn'}\right)\\
I^2_{nmn'} &= \frac{k^2_{n',m+2}}{4}\left(L^4_{nmn'} - 2L^5_{nmn'} + L^6_{nmn'}\right)\\
I^3_{nmn'} &= \frac{k^2_{n',m-2}}{4}\left(L^7_{nmn'} - 2L^8_{nmn'} + L^9_{nmn'}\right)\\
I^4_{nmn'} &= \frac{k_{m,n'}}{2m}\left(L^{10}_{nmn'} + L^{11}_{nmn'}\right)\\
I^5_{nmn'} &= \frac{k_{m-2,n'}}{2(m-2)}\left(L^{12}_{nmn'} + L^{13}_{nmn'}\right)\\
I^6_{nmn'} &= \frac{k_{m+2,n'}}{2(m+2)}\left(L^{14}_{nmn'} + L^{15}_{nmn'}\right)\\
I^7_{nmn'} &= \frac{k_{m,n'}}{2}\left(L^{10}_{nmn'} - L^{11}_{nmn'}\right)\\
I^8_{nmn'} &= \frac{k_{m+2,n'}}{2}\left(L^{14}_{nmn'} - L^{15}_{nmn'}\right)\\
I^9_{nmn'} &= \frac{k_{m-2,n'}}{2}\left(L^{12}_{nmn'} - L^{13}_{nmn'}\right)\\
I^{10}_{nmn'} &= L^{16}_{nmn'}\\
I^{11}_{nmn'} &= L^{17}_{nmn'}\\
I^{12}_{nmn'} &= L^{18}_{nmn'}
\end{aligned}$$

B.3 Matrix elements, short form

$$\begin{aligned}
\langle\Lambda|\,H_2\,|\Lambda\rangle = \frac{2\hbar^2}{\mu a^2(t)}\sum_{nmn'}\frac{c^*_{nm}(t)}{J_{m+1}(k_{m,n})}\Bigg(&\frac{(m-2)c_{n',m-2}(t)}{4J_{m-1}(k_{m-2,n'})}I^5_{nmn'}\\
&- \frac{(m+2)c_{n',m+2}(t)}{4J_{m+3}(k_{m+2,n'})}I^6_{nmn'}\Bigg)
\end{aligned}\tag{B.12}$$

$$\begin{aligned}
\langle\Lambda|\,H_3\,|\Lambda\rangle = \frac{-2\hbar^2}{\mu a^2(t)}\sum_{nmn'}\frac{c^*_{nm}(t)}{J_{m+1}(k_{m,n})}\Bigg(&\frac{(m-2)c_{n',m-2}(t)}{4J_{m-1}(k_{m-2,n'})}I^9_{nmn'}\\
&- \frac{(m+2)c_{n',m+2}(t)}{4J_{m+3}(k_{m+2,n'})}I^8_{nmn'}\Bigg)
\end{aligned}\tag{B.13}$$

$$\begin{aligned}\langle\Lambda|\,H_4\,|\Lambda\rangle = \frac{-\hbar^2}{\mu a^2(t)}\sum_{nmn'}\frac{c^*_{nm}(t)}{J_{m+1}(k_{m,n})}\bigg(&\frac{c_{n',m-2}(t)}{4J_{m-1}(k_{m-2,n'})}I^9_{nmn'}\\&+\frac{c_{n',m+2}(t)}{4J_{m+3}(k_{m+2,n'})}I^8_{nmn'}+\frac{c_{n',m}(t)}{2J_{m+1}(k_{m,n'})}I^7_{nmn'}\bigg)\end{aligned}\tag{B.14}$$

$$\begin{aligned}\langle\Lambda|\,H_5\,|\Lambda\rangle = \frac{\hbar^2}{\mu a^2(t)}\sum_{nmn'}\frac{c^*_{nm}(t)}{J_{m+1}(k_{m,n})}\bigg(&\frac{(m-2)^2c_{n',m-2}(t)}{4J_{m-1}(k_{m-2,n'})}I^5_{nmn'}\\&+\frac{(m+2)^2c_{n',m+2}(t)}{4J_{m+3}(k_{m+2,n'})}I^6_{nmn'}+\frac{m^2c_{n',m}(t)}{2J_{m+1}(k_{m,n'})}I^4_{nmn'}\bigg)\end{aligned}\tag{B.15}$$

$$\begin{aligned}\langle\Lambda|\,H_6\,|\Lambda\rangle = \frac{-\hbar^2}{\mu b^2(t)}\sum_{nmn'}\frac{c^*_{nm}(t)}{J_{m+1}(k_{m,n})}\bigg(&\frac{c_{n'm}(t)}{2J_{m+1}(k_{n'm})}I^1_{nmn'}\\&+\frac{c_{n',m-2}(t)}{4J_{m-1}(k_{m-2,n'})}I^3_{nmn'}+\frac{c_{n',m+2}(t)}{4J_{m+3}(k_{m+2,n'})}I^2_{nmn'}\bigg)\end{aligned}\tag{B.16}$$

$$\begin{aligned}\langle\Lambda|\,H_7\,|\Lambda\rangle = \frac{-2\hbar^2}{\mu b^2(t)}\sum_{nmn'}\frac{c^*_{nm}(t)}{J_{m+1}(k_{m,n})}\bigg(&\frac{(m-2)c_{n',m-2}(t)}{4J_{m-1}(k_{m-2,n'})}I^5_{nmn'}\\&-\frac{(m+2)c_{n',m+2}(t)}{4J_{m+3}(k_{m+2,n'})}I^6_{nmn'}\bigg)\end{aligned}\tag{B.17}$$

$$\begin{aligned}\langle\Lambda|\,H_8\,|\Lambda\rangle = \frac{2\hbar^2}{\mu b^2(t)}\sum_{nmn'}\frac{c^*_{nm}(t)}{J_{m+1}(k_{m,n})}\bigg(&\frac{(m-2)c_{n',m-2}(t)}{4J_{m-1}(k_{m-2,n'})}I^9_{nmn'}\\&-\frac{(m+2)c_{n',m+2}(t)}{4J_{m+3}(k_{m+2,n'})}I^8_{nmn'}\bigg)\end{aligned}\tag{B.18}$$

$$\begin{aligned}\langle\Lambda|\,H_9\,|\Lambda\rangle = \frac{-\hbar^2}{\mu b^2(t)}\sum_{nmn'}\frac{c^*_{nm}(t)}{J_{m+1}(k_{m,n})}\bigg(&-\frac{c_{n',m-2}(t)}{4J_{m-1}(k_{m-2,n'})}I^9_{nmn'}\\&-\frac{c_{n',m+2}(t)}{4J_{m+3}(k_{m+2,n'})}I^8_{nmn'}+\frac{c_{n',m}(t)}{2J_{m+1}(k_{m,n'})}I^7_{nmn'}\bigg)\end{aligned}\tag{B.19}$$

$$\begin{aligned}\langle\Lambda|\,H_{10}\,|\Lambda\rangle = \frac{-\hbar^2}{\mu b^2(t)}\sum_{nmn'}\frac{c^*_{nm}(t)}{J_{m+1}(k_{m,n})}\bigg(&\frac{(m-2)^2c_{n',m-2}(t)}{4J_{m-1}(k_{m-2,n'})}I^5_{nmn'}\\&+\frac{(m+2)^2c_{n',m+2}(t)}{4J_{m+3}(k_{m+2,n'})}I^6_{nmn'}-\frac{m^2c_{n',m}(t)}{2J_{m+1}(k_{m,n'})}I^4_{nmn'}\bigg)\end{aligned}\tag{B.20}$$

$$\begin{aligned}\langle\Lambda|\, H_{11}\,|\Lambda\rangle = \mu a(t)\ddot{a}(t)\sum_{nmn'}\frac{c^*_{nm}(t)}{J_{m+1}(k_{m,n})}\bigg(&\frac{c_{n',m-2}(t)}{4J_{m-1}(k_{m-2,n'})}I^{12}_{nmn'}\\ &+\frac{c_{n',m+2}(t)}{4J_{m+3}(k_{m+2,n'})}I^{11}_{nmn'}+\frac{c_{n',m}(t)}{2J_{m+1}(k_{m,n'})}I^{10}_{nmn'}\bigg)\end{aligned} \qquad \text{(B.21)}$$

$$\begin{aligned}\langle\Lambda|\, H_{12}\,|\Lambda\rangle = \mu b(t)\ddot{b}(t)\sum_{nmn'}\frac{c^*_{nm}(t)}{J_{m+1}(k_{m,n})}\bigg(&-\frac{c_{n',m-2}(t)}{4J_{m-1}(k_{m-2,n'})}I^{12}_{nmn'}\\ &-\frac{c_{n',m+2}(t)}{4J_{m+3}(k_{m+2,n'})}I^{11}_{nmn'}+\frac{c_{n',m}(t)}{2J_{m+1}(k_{m,n'})}I^{10}_{nmn'}\bigg)\end{aligned} \qquad \text{(B.22)}$$

B.4 Derivation of the ODE system

Collecting all the matrix elements $\langle\Lambda|\, H_i\,|\Lambda\rangle$, $i = 1, 2, \ldots 12$, the system of coupled differential equations for the $c_{nm}(t)$ can be written as:

$$\begin{aligned}i\hbar\dot{c}_{n,m}(t) = \frac{1}{J_{m+1}(k_{m,n})}\sum_{n'}\bigg\{&\frac{c_{n',m}(t)}{J_{m+1}(k_{m,n'})}\bigg[\frac{-\hbar^2}{\mu a^2(t)}\bigg(\frac{1}{2}I^1_{nmn'}+\frac{1}{2}I^7_{nmn'}-\frac{m^2}{2}I^4_{nmn'}\bigg)\\
&-\frac{\hbar^2}{\mu b^2(t)}\bigg(\frac{1}{2}I^1_{nmn'}+\frac{1}{2}I^7_{nmn'}-\frac{m^2}{2}I^4_{nmn'}\bigg)+\frac{\mu I^{10}_{nmn'}}{2}\Big(a(t)\ddot{a}(t)+b(t)\ddot{b}(t)\Big)\bigg]+\\
&\frac{c_{n',m-2}(t)}{J_{m-1}(k_{m-2,n'})}\bigg[\frac{-\hbar^2}{\mu a^2(t)}\bigg(-\frac{1}{4}I^3_{nmn'}-\frac{(m-2)}{2}I^5_{nmn'}+\frac{2m-3}{4}I^9_{nmn'}-\frac{(m-2)^2}{4}I^5_{nmn'}\bigg)\\
&-\frac{\hbar^2}{\mu b^2(t)}\bigg(\frac{1}{4}I^3_{nmn'}+\frac{(m-2)}{2}I^5_{nmn'}-\frac{(m-2)}{2}I^9_{nmn'}-\frac{1}{4}I^9_{nmn'}+\frac{(m-2)^2}{4}I^5_{nmn'}\bigg)+\\
&\frac{\mu I^{12}_{nmn'}}{4}\Big(a(t)\ddot{a}(t)-b(t)\ddot{b}(t)\Big)\bigg]+\frac{c_{n',m+2}(t)}{J_{m+3}(k_{m+2,n'})}\bigg[\frac{-\hbar^2}{\mu a^2(t)}\bigg(-\frac{1}{4}I^2_{nmn'}+\frac{(m+2)}{2}I^6_{nmn'}\\
&-\frac{(m+2)}{2}I^8_{nmn'}+\frac{1}{4}I^8_{nmn'}-\frac{(m+2)^2}{4}I^6_{nmn'}\bigg)-\frac{\hbar^2}{\mu b^2(t)}\bigg(\frac{1}{4}I^2_{nmn'}-\frac{(m+2)}{2}I^6_{nmn'}+\\
&\frac{(m+2)}{2}I^8_{nmn'}-\frac{1}{4}I^8_{nmn'}+\frac{(m+2)^2}{4}I^6_{nmn'}\bigg)+\frac{\mu I^{11}_{nmn'}}{4}\Big(a(t)\ddot{a}(t)-b(t)\ddot{b}(t)\Big)\bigg]\bigg\}.\end{aligned} \qquad \text{(B.23)}$$

ODE system, short form

$$i\hbar\dot{c}_{n,m}(t) = \sum_{n'}\big\{c_{n',m}(t)d^1_{nmn'}(t)+c_{n',m-2}(t)d^2_{nmn'}(t)+c_{n',m+2}(t)d^3_{nmn'}(t)\big\} \qquad \text{(B.24)}$$

where $d^j_{nmn'}$, $j = 1, 2, 3$ are time-dependent coefficients given by

$$\begin{aligned}d^1_{nmn'} = \frac{1}{J_{m+1}(k_{m,n})J_{m+1}(k_{m,n'})}\bigg[&\frac{-\hbar^2}{\mu a^2(t)}\bigg(\frac{1}{2}I^1_{nmn'}+\frac{1}{2}I^7_{nmn'}-\frac{m^2}{2}I^4_{nmn'}\bigg)\\
&-\frac{\hbar^2}{\mu b^2(t)}\bigg(\frac{1}{2}I^1_{nmn'}+\frac{1}{2}I^7_{nmn'}-\frac{m^2}{2}I^4_{nmn'}\bigg)+\frac{\mu I^{10}_{nmn'}}{2}\Big(a(t)\ddot{a}(t)+b(t)\ddot{b}(t)\Big)\bigg]\end{aligned} \qquad \text{(B.25)}$$

$$
\begin{aligned}
d^2_{nmn'} = {} & \frac{1}{J_{m+1}(k_{m,n})J_{m-1}(k_{m-2,n'})}\Bigg[\frac{-\hbar^2}{\mu a^2(t)}\Bigg(-\frac{1}{4}I^3_{nmn'} - \frac{(m-2)}{2}I^5_{nmn'} + \\
& \frac{(m-2)}{2}I^9_{nmn'} + \frac{1}{4}I^9_{nmn'} - \frac{(m-2)^2}{4}I^5_{nmn'}\Bigg) - \frac{\hbar^2}{\mu b^2(t)}\Bigg(\frac{1}{4}I^3_{nmn'} + \frac{(m-2)}{2}I^5_{nmn'} \\
& - \frac{(m-2)}{2}I^9_{nmn'} - \frac{1}{4}I^9_{nmn'} + \frac{(m-2)^2}{4}I^5_{nmn'}\Bigg) + \frac{\mu I^{12}_{nmn'}}{4}\Big(a(t)\ddot{a}(t) - b(t)\ddot{b}(t)\Big)\Bigg]
\end{aligned}
\tag{B.26}
$$

$$
\begin{aligned}
d^3_{nmn'} = {} & \frac{1}{J_{m+1}(k_{m,n})J_{m+3}(k_{m+2,n'})}\Bigg[\frac{-\hbar^2}{\mu a^2(t)}\Bigg(-\frac{1}{4}I^2_{nmn'} + \frac{(m+2)}{2}I^6_{nmn'} - \\
& \frac{(m+2)}{2}I^8_{nmn'} + \frac{1}{4}I^8_{nmn'} - \frac{(m+2)^2}{4}I^6_{nmn'}\Bigg) - \frac{\hbar^2}{\mu b^2(t)}\Bigg(\frac{1}{4}I^2_{nmn'} - \frac{(m+2)}{2}I^6_{nmn'} + \\
& \frac{(m+2)}{2}I^8_{nmn'} - \frac{1}{4}I^8_{nmn'} + \frac{(m+2)^2}{4}I^6_{nmn'}\Bigg) + \frac{\mu I^{11}_{nmn'}}{4}\Big(a(t)\ddot{a}(t) - b(t)\ddot{b}(t)\Big)\Bigg]
\end{aligned}
\tag{B.27}
$$

Or in terms of the $L^i_{nmn'}$

$$
\begin{aligned}
d^1_{nmn'} = {} & \frac{1}{J_{m+1}(k_{m,n})J_{m+1}(k_{m,n'})}\Bigg[\Bigg(-\frac{\hbar^2}{\mu a^2(t)} - \frac{\hbar^2}{\mu b^2(t)}\Bigg)\Bigg(\frac{k^2_{m,n'}}{8}(L^1_{nmn'} \\
& - 2L^2_{nmn'} + L^3_{nmn'}) + \frac{k_{m,n'}}{4}(L^{10}_{nmn'} - L^{11}_{nmn'}) - \frac{mk_{m,n'}}{4}(L^{10}_{nmn'} + L^{11}_{nmn'})\Bigg) \\
& + \frac{\mu L^{16}_{nmn'}}{2}\Big(a(t)\ddot{a}(t) + b(t)\ddot{b}(t)\Big)\Bigg]
\end{aligned}
\tag{B.28}
$$

$$
\begin{aligned}
d^2_{nmn'} = {} & \frac{1}{J_{m+1}(k_{m,n})J_{m-1}(k_{m-2,n'})}\Bigg[\Bigg(\frac{\hbar^2}{\mu a^2(t)} - \frac{\hbar^2}{\mu b^2(t)}\Bigg)\Bigg(\frac{k^2_{m-2,n'}}{16}(L^7_{nmn'} \\
& - 2L^8_{nmn'} + L^9_{nmn'}) + \frac{k_{m-2,n'}}{4}(L^{12}_{nmn'} + L^{13}_{nmn'}) - \frac{(m-2)k_{m-2,n'}}{4}(L^{12}_{nmn'} - L^{13}_{nmn'}) \\
& - \frac{k_{m-2,n'}}{8}(L^{12}_{nmn'} - L^{13}_{nmn'}) + \frac{(m-2)k_{m-2,n'}}{8}(L^{12}_{nmn'} + L^{13}_{nmn'})\Bigg) \\
& + \frac{\mu L^{18}_{nmn'}}{4}\Big(a(t)\ddot{a}(t) - b(t)\ddot{b}(t)\Big)\Bigg]
\end{aligned}
\tag{B.29}
$$

$$
\begin{aligned}
d^3_{nmn'} = {} & \frac{1}{J_{m+1}(k_{m,n})J_{m+3}(k_{m+2,n'})}\Bigg[\Bigg(\frac{\hbar^2}{\mu a^2(t)} - \frac{\hbar^2}{\mu b^2(t)}\Bigg)\Bigg(\frac{k^2_{m+2,n'}}{16}(L^4_{nmn'} \\
& - 2L^5_{nmn'} + L^6_{nmn'}) - \frac{k_{m+2,n'}}{4}(L^{14}_{nmn'} + L^{15}_{nmn'}) + \frac{(m+2)k_{m+2,n'}}{4}(L^{14}_{nmn'} - L^{15}_{nmn'}) \\
& - \frac{k_{m+2,n'}}{8}(L^{14}_{nmn'} - L^{15}_{nmn'}) + \frac{(m+2)k_{m+2,n'}}{8}(L^{14}_{nmn'} + L^{15}_{nmn'})\Bigg) \\
& + \frac{\mu L^{17}_{nmn'}}{4}\Big(a(t)\ddot{a}(t) - b(t)\ddot{b}(t)\Big)\Bigg].
\end{aligned}
\tag{B.30}
$$

Collecting all terms with the same L^i yields the expressions for the $d^i_{nmn'}$ given in Eqs. (8.51), (8.53) and (8.53).

B.5 Definition of the $f^i_{n,-m,n'}$

$$\begin{aligned}
f^1_{n-mn'} &= \frac{k^2_{m,n'}(L^1_{nmn'} - 2L^2_{nmn'} + L^3_{nmn'}) - 2k_{m,n'}(m+1)L^{11}_{nmn'}}{8J_{m-1}(k_{m,n})J_{m-1}(k_{n'm})} \\
&\quad - \frac{2k_{m,n'}(m-1)L^{10}_{nmn'}}{8J_{m-1}(k_{m,n})J_{m-1}(k_{n'm})} \qquad \text{(B.31a)} \\
f^2_{n-mn'} &= \frac{L^{16}_{nmn'}}{2J_{m-1}(k_{m,n})J_{m-1}(k_{n'm})} \qquad \text{(B.31b)} \\
f^3_{n-mn'} &= \frac{k^2_{m+2,n'}(L^6_{nmn'} - 2L^5_{nmn'} + L^4_{nmn'}) + 6k_{m+2,n'}(m+1)L^{14}_{nmn'}}{16J_{m-1}(k_{m,n})J_{m+1}(k_{m+2,n'})} \\
&\quad - \frac{2k_{m+2,n'}(m+3)L^{15}_{nmn'}}{16J_{m-1}(k_{m,n})J_{m+1}(k_{m+2,n'})} \qquad \text{(B.31c)} \\
f^4_{n-mn'} &= \frac{L^{17}_{nmn'}}{4J_{m-1}(k_{m,n})J_{m+1}(k_{m+2,n'})} \qquad \text{(B.31d)} \\
f^5_{n-mn'} &= \frac{k^2_{m-2,n'}(L^9_{nmn'} - 2L^8_{nmn'} + L^7_{nmn'}) + 6k_{m-2,n'}(m-1)L^{13}_{nmn'}}{16J_{m-1}(k_{m,n})J_{m-3}(k_{m-2,n'})} \\
&\quad - \frac{2k_{m-2,n'}(m-3)L^{12}_{nmn'}}{16J_{m-1}(k_{m,n})J_{m-3}(k_{m-2,n'})} \qquad \text{(B.31e)} \\
f^6_{n-mn'} &= \frac{L^{18}_{nmn'}}{4J_{m-1}(k_{m,n})J_{m-3}(k_{m-2,n'})} \qquad \text{(B.31f)}
\end{aligned}$$

B.6 Matrix elements, energy

Applying the Hamiltonian (8.23) on

$$\tilde{\Psi}_{n',m'}(r,\phi,t) = 2e^{\frac{i\mu}{2\hbar}r^2\left(\dot{a}a+\sin^2\phi(\dot{b}b-\dot{a}a),\right)}\Phi_{n',m'}(r,\phi), \qquad \text{(B.32)}$$

multiplying the result with $\tilde{\Psi}_{n,m}(r,\phi,t)$, integrating over the angular coordinate ϕ and summing over the index m' yields

$$
\begin{aligned}
&\sum_{m'} \int_0^{2\pi} \tilde{\Psi}^*_{nm}(r,\phi)\mathcal{H}(r,\phi,t)\tilde{\Psi}_{n'm'}(r,\phi)d\phi = -\frac{J_m(k_{mn}r)}{4a^2b^2\mu r^2 J_{m+1}(k_{mn})}\Bigg\{ r^2\hbar^2 \times \\
&\frac{2k^2_{mn'}(a^2+b^2)}{J_{m+1}(k_{mn'})}\Big[J_{m-2}(k_{mn'}r) - 2J_m(k_{mn'}r) + J_{m+2}(k_{mn'}r)\Big] + \frac{k^2_{m+2,n'}(a^2-b^2)}{J_{m+3}(k_{m+2,n'})}\times \\
&\Big[J_m(k_{m+2,n'}r) - 2J_{m+2}(k_{m+2,n'}r) + J_{m+4}(k_{m+2,n'}r)\Big] + \frac{k^2_{m-2,n'}(a^2-b^2)}{J_{m-1}(k_{m-2,n'})}\times \\
&\Big[J_{m-4}(k_{m-2,n'}r) - 2J_{m-2}(k_{m-2,n'}r) + J_m(k_{m-2,n'}r)\Big] + 8i\hbar k_{mn'}\left(\dot{a}a^3 + b^3\dot{b}\right)\mu r^3 \times \\
&\frac{J_{m-1}(k_{mn'}r) - J_{m+1}(k_{mn'}r)}{J_{m+1}(k_{mn'})} + 4r\hbar^2 k_{mn'}\left(a^2+b^2\right)\frac{J_{m-1}(k_{mn'}r) - J_{m+1}(k_{mn'}r)}{J_{m+1}(k_{mn'})} + \\
&2r\hbar\Bigg(2i\left(a^3\dot{a} - b^3\dot{b}\right)\mu r^2 + \left(b^2-a^2\right)\hbar\Bigg)\Bigg[k_{m+2,n'}\frac{J_{m+1}(k_{m+2,n'}r) - J_{m+3}(k_{m+2,n'}r)}{J_{m+3}(k_{m+2,n'})} + \\
&k_{m-2,n'}\frac{J_{m-3}(k_{m-2,n'}r) - J_{m-1}(k_{m-2,n'}r)}{J_{m-1}(k_{m-2,n'})}\Bigg] + 4r\hbar^2\left(a^2-b^2\right)\Bigg[k_{m+2,n'}(m+2)\times \\
&\frac{J_{m+1}(k_{m+2,n'}r) - J_{m+3}(k_{m+2,n'}r)}{J_{m+3}(k_{m+2,n'})} - k_{m-2,n'}(m-2)\frac{J_{m-3}(k_{m-2,n'}r) - J_{m-1}(k_{m-2,n'}r)}{J_{m-1}(k_{m-2,n'})}\Bigg] \\
&- 8\left(\dot{a}^2a^4 + b^4\dot{b}^2\right)\mu^2r^4\frac{J_m(k_{mn'}r)}{J_{m+1}(k_{mn'})} + 16i\left(\dot{a}a^3 + b^3\dot{b}\right)\mu\hbar r^2\frac{J_m(k_{mn'}r)}{J_{m+1}(k_{mn'})} \\
&- 8\left(a^2+b^2\right)m^2\hbar^2\frac{J_m(k_{mn'}r)}{J_{m+1}(k_{mn'})} - 4\left(a^4\dot{a}^2 - b^4\dot{b}^2\right)\mu^2r^4\Bigg[\frac{J_{m+2}(k_{m+2,n'}r)}{J_{m+3}(k_{m+2,n'})} \\
&+ \frac{J_{m-2}(k_{m-2,n'}r)}{J_{m-1}(k_{m-2,n'})}\Bigg] - 4\left(b^2-a^2\right)\hbar^2\Bigg[(m+2)^2\frac{J_{m+2}(k_{m+2,n'}r)}{J_{m+3}(k_{m+2,n'})} + (m-2)^2\times \\
&\frac{J_{m-2}(k_{m-2,n'}r)}{J_{m-1}(k_{m-2,n'})}\Bigg] - 8i\hbar\left(\left(b^3\dot{b} - a^3\dot{a}\right)\mu r^2 - i\left(a^2-b^2\right)\hbar\right)\times \\
&\Bigg[(m+2)\frac{J_{m+2}(k_{m+2,n'}r)}{J_{m+3}(k_{m+2,n'})} - (m-2)\frac{J_{m-2}(k_{m-2,n'}r)}{J_{m-1}(k_{m-2,n'})}\Bigg]\Bigg\}. \qquad \text{(B.33)}
\end{aligned}
$$

Now the energy is given by

$$
\begin{aligned}
&E(t) = \langle\Psi|\, H(t)\, |\Psi\rangle = \sum_{m',n',m,n}\int_0^1\int_0^{2\pi}\Phi^*_{n'm'}(r,\phi)H(r,\phi,t)\Phi_{nm}(r,\phi)drd\phi = \\
&\sum_{m,n,n'} c^*_{m,n'}(t)\Big[c_{m,n}(t)s^1_{n,m,n'}(t) + c_{m-2,n}(t)s^2_{n,m,n'}(t) + c_{m+2,n}(t)s^3_{n,m,n'}(t)\Big], \qquad \text{(B.34)}
\end{aligned}
$$

where the $s^i_{n,m,n'}(t)$ are defined by

$$\begin{aligned}
s^1_{n,m,n'}(t) = -\frac{1}{4a^2b^2\mu J_{m+1}(k_{mn})J_{m+1}(k_{mn'})}\Bigg\{ & 2\hbar^2 k^2_{mn'}(a^2+b^2)\Big[L^1_{nmn'} - 2L^2_{nmn'} + \\
L^3_{nmn'}\Big] + 8i\hbar k_{mn'}\left(\dot{a}a^3 + b^3\dot{b}\right)\mu\left[L^{19}_{nmn'} - L^{20}_{nmn'}\right] & + 4\hbar^2 k_{mn'}(a^2+b^2)\left[L^{10}_{nmn'} - L^{11}_{nmn'}\right] \\
- 8\left(\dot{a}^2a^4 + b^4\dot{b}^2\right)\mu^2 L^{16}_{nmn'} & + 16i\left(\dot{a}a^3 + b^3\dot{b}\right)M\mu\hbar L^2_{nmn'} \\
& - 4k_{mn'}(a^2+b^2)m\hbar^2\left[L^{10}_{nmn'} + L^{11}_{nmn'}\right]\Bigg\} \qquad (B.35)
\end{aligned}$$

$$\begin{aligned}
s^2_{n,m,n'}(t) = -\frac{1}{4a^2b^2\mu J_{m+1}(k_{mn})J_{m-1}(k_{m-2,n'})}\Bigg\{ & \hbar^2 k^2_{m-2,n'}(a^2-b^2)\Big[L^7_{nmn'} - 2L^8_{nmn'} \\
+ L^9_{nmn'}\Big] + k_{m-2,n'}(L^{23}_{nmn'} - L^{24}_{nmn'})4i\hbar\mu\left(\dot{a}a^3 - \dot{b}b^3\right) & + k_{m-2,n'}(L^{12}_{nmn'} - L^{13}_{nmn'})2\hbar^2(b^2-a^2) \\
- 4k_{m-2,n'}\hbar^2(m-2)(a^2-b^2)(L^{12}_{nmn'} - L^{13}_{nmn'}) & - 4\left(a^4\dot{a}^2 - b^4\dot{b}^2\right)\mu^2 L^{18}_{nmn'} - \\
2\hbar^2 k_{m-2,n'}(m-2)(b^2-a^2)(L^{12}_{nmn'} + L^{13}_{nmn'}) & + 8i\hbar\mu\left(b^3\dot{b} - a^3\dot{a}\right)(m-2)L^8_{nmn'} \\
& + 4k_{m-2,n'}\hbar^2(a^2-b^2)(L^{12}_{nmn'} + L^{13}_{nmn'})\Bigg\} \qquad (B.36)
\end{aligned}$$

$$\begin{aligned}
s^3_{n,m,n'}(t) = -\frac{1}{4a^2b^2\mu J_{m+1}(k_{mn})J_{m+3}(k_{m+2,n'})}\Bigg\{ & \hbar^2 k^2_{m+2,n'}(a^2-b^2)\Big[L^4_{nmn'} - 2L^5_{nmn'} \\
+ L^6_{nmn'}\Big] + k_{m+2,n'}(L^{21}_{nmn'} - L^{22}_{nmn'})4i\hbar\mu\left(\dot{a}a^3 - \dot{b}b^3\right) & + k_{m+2,n'}(L^{14}_{nmn'} - L^{15}_{nmn'})2\hbar^2(b^2-a^2) \\
+ 4\hbar^2 k_{m+2,n'}(m+2)(a^2-b^2)(L^{14}_{nmn'} - L^{15}_{nmn'}) & - 4\left(a^4\dot{a}^2 - b^4\dot{b}^2\right)\mu^2 L^{17}_{nmn'} - \\
2k_{m+2,n'}\hbar^2(m+2)(b^2-a^2)(L^{14}_{nmn'} + L^{15}_{nmn'}) & - 8i\hbar\mu\left(b^3\dot{b} - a^3\dot{a}\right)(m+2)L^5_{nmn'} \\
& - 4k_{m+2,n'}\hbar^2(a^2-b^2)(L^{14}_{nmn'} + L^{15}_{nmn'})\Bigg\}. \qquad (B.37)
\end{aligned}$$

B.7 Symmetries

$$\begin{aligned}
L^{19}_{n,-m,n'} &= -L^{20}_{n,m,n'} \\
L^{20}_{n,-m,n'} &= -L^{19}_{n,m,n'} \\
L^{21}_{n,-m,n'} &= -L^{24}_{n,m,n'} \\
L^{22}_{n,-m,n'} &= -L^{23}_{n,m,n'} \\
L^{23}_{n,-m,n'} &= -L^{22}_{n,m,n'} \\
L^{24}_{n,-m,n'} &= -L^{21}_{n,m,n'}
\end{aligned}$$

$$
\begin{aligned}
f^7_{n,-m,n'} &= f^7_{n,m,n'} \\
f^8_{n,-m,n'} &= f^9_{n,m,n'} \\
f^9_{n,-m,n'} &= f^8_{n,m,n'}
\end{aligned}
$$

$$
\begin{aligned}
s^1_{n,-m,n'} &= s^1_{n,m,n'} \\
s^2_{n,-m,n'} &= s^3_{n,m,n'} \\
s^3_{n,-m,n'} &= s^2_{n,m,n'}
\end{aligned}
$$

$$s^1_{n,m,n'} = s^{1*}_{n',m,n}$$
$$s^2_{n,m,n'} = s^{2*}_{n',-m+2,n}$$
$$s^3_{n,m,n'} = s^{3*}_{n',-m-2,n}$$

Bibliography

[1] H.-J. Stöckmann, *Quantum Chaos: An Introduction*, Cambridge University Press, 1999.

[2] D. Weiss, M. L. Roukes, A. Menschig, P. Grambow, K. von Klitzing, and G. Weimann, *Electron pinball and commensurate orbits in a periodic array of scatterers*, Physical Review Letters **66**, 2790 (1991).

[3] C. M. Marcus, R. M. Westervelt, P. F. Hopkins, and A. C. Gossard, *Phase breaking in ballistic quantum dots: Experiment and analysis based on chaotic scattering*, Physical Review Letters **69**, 2460 (1992).

[4] V. Milner, J. L. Hanssen, W. C. Campbell, and M. G. Raizen, *Optical Billiards for Atoms*, Physical Review Letters **86**, 1514 (2001).

[5] N. Friedman, A. Kaplan, D. Carasso, and N. Davidson, *Observation of Chaotic and Regular Dynamics in Atom-Optics Billiards*, Physical Review Letters **86**, 1518 (2001).

[6] H.-J. Stöckmann and J. Stein, *Quantum chaos in blliards studied by microwave absorption*, Physical Review Letters **94**, 2215 (1990).

[7] H. D. Gräf, H. L. Harney, H. Lengeler, C. H. Lewenkopf, C. Rangacharyulu, A. Richter, P. Schardt, and H. A. Weidenmüller, *Distribution of eigenmodes in a superconducting stadium blliard with chaotic dynamics*, Physical Review Letters **69**, 1296 (1992).

[8] J. U. Nöckel and A. D. Stone, *Ray and wave chaos in asymmetric resonant optical cavities*, Nature **385**, 45 (1997).

[9] C. Gmachl, F. Capasso, E. E. Narimanov, J. U. Nöckel, A. D. Stone, J. Faist, D. L. Sivco, and A. Y. Cho, *High-Power Directional Emission from Microlasers with Chaotic Resonators*, Science **280**, 1556 (1998).

[10] S.-Y. Lee, S. Rim, J.-W. Ryu, T.-Y. Kwon, M. Choi, and C.-M. Kim, *Quasiscarred Resonances in a Spiral-Shaped Microcavity*, Physical Review Letters **93**, 164102 (2004).

[11] S. C. Creagh, *Directional Emission from Weakly Eccentric Resonators*, Physical Review Letters **98**, 153901 (2007).

[12] J. Lee, S. Rim, J. Cho, and C.-M. Kim, *Resonances near the Classical Separatrix of a Weakly Deformed Circular Microcavity*, Physical Review Letters **101**, 064101 (2008).

[13] T.-D. Lee, C.-Y. Chen, Y. Lin, M.-C. Chou, T. ho Wu, and R.-K. Lee, *Surface-Structure-Assisted Chaotic Mode Lasing in Vertical Cavity Surface Emitting Lasers*, Physical Review Letters **101**, 084101 (2008).

[14] G. Casati, C. Mejia-Monasterio, and T. Prosen, *Increasing Thermoelectric Efficiency: A Dynamical Systems Approach*, Physical Review Letters **101**, 016601 (2008).

[15] G. M. Zaslavsky, *Chaotic dynamics and the origin of statistical laws*, Physics Today **52**, 39 (1999).

[16] D. A. Egolf, *Equilibrium regained: from nonequilibrium chaos to statistical mechanics*, Science **287**, 101 (2000).

[17] L. A. Bunimovich and C. P. Dettmann, *Open Circular Billiards and the Riemann Hypothesis*, Physical Review Letters **94**, 100201 (2005).

[18] A. Pais, *Niels Bohr's Times - Physics, Philosophy and Policy*, Oxford University Press, 1991.

[19] G. Abal, R. Donangelo, and C. O. Dorso, *One-body dissipation at intermediate nuclear connection regimes*, Physical Review C **46**, 380 (1992).

[20] E. Fermi, *On the Origin of the Cosmic Radiation*, Physical Review **75**, 1169 (1949).

[21] G. D. Birkhoff, *Dynamical systems*, Colloquium publications, American Mathematical Society; 9, American Math. Society, 1927.

[22] M. V. Berry, *Regularity and chaos in classical mechanics, illustrated by three deformations of a circular 'billiard'*, European Journal of Physics **2**, 91 (1981).

[23] L. A. Bunimovich, *On billiards close to dispersing*, Mathematical USSR Sbornik **95**, 49 (1974).

[24] L. A. Bunimovich, *The ergodic properties of certain billiards*, Funkt. Anal. Prilozh. **8**, 73 (1974).

[25] L. A. Bunimovich, *On the ergodic properties of nowhere dispersing billiards*, Communications in Mathematical Physics **65**, 295 (1979).

[26] L. A. Bunimovich, Y. G. Sinai, and N. I. Chernov, *Markov paritions for dispersing billiards*, Communications in Mathematical Physics **78**, 247 (1980).

[27] L. A. Bunimovich, *A theorem on ergodicity of two-dimensional hyperbolic billiards*, Communications in Mathematical Physics **130**, 599 (1990).

[28] Y. G. Sinai, *Dynamical systems with elastic reflections. Ergodic properties of dispersing billiards*, Russian Mathematical Surveys **25**, 137 (1970).

[29] L. Bunimovich, *Mushrooms and other billiards with divided phase space*, Chaos **11**, 802 (2001).

[30] B. Dietz, T. Friedrich, M. Miski-Oglu, A. Richter, T. H. Seligman, and K. Zapfe, *Nonperiodic echoes from mushroom billiard hats*, Physical Review E **74**, 056207 (2006).

[31] E. G. Altmann, A. E. Motter, and H. Kantz, *Stickiness in mushroom billiards*, Chaos **15**, 033105 (2005).

[32] E. G. Altmann, A. E. Motter, and H. Kantz, *Stickiness in Hamiltonian systems: From sharply divided to hierarchical phase space*, Physical Review E **73**, 026207 (2006).

[33] L. A. Bunimovich and G. Del Magno, *Track Billiards*, Communications in Mathematical Physics **288**, 699 (2009).

[34] M. Tabor, *Chaos and integrability in nonlinear dynamics*, Wiley, New York, 1989.

[35] M. C. Gutzwiller, *Chaos in Classical and Quantum Mechanics*, Springer, New York, 1990.

[36] O. Bohigas, M. J. Giannoni, and C. Schmit, *Characterization of Chaotic Quantum Spectra and Universality of Level Fluctuation Laws*, Physical Review Letters **52**, 1 (1984).

[37] J. D. Jackson, *Classical electrodynamics*, John Wiley & Sons, New York, 1999.

[38] F. Melde, *Chladnis's Leben und Wirken*, N. G. Elwert'sche Verlagsbuchhandlung, Marburg, 1888.

[39] H. Alt, H. D. Gräf, H. L. Harney, R. Hofferbert, H. Lengeler, A. Richter, P. Schardt, and H. A. Weidenmüller, *Gaussian Orthogonal Ensemble Statistics in a Microwave Stadium Billiard with Chaotic Dynamics: Porter-Thomas Distribution and Algebraic Decay of Time Correlations*, Physical Review Letters **74**, 62 (1995).

[40] B. Dietz, T. Friedrich, M. Miski-Oglu, A. Richter, and F. Schaefer, *Spectral properties of Bunimovich mushroom billiards*, Physical Review E **75**, 035203 (2007).

[41] T. Miyaguchi, *Escape time statistics for mushroom billiards*, Physical Review E **75**, 066215 (2007).

[42] A. Y. Abul-Magd, B. Dietz, T. Friedrich, and A. Richter, *Spectral fluctuations of billiards with mixed dynamics: From time series to superstatistics*, Physical Review E **77**, 046202 (2008).

[43] B. Dietz, T. Friedrich, M. Miski-Oglu, A. Richter, and F. Schafer, *Properties of nodal domains in a pseudointegrable barrier billiard*, Physical Review E **78**, 045201 (2008).

[44] J. D. Bodyfelt, M. C. Zheng, T. Kottos, U. Kuhl, and H.-J. Stockmann, *Probing Localization in Absorbing Systems via Loschmidt Echos*, Physical Review Letters **102**, 253901 (2009).

[45] B. Dietz, T. Friedrich, H. L. Harney, M. Miski-Oglu, A. Richter, F. Schafer, J. Verbaarschot, and H. A. Weidenmuller, *Induced Violation of Time-Reversal Invariance in the Regime of Weakly Overlapping Resonances*, Physical Review Letters **103**, 064101 (2009).

[46] T. Tudorovskiy, R. Höhmann, U. Kuhl, and H.-J. Stöckmann, *On the theory of cavities with point-like perturbations: part I. General theory*, Journal of Physics A: Mathematical and Theoretical **41**, 275101 (22pp) (2008).

[47] S. Datta, *Electronic transport in mesoscopic systems*, Cambridge studies in semiconductor physics and microelectronic engineering, Cambridge Univ. Press, 2003.

[48] D. Weiss and K. Richter, *Complex and quantized electron motion in antidot arrays*, Physica D **83**, 290 (1995).

[49] M. F. Crommie, C. P. Lutz, and D. M. Eigler, *Confinement of electrons to quantum corrals on a metal surface*, Science **262**, 218 (1993).

[50] M. F. Crommie, C. P. Lutz, and D. M. Eigler, *Imaging standing waves in a two-dimensional electron gas*, Nature **363**, 524 (1993).

[51] N. Friedmann, L. Khaykovich, R. Ozeri, and N. Davidson, *Compression of cold atoms to very high densities in a rotating-beam blue-detuned optical trap*, Physical Review A **61**, 031403 (2000).

[52] A. Kaplan, N. Friedman, M. Andersen, and N. Davidson, *Observation of Islands fo Stability in Soft Wall Atom-Optics Billiards*, Physical Review Letters **87**, 2741011 (2001).

[53] M. F. Andersen, A. Kaplan, N. Friedmann, and N. Davidson, *Stable islands in chaotic atom-optics billiards, caused by curved trajectories*, Journal of Physics B: Atomic, Molecular and Optical Physics **35**, 2183 (2002).

[54] R. Blandford and D. Eichler, *Particle acceleration at astrophysical shocks: A theory of cosmic ray origin*, Physics Reports **154**, 1 (1987).

[55] A. Veltri and V. Carbone, *Radiative Intermittent Events during Fermi's Stochastic Acceleration*, Physical Review Letters **92**, 143901 (2004).

[56] K. Kobayakawa, Y. S. Honda, and T. Samura, *Acceleration by oblique shocks at supernova remnants and cosmic ray spectra around the knee region*, Physical Review D **66**, 083004 (2002).

[57] M. A. Malkov, *Ion leakage from quasiparallel collisionless shocks: Implications for injection and shock dissipation*, Physical Review E **58**, 4911 (1998).

[58] G. Michalek, M. Ostrowski, and R. Schlickeiser, *Cosmic-Ray Momentum Diffusion in Magnetosonic versus Alfvénic Turbulent Field*, Solar Physics **184**, 339 (1999).

[59] A. V. Milovanov and L. M. Zelenyi, *"Strange" Fermi processes and power-law nonthermal tails from a self-consistent fractional kinetic equation*, Physical Review E **64**, 052101 (2001).

[60] F. Saif, I. Bialynicki-Birula, M. Fortunato, and W. P. Schleich, *Fermi accelerator in atom optics*, Physical Review A **58**, 4779 (1998).

[61] A. Steane, P. Szriftgiser, P. Desbiolles, and J. Dalibard, *Phase Modulation of Atomic de Broglie Waves*, Physical Review Letters **74**, 4972 (1995).

[62] G. Lanzanò, E. De Filippo, D. Mahboub, H. Rothard, S. Aiello, A. Anzalone, S. Cavallaro, A. Elanique, E. Geraci, M. Geraci, F. Giustolisi, A. Pagano, and G. Politi, *Fast Electron Production at Intermediate Energies: Evidence for Fermi Shuttle Acceleration and for Deviations from Simple Relativistic Kinematics*, Physical Review Letters **83**, 4518 (1999).

[63] M. A. Lieberman and A. J. Lichtenberg, *Stochastic and Adiabatic Behavior of Particles Accelerated by Periodic Forces*, Physical Review A **5**, 1852 (1972).

[64] L. D. Pustyl'nikov, *On Ulam's problem*, Theoretical and Mathematical Physics **57**, 1035 (1983).

[65] A. J. Lichtenberg, M. A. Lieberman, and R. H. Cohen, *Fermi acceleration revisited*, Physica D **1**, 291 (1980).

[66] A. J. Lichtenberg and M. A. Lieberman, *Regular and chaotic dynamics*, Applied mathematical sciences; Vol. 38, Springer, 1992.

[67] E. D. Leonel and P. V. E. McClintock, *A hybrid Fermi-Ulam-bouncer model*, Journal of Physics A: Mathematical and General **38**, 823 (2005).

[68] A. K. Karlis, P. K. Papachristou, F. K. Diakonos, V. Constantoudis, and P. Schmelcher, *Hyperacceleration in a Stochastic Fermi-Ulam Model*, Physical Review Letters **97**, 194102 (2006).

[69] D. G. Ladeira and J. K. L. da Silva, *Scaling properties of a simplified bouncer model and of Chirikov's standard map*, Journal of Physics A: Mathematical and Theoretical **40**, 11467 (2007).

[70] A. L. P. Livorati, D. G. Ladeira, and E. D. Leonel, *Scaling investigation of Fermi acceleration on a dissipative bouncer model*, Physical Review E **78**, 056205 (2008).

[71] K.-C. Liu, J. Friend, and L. Yeo, *The behavior of bouncing disks and pizza tossing*, Europhysics Letters **85**, 60002 (5pp) (2009).

[72] J. J. Barroso, M. V. Carneiro, and E. E. N. Macau, *Bouncing ball problem: Stability of the periodic modes*, Physical Review E **79**, 026206 (2009).

[73] Z. J. Kowalik, M. Franaszek, and P. Pierański, *Self-reanimating chaos in the bouncing-ball system*, Physical Review A **37**, 4016 (1988).

[74] S. Celaschi and R. L. Zimmerman, *Evolution of a two-parameter chaotic dynamics from universal attractors*, Physics Letters A **120**, 447 (1987).

[75] G. D. Valle, M. Savoini, M. Ornigotti, P. Laporta, V. Foglietti, M. Finazzi, L. Duo, and S. Longhi, *Experimental Observation of a Photon Bouncing Ball*, Physical Review Letters **102**, 180402 (2009).

[76] A. Y. Loskutov, A. B. Ryabov, and L. G. Akinshin, *Mechanism of Fermi acceleration in dispersing billiards with time-dependent boundaries.*, Journal of Experimental & Theoretical Physics **89**, 966 (1999).

[77] A. Loskutov, A. B. Ryabov, and L. G. Akinshin, *Properties of some chaotic billiards with time-dependent boundaries*, Journal of Physics A: Mathematical and General **33**, 7973 (2000).

[78] A. Loskutov and A. Ryabov, *Particle Dynamics in Time-Dependent Stadium-Like Billiards*, Journal of Statistical Physics **108**, 995 (2002).

[79] S. O. Kamphorst and S. P. de Carvalho, *Bounded gain of energy on the breathing circle billiard*, Nonlinearity **12**, 1363 (1999).

[80] D. G. Ladeira and J. K. L. da Silva, *Scaling features of a breathing circular billiard*, Journal of Physics A: Mathematical and Theoretical **41**, 365101 (13pp) (2008).

[81] R. E. de Carvalho, F. C. Souza, and E. D. Leonel, *Fermi acceleration on the annular billiard*, Physical Review E **73**, 066229 (2006).

[82] R. E. de Carvalho, F. C. de Souza, and E. D. Leonel, *Fermi acceleration on the annular billiard: a simplified version*, Journal of Physics A: Mathematical and General **39**, 3561 (2006).

[83] J. Koiller, R. Markarian, S. O. Kamphorst, and S. P. de Carvalho, *Time-dependent billiards*, Nonlinearity **8**, 983 (1995).

[84] J. Koiller, R. Markarian, S. O. Kamphorst, and S. P. de Carvalho, *Static and Time-Dependent Perturbations of the Classical Elliptical Billiard*, Journal of Statistical Physics **83**, 127 (1996).

[85] S. O. Kamphorst, E. D. Leonel, and J. K. L. da Silva, *The presence and lack of Fermi acceleration in nonintegrable billiards*, Journal of Physics A: Mathematical and Theoretical **40**, F887 (2007).

[86] A. P. Itin, A. I. Neishtadt, and A. A. Vasiliev, *Resonant phenomena in slowly pertubed rectangular billiards*, Physics Letters A **291**, 133 (2001).

[87] A. P. Itin and A. I. Neishtadt, *Resonant phenomena in slowly perturbed elliptic billiards*, Regular and Chaotic Dynamics **8**, 59 (2003).

[88] F. Lenz, F. K. Diakonos, and P. Schmelcher, *Scattering dynamics of driven closed billiards*, Europhysics Letters **79**, 20002 (2007).

[89] F. Lenz, F. K. Diakonos, and P. Schmelcher, *Classical dynamics of the time-dependent elliptical billiard*, Physical Review E **76**, 066213 (2007).

[90] F. Lenz, Time-dependent Classical Billiards, Diploma Thesis, University of Heidelberg, Germany, 2006.

[91] S. W. Doescher and M. H. Rice, *Infinite Square-Well Potential with a Moving Wall*, American Journal of Physics **37**, 1246 (1969).

[92] P. Seba, *Quantum chaos in the Fermi-accelerator model*, Physical Review A **41**, 2306 (1990).

[93] A. J. Makowski and S. T. Dembinski, *Exactly solvable models with time-dependent boundary conditions*, Physics Letters A **154**, 217 (1991).

[94] A. J. Makowski and P. Peplowski, *On the behaviour of quantum systems with time-dependent boundary conditions*, Physics Letters A **163**, 143 (1992).

[95] V. V. Dodonov, A. B. Klimov, and D. E. Nikonov, *Quantum particle in a box with moving walls*, Journal of Mathematical Physics **34**, 3391 (1993).

[96] C. Grosche, *Path ingetral solution of a class of explicitly time-dependent potentials*, Physics Letters A **182**, 28 (1993).

[97] G. Karner, *The Simplified Fermi Accelerator in Classical and Quantum Mechanics*, Journal of Statistical Physics **77**, 867 (1994).

[98] J. F. Willemsen, *Exact solution of the wave dynamics of a particle bouncing chaotically on a periodically oscillating wall*, Physical Review E **50**, 3116 (1994).

[99] D. A. Morales, Z. Parra, and R. Almeida, *On the solution of the Schrdinger equation with time dependent boundary conditions*, Physics Letters A **185**, 273 (1994).

[100] C. Yüce, *Exact solvability of moving boundary problems*, Physics Letters A **327**, 107 (2004).

[101] T. Jana and P. Roy, *A class of exactly solvable Schrdinger equation with moving boundary condition*, Physics Letters A **372**, 2368 (2008).

[102] M. Glasser, J. Mateo, J. Negro, and L. Nieto, *Quantum infinite square well with an oscillating wall*, Chaos, Solitons & Fractals **41**, 2067 (2009).

[103] M. G. Raizen, *Quantum chaos with cold atoms*, Advances in Atomic, Molecular, and Optical Physics **41**, 43 (199).

[104] R. L. Liboff and M. A. Porter, *Quantum chaos for the radially vibrating spherical billiard*, Chaos **10**, 366 (2000).

[105] D. Cohen and D. A. Wisniacki, *Stadium billiard with moving walls*, Physical Review E **67**, 026206 (2003).

[106] S.-J. Chang and R. Friedberg, *Elliptical billiards and Poncelet's theorem*, Journal of Mathematical Physics **29**, 1537 (1988).

[107] M. V. Berry and M. Tabor, *Closed Orbits and regular bound spectrum*, Proceedings of the Royal Society of London, Series A **349**, 101 (1976).

[108] J. C. Gutiérrez-Vega and S. Chávez-Cerda, *Probability distributions in classical and quantum elliptic billiards*, Revista Mexicana de Física **47**, 480 (2001).

[109] C. Petri, Fermi acceleration in the driven ellipse, Diploma Thesis, University of Heidelberg, Germany, 2008.

[110] W. H. Press, *Numerical Recipes in C - The art of scientific computing*, Cambridge Univ. Press, Cambridge, 2002.

[111] E. Ott, *Chaos in dynamical systems*, Cambridge Univ. Press, Cambridge [u.a.], 2008.

[112] G. Benettin, L. Galgani, and J.-M. Strelcyn, *Kolmogorov entropy and numerical experiments*, Physical Review A **14**, 2338 (1976).

[113] G. Benettin, L. Galgani, A. Giorgilli, and J. M. Strelcyn, *Lyapunov characteristic exponents for smooth dynamical systems and for Hamiltonian systems; a method for computing all of them*, Meccanica **15**, 9 (1980).

[114] F. Lenz, C. Petri, F. R. N. Koch, F. K. Diakonos, and P. Schmelcher, *Evolutionary phase space in driven elliptical billiards*, New Journal of Physics **11**, 083035 (2009).

[115] M. H. Abramowitz, *Handbook of mathematical functions*, Dover Publ., New York, 1972.

[116] P. Schmelcher and F. K. Diakonos, *Detecting Unstable Periodic Orbits of Chaotic Dynamical Systems*, Physical Review Letters **78**, 4733 (1997).

[117] P. Schmelcher and F. K. Diakonos, *General approach to the localization of unstable periodic orbits in chaotic dynamical systems*, Physical Review E **57**, 2739 (1998).

[118] D. Pingel, P. Schmelcher, and F. K. Diakonos, *Stability transformation: a tool to solve nonlinear problems*, Physics Reports **400**, 67 (2004).

[119] G. Contopoulos, *Orbits in Highly Perturbed Dynamical Systems. 111. Nonperiodic Orbits*, The Astronomical Journal **76**, 147 (1971).

[120] L. A. Bunimovich, *Relative volume of Kolmogorov-Arnold-Moser tori and uniform distribution, stickiness and nonstickiness in Hamiltonian systems*, Nonlinearity **21**, T13 (2008).

[121] E. G. Altmann, *Intermittend Chaos in Hamiltonian Dynamical Systems*, PhD thesis, University of Wuppertal, 2007.

[122] J. R. Cary, D. F. Escande, and J. L. Tennyson, *Adiabatic-invariant change due to separatrix crossing*, Physical Review A **34**, 4256 (1986).

[123] I. Procaccia and H. Schuster, *Functional renormalization-group theory of universal $1/f$ noise in dynamical systems*, Physical Review A **28**, 1210 (1983).

[124] H. G. Schuster, *Deterministic chaos*, Physik-Verl., Weinheim, 1984.

[125] M. E. J. Newman, *Power laws, Pareto distributions and Zipf's law.*, Contemporary Physics **46**, 323 (2005).

[126] A. Clauset, C. R. Shalizi, and M. E. J. Newman, *Power-law distributions in empirical data*, SIAM Reviews (in press) (2009).

[127] I. C. Percival, *A variational principle for invariant tori of fixed frequency*, Journal of Physics A: Mathematical and General **12**, L57 (1979).

[128] J. D. Meiss, *Symplectic maps, variational principles, and transport*, Review of Modern Physics **64**, 795 (1992).

[129] R. Mackay, J. Meiss, and I. Percival, *Transport in Hamiltonian systems*, Physica D **13**, 55 (1984).

[130] S. Dawson, C. Grebogi, T. Sauer, and J. A. Yorke, *Obstructions to Shadowing When a Lyapunov Exponent Fluctuates about Zero*, Physical Review Letters **73**, 1927 (1994).

[131] T. Sauer, C. Grebogi, and J. A. Yorke, *How Long Do Numerical Chaotic Solutions Remain Valid?*, Physical Review Letters **79**, 59 (1997).

[132] Y.-C. Lai, Z. Liu, G.-W. Wei, and C.-H. Lai, *Shadowability of Statistical Averages in Chaotic Systems*, Physical Review Letters **89**, 184101 (2002).

[133] T. Sauer, *Chaotic itinerancy based on attractors of one-dimensional maps*, Chaos **13**, 947 (2003).

[134] W. Ott and J. A. Yorke, *When Lyapunov exponents fail to exist*, Physical Review E **78**, 056203 (2008).

[135] F. Lenz, F. K. Diakonos, and P. Schmelcher, *Tunable Fermi Acceleration in the Driven Elliptical Billiard*, Physical Review Letters **100**, 014103 (2008).

[136] M. I. Miah, *Diffusive to drift-diffusion crossover of spin transport in the low-field regime*, Applied Physics Letters **92**, 092104 (2008).

[137] E. W. Montroll and G. H. Weiss, *Random Walks on Lattices. II*, Journal of Mathematical Physics **6**, 167 (1965).

[138] V. Gelfreich and D. Turaev, *Fermi acceleration in non-autonomous billiards*, Journal of Physics A: Mathematical and Theoretical **41**, 212003 (2008).

[139] V. Gelfreich and D. Turaev, *Unbounded Energy Growth in Hamiltonian Systems with a Slowly Varying Parameter*, Communications in Mathematical Physics **283**, 769 (2008).

[140] F. Lenz, C. Petri, F. R. N. Koch, and P. Schmelcher, A fresh view on Fermi acceleration in driven two-dimensional billiards, in *Complex Phenomena in Nanoscale Systems*, edited by D. Matrasulov and G. Casati, NATO Science for Peace and Security Series - B: Physics and Biophysics, page 209, Springer, Netherlands, 2009.

[141] F. Lenz, C. Petri, F. K. Diakonos, and P. Schmelcher, *Dynamical crossover from sub- to normal diffusion in driven elliptical billiards*, submitted to Phys. Rev. E, 2009.

[142] E. D. Leonel, D. F. M. Oliveira, and A. Loskutov, *Fermi acceleration and scaling properties of a time dependent oval billiard*, Chaos **19**, 033142 (2009).

[143] R. van Zon and T. W. Ruijgrok, *The elliptic billiard: subtleties of separability*, European Journal of Physics **19**, 77 (1998).

[144] A. J. S. Traiber, A. J. Fendrik, and M. Bernath, *Level crossings and commuting observables for the quantum elliptic billiard*, Journal of Physics A: Mathematical and General **22**, L365 (1989).

[145] Y. Ayant and R. Arvieu, *Semiclassical study of particle motion in two-dimensional and three-dimensional elliptical boxes. I*, Journal of Physics A: Mathematical and General **20**, 397 (1987).

[146] R. Arvieu and Y. Ayant, *Semiclassical study of particle motion in two-dimensional and three-dimensional elliptical boxes. II*, Journal of Physics A: Mathematical and General **20**, 1115 (1987).

[147] H. Waalkens, J. Wiersig, and H. R. Dullin, *Elliptic Quantum Billiard*, Annals of Physics **260**, 50 (1997).

[148] J. C. Gutiérrez-Vega, S. Chávez-Cerda, and R. M. Rodríguez-Dagnino, *Free oscillations in an elliptic membrane*, Revista Mexicana de Física **46**, 613 (1999).

[149] P. M. Morse and H. Feshbach, *Methods of theoretical physics*, McGraw-Hill, New York, 1953.

[150] R. W. Robinett, *Visualizing the solutions for the circular infinite well in quantum and classical mechanics*, American Journal of Physics **64**, 440 (1996).

[151] R. W. Robinett, *Quantum mechanics of the two-dimensional circular billiard plus baffle system and half-integral angular momentum*, European Journal of Physics **24**, 231 (2003).

[152] J. Gungman and B. Gough, *GSL: GNU Scientific Library.*

[153] F. K. Diakonos, Private communications, 2009.

[154] G. Bader and P. Deuflhard, *A Semi-Implicit Mid-Point Rule for Stiff Systems of Ordinary Differential Equations.*, Numerische Mathematik **41**, 373 (1983).

[155] G. Casati, B. V. Chirikov, F. M. Izraelev, and J. Ford, Stochastic behavior of a quantum pendulum under a periodic perturbation, in *Stochastic Behavior in Classsical and Quantum Hamiltonian Systems*, edited by G. Casati and J. Ford, volume 93 of *Lecture Notes in Physics*, Springer-Verlag Berlin, 1979.

[156] B. V. Chirikov, F. M. Izrailev, and D. L. Shepelyansky, *Dynamical stochasticity in classical and quantum mechanics*, Sov. Sci. Rev. C **2**, 209 (1981).

[157] B. V. Chirikov, F. M. Izrailev, and D. L. Shepelyansky, *Quantum chaos: localization vs. ergodicity*, Physica D **33**, 77 (1988).

[158] P. W. Anderson, *Absence of Diffusion in Certain Random Lattices*, Physical Review **109**, 1492 (1958).

[159] L. Landau, *On the theory of transfer of energy at collisions II*, Phys. Z. Sowjetunion **2**, 46 (1932).

[160] C. Zener, *Non-Adiabatic Crossing of Energy Levels*, Proceedings of the Royal Society of London, Series A **137**, 696 (1932).

Danksagung

Bedanken möchte ich mich vor allem bei meinem Betreuer **Peter Schmelcher** für die fruchtbare Zusammenarbeit während der letzten drei Jahre. Die zahlreichen wissenschaftlichen Diskussionen fanden stets in einer sehr angenehmen Atmosphäre statt und waren oft inspirierend.

Special thanks goes to **Fotis Diakonos**, who had always time when I had a problem and, even better, in most of the cases an answer. I enjoyed his company very much, especially when snorkeling together on Crete.

Danken möchte ich auch meinem Kollegen **Christoph Petri**, einiges der hier vorgestellten Arbeit habe ich gemeinsam mit ihm gemacht. Bei ihm und **Bernd Hezel** möchte ich mich auch für die immer abwechslungsreiche Atmosphäre im Büro bedanken.

Dank geht an **Michael Mayle** für die Beantwortung der LaTeX-Fragen sowie für die LaTeX-Vorlagen.

Eine nette Abwechslung waren die Doppelkopfrunden und die Kickerspiele, danke an **Michael M, Michael B, Stephan, Martin, Siggi, Kaspar, Bernd, Christoph P, Alex, Marc, Johannes, Georg, Christoph H**.

Danke an **Marko Robnik** und **Davron Matrasulov** für die schönen Aufenthalte in Slowenien bzw. Usbekistan.

Bedanken möchte ich mich bei allen **Freunden** und meiner **Familie** für die Unterstützung während der letzten drei Jahre, insbesondere bei meinem **Vater** für das Korrekturlesen.

Ein ganz besonderer Dank geht an **Christine**, die mich immer unterstützt hat und auch immer Verständnis für die Arbeitszeiten eines Physik-Doktorandens hatte.